

GC
7.1
C43
1982

THE DEVELOPMENT OF NONLINEAR SURFACE AND
INTERNAL WAVE GROUPS

by

TERESA KATHLEEN CHERESKIN
B.S. University of Wisconsin-Madison
1976

SUBMITTED IN PARTIAL FULFILLMENT
OF THE REQUIREMENTS FOR THE
DEGREE OF
DOCTOR OF PHILOSOPHY

at the
MASSACHUSETTS INSTITUTE OF TECHNOLOGY

and the

WOODS HOLE OCEANOGRAPHIC INSTITUTION
August 1982

Signature of Author _____

Joint Program in Oceanography, Massachusetts Institute of
Technology - Woods Hole Oceanographic Institution, and
the Department of Meteorology and Physical Oceanography,
Massachusetts Institute of Technology, August 1982.

Certified by _____

Erik Mollo-Christensen
Thesis supervisor

Accepted by _____

Joseph Pedlosky
Chairman, Joint Committee for Physical Oceanography

1983

W.H.O.I.

THE DEVELOPMENT OF NONLINEAR SURFACE AND
INTERNAL WAVE GROUPS

by

Teresa Kathleen Chereskin

Submitted to the MIT-WHOI Joint Program
in Physical Oceanography on 6 August 1982
in partial fulfillment of the requirements
for the degree of Doctor of Philosophy

ABSTRACT

The development of nonlinear surface and internal wave groups is investigated. Surface wave evolution was observed in an unusually long wave channel as a function of steepness and group length. Dissipation and frequency downshifting were important characteristics of the long-time evolution. The amplitude and phase modulations were obtained using the Hilbert transform and specified as an initial condition to the cubic nonlinear Schrodinger equation, which was solved numerically. This equation is known to govern the slowly varying complex modulation envelope of gravity waves on deep water. When dissipation was included, the model compared quite well with the observations. Phase modulation was used to interpret the long-time behavior, using the phase evolution of exact asymptotic solutions as a guide. The wave groups exhibited a long-time coherence but not the recurrence predicted by the inviscid theory.

An oceanic field study of the generation of groups of large amplitude internal waves by stratified tidal flow over a submarine ridge indicates that the large amplitude and asymmetry of the topography are critical in determining the type of flow response. The calculated Froude numbers, response length scale and duration differ markedly between the two phases of the tide due to the asymmetry.

Thesis supervisor: Dr. Erik Mollo-Christensen
Professor of Physical Oceanography, MIT

ACKNOWLEDGEMENTS

I would like to especially thank my advisor, Erik Mollo-Christensen, for introducing me to surface waves and for infusing me with some of his insight and enthusiasm for the subject. In particular, I thank him for his confidence in my abilities, his patience while my ideas jelled and for allowing me a great deal of independence. I thank all the members of my thesis committee for their discussions and suggestions. To Bob Beardsley for discussion of the Massachusetts Bay experiment, to C. C. Mei for suggesting use of the Schrodinger model and the bound state phenomenon and to Ken Melville for suggesting the Hilbert transform technique, I am grateful.

The surface wave experiments were carried out at Bay St. Louis, MI. in cooperation with Dr. Ming Su of NORDA. I thank him for making available the experimental facility, for his help with the experiments and for doing additional repeat experiments. I also thank Paul Marler and Richard Myrick for their assistance with the experiments.

A great many people helped with the Massachusetts Bay field study. I thank Mel Briscoe for suggesting the study, and Bill Dewar for helping to plan it. Without the support of Bob Beardsley and Erik Mollo-Christensen the work could not have been done. The Departments of Earth and Planetary Sciences and Meteorology and Physical Oceanography generously donated their educational time on the Sea Grant vessel R/V Edgerton. The cooperation of H. Ossinger and A. Turner of R/V Edgerton is gratefully acknowledged. Finally, I thank D. Aubrey, M. Briscoe, J. Dean, M. Delaney, J. Ellis, R. Limeburner, A. Mascarenhas, K. Morey, M. Orr and J. Vermesch for equipment, advice and help on the cruise.

I am grateful to Gideon Sahar, Ken Morey, Dick Yue and Sandro Rimbaldi for use of their computer programs. Gideon Sahar was particularly generous in providing software. I wish to thank Ken Morey for keeping the computer going when I needed it and for his engineering expertise. For the havoc I hath wrought on his computers, I humbly apologize.

Thanks to Jane McNabb and Virginia Mills for the riverside view and to Sam Ricci and Betsey Connors for drafting assistance.

Finally, I wish to thank my family, friends and colleagues for their friendship and support.

I am grateful for the research assistantship provided by the Office of Naval Research contract no. N00014-80-C-0273.

Table of Contents

Abstract	2
Acknowledgments	3
Description of figures	6
List of tables	22
CHAPTER 1. INTRODUCTION	23
1.1 Background	23
1.2 Surface waves	26
1.3 Internal waves	35
CHAPTER 2. LABORATORY OBSERVATIONS OF SURFACE WAVE GROUP DEVELOPMENT	39
2.1 Introduction	39
2.2 Measurements	42
2.3 Analysis and results	48
2.3.1 Description of evolution	48
2.3.2 Downshifting	65
2.3.3 Dissipation of wave energy	81
2.3.4 Modulations	92
2.4 Discussion and summary	113
APPENDIX 2.A DATA PROCESSING METHODS	117
CHAPTER 3. MODELLING OF SURFACE WAVE GROUP DEVELOPMENT	126
3.1 Introduction	126
3.2 Formulation of the Schrodinger model	131
3.2.1 Background	131
3.2.2 Simple derivation	136
3.2.3 Properties of the Schrodinger equation	140
3.3 Numerical model	144

3.4	Exact solutions	146
3.4.1	Radiation	148
3.4.2	Soliton	155
3.4.3	Bound state	155
3.4.4	Soliton plus radiation	167
3.4.5	Bound state plus radiation	175
3.4.6	Divergent solitons	183
3.4.7	Summary	193
3.5	Inclusion of dissipation	194
3.6	Comparison of model and observations	197
3.7	Discussion and summary	272
CHAPTER 4.	OCEANIC OBSERVATIONS OF INTERNAL WAVE GROUP DEVELOPMENT	277
4.1	Introduction	277
4.2	Measurements	283
4.3	Analysis and Results	287
4.4	Discussion	307
4.5	Summary	314
CHAPTER 5.	CONCLUSIONS	316
5.1	Surface waves	316
5.2	Internal waves	319
References		321
Biographical statement		327

DESCRIPTION OF FIGURES

- 2.1 Experimental facility. Outdoor flood plain, Bay St. Louis, MI.
- 2.2 Orientation of wavemaker and wave channel within the 100 by 340 meter basin and the profile of the hyperbolic forward face of the wavemaker.
- 2.3 Wave group development with fetch for a group of 10 waves of initial steepness $ak = .03$ (Exp 78). Amplitude is in centimeters of surface displacement (mean removed). Fetch increases upwards.
- 2.4 Wave group development with fetch for a group of 25 waves of initial steepness $ak = .07$ (Exp 77).
- 2.5 Wave group development with fetch for a group of 10 waves of initial steepness $ak = .10$ (Exp 86).
- 2.6 Wave group development with fetch for a group of 15 waves of initial steepness $ak = .10$ (Exp 87).
- 2.7 Wave group development with fetch for a group of 25 waves of initial steepness $ak = .10$ (Exp 88).
- 2.8 Wave group development with fetch for a group of 15 waves of initial steepness $ak = .15$ (Exp 62).
- 2.9 Wave group development with fetch for a group of 10 waves of initial steepness $ak = .16$ (Exp 21).
- 2.10 Wave group development with fetch for a group of 15 waves of initial steepness $ak = .16$ (Exp 22).
- 2.11 Wave group development with fetch for a group of 25 waves of initial steepness $ak = .16$ (Exp 23)

- 2.12 Maximum entropy (MEM) spectral evolution with fetch for a group of 10 waves of steepness $ak = .03$ (Exp 78). Fetches as indicated. Group was bandpassed on the interval $[.3, 1.3]$ hz centered on the initial carrier frequency 0.80 hz. Filter rolloff occurs at the bandedges.
- 2.13 Maximum entropy (MEM) spectral evolution with fetch for a group of 25 waves of steepness $ak = .07$ (Exp 77). Fetches as indicated. Group was bandpassed on the interval $[.5, 1.5]$ hz centered on the initial carrier frequency 0.96 hz. Filter rolloff occurs at the bandedges.
- 2.14 Maximum entropy (MEM) spectral evolution with fetch for a group of 25 waves of steepness $ak = .10$ (Exp 88). Fetches as indicated. Group was bandpassed on the interval $[.5, 1.5]$ hz centered on the initial carrier frequency 0.96 hz. Filter rolloff occurs at the bandedges.
- 2.15 Same as previous (2.14) except data is unfiltered and spectrum is done on larger interval $[.1, 3.0]$ hz. Notice the first harmonic peak, the loss in resolution of sidebands (15.2 m) and the removal of spurious peaks at the bandedges of the filter.
- 2.16 Maximum entropy (MEM) spectral evolution with fetch for a group of 15 waves of steepness $ak = .15$ (Exp 62). Fetches as indicated. Group was bandpassed on the interval $[.7, 1.7]$ hz centered on the initial carrier frequency 1.20 hz. Filter rolloff occurs at the bandedges.
- 2.17 Maximum entropy (MEM) spectral evolution with fetch for a group of 25 waves of steepness $ak = .16$ (Exp 23). Fetches as indicated. Group was bandpassed on the interval $[.7, 1.7]$ hz centered on the initial carrier frequency 1.20 hz. Filter rolloff occurs at the bandedges.
- 2.18 Same as previous (2.17) except data is unfiltered and spectrum is done on larger interval $[.1, 3.0]$ hz. Notice

the first harmonic peak (6.1 m), the loss in resolution of sidebands (30.5 m) and the removal of spurious peaks at the bandedges of the filter.

- 2.19 Logarithm of packet energy normalized by its initial value plotted versus fetch for a wave group of 10 waves, $ak = .03$ (Exp 78). Least squares line fit to data is also shown.
- 2.20 Logarithm of packet energy normalized by its initial value plotted versus fetch for a wave group of 25 waves, $ak = .07$ (Exp 77). Least squares line fit to data is also shown.
- 2.21 Logarithm of packet energy normalized by its initial value plotted versus fetch for a wave group of 25 waves, $ak = .10$ (Exp 88). Least squares line fit to data is also shown.
- 2.22 Logarithm of packet energy normalized by its initial value plotted versus fetch for a wave group of 15 waves, $ak = .15$ (Exp 62). Least squares line fit to data is also shown.
- 2.23 Logarithm of packet energy normalized by its initial value plotted versus fetch for a wave group of 25 waves, $ak = .16$ (Exp 23). Least squares line fit to data is also shown.
- 2.24 Amplitude, phase and frequency modulations at 6.1 m for a group of 10 waves of initial steepness $ak = .03$ (Exp 78). Amplitude modulation is in centimeters, phase modulation is in radians and frequency modulation is in radians/sec.
- 2.25 Amplitude, phase and frequency modulations at 30.5 m for a group of 10 waves of initial steepness $ak = .03$ (Exp 78).
- 2.26 Amplitude, phase and frequency modulations at 61.1 m for a group of 10 waves of initial steepness $ak = .03$

(Exp 78).

- 2.27 Amplitude, phase and frequency modulations at 91.4 m for a group of 10 waves of initial steepness $ak = .03$ (Exp 78).
- 2.28 Amplitude, phase and frequency modulations at 106.7 m for a group of 10 waves of initial steepness $ak = .03$ (Exp 78).
- 2.29 Amplitude, phase and frequency modulations at 137.2 m for a group of 10 waves of initial steepness $ak = .03$ (Exp 78).
- 2.30 Amplitude, phase and frequency modulations at 6.1 m for a group of 15 waves of initial steepness $ak = .10$ (Exp 87).
- 2.31 Amplitude, phase and frequency modulations at 30.5 m for a group of 15 waves of initial steepness $ak = .10$ (Exp 87).
- 2.32 Amplitude, phase and frequency modulations at 61.1 m for a group of 15 waves of initial steepness $ak = .10$ (Exp 87).
- 2.33 Amplitude, phase and frequency modulations at 91.4 m for a group of 15 waves of initial steepness $ak = .10$ (Exp 87).
- 2.34 Amplitude, phase and frequency modulations at 106.7 m for a group of 15 waves of initial steepness $ak = .10$ (Exp 87).
- 2.35 Amplitude, phase and frequency modulations at 137.2 m for a group of 15 waves of initial steepness $ak = .10$ (Exp 87).
- 2.36 Amplitude, phase and frequency modulations at 6.1 m for

- a group of 25 waves of initial steepness $ak = .16$ (Exp 23).
- 2.37 Amplitude, phase and frequency modulations at 30.5 m for a group of 25 waves of initial steepness $ak = .16$ (Exp 23).
- 2.38 Amplitude, phase and frequency modulations at 61.1 m for a group of 25 waves of initial steepness $ak = .16$ (Exp 23).
- 2.39 Amplitude, phase and frequency modulations at 91.4 m for a group of 25 waves of initial steepness $ak = .16$ (Exp 23).
- 2.40 Amplitude, phase and frequency modulations at 106.7 m for a group of 25 waves of initial steepness $ak = .16$ (Exp 23).
- 2.41 Amplitude, phase and frequency modulations at 137.2 m for a group of 25 waves of initial steepness $ak = .16$ (Exp 23).
- 2.A1 Block diagram of data processing sequence.
- 3.1 Numerical evolution of a steeper-than-soliton initial profile (1/2-soliton). The magnitude of the complex envelope is plotted in a spatial frame that propagates at the linear group velocity, $-12.5 < X < 12.5$. The length of the time evolution corresponds to $T = 10$.
- 3.2a Evolution of the magnitude of the complex envelope plotted at 7 successive time steps (time increases upwards) for the 1/2-soliton initial condition.
- 3.2b Evolution of the principal value of the phase modulation, normalized by π , at 7 successive time steps corresponding to the amplitude modulation of fig. 3.2a.

- 3.3a Superposition of amplitude modulation at 4 different times, $T = 0, 2, 6, 10$, corresponding to the 1/2-soliton initial condition.
- 3.3b Superposition of phase modulation at 4 different times, $T = 0, 2, 6, 10$, corresponding to the amplitude modulation superposition of fig. 3.3a.
- 3.4 Numerical evolution of a one-soliton initial profile. The magnitude of the complex envelope is plotted in a spatial frame that propagates at the linear group velocity, $-12.5 < X < 12.5$. The length of the time evolution corresponds to $T = 10$.
- 3.5a Evolution of the magnitude of the complex envelope plotted at 7 successive time steps (time increases upwards) for the 1-soliton initial condition.
- 3.5b Evolution of the principal value of the phase modulation, normalized by π , at 7 successive time steps corresponding to the amplitude modulation of fig. 3.5a.
- 3.6a Superposition of amplitude modulation at 4 different times, $T = 0, 2, 6, 10$, corresponding to the 1-soliton initial condition.
- 3.6b Superposition of phase modulation at 4 different times, $T = 0, 2, 6, 10$, corresponding to the amplitude modulation superposition of fig. 3.6a.
- 3.7 Numerical evolution of a two-soliton initial profile. The magnitude of the complex envelope is plotted in a spatial frame that propagates at the linear group velocity, $-12.5 < X < 12.5$. The length of the time evolution corresponds to $T = 30$.
- 3.8a Evolution of the magnitude of the complex envelope plotted at 7 successive time steps (time increases upwards) for the 2-soliton initial condition.

- 3.8b Evolution of the principal value of the phase modulation, normalized by π , at 7 successive time steps corresponding to the amplitude modulation of fig. 3.8a.
- 3.9a Superposition of amplitude modulation at 4 different times, $T = 0, 6.3, 12.6, 18.9$, corresponding to the 2-soliton initial condition.
- 3.9b Superposition of phase modulation at 4 different times, $T = 0, 6.3, 12.6, 18.9$, corresponding to the amplitude modulation superposition of fig. 3.9a.
- 3.10 Numerical evolution of a soliton plus radiation ($3/2$ -soliton) initial profile. The magnitude of the complex envelope is plotted in a spatial frame that propagates at the linear group velocity, $-12.5 < X < 12.5$. The length of the time evolution corresponds to $T = 30$.
- 3.11a Evolution of the magnitude of the complex envelope plotted at 7 successive time steps (time increases upwards) for the $3/2$ -soliton initial condition.
- 3.11b Evolution of the principal value of the phase modulation, normalized by π , at 7 successive time steps corresponding to the amplitude modulation of fig. 3.11a.
- 3.11c Further evolution of the magnitude of the complex envelope plotted at 7 successive time steps (time increases upwards) for the $3/2$ -soliton initial condition.
- 3.11d Further evolution of the principal value of the phase modulation, normalized by π , at 7 successive time steps corresponding to the amplitude modulation of fig. 3.11c.

- 3.12 Numerical evolution of a bound state plus radiation (5/2-soliton) initial profile. The magnitude of the complex envelope is plotted in a spatial frame that propagates at the linear group velocity, $-12.5 < X < 12.5$. The length of the time evolution corresponds to $T = 30$.
- 3.13a Evolution of the magnitude of the complex envelope plotted at 7 successive time steps (time increases upwards) for the 5/2-soliton initial condition.
- 3.13b Evolution of the principal value of the phase modulation, normalized by π , at 7 successive time steps corresponding to the amplitude modulation of fig. 3.13a.
- 3.13c Further evolution of the magnitude of the complex envelope plotted at 7 successive time steps (time increases upwards) for the 5/2-soliton initial condition.
- 3.13d Further evolution of the principal value of the phase modulation, normalized by π , at 7 successive time steps corresponding to the amplitude modulation of fig. 3.13c.
- 3.14a Superposition of amplitude modulation at 4 different times, $T = 0, 6.3, 12.6, 18.9$, corresponding to the 5/2-soliton initial condition.
- 3.14b Superposition of phase modulation at 4 different times, $T = 0, 6.3, 12.6, 18.9$, corresponding to the amplitude modulation superposition of fig. 3.14a.
- 3.15 Numerical evolution of divergent solitons from an antisymmetric initial profile corresponding to figure 5 of Satsuma and Yajima [1974]. The magnitude of the complex envelope is plotted in a spatial frame that propagates at the linear group velocity, $-12.5 < X < 12.5$. The length of the time evolution corresponds to $T = 30$.

- 3.16a Evolution of the magnitude of the complex envelope plotted at 7 successive time steps (time increases upwards) for the divergent soliton initial condition.
- 3.16b Further evolution of the magnitude of the complex envelope plotted at 7 successive time steps (time increases upwards) for the divergent soliton initial condition.
- 3.16c Evolution of the principal value of the phase modulation, normalized by π , at 7 successive time steps corresponding to the amplitude modulation of fig. 3.16a.
- 3.16d Further evolution of the principal value of the phase modulation, normalized by π , at 7 successive time steps corresponding to the amplitude modulation of fig. 3.16b.
- 3.17a Superposition of amplitude modulation at 4 different times, $T = 0, 6.3, 12.6, 18.9$, corresponding to the divergent soliton initial condition.
- 3.17b Superposition of phase modulation at 4 different times, $T = 0, 6.3, 12.6, 18.9$, corresponding to the amplitude modulation superposition of fig. 3.17a.
- 3.17c Superposition of amplitude modulation at 4 different times, $T = 22, 24, 26, 30$, corresponding to the divergent soliton initial condition.
- 3.17d Superposition of phase modulation at 4 different times, $T = 22, 24, 26, 30$, corresponding to the amplitude modulation superposition of fig. 3.17c.
- 3.18 Inviscid NLS numerical evolution for a wave group of 10 waves, initial steepness $ak = .03$ (Exp 78). Spatial frame $-9 < X < 9$ and time interval $0 < T < 2.5$.

- 3.19 Viscous NLS numerical evolution for a wave group of 10 waves, initial steepness $ak = .03$ (Exp 78). Spatial frame $-9 < X < 9$ and time interval $0 < T < 2.5$.
- 3.20 Initial condition at 6.1 m for numerical evolutions in figs. 3.18 and 3.19.
- 3.21 Amplitude modulations for the evolution of a group of 10 waves, initial steepness $ak = .03$ (Exp 78). (a) observations, nondimensionalized at each fetch by the initial condition scaling. (b) inviscid NLS solutions at times corresponding to the fetches in a. (c) viscous NLS solutions at times corresponding to the fetches in a.
- 3.22 Phase modulations for the evolution of a group of 10 waves, initial steepness $ak = .03$ (Exp 78). (a) observations, principal value and normalized by π for successive fetches. (b) inviscid NLS solutions at times corresponding to the fetches in a. (c) viscous NLS solutions at times corresponding to the fetches in a.
- 3.23 Inviscid NLS numerical evolution for a wave group of 25 waves, initial steepness $ak = .07$ (Exp 77). Spatial frame $-21 < X < 21$ and time interval $0 < T < 5$.
- 3.24 Viscous NLS numerical evolution for a wave group of 25 waves, initial steepness $ak = .07$ (Exp 77). Spatial frame $-21 < X < 21$ and time interval $0 < T < 5$.
- 3.25 Initial condition at 6.1 m for numerical evolutions in figs. 3.23 and 3.24.
- 3.26 Amplitude modulations for the evolution of a group of 25 waves, initial steepness $ak = .07$ (Exp 77). (a) observations, nondimensionalized at each fetch by the initial condition scaling. (b) inviscid NLS solutions at times corresponding to the fetches in a. (c) viscous NLS solutions at times corresponding to the fetches in a.

- 3.27 Phase modulations for the evolution of a group of 25 waves, initial steepness $ak = .07$ (Exp 77). (a) observations, principal value and normalized by π for successive fetches. (b) inviscid NLS solutions at times corresponding to the fetches in a. (c) viscous NLS solutions at times corresponding to the fetches in a.
- 3.28 Inviscid NLS numerical evolution for a wave group of 15 waves, initial steepness $ak = .10$ (Exp 87). Spatial frame $-29.3 < X < 29.3$ and time interval $0 < T < 10$.
- 3.29 Viscous NLS numerical evolution for a wave group of 15 waves, initial steepness $ak = .10$ (Exp 87). Spatial frame $-29.3 < X < 29.3$ and time interval $0 < T < 10$.
- 3.30 Initial condition at 6.1 m for numerical evolutions in figs. 3.28 and 3.29.
- 3.31 Amplitude modulations for the evolution of a group of 15 waves, initial steepness $ak = .10$ (Exp 87). (a) observations, nondimensionalized at each fetch by the initial condition scaling. (b) inviscid NLS solutions at times corresponding to the fetches in a. (c) viscous NLS solutions at times corresponding to the fetches in a.
- 3.32 Phase modulations for the evolution of a group of 15 waves, initial steepness $ak = .10$ (Exp 87). (a) observations, principal value and normalized by π for successive fetches. (b) inviscid NLS solutions at times corresponding to the fetches in a. (c) viscous NLS solutions at times corresponding to the fetches in a.
- 3.33 Inviscid NLS numerical evolution for a wave group of 25 waves, initial steepness $ak = .10$ (Exp 88). Spatial frame $-31.3 < X < 31.3$ and time interval $0 < T < 10$.
- 3.34 Viscous NLS numerical evolution for a wave group of 25 waves, initial steepness $ak = .10$ (Exp 88). Spatial

frame $-31.3 < X < 31.3$ and time interval $0 < T < 10$.

- 3.35 Initial condition at 6.1 m for numerical evolutions in figs. 3.33 and 3.34.
- 3.36 Amplitude modulations for the evolution of a group of 25 waves, initial steepness $ak = .10$ (Exp 88). (a) observations, nondimensionalized at each fetch by the initial condition scaling. (b) inviscid NLS solutions at times corresponding to the fetches in a. (c) viscous NLS solutions at times corresponding to the fetches in a.
- 3.37 Phase modulations for the evolution of a group of 25 waves, initial steepness $ak = .10$ (Exp 88). (a) observations, principal value and normalized by π for successive fetches. (b) inviscid NLS solutions at times corresponding to the fetches in a. (c) viscous NLS solutions at times corresponding to the fetches in a.
- 3.38 Inviscid NLS numerical evolution for a wave group of 15 waves, initial steepness $ak = .15$ (Exp 62). Spatial frame $-31.5 < X < 31.5$ and time interval $0 < T < 40$.
- 3.39 Viscous NLS numerical evolution for a wave group of 15 waves, initial steepness $ak = .15$ (Exp 62). Spatial frame $-31.5 < X < 31.5$ and time interval $0 < T < 40$.
- 3.40 Initial condition at 6.1 m for numerical evolutions in figs. 3.38 and 3.39.
- 3.41 Amplitude modulations for the evolution of a group of 15 waves, initial steepness $ak = .15$ (Exp 62). (a) observations, nondimensionalized at each fetch by the initial condition scaling. (b) inviscid NLS solutions at times corresponding to the fetches in a. (c) viscous NLS solutions at times corresponding to the fetches in a.
- 3.42 Phase modulations for the evolution of a group of 15

waves, initial steepness $ak = .15$ (Exp 62). (a) observations, principal value and normalized by π for successive fetches. (b) inviscid NLS solutions at times corresponding to the fetches in a. (c) viscous NLS solutions at times corresponding to the fetches in a.

- 3.43 Inviscid NLS numerical evolution for a wave group of 15 waves, initial steepness $ak = .16$ (Exp 22). Spatial frame $-33.5 < X < 33.5$ and time interval $0 < T < 45$.
- 3.44 Viscous NLS numerical evolution for a wave group of 15 waves, initial steepness $ak = .16$ (Exp 22). Spatial frame $-33.5 < X < 33.5$ and time interval $0 < T < 45$.
- 3.45 Initial condition at 6.1 m for numerical evolutions in figs. 3.43 and 3.44.
- 3.46 Amplitude modulations for the evolution of a group of 15 waves, initial steepness $ak = .16$ (Exp 22). (a) observations, nondimensionalized at each fetch by the initial condition scaling. (b) inviscid NLS solutions at times corresponding to the fetches in a. (c) viscous NLS solutions at times corresponding to the fetches in a.
- 3.47 Phase modulations for the evolution of a group of 15 waves, initial steepness $ak = .16$ (Exp 22). (a) observations, principal value and normalized by π for successive fetches. (b) inviscid NLS solutions at times corresponding to the fetches in a. (c) viscous NLS solutions at times corresponding to the fetches in a.
- 3.48 Inviscid NLS numerical evolution for a wave group of 25 waves, initial steepness $ak = .16$ (Exp 23). Spatial frame $-29.1 < X < 29.1$ and time interval $0 < T < 40$.
- 3.49 Viscous NLS numerical evolution for a wave group of 25 waves, initial steepness $ak = .16$ (Exp 23). Spatial frame $-29.1 < X < 29.1$ and time interval $0 < T < 40$.

- 3.50 Initial condition at 6.1 m for numerical evolutions in figs. 3.48 and 3.49.
- 3.51 Amplitude modulations for the evolution of a group of 25 waves, initial steepness $ak = .16$ (Exp 23). (a) observations, nondimensionalized at each fetch by the initial condition scaling. (b) inviscid NLS solutions at times corresponding to the fetches in a. (c) viscous NLS solutions at times corresponding to the fetches in a.
- 3.52 Phase modulations for the evolution of a group of 25 waves, initial steepness $ak = .16$ (Exp 23). (a) observations, principal value and normalized by π for successive fetches. (b) inviscid NLS solutions at times corresponding to the fetches in a. (c) viscous NLS solutions at times corresponding to the fetches in a.
- 4.1 CD shows the steaming track for the acoustic transect, and B is the location of the buoy from the present field experiment. Sites of measurements made in previous studies are also indicated. EF marks an XBT survey by HBO (1979). T denotes the location of Halpern's (1971a,b) observations. The solid triangles show the position of Orr's acoustic observations of the packet (HBO, 1979). (Map after HBO, 1979).
- 4.2 2A is a Raytheon acoustic image made while steaming at approximately 9 knots eastward across the bank as the ebb tide slackened. The flow is from left to right and is close to zero. The image shows a large scale near-surface low-scattering region coherent with the depression of the thermocline seen in 2B. The numbers at the top of the figures indicate stations where XBT casts were made. Temperatures from expanded scale XBT traces were hand read and contoured in 2B on the same scale as the acoustic image of 2A.
- 4.3 Vertical profile of Brunt-Vaisala frequency and the first three vertical eigenmodes. The Brunt-Vaisala frequency was calculated from density inferred from an average of 6 hand-lowered CTD casts made in the

vicinity of the mooring. The surface mixed layer resulted from the passage of a storm. The eigenmodes were also calculated from inferred density using a fourth order Runge-Kutta shooting method. The corresponding first three modal phase speeds were 23 cm/sec, 10.4 cm/sec and 7.1 cm/sec respectively.

- 4.4 Schematic of the movement of two clear (low-scattering) regions in the acoustic images. The near-surface region is identified in the text as a lee wave. The bottom clear region may be associated with a pattern of flow separation. 4A-4D show the set-up and stationarity of the ebb tide lee wave. The patch of clear bottom water is seen to move from the sill crest to the east of the bank. 4E-4F show the lee wave shortening and steepening; the bottom water begins to move back up the bank. 4G-4H show the set-up of 1-2 lee waves by the flood tide and the propagation of 4-5 of these lee waves as the tide turns. The bottom water has moved back up and over the sill crest. The arrows indicate the direction of the flow. The time in hours and the mean flow are marked in each schematic. These values correspond to the Froude number time series listed in Table 1.
- 4.5 Magnitude of the mean cross-component of current. Also plotted is the first mode internal wave phase speed (23 cm/sec). When the current speed exceeds the lowest mode phase speed, the flow is supercritical with respect to the three lowest modes. This figure brings together the Froude number calculation of Table 1 and the schematic of Figure 4.4. The times of the individual elements of the schematic are indicated, thus showing their timing relative to the tidal cycle and the flow criticality.
- 4.6 Raytheon acoustic image corresponding to Figure 4.4A.
- 4.7 Raytheon acoustic image corresponding to Figure 4.4E.
- 4.8 Raytheon acoustic image corresponding to Figure 4.4G.
- 4.9 Raytheon acoustic image corresponding to Figure 4.4H.

4.10 Raytheon acoustic image of high frequency internal wave packet observed while ship was freely drifting 5 km west of Stellwagen at point C.

LIST OF TABLES

- 2.1 Experimental parameters
- 2.2 Soliton estimation
- 2.3 Frictional parameters
- 4.1 Time series of Froude numbers

CHAPTER 1

INTRODUCTION

1.1 BACKGROUND

Both field and laboratory observations of surface and internal waves suggest that linear theory can not account for all of the observed features in the data. For example, the large amplitudes that are observed violate the small steepness assumption required for linearization, and the inferred phase speeds are higher than linear theory predicts.

Mollo-Christensen and Ramamonjiarisoa (1978) review some studies of surface wind waves (mostly laboratory but some field observations) and find that linear dispersion does not adequately describe wind wave propagation. They find that wind waves propagate at higher phase velocities than the dispersion relation predicts and that for frequencies exceeding the frequency of the spectral maximum, the phase speed is nearly constant. Laboratory (Maxworthy 1979) and field (Osborne and Burch 1980) observations of internal waves

also point towards the existence of large amplitude internal waves whose propagation is not described by linear dispersion. Although in recent years much theoretical work has been done on the stability and interactions of nonlinear waves (Benjamin and Feir 1967; Whitham 1974; Longuet-Higgins 1978), observational and experimental studies have lagged behind. In particular, an application of these theoretical results in interpreting observations and in the modelling of oceanic waves is lacking.

Although linear theory can not account for all of the observed wave properties, admittedly it has worked fairly well. In addition, it has the distinct advantage that solutions superpose so that one can hope to describe a random field of waves using a Fourier decomposition: interpreting the field as independently propagating Fourier components. There is no general way to describe a random field of nonlinear waves, although Mollo-Christensen and Ramamonjiarisoa have attempted to do so using wave groups (1978). Their model was motivated by evidence they saw which suggested that the surface wave field does not exist solely of independently propagating Fourier components but at least partially of wave groups of permanent type. The existence of internal waves of permanent type has also been documented in the laboratory (Davis and Acrivos 1967), and evidence of their occurrence in groups has been obtained in the field (Halpern

1971; Lee and Beardsley 1974; Gargett 1976).

This thesis addresses the evolution of nonlinear surface and internal wave groups. It is an attempt to apply some of the wealth of existing theory on nonlinear waves to observations, and also to model some of these observations numerically. The surface wave observations were made in a laboratory wave channel and modelled numerically using the cubic-nonlinear Schrodinger equation. The internal wave observations were made during an oceanic field experiment, and the results are interpreted in the context of an internal Korteweg-deVries model.

There are several reasons to examine wave groups. At least for sea surface waves, evidence points towards a sea surface composed not just of independently propagating Fourier components but also of bound higher harmonics. Although difficult to model, one can argue heuristically that a more realistic point of view is one that looks at the sea surface as a collection of groups of nonlinear waves exhibiting coherence over certain space and time scales. The nonlinear interactions of individual waves may create groups whose identities are maintained through a balance of nonlinearity and dispersion for some distance and time. These wave groups of quasi-permanent form may then eventually disintegrate due to instabilities or possibly the effects of external forcing

and dissipation. This heuristic argument motivates the need for a further understanding of wave groups. A second motivation to examine groups is that interactions are easier to observe in a group than in a continuous wavetrain. The group is a well-defined entity in both space and time; hence, interactions are isolated. Finally, both of the nonlinear models which I apply to the observations of surface and internal waves belong to a class of partial differential equations which can be solved exactly for arbitrary pulse-like initial conditions using the inverse scattering transform. A wave group is a pulse-like initial condition, and although I will not use inverse scattering per se, properties predicted by the exact solutions of the above two models based on inverse scattering theory will be used in describing and interpreting the results.

Separate treatment will be given to the topics of surface and internal wave group development. Apart from a related theme, the studies done for each are actually quite different both in the measurements that were made and the subsequent analysis.

1.2 SURFACE WAVES

Surface water waves are among the most widespread and

easily observable instances of wave motion in nature. They have been studied for well over one hundred years in a number of different disciplines (for an overall review see Barnett and Kenyon 1975; for a review of recent advances in nonlinear waves see Yuen and Lake 1980). Although the earliest periodic solution for finite amplitude deep water waves was derived by Stokes in 1847, it was not until 1925 that Levi-Civita proved the convergence of Stokes series solution. Oddly enough, the stability of the Stokes deep water wavetrain was not questioned for more than one hundred years after its discovery. Lighthill (1965), using Whitham's theory, showed that the Stokes wavetrain is modulationally unstable. Benjamin and Feir (1967) theoretically confirmed the modulational instability of weakly nonlinear wavetrains and made experiments which gave good agreement with the theoretical prediction for small wave steepness. These instability analyses were for sideband perturbations to the initial wavetrain. Longuet-Higgins (1978) did a numerical study of the stability of a finite amplitude deep water Stokes wavetrain to linear normal mode perturbations as a function of steepness. These perturbations were of both shorter and longer wavelengths than the fundamental (super and sub harmonics). He also confirmed the modulational instability for weakly nonlinear wavetrains as well as discovering that the wavetrain actually restabilizes at some higher steepness $ak = .346$ ($ak = \text{amplitude} \times \text{wavenumber}$). At still higher

values of steepness ($ak = .41$) a new type of subharmonic instability appears; it has a much higher growth rate than the modulational instability.

Coincident with work on stability was the discovery that the complex modulation envelope of periodic gravity waves on deep water evolves according to the cubic nonlinear Schrodinger (NLS) equation. The earliest theoretical work appears to be due to Zakharov (1968) who used a multiple scales technique to derive the two dimensional cubic NLS equation. The Schrodinger equation has been in use for quite some time, in particular in the field of nonlinear optics. But unlike the Korteweg-deVries (KdV) equation, which has long been known to describe shallow water waves, it is only in the past two decades that this equation has been associated with deep water waves.

The cubic NLS and the KdV equations belong to a class of nonlinear partial differential equations which have soliton solutions. They can be solved exactly for arbitrary initial conditions which decay sufficiently rapidly (pulse-like initial conditions) using the inverse scattering transform derived by Gardner et al (1967). Thus, although historically surface waves have been examined from the point of view of wavetrains, this technique focused attention on wave groups. I.E., the pulse-like envelope of some fundamental carrier wave

gives rise to envelope solitons. Zakharov and Shabat [1972] solved the one dimensional cubic nonlinear Schrodinger equation exactly using the inverse scattering transform. The exact solution predicted some interesting wave properties.

First, they found that an arbitrary initial condition will disintegrate into a number of solitons and an oscillatory tail. The velocities and amplitudes of the solitons are proportional to the real and imaginary parts, respectively, of the eigenvalues of the related scattering problem. The tail is relatively small and unimportant. The number and structure of both the solitons and the tail are determined by the initial condition. These envelope solitons are stable. They survive pairwise collisions with no permanent change except for a possible shift in phase and position. The amplitudes and velocities remain unaltered. Unlike the soliton solutions of the KdV equation, the velocity and amplitude of these solitons are independent of each other. What is principally new compared to KdV solitons is the possibility of the formation of a "bound" state of a finite number of solitons having identical velocities. The solitons remain superposed and continue to interact; the modulation is characterized by a discrete number of frequencies. Energy is transferred through a discrete number of modes. The simplest case of two solitons is a periodic-in-time solution characterized by a single frequency. In the case of the N-soliton bound state,

it is an arbitrarily periodic solution characterized by $N(N-1)/2$ frequencies. If this bound state is physically realizable, it suggests a mechanism whereby a modulated group of surface waves could exhibit relatively long time and space coherence.

Yuen and Lake [1975] showed the equivalence of the Schrodinger equation and higher order theory of Whitham. Their experiments verified the existence of deep water envelope solitons and gave good comparison with numerical solutions of the Schrodinger equation. They also made laboratory and numerical comparisons for the evolution of a wavetrain [Lake et al 1977]. Although a weakly nonlinear wavetrain is modulationally unstable to a band of wavenumbers, the existence of a high wavenumber cutoff (in one dimension) suggests that the energy of the wavetrain may be confined to a discrete number of modes and hence that in long-time evolution, thermalization of wave energy (in the sense of equipartition among all modes) will not occur. This was borne out by numerical computations and confirmed by laboratory experiments. Namely, in the absence of viscous dissipation, the wavetrain goes through a series of modulation/demodulation cycles characteristic of nonlinear systems and known as the Fermi-Pasta-Ulam (FPU) recurrence phenomenon. Basically, the energy does not thermalize but excites a discrete number of modes, with the possibility of exact recurrence of the initial

condition. It should be emphasized that FPU recurrence in a Stokes wavetrain is equivalent to the N-soliton bound state for a nonlinear wavepacket. Only in the bound state can FPU recurrence take place in a wave group because only then do the solitons remain superposed and continue to interact. The bound state together with the quantum properties of the solution, namely that there exists a discrete number of modes possible, results in recurrence. The significance of recurrence is that it indicates a long-time "memory" of the initial condition. Considering the intractability of the general nonlinear problem, it is perhaps encouraging that so much can be known from the initial condition. Also encouraging for the concept of a wavetrain is the implication that a wavetrain may not be just an artificial idealized entity that can not be sustained naturally. It implies that a wavetrain maintains its coherence during evolution, similarly for groups. However, FPU recurrence has not been experimentally verified for long-time evolution because of restrictions in wave tank length. It is predicted from an inviscid theory, and over long time one expects dissipation to be important. Thus experiments are needed to establish whether recurrence is physically realizable.

Although the practical significance to oceanic waves is questionable due to the one space dimension restriction, the one space dimension results may extend to two dimensions more

than was previously thought. Initial attempts to extend the analysis to two dimensions involved the two space dimension cubic NLS equation. This equation has solutions of permanent type [Hui and Hamilton 1979]. Although FPU recurrence still occurs for a variety of initial conditions, there is no longer a high wavenumber cutoff, and there is a gradual leak of energy to higher modes (thermalization) [Yuen and Ferguson 1978]. However, a second equation, the Zakharov integral equation [Zakharov 1968] which recovers the NLS equation in the appropriate limits, gives promising results and exhibits a high wavenumber cutoff.

One of the questions that this thesis addresses is the long-time evolution of nonlinear deep water surface gravity wavepackets. First, it is an attempt to describe this evolution from experiments that were made in an unusually long wave tank (137.2 m). These observations can be used to answer several questions. How do the wave groups evolve? Is the bound state (FPU recurrence, long-time coherence) physically realizable in the laboratory? On what time scale does dissipation act? Does dissipation effectively rule out recurrence? Is the Schrodinger equation an appropriate model for the long-time evolution (since it is only weakly nonlinear)? Can a satisfactory Schrodinger equation model including dissipation be derived and results compared with actual observations?

A theoretical and numerical study by Satsuma and Yajima [1974] indicated that for a variety of cases the bound state could be predicted from the phase of the initial condition. Historically the phase of the waves has not been considered very important. In linear wave theory, the phase information obtained from Fourier analysis is ignored. Yuen and Lake's [1975] wave group experiments only examined the amplitude modulation obtained by rectifying and low-pass filtering. In part there has been a lack of motivation to examine phase since physically its significance is unclear and since there did not exist any method in fluid mechanics for demodulating both amplitude and phase. Feir [1967], in one of the earliest experimental studies done on wave groups, used measured time between crests to determine the frequency modulation. The disadvantage of this method is its lack of resolution; it yields frequency averaged over half a carrier period. This thesis uses a method introduced by Melville [1981] from communications theory and used by him to examine the amplitude and phase modulations of breaking waves. With relatively weak restrictions, he shows that the measurement of surface displacement can be used to obtain a time series of both amplitude and phase modulation at a point. From the phase modulation the frequency modulation can be calculated and using a second neighboring space measurement the wavenumber modulation can be determined.

There are several aspects of the wave phase that we are interested in looking at. First we can describe the phase and frequency modulations with increasing fetch and compare them to numerical solutions of the NLS equation which evolve from the same data. Previous comparisons have only been done for the amplitude modulation. Secondly we can test the result of Satsuma and Yajima [1974] that indicates that the occurrence of the bound state can be predicted (in some cases) from the phase of the initial condition.

The dispersion relation is a relation that involves the phase of the waves (a relation between wavenumber, frequency and amplitude). Melville [1981] has used the Hilbert transform to confirm the nonlinear dispersion relation to order $O((\alpha k)^2)$ for modulated waves. A final question involving phase and related to dispersion which this thesis will address in part is the observed frequency downshift. This is the phenomenon of a nearly uniform wavetrain of carrier frequency f_0 modulating and demodulating, eventually reforming into a nearly uniform wavetrain with slightly lower carrier frequency f_1 . Originally, this was observed in ocean wind wave spectra [Kinsman 1965] and in laboratory wind waves [Mollo-Christensen and Ramamonjiarisoa 1982]. However, it has also been well documented in laboratory waves in the absence of wind [Ramamonjiarisoa (personal communication); Lake et al 1977]. It can not be predicted from a model such as the NLS

equation which is narrow-banded (valid for slow modulations about a constant carrier frequency and wavenumber), unless some new effect such as dissipation, higher order nonlinearity, or forcing is included. Viscous damping or some other physical process which causes a secular change in the phase (and hence the dispersion relation) could account for the observed downshift. Normally, studies have focused on the damping of amplitude only. This thesis will explore to some extent the effect that dissipation may have on phase.

1.3 INTERNAL WAVES

Internal waves of permanent form, although more difficult to observe and measure than surface waves, have also been examined theoretically and experimentally in both the laboratory and the field (Benjamin 1966; Davis and Acrivos 1967; Osborne and Burch 1980). In the field they have mostly been observed propagating in groups in near-shore regions. In these regions strong coastal currents, enhanced density gradients from river outflow and from greater influence of seasonal heating, as well as large amplitude topography (relative to water depth) all combine to produce a large amplitude response to forcing.

Halpern (1971a) observed groups of large amplitude internal waves propagating in Massachusetts Bay that seemed to result from tidal interaction with a submarine sill. The propagation of these waves was looked at more recently by Haury, Briscoe and Orr (1979). Halpern's field observations motivated a theoretical (Lee and Beardsley 1974) and a laboratory (Maxworthy 1979) study which offered two different explanations of the generation mechanism of these waves. Although there have been several sets of field observations of the propagation of groups of large amplitude internal waves, there is not much documentation of their generation. Despite numerous theoretical and laboratory studies on this topic, direct application of the results to actual oceanic situations is questionable since the studies generally employ a simple stratification and an idealized topography.

Another observation of the propagation of similar waves is that of Gargett (1976) who observed large amplitude internal wavepackets in the southern Strait of Georgia, British Columbia. These packets are generated by tidal flow over the submarine ridges which lie across the mouths of the interisland passes of the southern strait. Apel et al (1975) have also made observations of tidally generated internal wavepackets over the continental shelf. The most dramatic observations are undoubtedly those of Osborne and Burch (1980) from the Andaman Sea. The observed amplitudes are as large as

60 meters, with phase speeds of order 200 cm/sec. Farmer and Smith (1980a,b) have made the most extensive series of measurements over a two year period in Knight Inlet, British Columbia. They have actually observed the wave generation. They see the formation of nonlinear lee wavetrains resulting from tidal flow over a sill. Although the physical situation is quite different from that in Massachusetts Bay, they have offered yet another interpretation of Halpern's field observations in light of their own measurements.

Thus although propagation of these types of waves has been well documented in numerous studies, several of which are cited above, there exist few actual observations of generation. The large amplitude and asymmetry of the topography are a determining feature of the fluid response, and there are few theoretical or laboratory studies which examine these effects. Knowledge of these waves, particularly in coastal regions, is important for a number of reasons. Among them are the design of offshore structures which can be affected by the large amplitudes and phase velocities of the waves. When wave breaking occurs, significant mixing can take place which affects nutrient distribution and hence primary production and marine animal feeding habits. These waves also introduce a sampling problem for other oceanic measurements. Mascarenhas (1979) computes from Halpern's data that the apparent depth of the upper mixed layer can vary by as much as

30% during a tidal cycle. Haury, Briscoe and Orr (1979) found strong inhomogeneities in the vertical and horizontal plankton distribution caused by wave passage.

This thesis addresses the question of the generation of large amplitude internal gravity wavepackets. This was done through a field experiment in Massachusetts Bay designed to observe the interaction over time of the tide with Stellwagen Bank, a local topographic feature. The goal of this study was to determine the mechanism and timing of the generation of the wavepackets previously observed by Halpern (1971a,b) and by Haury, Briscoe and Orr (1979). Since internal waves are more difficult to observe than surface waves, a key tool in this study was a commercially available Raytheon ship fathometer which was used as a remote sensor of isopycnal motion. This remote sensing technique to observe internal wave motion has been used previously, by Farmer and Smith (1980a,b) and by Haury, Briscoe and Orr (1979) among others.

CHAPTER 2

LABORATORY OBSERVATIONS OF SURFACE WAVE GROUP DEVELOPMENT

2.1 INTRODUCTION

In March 1981 experiments were made to investigate the long-time evolution of nonlinear deep water surface gravity wave groups. This long-time observation was made possible by the unusual length of the test facility (137.2 m). The experiments were made in a wave channel constructed in the outdoor flood plain in Bay St. Louis, MI (Figs. 2.1, 2.2). They were carried out in cooperation with Dr. Ming Su of NORDA.

There have been relatively few experimental studies of wave group development. The most notable exceptions are the pulse experiments of Feir (1967), the wave group experiments of Yuen and Lake (1975) and the wind wave group experiments of Mollo-Christensen and Ramamonjiarisoa (1982). There are several reasons to look at the development of groups. Since most previous studies have been done for continuous

wavetrains, it is interesting to see if wave groups exhibit the same characteristic evolution as continuous wavetrains. Secondly, results for wave groups are probably more relevant to oceanic waves. Also, interactions are isolated and easier to observe in wave groups.

The experiments were very simple in nature: constant amplitude, single frequency wave groups were generated using a plunger-type wavemaker. This simplicity was motivated in part by previous laboratory experiments (Mollo-Christensen and Ramamonjiarisoa 1982) in which mechanically generated groups were injected into an ambient wind wave field. The frequency of the mechanically generated groups was chosen to correspond to the spectral peak of the wind waves. Initially the distinct groups could be followed, but the evolution quickly became quite confused and complicated. This study addresses the dynamics of the isolated, mechanically generated wave groups. The observations were made outdoors under windless conditions. Two parameters, the wave steepness ak ($ak = \text{amplitude} \times \text{wavenumber}$) and the group length (number of waves) were varied. The steepness ranged from weak ($ak = .03$) to moderate ($ak = .16$) nonlinearity. Three group lengths were used: 10, 15 and 25 waves, nominally.

Some qualitative aspects of the wave group evolution as a function of wave steepness and group length are described.

The initial group is seen to modulate with fetch. This modulation gives the impression of a splitting into several groups. However, these 'split' groups do not diverge from each other even over very long fetch. The entire modulated wave packet lengthens and decreases in amplitude. Qualitatively, increasing the steepness increases the number of groups in the split-up process. Increasing the group length delays the splitting process.

In comparison with continuous wavetrains, the frequency downshift observed in wavetrains (Lake et al, 1977) seems to occur also for groups. A weakly nonlinear wavetrain is modulationally unstable to sideband perturbations. The wavetrain is observed to modulate with fetch, then demodulate and reform into a nearly uniform wavetrain but at slightly lower frequency. For groups of sufficient steepness, wave packets also exhibit this phenomenon of frequency downshift. This downshift was examined using maximum entropy spectra. This type of spectra assumes an autoregressive model that gives high resolution for short time series.

A packet's energy is defined as the integral of the amplitude squared over the entire packet. The final observation of packet energy is seen to be typically 25% of its initial value. This indicates the importance of dissipation in the long-time evolution.

The concomitant amplitude, phase and frequency modulations are obtained using the Hilbert transform. The method and its assumptions are documented in Appendix 2.A. The amplitude modulation or group envelope evolution corresponds basically to the development seen visually. Phase and frequency modulations are also described; these are more difficult to interpret. Previously, most emphasis has been upon amplitude modulation, although Feir did try to obtain frequency modulation. However, his method had poor resolution.

A detailed description of the measurements is given in the next section. This is followed by an analysis of the data and a discussion of the results.

2.2 MEASUREMENTS

The measurements were made in the outdoor flood plain in Bay St. Louis, MI. Figure 2.1 shows an overall view of the facility. It is L-shaped with a mown grass bottom. The dimensions are 1500 meters by 100 meters by 1 meter. A movable constriction is situated 340 meters downstream of the head box. It consists of 30 separate connecting gates, 3.33 meters long, which can be used to produce various flow

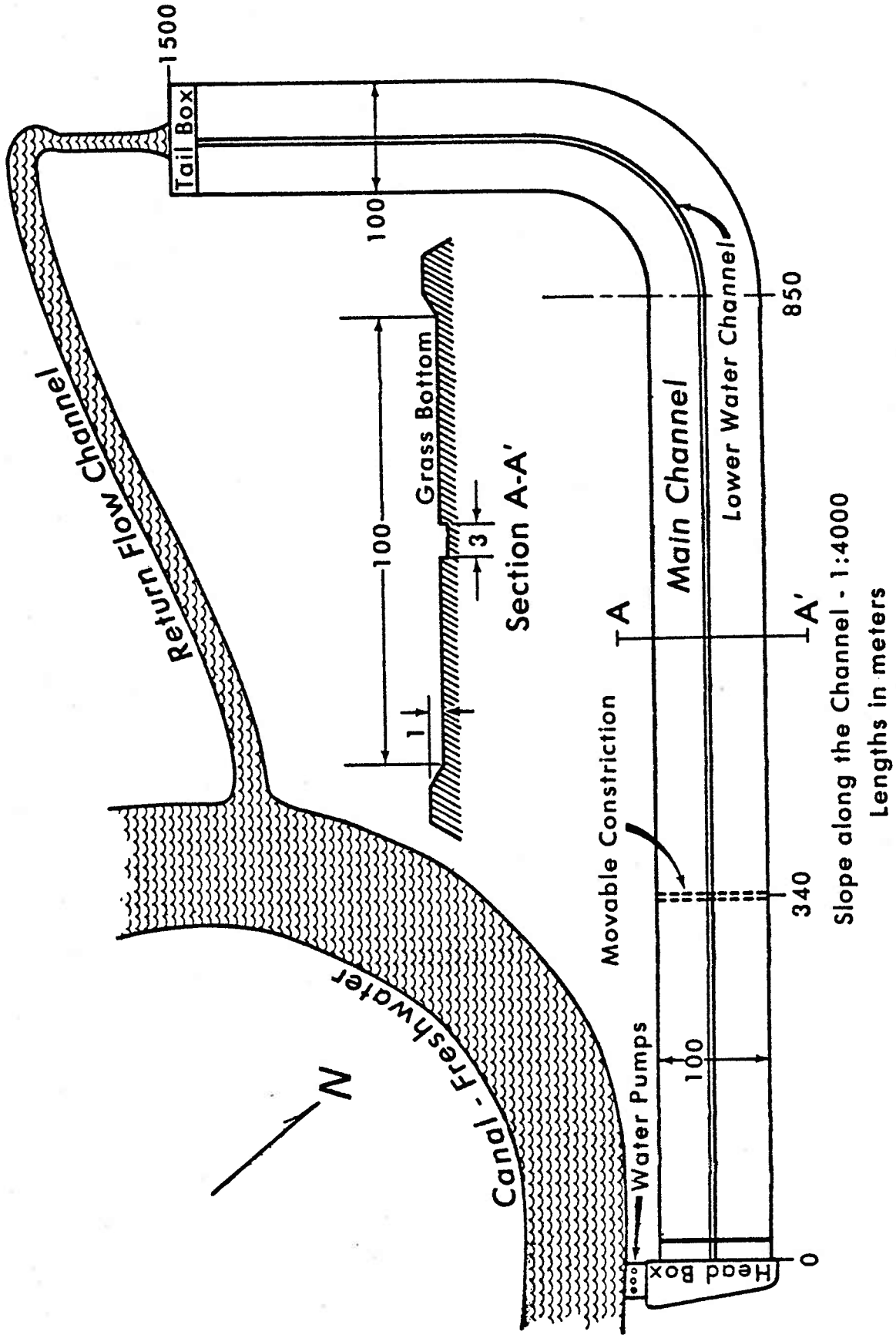


Fig. 2.1 Experimental facility. Outdoor flood plain, Bay St. Louis, MI.

configurations. For the present experiments, the constriction was completely closed to create a constant depth basin 100 meters by 340 meters. Within this basin a plywood wave channel was constructed which was 3.66 meters wide and 137.2 meters long. Figure 2.2 shows the location and orientation of the wave channel inside the basin. The basin was filled to a depth of .72 meters. The wavemaker was situated at the head of the channel; netting was stretched across the end to keep larger particulates from contaminating the water surface within the channel. There was no special treatment of the water surface, however.

The wavemaker used is a plunger-type with a hyperbolic forward face (Fig. 2.2). The maximum stroke setting is 30.5 cm and the maximum frequency range is 0.5 hz to 2.0 hz. For these experiments the stroke setting ranged from 5.1 to 7.6 cm, and the frequency ranged from .80 hz to 1.20 hz. The crest length of the wavemaker matches the channel width, 3.66 meters. The period of the wavemaker is measured at the drive shaft.

The wave height sensors were of capacitance type. They consisted of a single, double-coated, magnetic wire .5 mm in diameter. The change in capacitance caused by variation in water depth due to wave passage is converted to a DC voltage proportional to the surface displacement. The response is

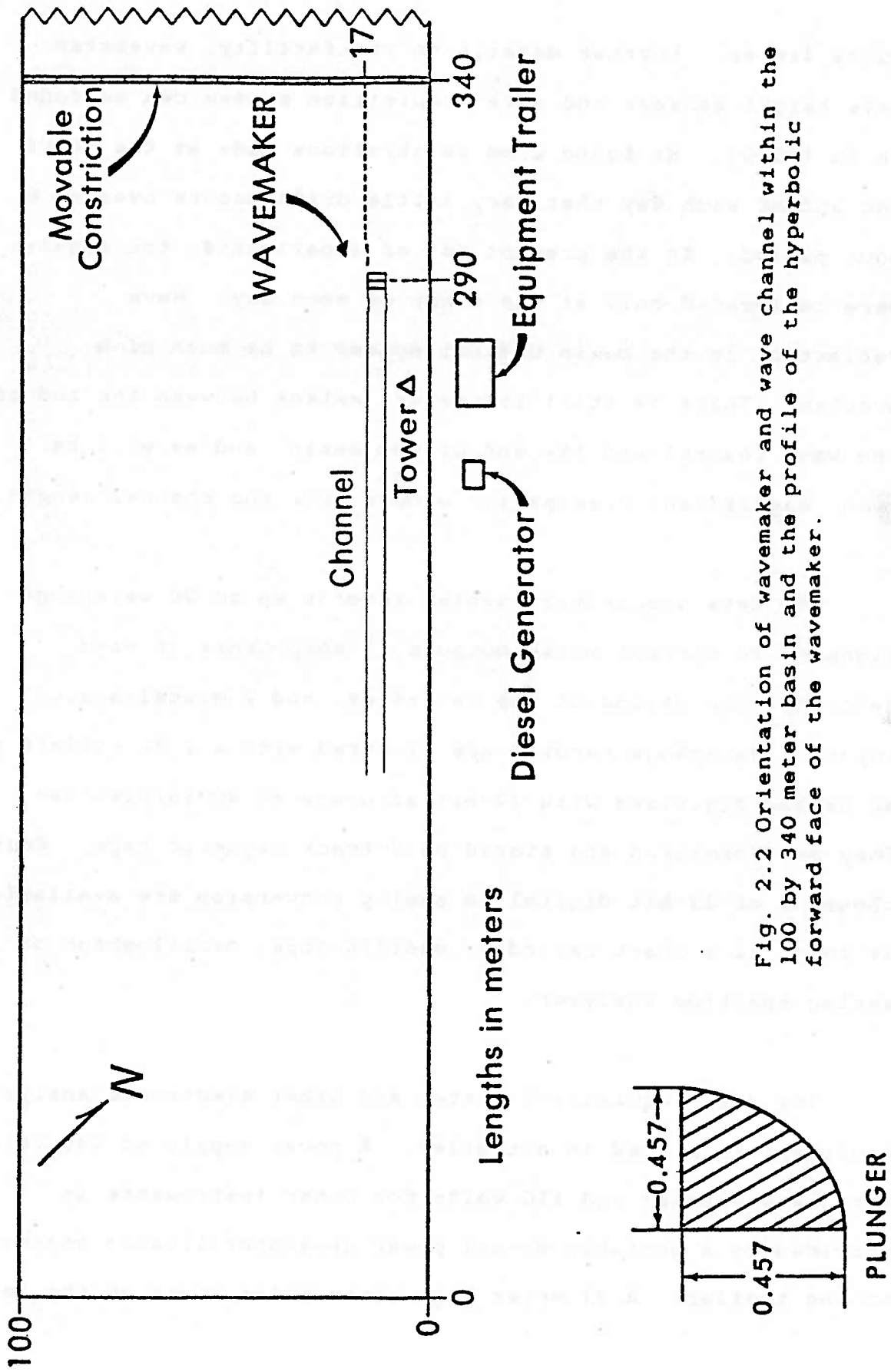


Fig. 2.2 Orientation of wavemaker and wave channel within the 100 by 340 meter basin and the profile of the hyperbolic forward face of the wavemaker.

quite linear. Further details on the facility, wavemaker, wave height sensors and data acquisition system can be found in Su (1980). He found from calibrations made at the start and end of each day that very little drift occurs over an 8 hour period. In the present set of experiments, the sensors were calibrated only at the start of each day. Wave reflection in the basin did not appear to be much of a problem. There is still 150 meters extent between the end of the wave channel and the end of the basin, and as will be seen, significant dissipation occurs over the channel length.

The data acquisition system records up to 20 wavegauge signals, 20 current meter outputs, 3 components of wind velocity, the period of the wavemaker, and 2 miscellaneous inputs. Wavegauge records are filtered with a 3 db rolloff at 40 hz and digitized with 12-bit accuracy at 40 samples/sec. They are formatted and stored on 9-track magnetic tape. Four channels of 12-bit digital to analog conversion are available as input to a chart recorder, oscilloscope, oscillograph or analog spectrum analyzer.

The data acquisition system and other electronic analysis equipment is housed in a trailer. A power supply of 440 volts for the wavemaker and 110 volts for other instruments is provided by a portable diesel power generator located adjacent to the trailer. A 21 meter high observation tower on the left

side of the wave channel provides a plan view of the tank and a platform for pictures or movies (Fig. 2.2).

For these experiments the measurements from 18 wave height sensors, the wind velocity, and the wavemaker period were recorded. The experiments were made under still wind conditions. For a given stroke and frequency setting (hence wave steepness), groups of 10, 15 and 25 waves were generated. Each wave group was allowed to propagate down the channel before generating the next group. The wavegauges were placed along the centerline of the channel, and measurements were made at the following fetches (distance is in meters): 6.1, 15.2, 30.5, 45.7, 61.1, 76.2, 91.4, 106.7, 121.9, 137.2. Most locations had wavegauge pairs separated by .30 m (roughly one quarter wavelength). The locations of the wavegauge pairs were: 6.1, 30.5, 61.1, 91.4, 106.7, 121.9, and 137.2 meters. In addition, a third wavegauge at 121.9 m was placed near the sidewall. The pairs were used to determine the wavenumber. Access to the sensors was provided by planks which ran from the bank of the basin over the top of the channel walls. Although it was attempted to generate wave groups of a single frequency and constant amplitude, small transients were present from starting and stopping the wavemaker.

2.3 ANALYSIS AND RESULTS

2.3.1 Description of evolution

The wave group evolution was observed as a function of two parameters: wave steepness and group length. Table 2.1 summarizes the experimental parameters for those experiments chosen for discussion. They represent a range of steepness from weak to moderate nonlinearity. For each steepness, three different group lengths were used. The number of waves per group represents a nominal estimate.

The initial frequency, f_0 , was determined by three different methods which gave very good agreement. The initial frequency was determined first from a measurement at the drive shaft of the wave generator. Secondly, it was calculated from the wave period using the measured time lag between successive wave peaks and troughs at the most upstream wavegauge (6.1 m). Finally, the frequency was also determined as the frequency of the spectral peak for the maximum entropy spectrum of the most upstream wavegauge. The criterion for a wave peak or trough was defined as 40% of the maximum wave amplitude. The average amplitude was calculated from the calibrated wave height measurement as one half the average wave height. The average wave height, in turn, was calculated as the average difference between the peak and trough amplitudes. The number of waves

Table 2.1

Experimental Parameters

Experiment	N_w	$\bar{a}k$	f_0 (hz)	\bar{k} (rad/cm)	f_1 (hz)	df/f_0
78	10	.03	0.80	0.025	0.80	.00
79	15	.03	0.80	0.025	0.80	.00
80	25	.03	0.80	0.025	0.80	.00
75	10	.07	0.97	0.036	0.97	.00
76	15	.07	0.96	0.036	0.96	.00
77	25	.07	0.96	0.036	0.96	.00
86	10	.10	0.96	0.037	0.95	.01
87	15	.10	0.96	0.037	0.95	.01
88	25	.10	0.96	0.037	0.94	.02
61	10	.15	1.20	0.06	1.06	.12
62	15	.15	1.20	0.06	1.04	.13
63	25	.15	1.21	0.06	1.04	.14
21	10	.16	1.21	0.05	1.05	.13
22	15	.16	1.21	0.05	1.02	.17
23	25	.16	1.21	0.05	1.01	.16

in the group that met the peak/trough criterion is tabulated in Table 2.2. Wavenumber was calculated from the measured phase lag between the most upstream wavegauge pair (6.1 m) which were separated by .3 m. The final frequency, f_1 , at the most downstream observation (137.2) was determined from the location of the spectral peak. The method using the time lag between successive peaks and troughs lacked resolution at this downstream location due to the difficulty of defining a crest/trough criterion. Typically at this distance, the waves were strongly attenuated.

Figures 2.3 to 2.11 show the wave group evolution with distance (fetch increases upwards), in order of increasing wave steepness. In each case the most upstream location, 6.1 m, was centered and plotted. The arrival time of the group center, if it propagated at half the phase speed (based on measured f_0 and k), was calculated for each wavegauge location. The remaining plots are centered on this extrapolated arrival time of the group center, based on linear group velocity. (This estimate is not actually the linear group velocity since separate estimates of frequency and wavenumber are made instead of using the dispersion relation between them. The estimate used is $w/2k$). As can be seen, the groups propagate faster than group velocity predicts. The smallest and largest steepnesses are seen to deviate the most. In the case of the smallest wave steepness (Fig. 2.3), this

Table 2.2

Soliton Estimation

Experiment	N PKS	-- ak	N S, T	N S, O
78	10	.03	0.4	0.0
79	14	.03	0.6	0.0
80	23	.03	0.9	0.0
75	10	.07	0.98	1.0
76	14	.07	1.4	1.0
77	24	.07	2.3	1.0
86	5	.10	0.7	1.0
87	13	.10	1.8	1.0
88	26	.10	2.3	2.0
61	7	.15	1.4	1.0
62	14	.15	2.9	4.0
63	23	.15	4.9	5.0
21	7	.16	1.6	1.0
22	14	.16	3.2	3.0
23	23	.16	5.2	4.0

is probably due to linear frequency dispersion (low frequency components running ahead of the group carrier) and due to the speed estimate being smaller than one based on frequency alone. (The linear group velocity for the smallest steepness experiment based on frequency alone is 97.5 cm/s and the estimate based on half the phase velocity using measured frequency and wavenumber is 89.4 cm/sec). In the case of the steepest wave groups (Figs. 2.8 to 2.11), this is probably due in part to frequency dispersion, but also due to nonlinear effects which in addition to increasing the group speed are observed to give rise to frequency downshifting of the carrier frequency. The phenomenon of frequency downshifting will be discussed in the next section. The middle steepnesses (Figs. 2.4 to 2.7) show propagation somewhat faster than linear group velocity predicts (6% faster for E88, Fig. 2.7). This is probably due to both frequency dispersion of lower frequency components and nonlinearity. Very little downshifting is evident for small initial wave steepnesses (Table 2.1). In this weakly nonlinear range ($ak = .07, .10$) we find the best balance between nonlinearity and dispersion.

Table 2.2 tabulates the number of peaks that met the crest criterion for the chosen experiments. It also compares the predicted and observed estimates of the number of solitons. The theoretical model will be formally derived in the next chapter, but for purposes of discussion we briefly

summarize the model and some pertinent properties of its exact solutions. In particular, we show how the theoretical estimate for the number of predicted solitons can be made.

Zakharov [1968] was the first to derive the two space dimension cubic NLS equation. This equation governs the evolution of the slowly varying complex modulation envelope of deep water surface gravity waves. The equation in one space dimension is :

$$i \left[\frac{\partial A}{\partial t} + \left(\frac{w_0}{2k_0} \right) \frac{\partial A}{\partial x} \right] - \left(\frac{w_0}{8k_0^2} \right) \frac{\partial^2 A}{\partial x^2} - \left(\frac{w_0 k_0}{2} \right) A A^* A = 0 \quad (2.1)$$

where $A(x,t)$ is the complex modulation envelope

$$A(x,t) = R(x,t) \exp(i p(x,t)) \quad (2.2)$$

and $A(x,t)$ is related to the free surface $n(x,t)$ as follows:

$$n(x,t) = \text{Re} \left(A(x,t) \exp \left[i \left(k_0 x - w_0 t \right) \right] \right) \quad (2.3)$$

w_0 and k_0 are the carrier frequency and wavenumber.

x is horizontal distance and t is time. The appropriate time and length scales for nondimensionalization are:

$$T = \left(\frac{ak_0}{w_0} \right)^2 w_0 t, \quad X = \left(\frac{ak_0}{k_0} \right) k_0 \left[x - \left(\frac{w_0}{2k_0} \right) t \right] \quad (2.4)$$

where ak_0 is wave steepness and X is a frame of reference that moves at the linear group velocity.

In addition, if we nondimensionalize the envelope by the

maximum wave amplitude, we arrive at the dimensionless form:

$$i \frac{\partial A}{\partial T} - \frac{1}{8} \frac{\partial^2 A}{\partial X^2} - \frac{1}{2} A^* A A = 0 \quad (2.5)$$

For initial conditions that decay sufficiently rapidly as $|X| \rightarrow \infty$, i.e. pulse envelopes, Eq. 2.5 was solved exactly by Zakharov and Shabat [1972] using the inverse scattering transform developed by Gardner et al [1967]. Particular solutions to 2.5 take the form:

$$A(X,T) = a \operatorname{sech} \left(\frac{1}{2} a (X - UT) \right) \exp \left(-i a^2 T/4 - 4iUX + 2iU^2 T \right) \quad (2.6)$$

These are progressive envelope pulses whose height and width are inversely proportional to each other but are independent of the speed of propagation U relative to the group velocity (unlike KdV solitons).

Properties of the exact solution are summarized by Zakharov and Shabat [1972] and by Yuen and Lake [1975]. For our purposes we note the following:

(a) An arbitrarily shaped one-dimensional envelope pulse will eventually disintegrate into a definite number of permanent progressive sech solitons of the form given by equation 2.6 and a linearly dispersive tail. The number and structure of the solitons and the structure of the tail are

completely determined by the initial condition.

(b) The linearly dispersive tail is small and relatively unimportant. The linear dispersion gives a $1/\sqrt{t}$ amplitude decay in the tail.

(c) The time scale of formation of these solitons (or transition time from initial to asymptotic state) is directly proportional to the pulse length and inversely proportional to the pulse amplitude.

(d) For a real initial profile, the number of solitons in the asymptotic state can be estimated by the formula:

$$N_{S,T} = \frac{\sqrt{2}}{\pi} \int_{-\infty}^{\infty} A(X,0) dX = \frac{\sqrt{2}}{\pi} \int_{-\infty}^{\infty} ak_0^2 f(x) dx \quad (2.7)$$

where $A(X,0) = f(x)$, $0 < f(x) < 1$

In section 2.3.4 we will see that there is very little phase variation in the initial pulse. Therefore, if we estimate the pulse as a top hat profile of length L we arrive at the following formula for estimating the expected number of solitons:

$$N_{S,T} = \frac{\sqrt{2}}{\pi} ak_0^2 L = \sqrt{2} ak_0 N_{PKS} \quad (2.8)$$

where N_{PKS} is the number of peaks (Table 2.2).

We now proceed to describe the qualitative features of the evolution seen in Figures 2.3 to 2.11.

Figure 2.3 (Exp 78) shows the evolution of a group of 10 waves of small steepness ($ak = .03$). There is an initial modulation of the group. In addition, we observe some lower frequency waves moving to the front of the group and some higher frequency waves trailing the group. This is typical of all the experiments and indicates linear dispersion. However, for groups of higher initial steepness this linear dispersion is of much lower amplitude than the group and separates from it as the waves propagate. For this case of relatively low amplitude the entire group seems dominated by frequency dispersion. Basically, the group spreads and attenuates as it propagates. No permanent-type solitons form nor are any predicted from the initial condition (Table 2.2).

Figure 2.4 (Exp 77) shows the evolution of a slightly steeper group ($ak = .07$) of 25 waves. The modulation starts from both ends of the group. This is typical of all the experiments, particularly for longer group lengths, and is probably due to the starting and stopping transients and the large number of frequencies present at the ends of the group. The modulation proceeds from four groups at 30.5 meters to three groups at 45.7 meters to two groups at 76.2 meters to one slightly modulated group at 137.2 meters. The amplitude has decayed over the distance propagated, and leading small amplitude low frequency waves and trailing small amplitude high frequency waves are observed. The predicted number of

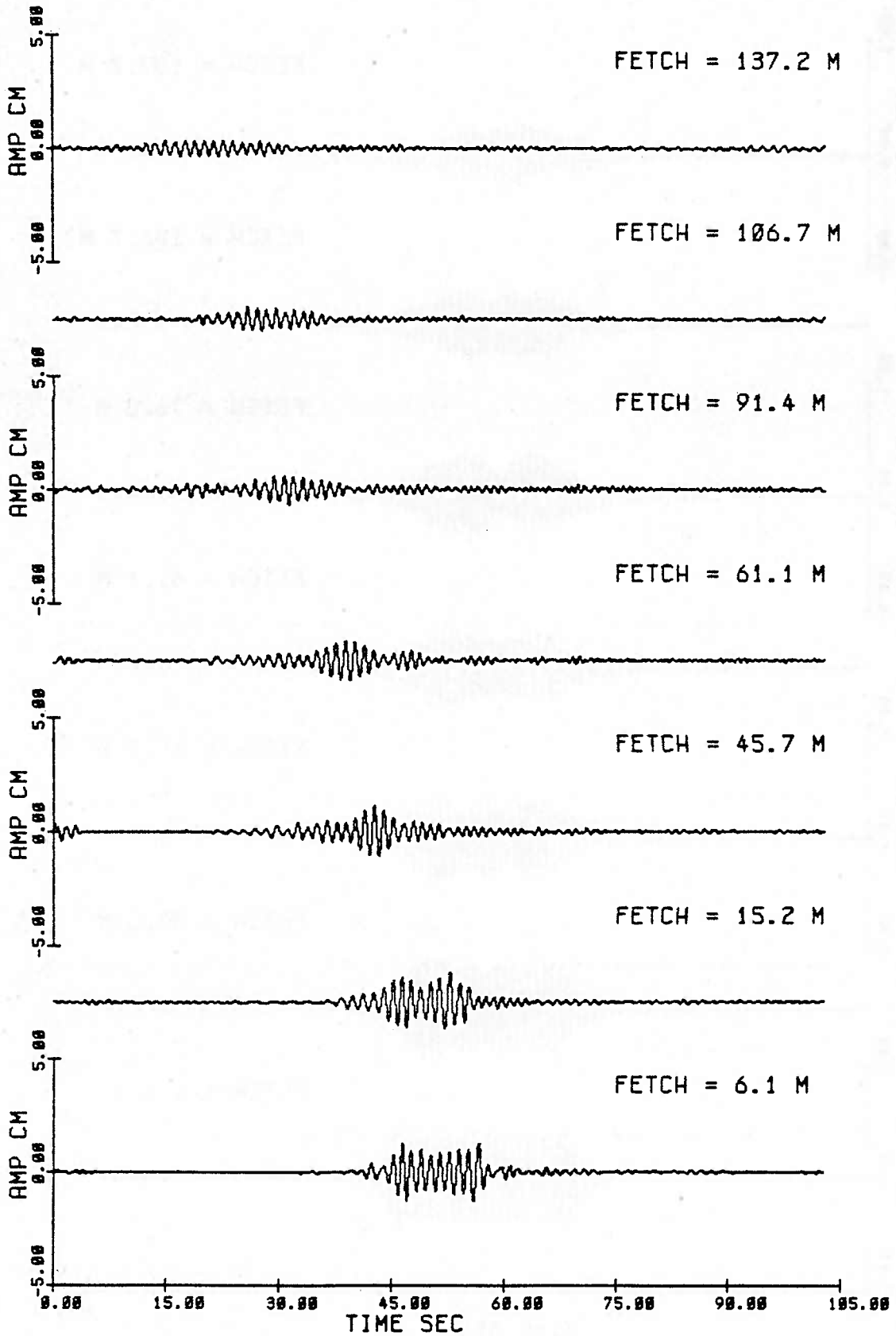


Fig. 2.3 Wave group development with fetch for a group of 10 waves of initial steepness $ak = .03$ (Exp 78).

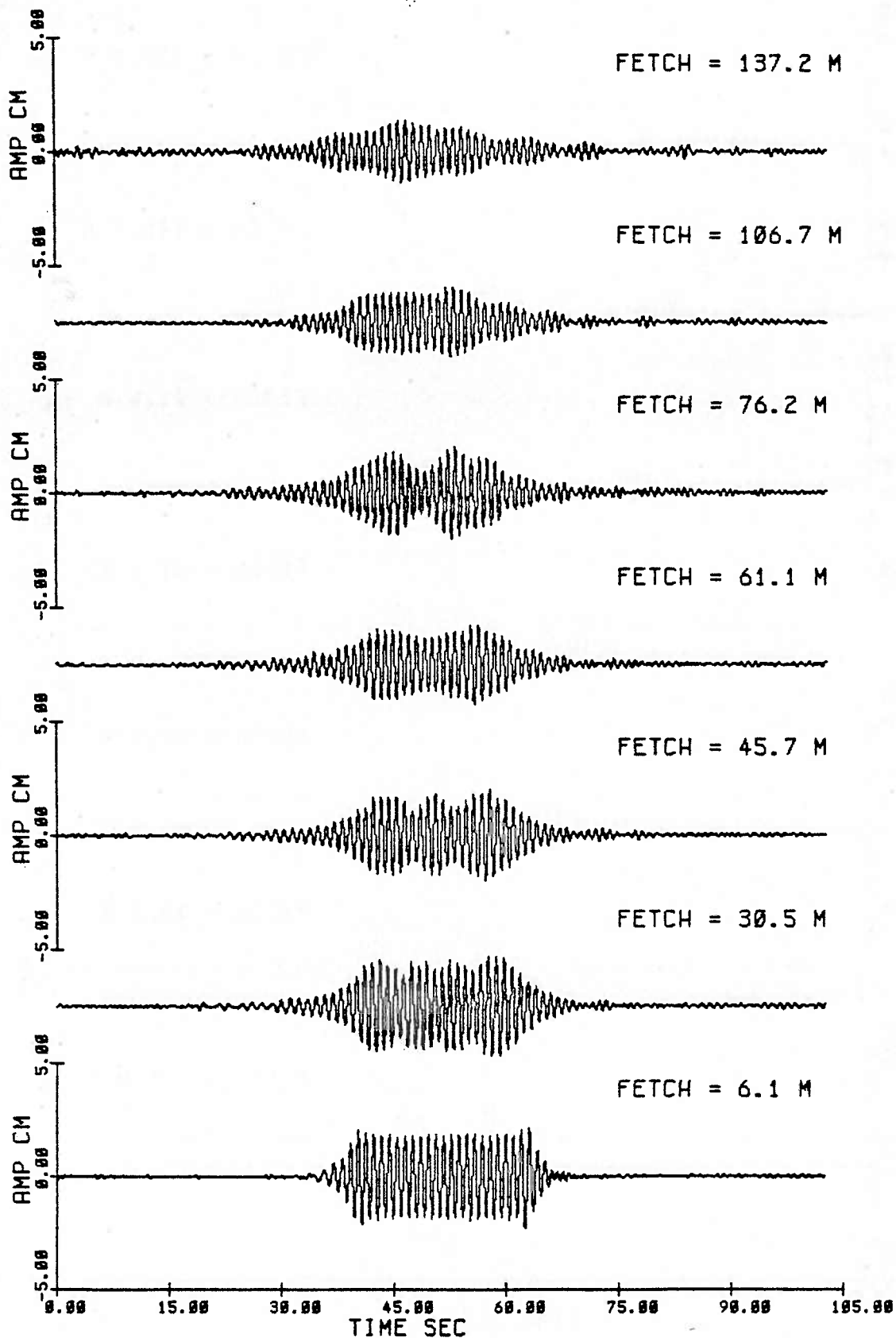


Fig. 2.4 Wave group development with fetch for a group of 25 waves of initial steepness $ak = .07$ (Exp 77).

solitons is one, and the observations indicate that this is possible, but the evolution appears to be incomplete at 137.2 meters. This is anticipated from predictions of the exact solution of the cubic NLS equation which states that the formation time scale of the solitons (or transition time from initial to asymptotic state) is in direct proportion to the length of the pulse and inversely proportional to the steepness. Hence, for long weakly nonlinear groups we expect the longest evolution time scale.

The next three figures (figs 2.5 to 2.7) show the evolution for three different group lengths with wave steepness $ak = .10$ (Exp 86, 87, 88). In figure 2.5 we see the initial pulse modulate and eventually form into a single envelope soliton at 45.7 meters. There is an initial group of small amplitude low frequency waves and a trailing group of higher frequency waves that disperse away from the central envelope as it propagates. The soliton remains fairly steady from 61.1 meters until 137.2 meters although there is some spreading within the group and a decay in amplitude. Due to dissipation, we cannot observe a wave group of permanent form. Rather, we seem to observe a wave group of quasi-permanent form. It appears to adjust in a shorter time than it dissipates, but due to energy loss it can not evolve into the steady asymptotic state that is predicted. This will be further discussed in section 2.3.3

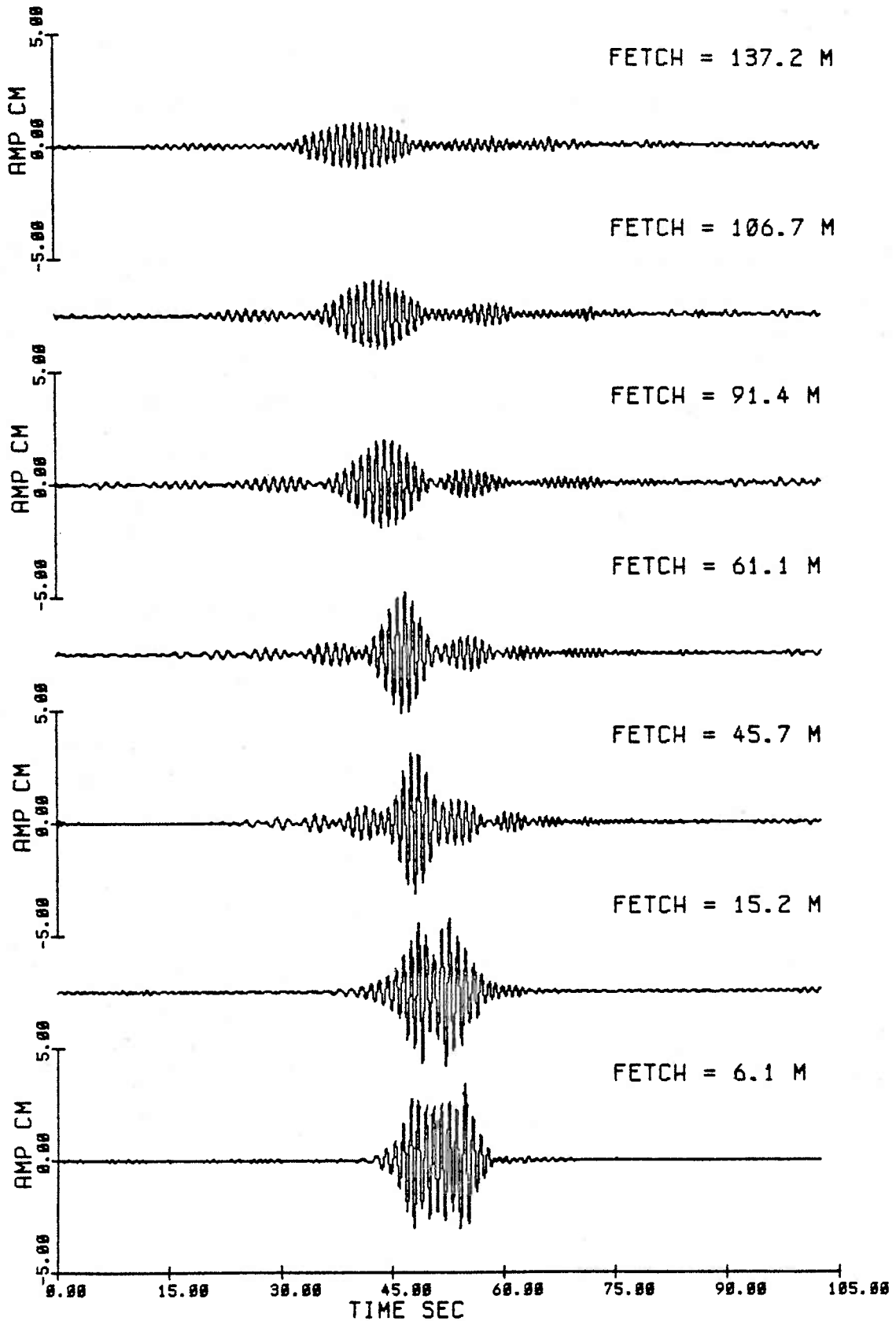


Fig. 2.5 Wave group development with fetch for a group of 10 waves of initial steepness $ak = .10$ (Exp 86).

A similar evolution is noted for Exp 87, figure 2.6. A modulation is seen to start at either end of the group. The formation of a single envelope soliton occurs at further fetch, 91.4 meters, than in the previous figure for evolution of a shorter pulse. Again, dispersive low frequency leading and high frequency trailing waves are seen.

Figure 2.7 shows the development of a still longer group (nominally 25, but actually about 30 waves) of the same steepness (.10) as in the previous two figures. It appears to form a pair of solitons, but the time scale of formation is longer than for the previous two group lengths. A pair is seen to form at 121.9 meters, but the group demodulates slightly at still further distance, and the evolution is incomplete.

Figure 2.8 shows the evolution of a group of 15 waves for one of the steeper experiments ($ak = .15$). For these steeper experiments, frequency downshifting was seen to occur. This will be discussed more fully in the next section. However, we here note that the strongest modulation occurs while the sideband perturbations to the carrier wave are growing. Once the downshifting of the carrier occurs, at 61.1 meters in figure 2.8, the modulation is weaker and the initial pulse appears to 'sort out' into a succession of envelope solitons. In figure 2.8, at 137.2 meters, we see four of these groups

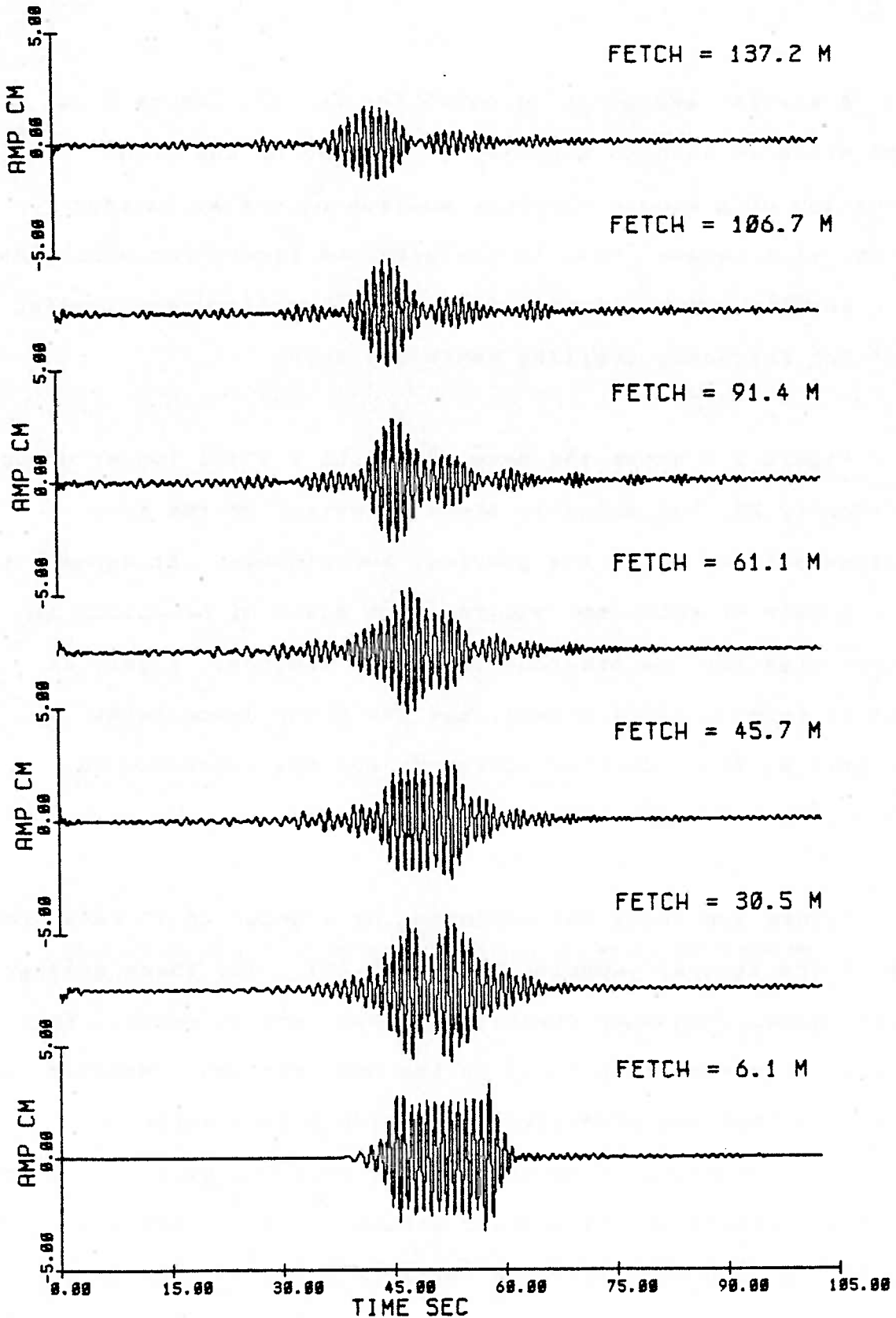


Fig. 2.6 Wave group development with fetch for a group of 15 waves of initial steepness $ak = .10$ (Exp 87).

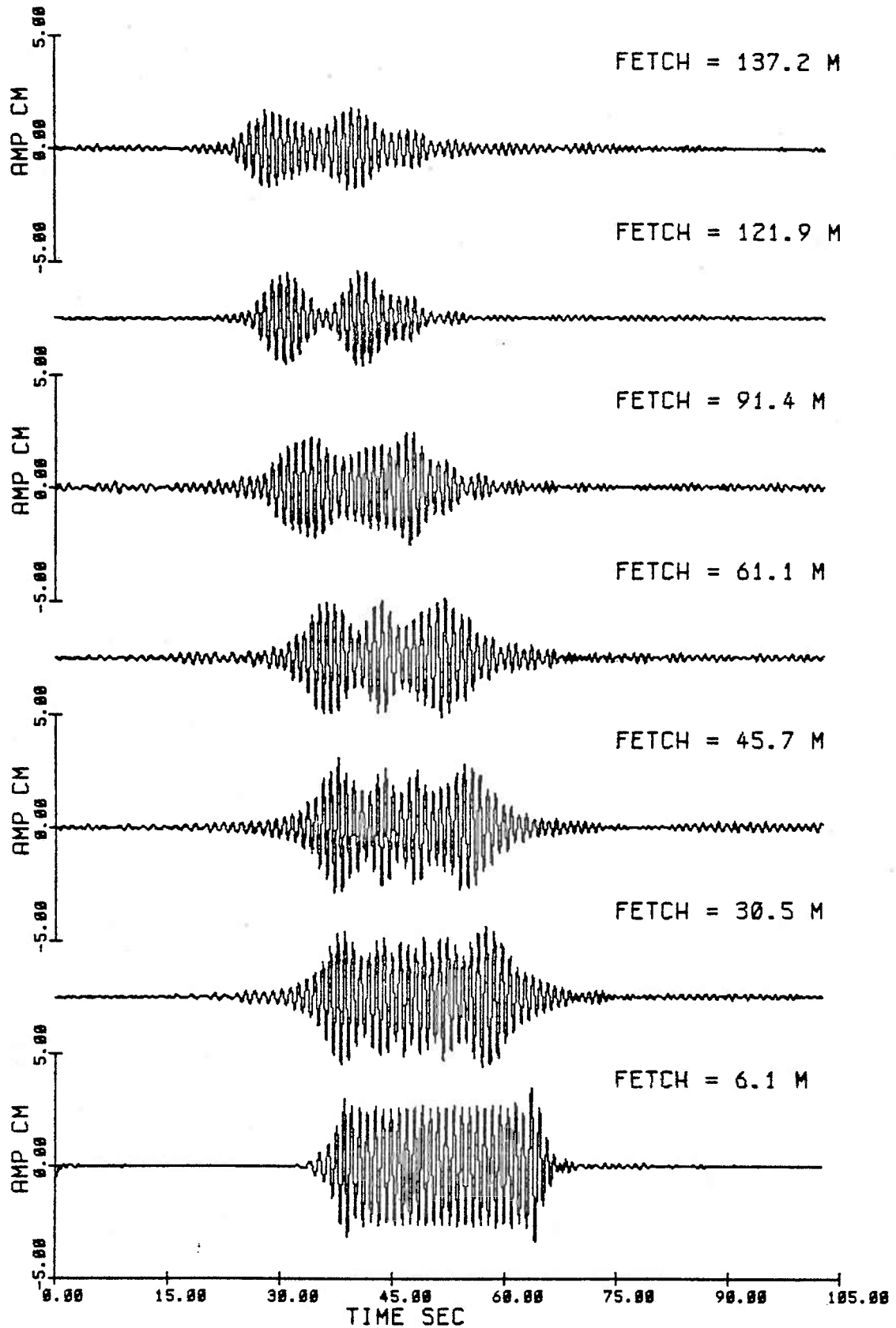


Fig. 2.7 Wave group development with fetch for a group of 25 waves of initial steepness $ak = .10$ (Exp 80).

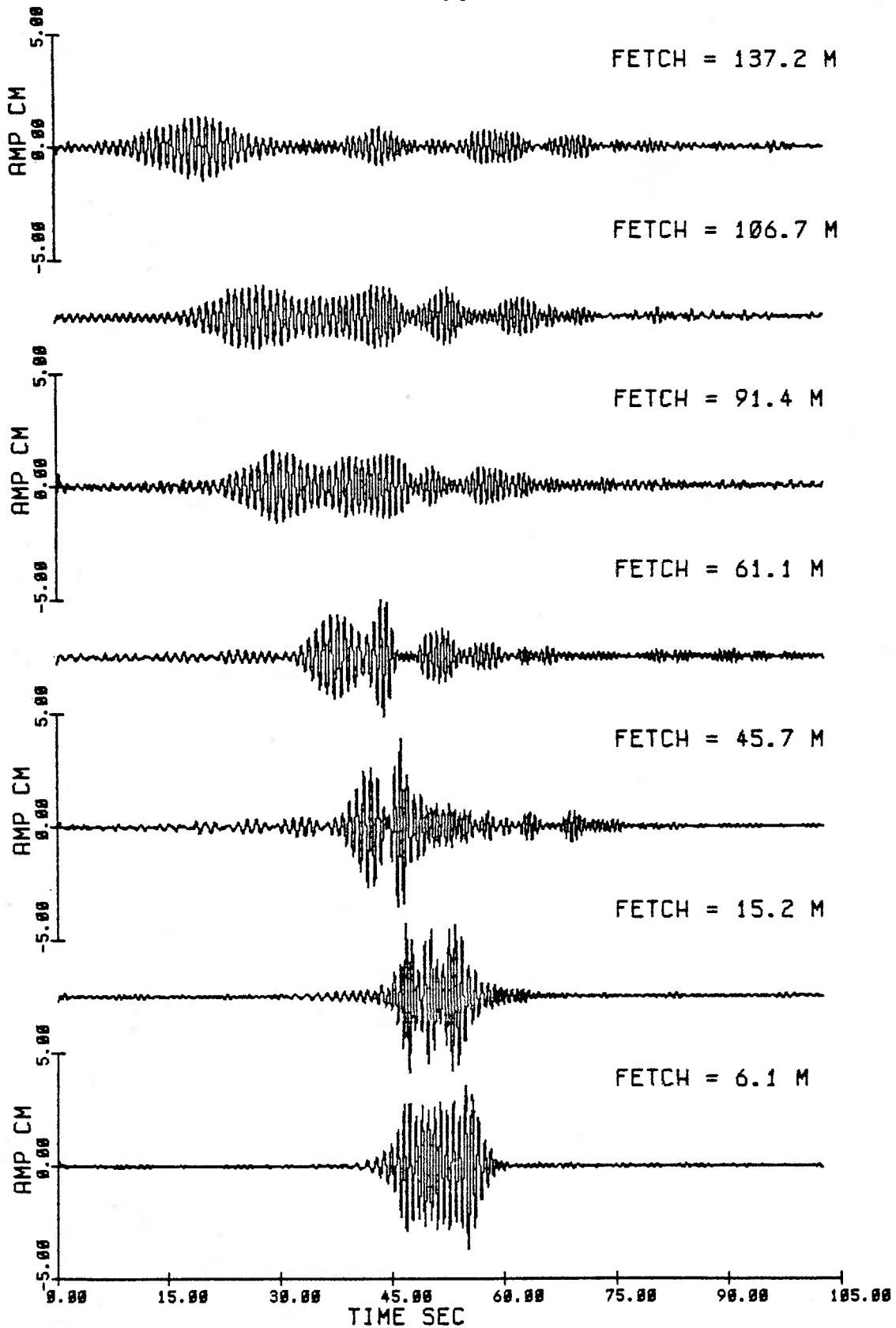


Fig. 2.8 Wave group development with fetch for a group of 15 waves of initial steepness $ak = .15$ (Exp 62).

with the leading groups of slightly lower frequency and larger amplitude.

Figures 2.9 to 2.11 show the evolution for three different group lengths for the steepest experiments ($ak = .16$). The number of predicted and observed solitons agree fairly well (Table 2.2). The 'sorting out' process again occurs when the frequency downshifting of the carrier is achieved. This 'sorting out' seems to take longer for a longer initial pulse. For the longest initial pulse, figure 2.11, the evolution appears to be still incomplete at 137.2 meters.

2.3.2 Downshifting

The phenomenon of frequency downshifting which has been observed in nonlinear continuous wavetrains was also observed to occur in wave groups of sufficient steepness. The downshift was examined using a maximum entropy spectral estimator. Use of traditional methods of power spectral density estimation to examine the spectral evolution of wave groups is limited by the length of the data records. Frequency resolution, the ability to distinguish distinct peaks that are relatively close together in the frequency domain, and a smeared spectral estimate, the result of windowing, are particularly troublesome for short time series.

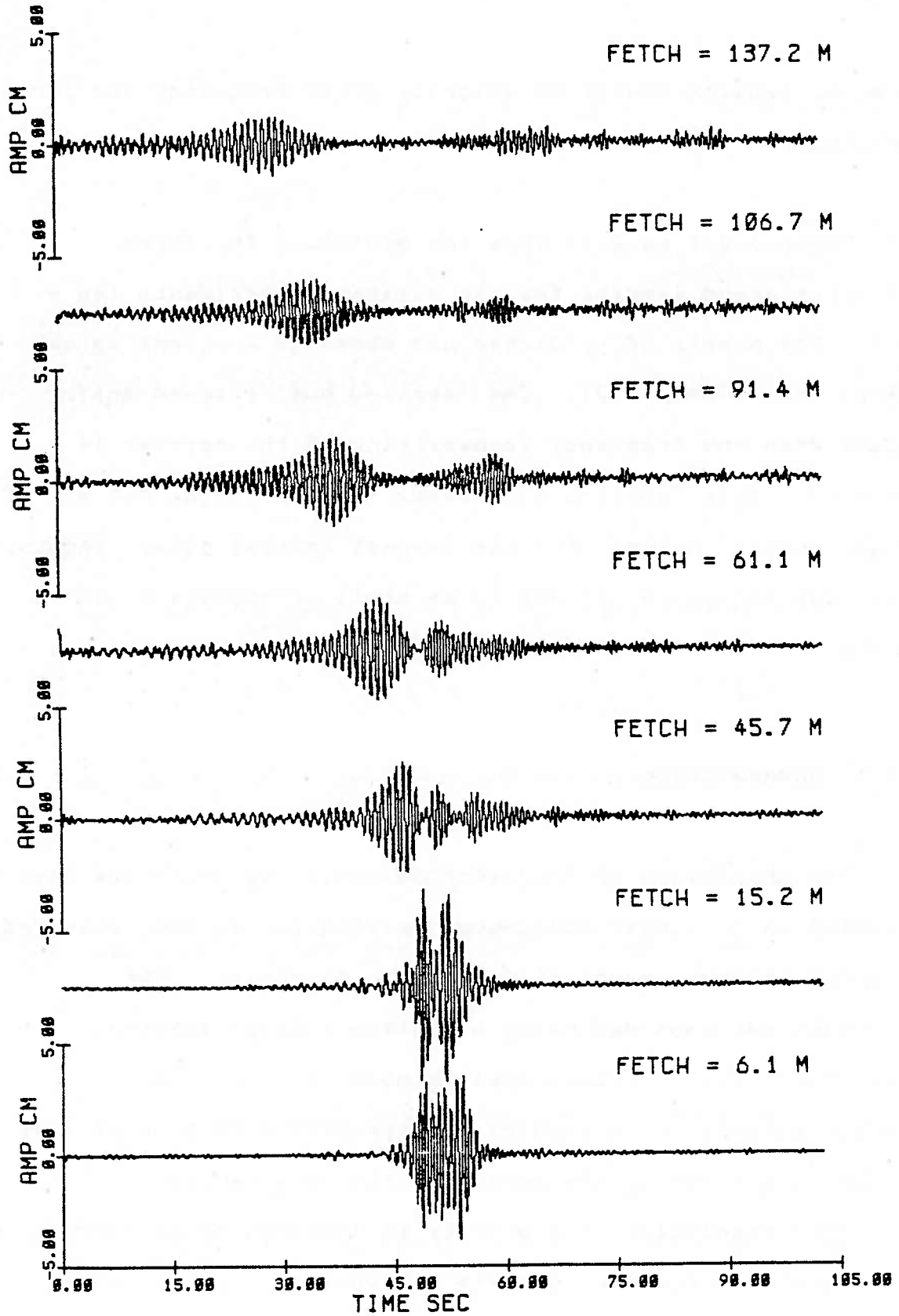


Fig. 2.9 Wave group development with fetch for a group of 10 waves of initial steepness $ak = .16$ (Exp 21).

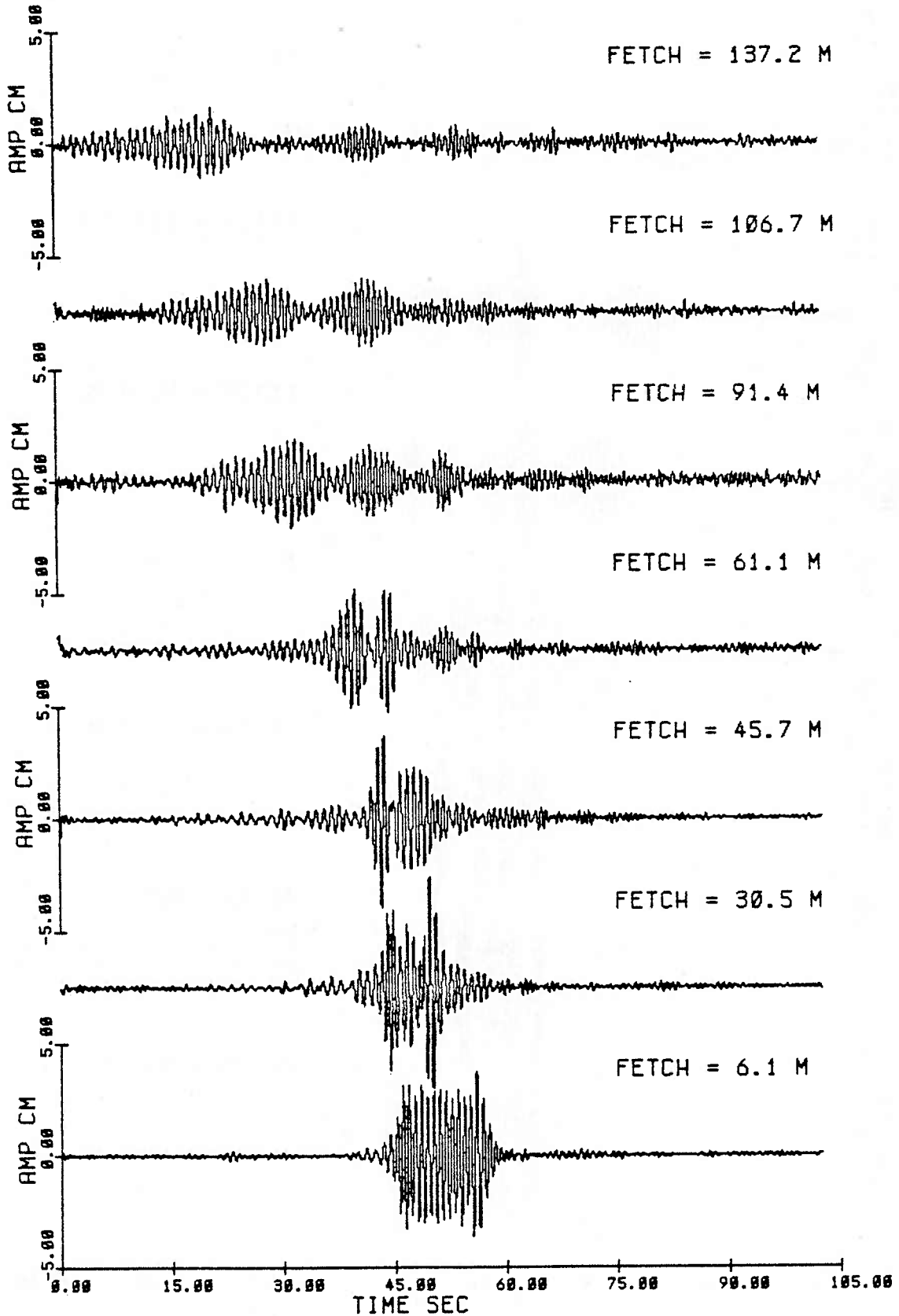


Fig. 2.10 Wave group development with fetch for a group of 15 waves of initial steepness $ak = .16$ (Exp 22).

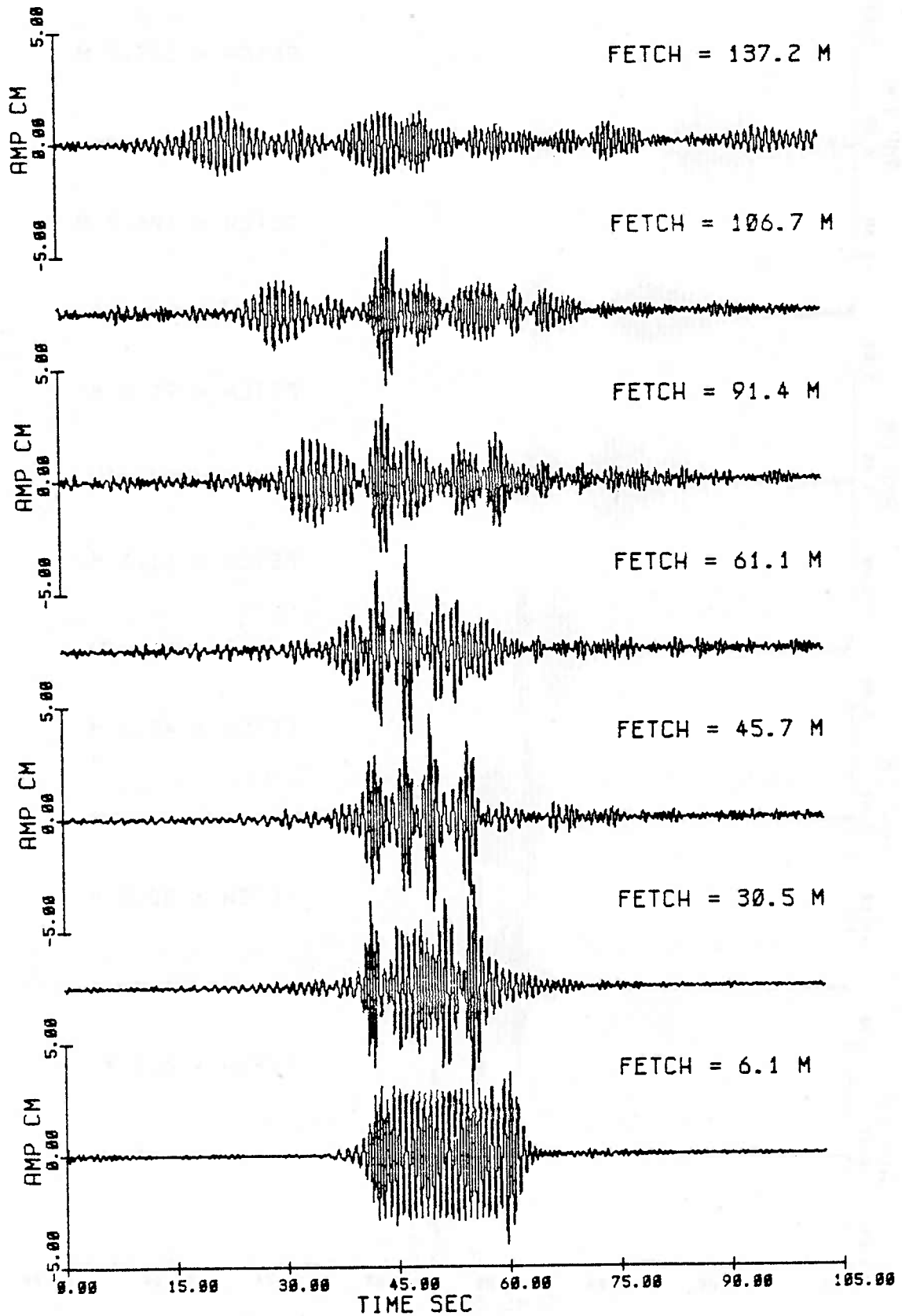


Fig. 2.11 Wave group development with fetch for a group of 25 waves of initial steepness $ak = .16$ (Exp 23).

We use the maximum entropy method (MEM) to look at the spectral evolution of the wave groups. This adopts a modelling approach to spectral estimation. The improved resolution and spectral fidelity result from making more realistic assumptions concerning the nature of the measured process outside of the measurement interval other than assuming it is zero or cyclic. The improvement is especially noticeable for short time series. From this modelling viewpoint, the traditional discrete periodogram estimate is equivalent to a least squares fit of the data to a harmonic (discrete Fourier series) model. The maximum entropy model assumes that the data is autoregressive. The method is outlined in Appendix 2.A.

Figures 2.12 to 2.18 show the spectral evolution for some of the experiments. The first step in data processing was to determine the carrier frequency f_0 and then to band pass filter around this initial carrier frequency. The band pass was one hertz in width, centered on the carrier. The spectra were done on the same one hertz frequency interval using 80 poles (80 autocorrelation lags). Figs. 2.15 and 2.18 are exceptions. The reason behind this choice of narrow frequency band was to achieve very good resolution of peaks close to the carrier frequency. In those experiments where downshifting occurred, the width of the interval always included the downshifted frequency. This was checked by comparison with

spectra of unfiltered data from the final wavegauge observation in the channel. Notice that the horizontal axis is much expanded; these are narrow-banded spectra. For comparison, two spectral evolutions for unfiltered data on the interval [0.1 hz - 3.0 hz] using 100 poles are shown (Figs. 2.15 and 2.18).

The frequency downshifting observed in wave groups seems to result from a modulational instability. Initially, for groups of sufficient wave steepness, sidebands are seen to grow. After a time the lower sideband grows at a faster rate than the upper sideband. The modulation is strongest when the lower sideband is smaller than the fundamental. Eventually, the lower sideband exceeds the fundamental peak. At this point the modulation appears to have 'sorted out' into a succession of quasi-permanent solitons with the larger amplitude, lower frequency groups leading. The downshifting process seems irreversible. Table 2.1 tabulates the frequency f_1 of the spectral peak from the final observation at 137.2 meters. The percentage downshift, df/f_0 , from the fundamental is also calculated. No downshifting is seen to occur for the experiments with lowest steepnesses ($ak = .03$ and $.07$). A small amount of downshifting, about 1 %, occurs for groups of steepness $ak = .10$. The biggest percentage downshift, on the order of 15 %, is seen to occur for the steepest experiments ($ak = .15, .16$). The longer groups tend to have slightly

larger downshifts.

Figure 2.12 shows the spectral evolution of a group of 10 waves of initial wave steepness $ak = .03$ (Exp 78). The time development of this group is shown in fig. 2.3. Initially at 6.1 meters we see that the spectrum is narrow-banded with a peak located at 0.80 hz. As the group evolves, the location of the spectral peak remains fixed, although the spectrum is seen to become more broad-banded. Recall that this wave group experiment showed the strongest linear dispersion. We see the effects of the filter rolloff at the band edges (.3 and 1.3 hz). In two later figures (2.15 and 2.18) we will show spectra of unfiltered data done on other experiments which eliminates the filter effect at the edges at the expense of resolving the sideband peaks. Finally, we note that for this short group of small initial steepness no sidebands were seen to grow, and no frequency downshifting occurred.

Figure 2.13 shows the evolution of a group of 25 waves with steepness $ak = .07$ (Exp 77) corresponding to the time evolution shown in fig. 2.4. The initial peak remains fixed and no sidebands are seen to grow. At 30.5 meters we see a suggestion of sideband presence, but the amplitudes are more than 40 db down from the fundamental and do not develop with distance. Again we see the effects of the filter rolloff at the band edges, this time at .5 and 1.5 hz, and the spectrum

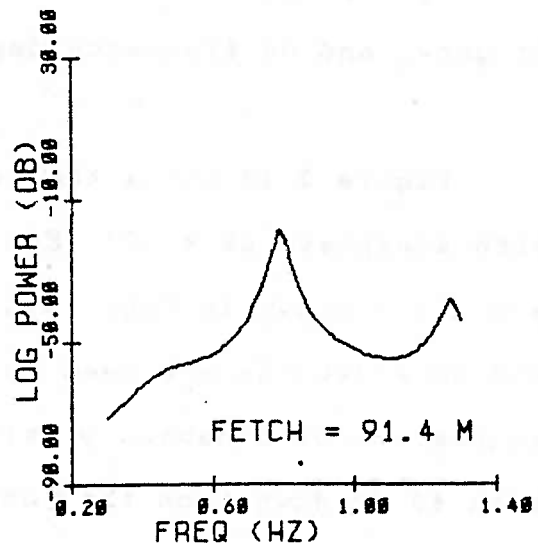
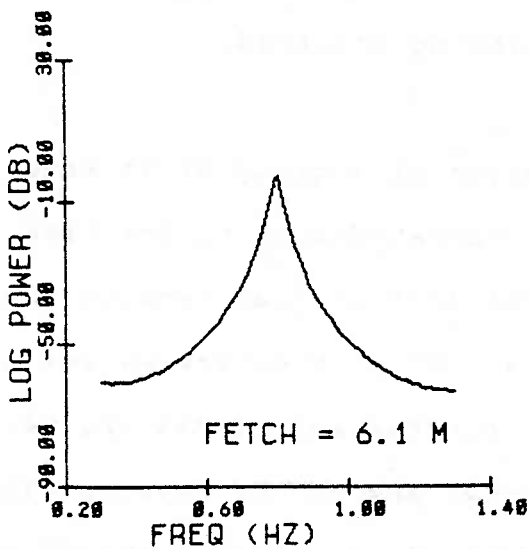
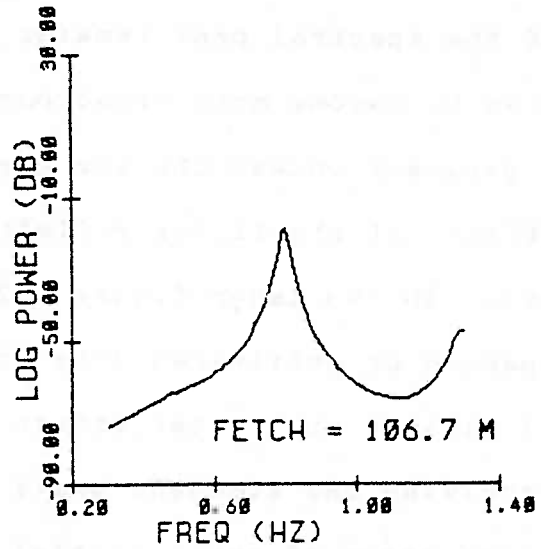
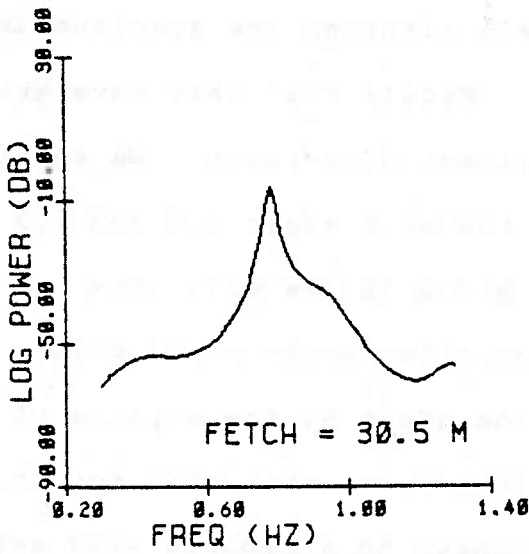
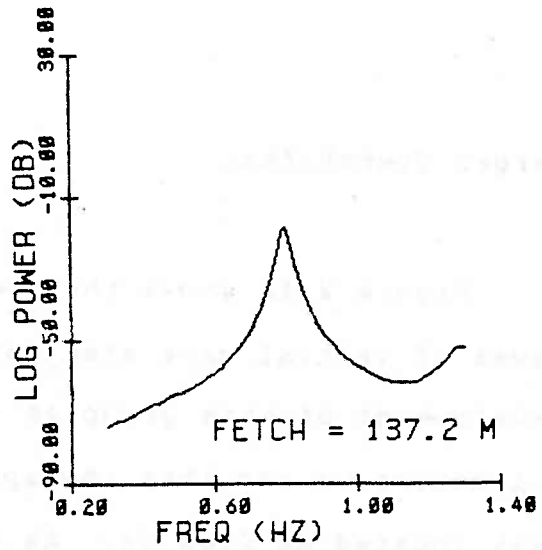
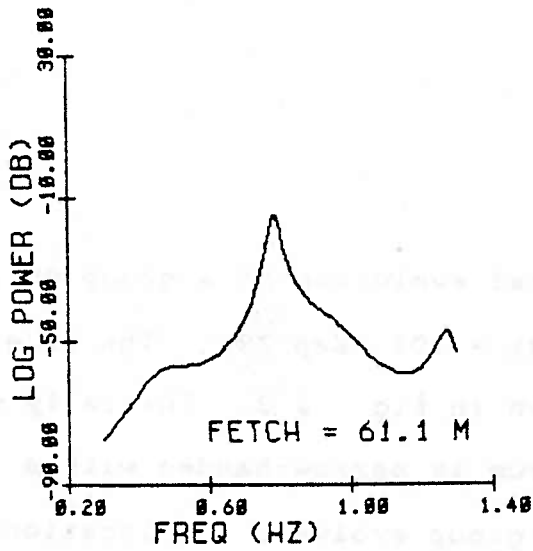


Fig. 2.12 Maximum entropy (MEM) spectral evolution with fetch for a group of 10 waves of steepness $ak = .03$ (Exp 78). Fetches as indicated. Group was bandpassed on the interval $[.3, 1.3]$ hz centered on the initial carrier frequency 0.80 hz. Filter rolloff occurs at the bandedges.

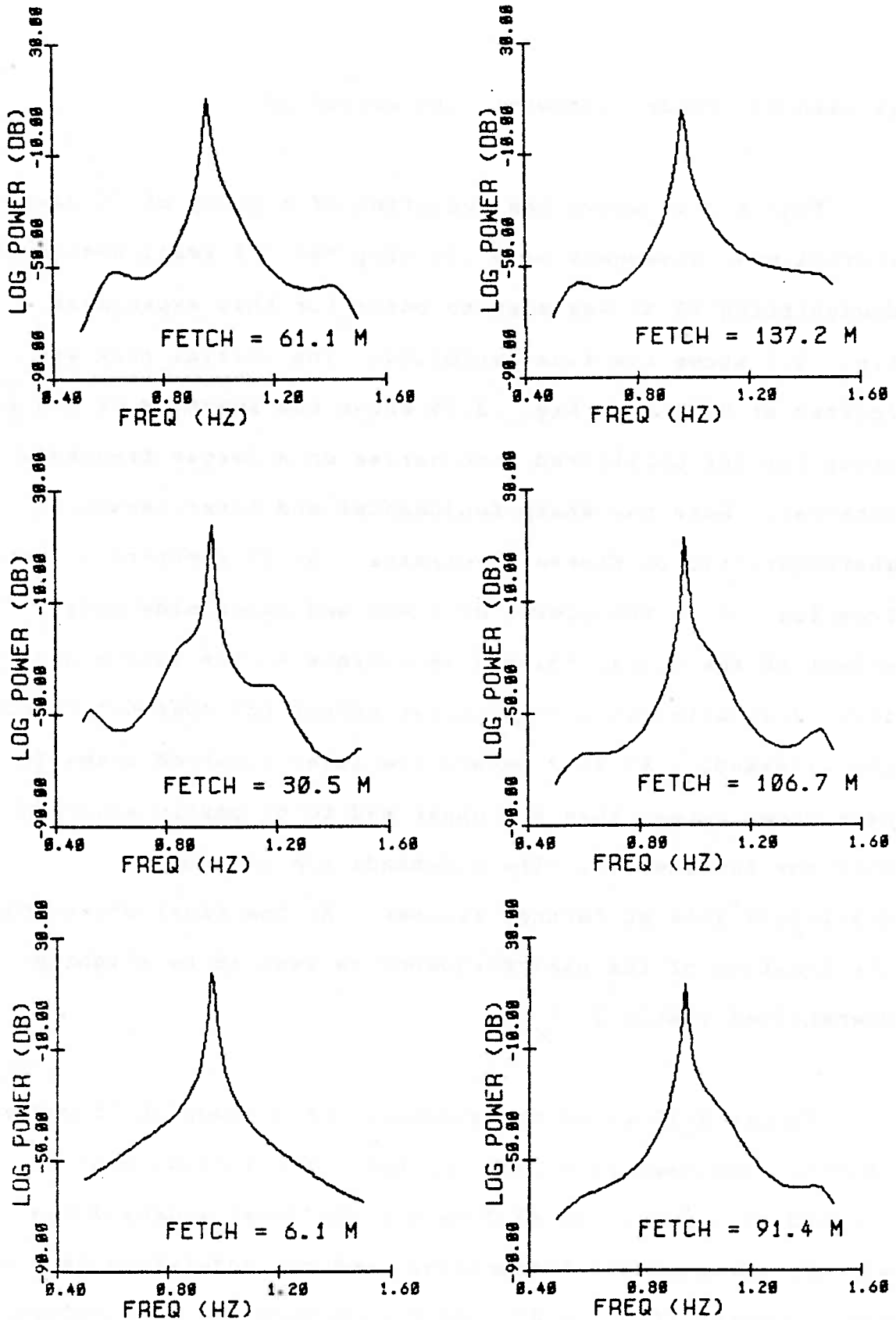


Fig. 2.13 Maximum entropy (MEM) spectral evolution with fetch for a group of 25 waves of steepness $ak = .07$ (Exp 77). Fetches as indicated. Group was bandpassed on the interval $[.5, 1.5]$ hz centered on the initial carrier frequency 0.96 hz. Filter rolloff occurs at the bandedges.

is seen to broaden somewhat with evolution.

Figure 2.14 shows the evolution of a group of 25 waves of initial wave steepness $ak = .10$ (Exp 88). A small amount of downshifting (2 %) was seen to occur for this experiment. Fig. 2.7 shows the time evolution. The initial peak was located at 0.96 hz. Fig. 2.15 shows the spectrum of the same group for the unfiltered time series on a larger frequency interval. Note the sharp fundamental and first harmonic characteristic of Stokes wavetrains. At 15.2 meters we see from fig. 2.14 the growth of lower and upper sidebands. The effect of the filter rolloff is visible at the band edges; fig. 2.15 eliminates this filter effect but does not resolve the sidebands. At 45.7 meters the lower sideband seems to have grown larger than the upper and to be partly absorbed into the fundamental. The sidebands are no longer distinguishable at further fetches. At the final observation the location of the peak frequency is seen to be slightly downshifted (Table 2.1).

Figure 2.16 shows the evolution of a group of 15 waves of initial steepness $ak = .15$ (Exp 62). The initial peak is located at 1.2 hz. At 45.7 meters the lower sideband has already exceeded the fundamental, and the modulation here is the strongest (fig. 2.8). At 61.1 meters the downshifting of the carrier is achieved, and the initial pulse appears to have

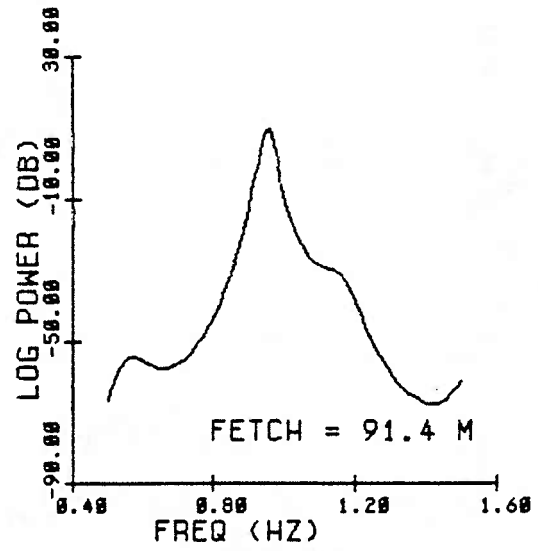
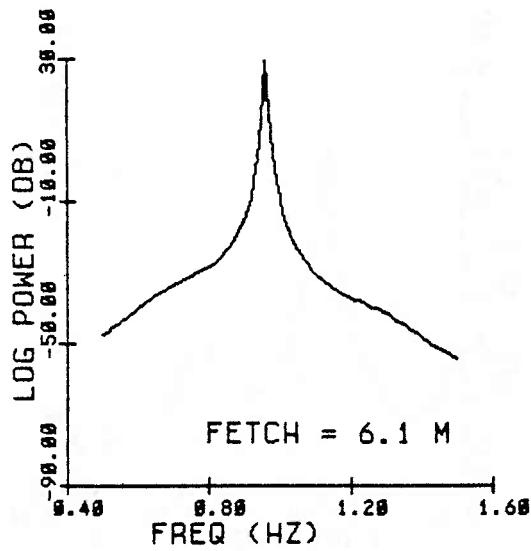
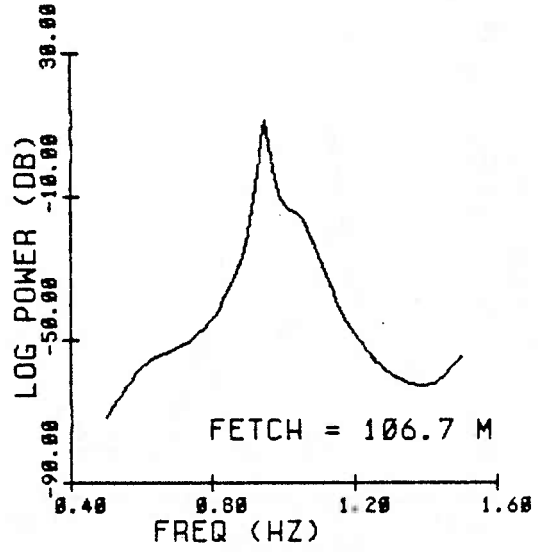
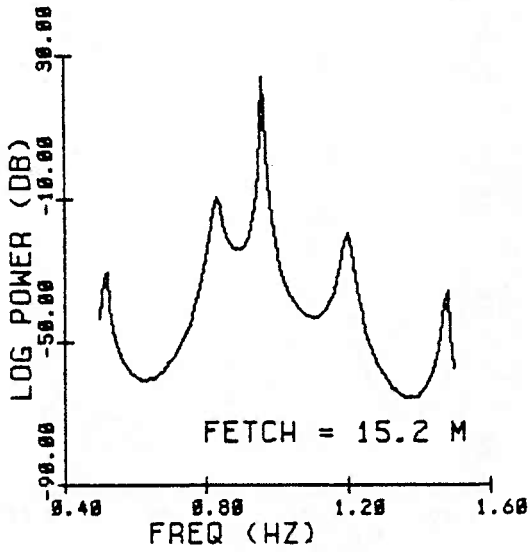
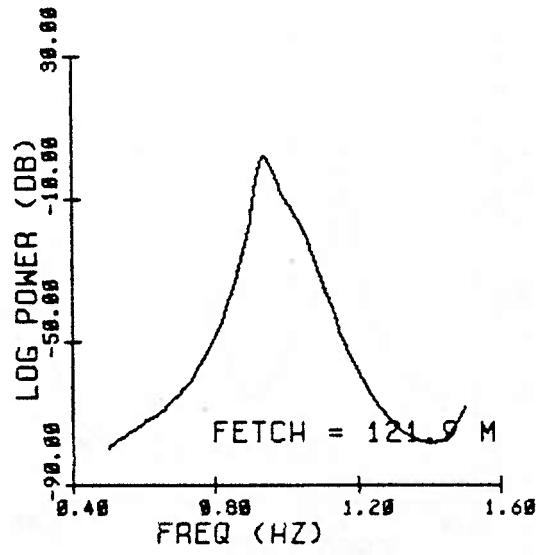
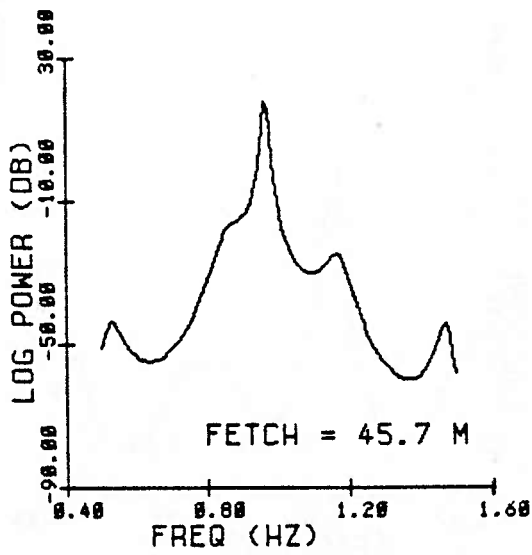


Fig. 2.14 Maximum entropy (MEM) spectral evolution with fetch for a group of 25 waves of steepness $ak = .10$ (Exp 88). Fetches as indicated. Group was bandpassed on the interval $[.5, 1.5]$ hz centered on the initial carrier frequency 0.96 hz. Filter rolloff occurs at the bandedges.

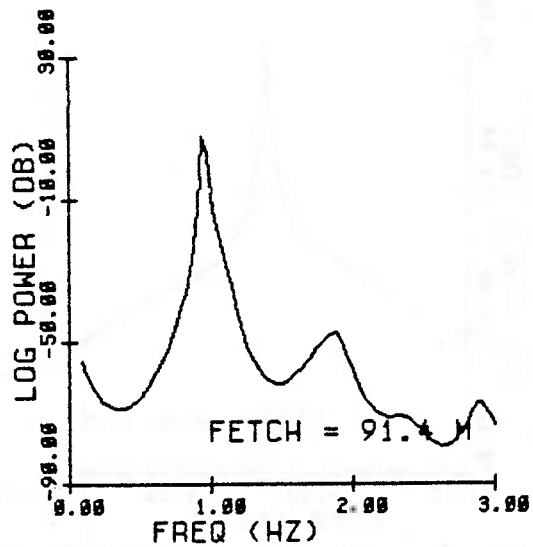
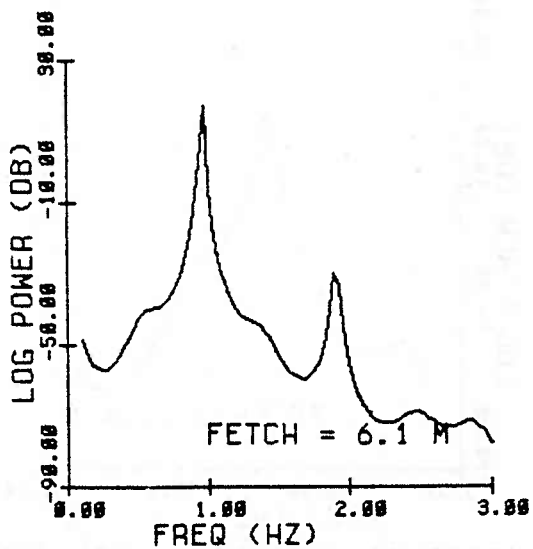
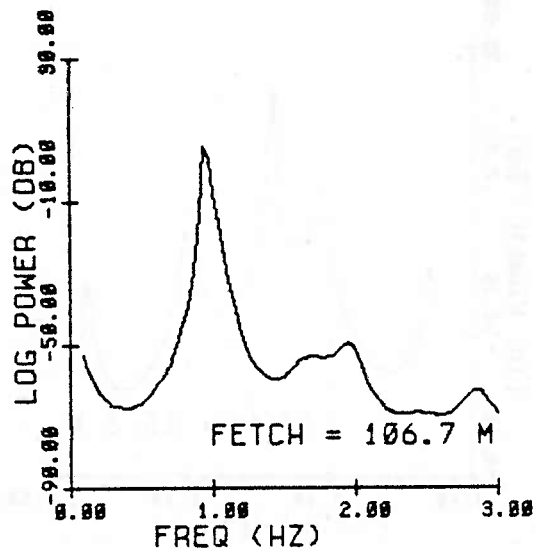
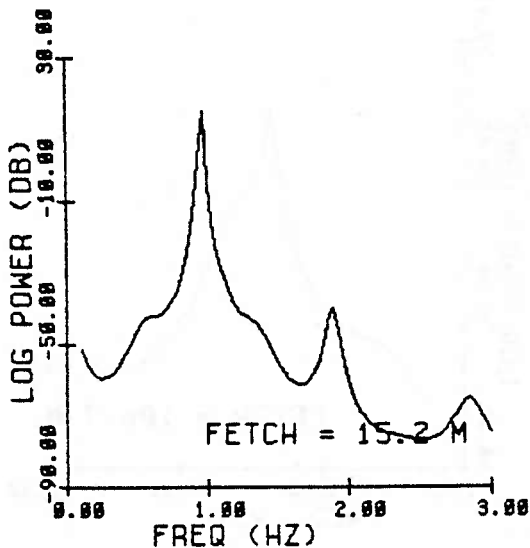
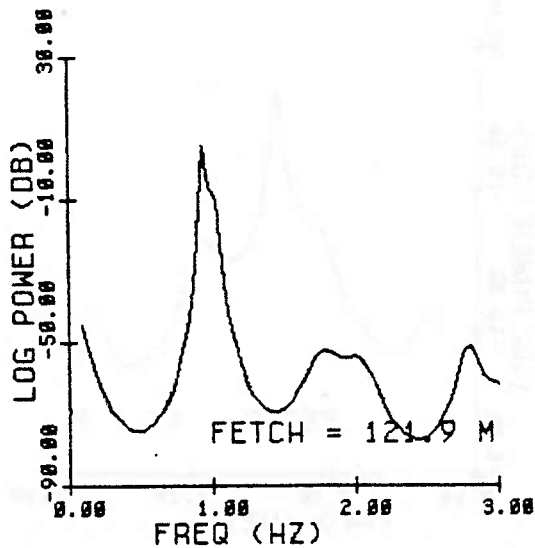
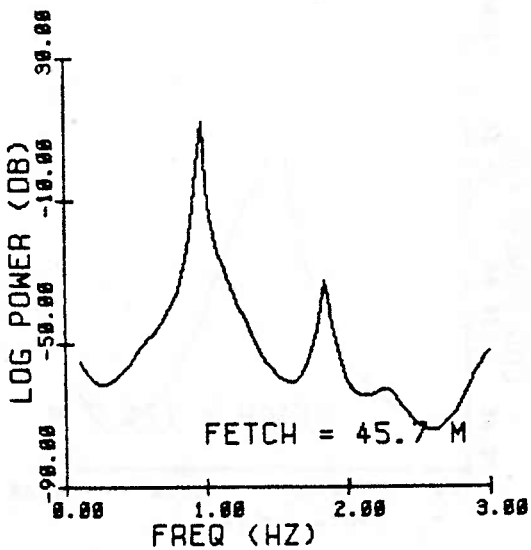


Fig. 2.15 Same as previous (2.14) except data is unfiltered and spectrum is done on larger interval [1,3.0]hz. Notice the first harmonic peak, the loss in resolution of sidebands (15.2 m) and the removal of spurious peaks at the bandedges of the filter.

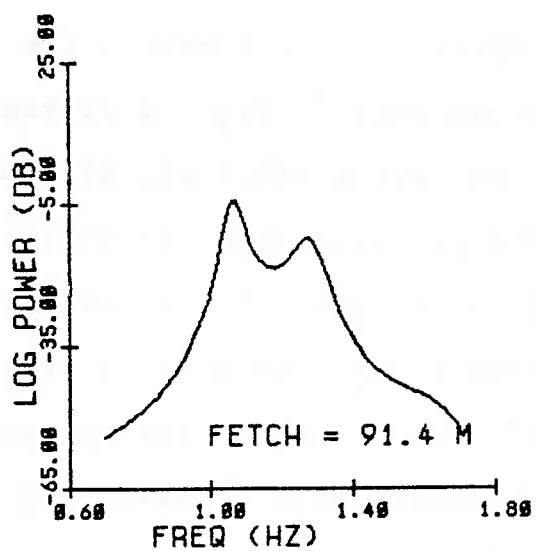
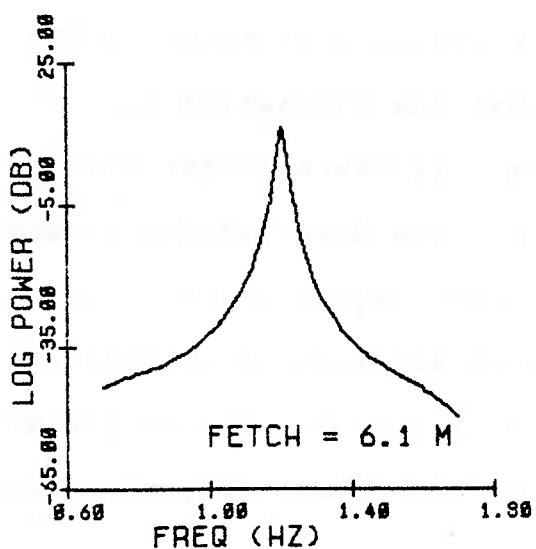
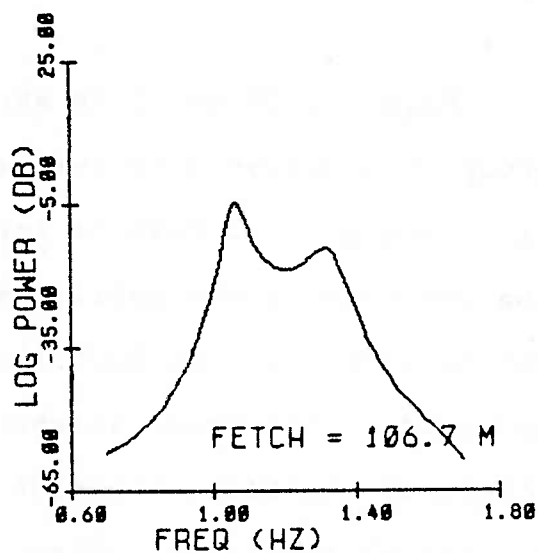
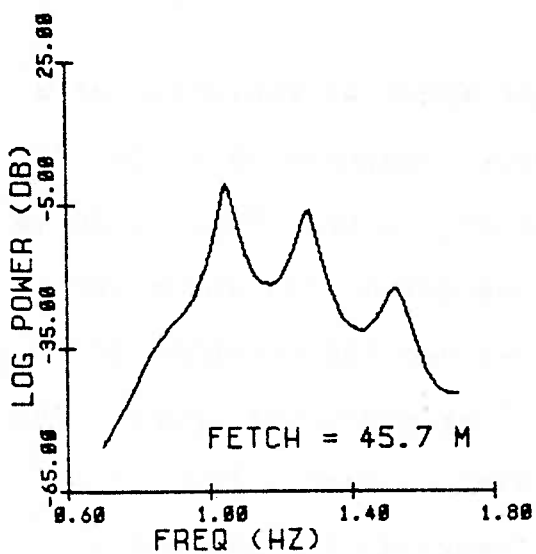
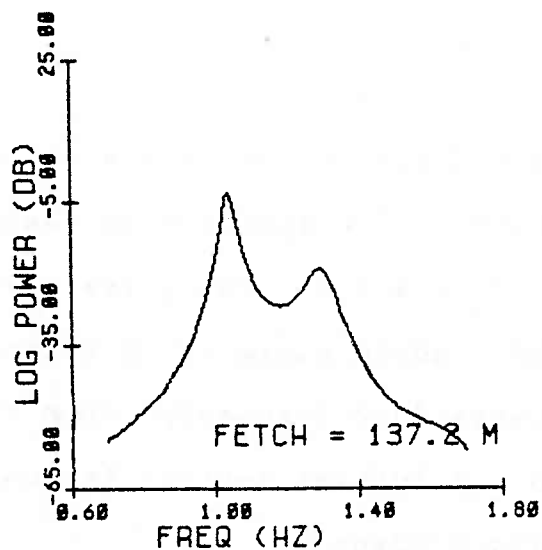
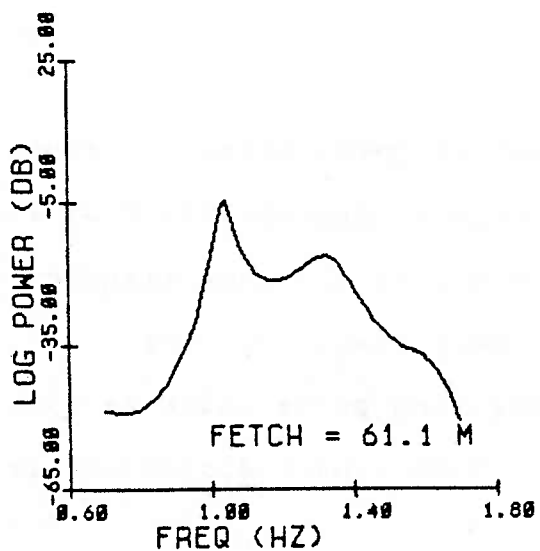


Fig. 2.16 Maximum entropy (MEM) spectral evolution with fetch for a group of 15 waves of steepness $ak = .15$ (Exp 62). Fetches as indicated. Group was bandpassed on the interval $[.7, 1.7]$ hz centered on the initial carrier frequency 1.20 hz. Filter rolloff occurs at the bandedges.

sorted itself out into a succession of quasi-steady envelope pulses. The spectrum is seen to broaden appreciably from its initial state. The pulses are not all of the same frequency. The leading pulse is of slightly lower frequency (the downshifted frequency) than the trailing pulse which is close to the initial carrier frequency. Some linear dispersion is also evident.

Figs. 2.17 and 2.18 show the spectral evolution of a group of 25 waves with initial wave steepness $ak = .16$ (Exp 23). The initial peak is located at 1.2 hz. Fig. 2.18 is the spectrum of the unfiltered time series and shows the second harmonic. At 30.5 meters we see the presence of sidebands; the lower sideband has exceeded the upper. The effect of the filter rolloff is also evident. Fig. 2.18 eliminates the filter effect but resolves the sidebands poorly. At 61.1 meters the lower sideband is equal to the fundamental. Fig. 2.11 shows that the modulation is strongest at 45.7 and 61.1 meters. It takes longer than in the previous spectral evolution for the downshifting to occur. At 91.4 meters the initial pulse seems again to have sorted itself out into a train of envelope solitons of increasing frequency. Again the spectra are seen to broaden as the group evolves. Both downshifting (15 %) and linear dispersion are present.

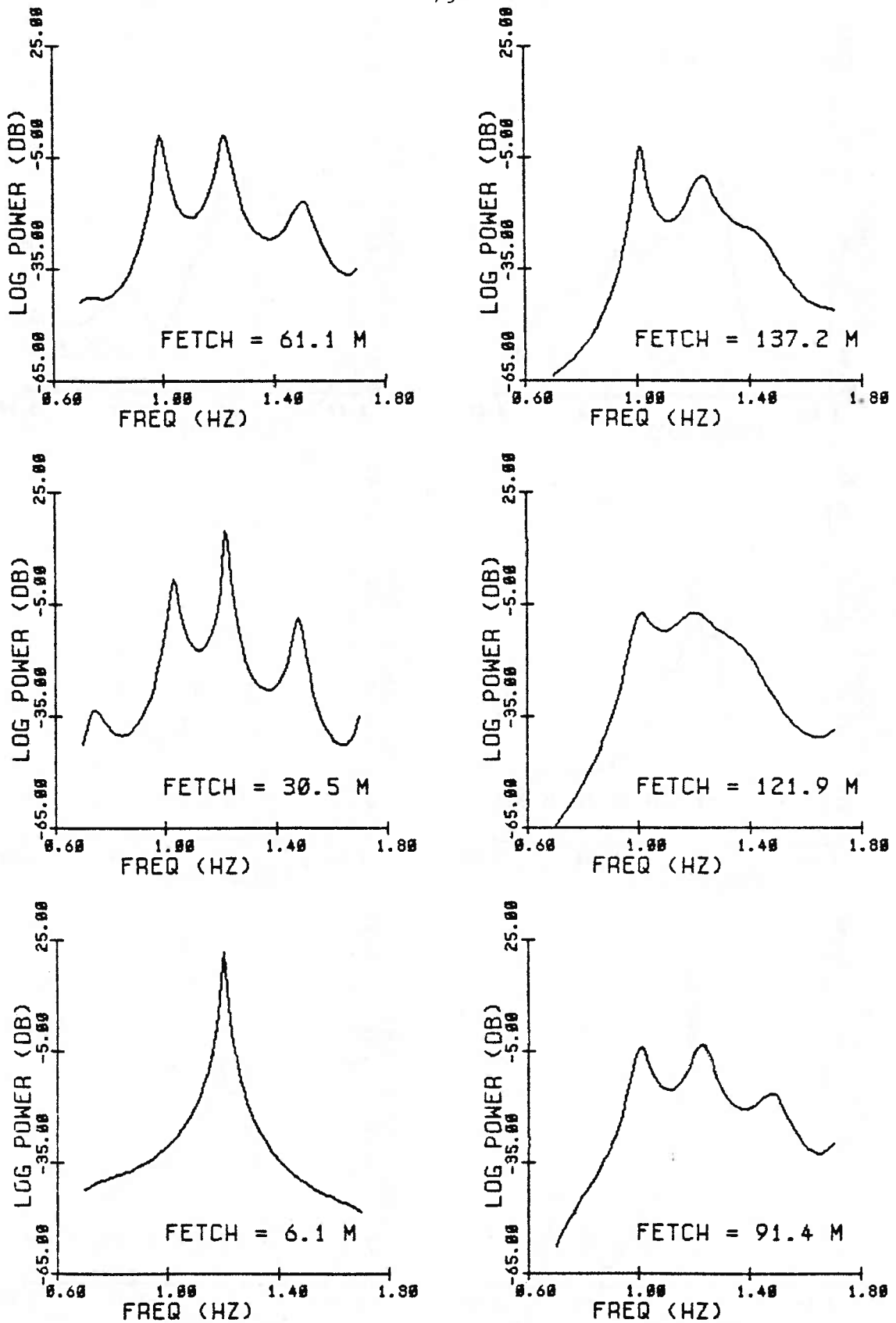


Fig. 2.17 Maximum entropy (MEM) spectral evolution with fetch for a group of 25 waves of steepness $ak = .16$ (Exp 23). Fetches as indicated. Group was bandpassed on the interval $[.7, 1.7]$ hz centered on the initial carrier frequency 1.20 hz. Filter rolloff occurs at the bandedges.

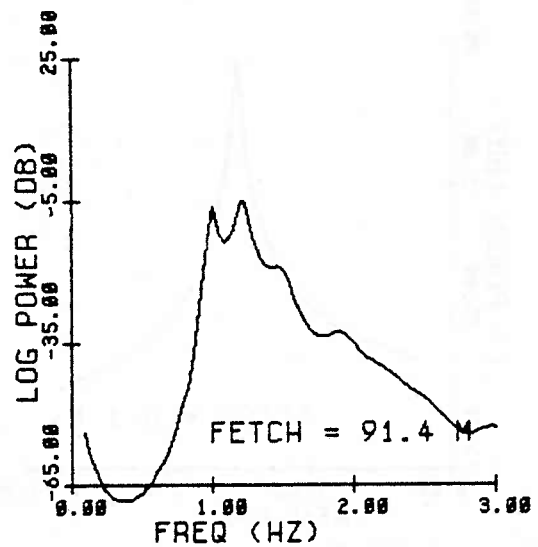
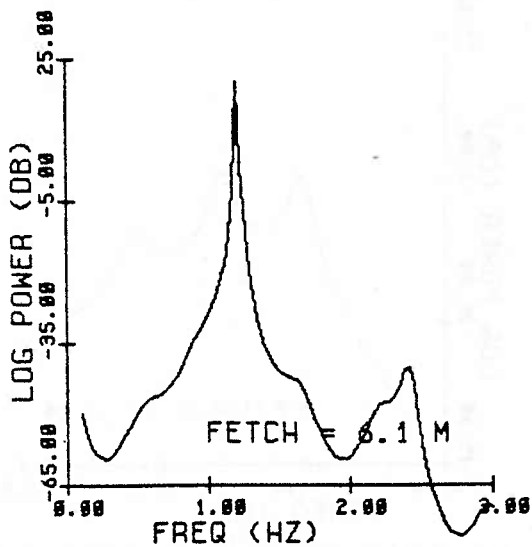
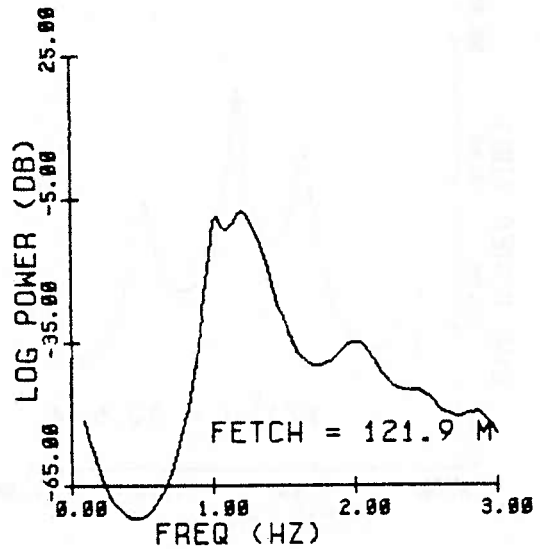
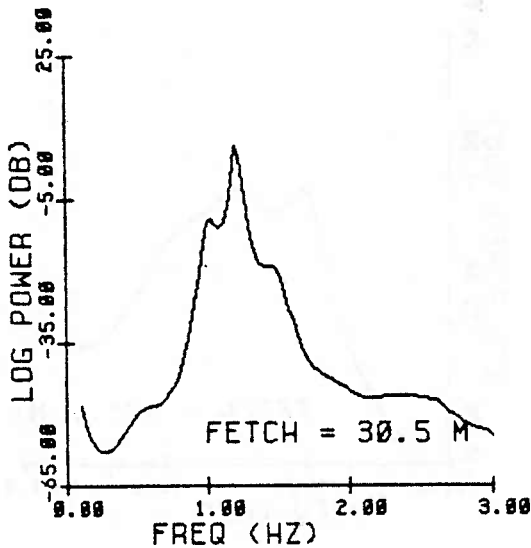
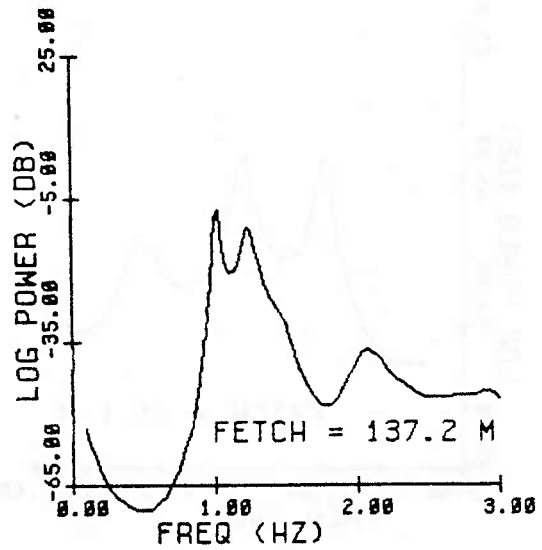
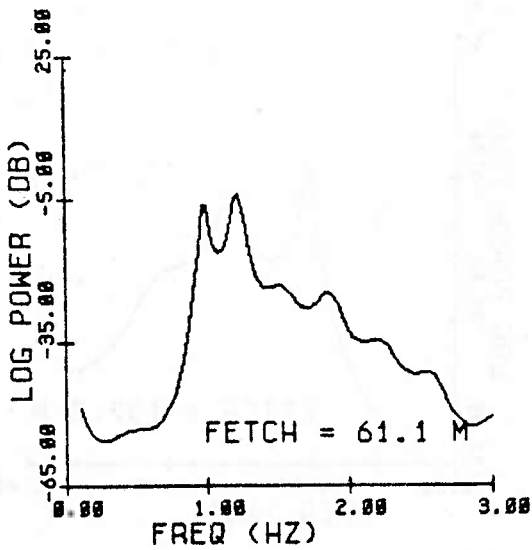


Fig. 2.18 Same as previous (2.17) except data is unfiltered and spectrum is done on larger interval [1,3.0]hz. Notice the first harmonic peak (6.1 m), the loss in resolution of sidebands (30.5 m) and the removal of spurious peaks at the bandedges of the filter.

2.3.3 Dissipation of wave energy

A significant amount of wave damping was observed for the wave group evolution in the channel. To estimate the total amount of dissipation, a wave packet energy was defined as follows:

$$E_p(x) = \int_{-\infty}^{\infty} a^2(x,t) dt \quad (2.9)$$

where $a(x,t)$ is the wave amplitude. For a wave packet observed at a fixed position x , we have that $a(x, \pm\infty) = 0$.

A modulus of decay (assumed constant) can be estimated using the energy equation:

$$\left\{ \frac{\partial}{\partial t} + c_{g,0} \frac{\partial}{\partial x} \right\} a^2 = -\sigma a^2 \quad (2.10)$$

where $c_{g,0}$ is the linear group velocity, and σ is the modulus of decay. For fixed position x , we integrate equation 2.10 in time to find:

$$c_{g,0} \frac{\partial}{\partial x} E_p(x) = -\sigma E_p(x) \quad (2.11)$$

If we now integrate in x from our initial observation at x_0 we find:

$$\ln [E_p(x) / E_0] = \frac{-\sigma}{c_{g,0}} (x-x_0) = -m(x-x_0) \quad (2.12)$$

where E_0 is the initial packet energy and m is the damping coefficient which is related to the modulus of decay using the linear group velocity.

Figures 2.19 to 2.23 show the logarithm of the packet energy normalized by its initial value (at 6.1 m) plotted versus distance along the channel. Also shown is the least squares line fit to the data points. The slope of this line was used to determine the energy damping coefficient m . The wave amplitude damping coefficient, α , was taken to be half this value since energy is proportional to amplitude squared, i.e.,

$$\text{if } E_p(x) = E_0 \exp \{ -m(x-x_0) \} \quad (2.13)$$

$$\text{then } a(x) = a_0 \exp \left\{ \frac{-m}{a} (x-x_0) \right\} = a_0 e^{-\alpha(x-x_0)} \quad (2.14)$$

The value of this amplitude damping coefficient, α , is tabulated in Table 2.3.

There are three primary sources of dissipation for laboratory surface waves: viscous damping at the bottom and sidewall (solid) boundaries, viscous dissipation at the surface from a contaminating surface film, and capillary hysteresis associated with the meniscus at the contact line between the free surface and the channel wall.

Hunt [1952] examined the damping at the bottom and sidewall boundaries by invoking viscous boundary layers with an interior inviscid potential flow. Van Dorn [1966] examined the damping due to an additional surface boundary layer which

AK = .03 NW = 10 (EXP 78)

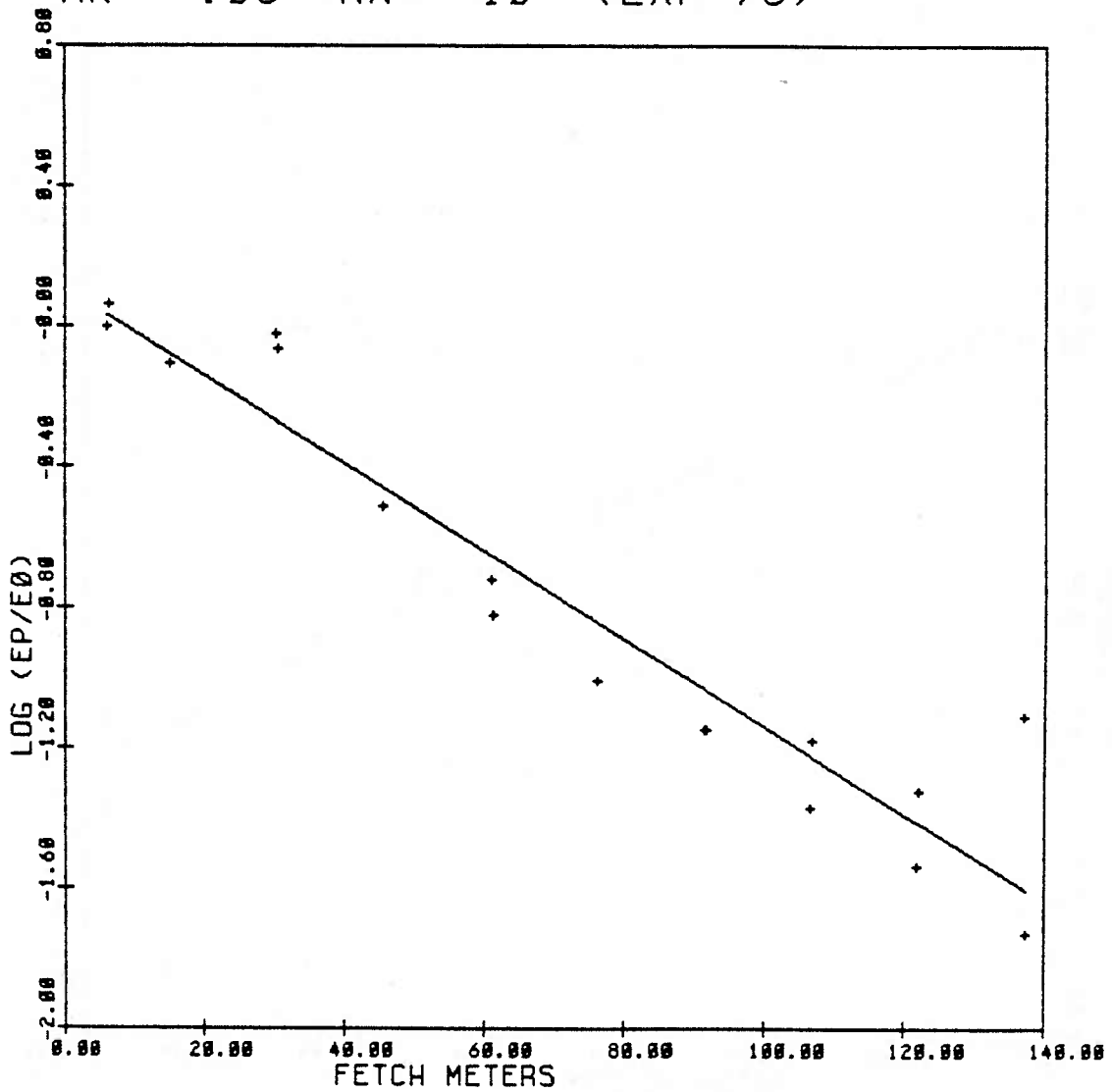


Fig. 2.19 Logarithm of packet energy normalized by its initial value plotted versus fetch for a wave group of 10 waves, $ak = .03$ (Exp 78). Least squares line fit to data is also shown.

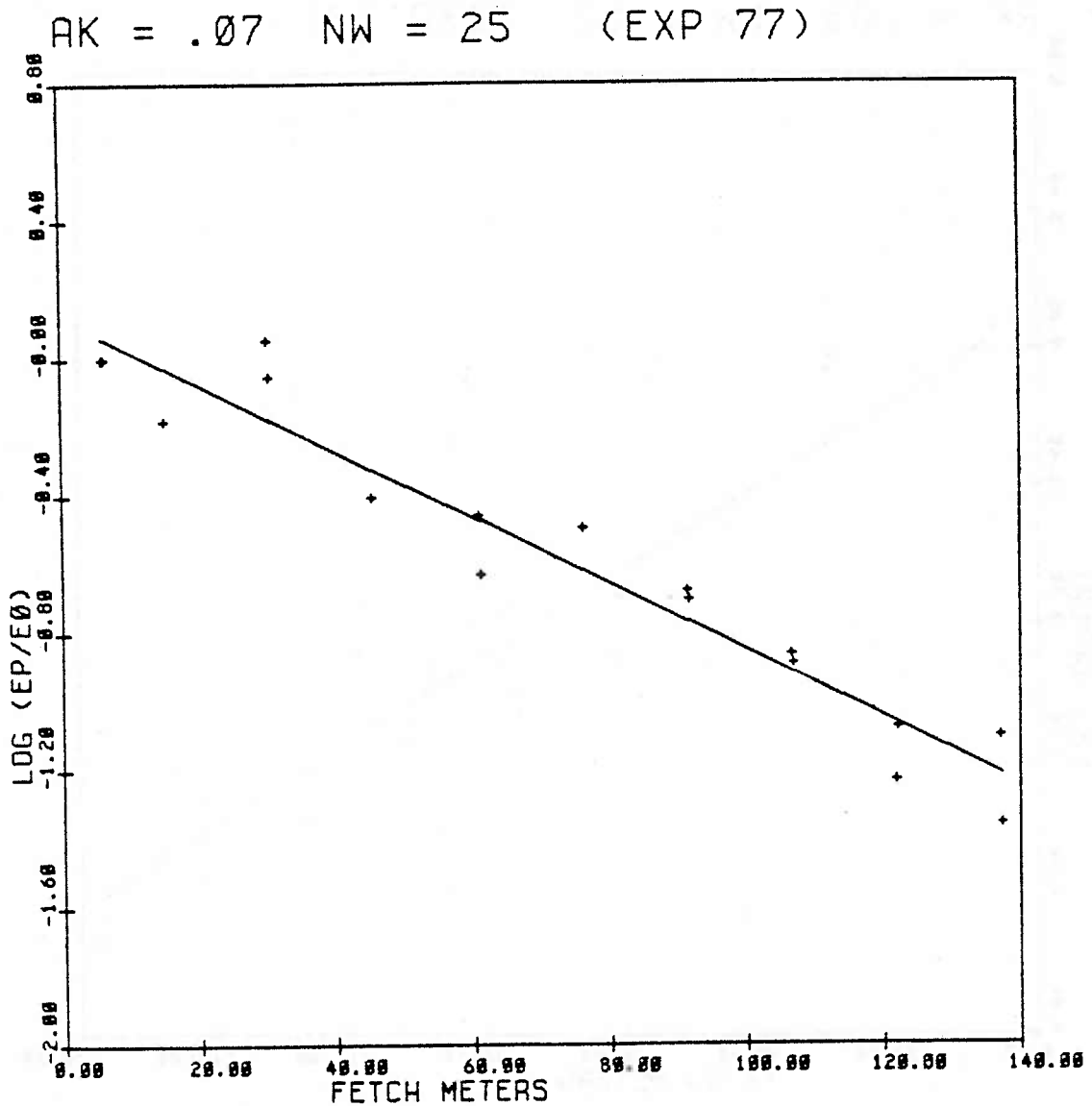


Fig. 2.20 Logarithm of packet energy normalized by its initial value plotted versus fetch for a wave group of 25 waves, $ak = .07$ (Exp 77). Least squares line fit to data is also shown.

AK = .10 NW = 25 (EXP 88)

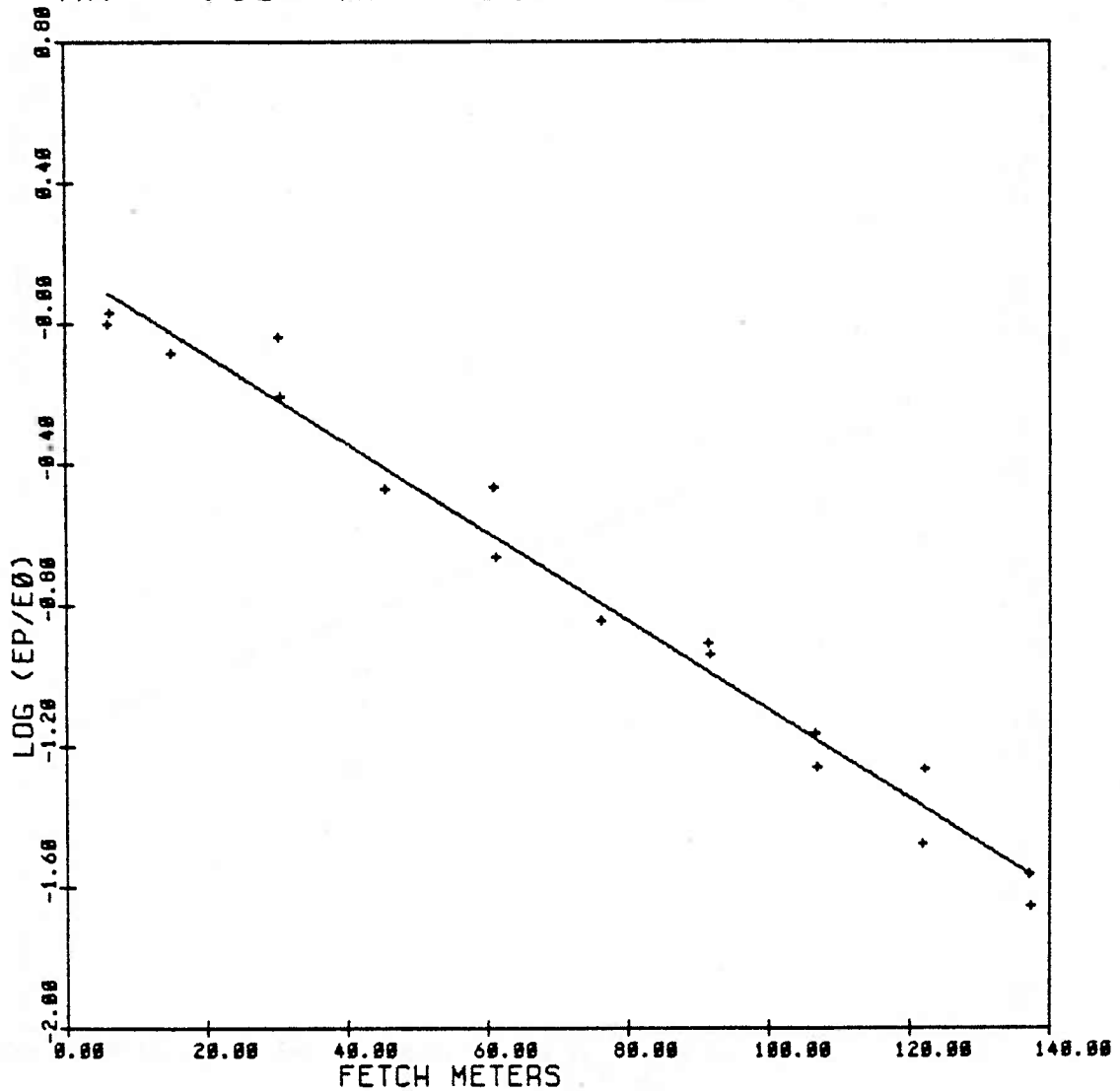


Fig. 2.21 Logarithm of packet energy normalized by its initial value plotted versus fetch for a wave group of 25 waves, $ak = .10$ (Exp 88). Least squares line fit to data is also shown.

AK = .15 NW = 15 (EXP 62)

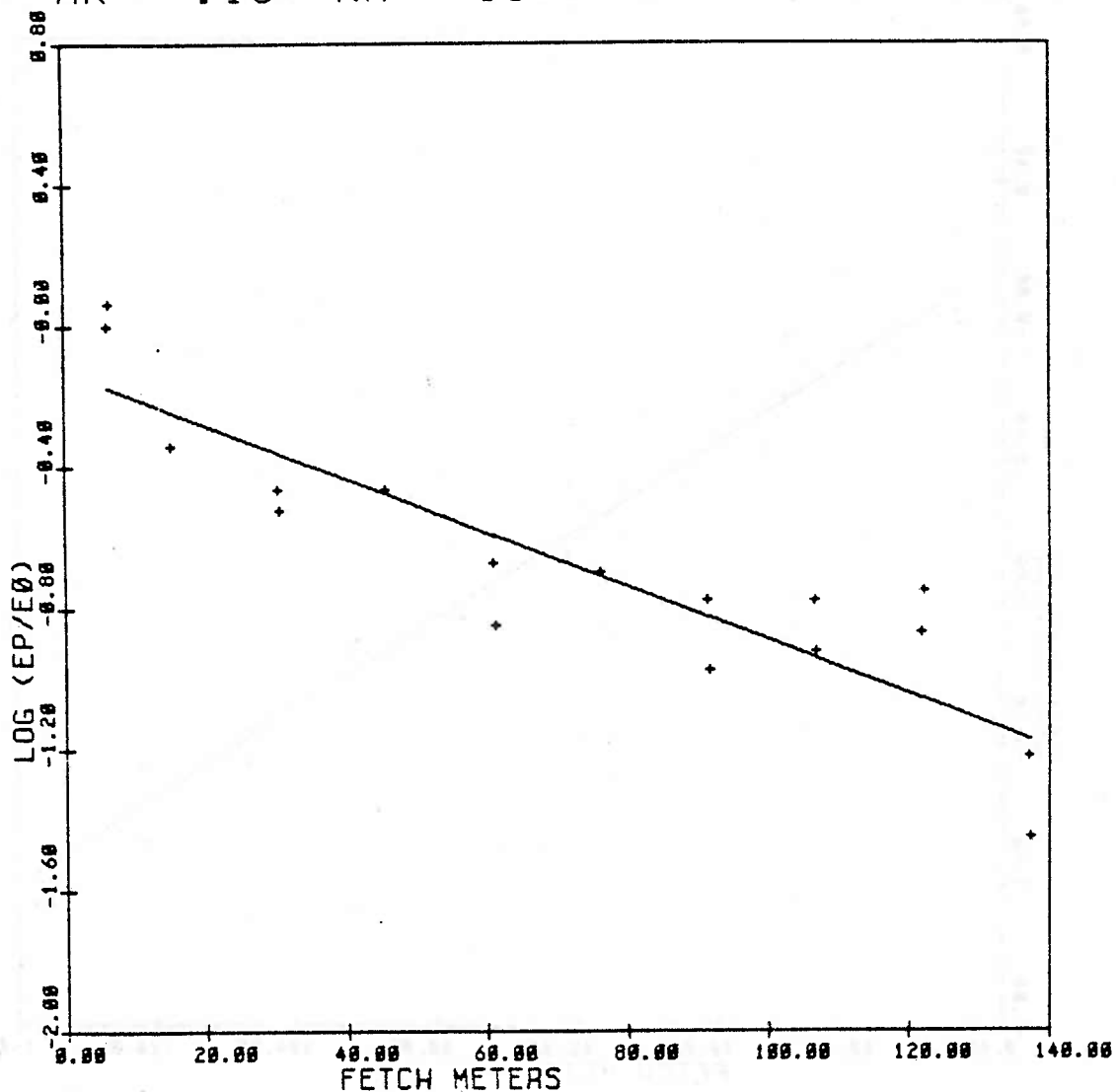


Fig. 2.22 Logarithm of packet energy normalized by its initial value plotted versus fetch for a wave group of 15 waves, $ak = .15$ (Exp 62). Least squares line fit to data is also shown.

AK = .16 NW = 25 (EXP 23)

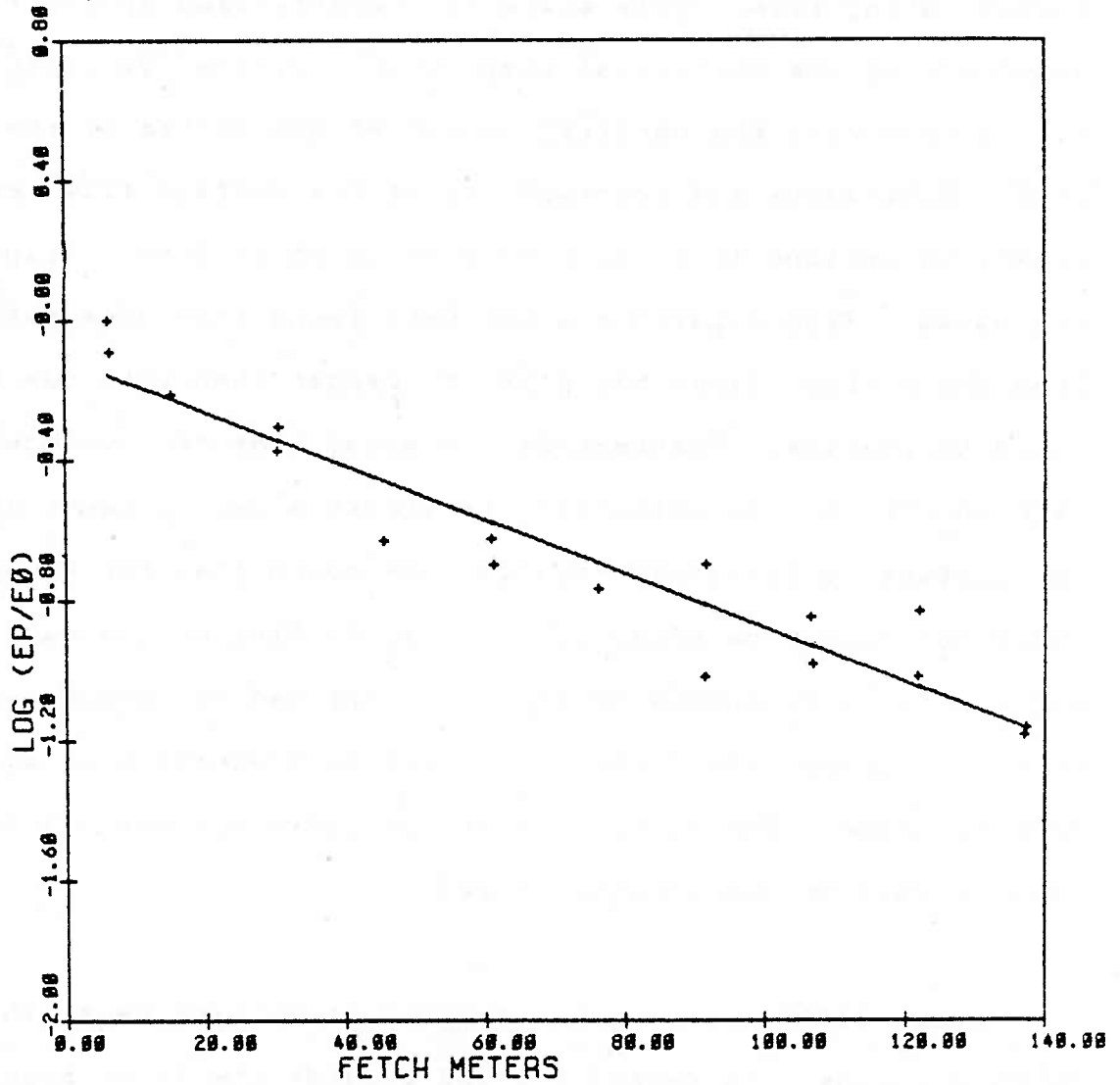


Fig. 2.23 Logarithm of packet energy normalized by its initial value plotted versus fetch for a wave group of 25 waves, $ak = .16$ (Exp 23). Least squares line fit to data is also shown.

considered the surface to be horizontally immobilized by a contaminating film. This state is characterized by the total annulment of the horizontal component of orbital velocity at the surface with the vertical component unaffected by the film. Extensions and contractions of the surface film act to create variations in surface tension which in turn dissipate the waves. From experiments Van Dorn found that dissipation from the surface layer may often be larger than that due to solid boundaries. Furthermore, he noted that the surface tension effect (contamination) is almost always present unless the surface is specially treated. He found that the effect increased with time after the initial filling of the wave tank until a fully contaminated state was arrived at (about one hour). However, there was no visible manifestation of surface contamination. The appearance of the water surface was the same as when it was freshly filled.

Miles [1967] reviews the damping of surface waves in bounded basins. He reproduces and extends the above boundary layer results and analyzes the damping due to capillary hysteresis. From comparison with observed decay rates, which typically exceed predicted rates based on wall damping alone by factors of between 2 and 3, he concludes that both surface films and capillary hysteresis are important and can account for the observed discrepancies.

(1966).

Capillary hysteresis may well have been an important source of damping, but it can not be estimated from the data. Another source of dissipation in our experiments that 2.15 does not account for was gentle wave breaking (no air entrainment) that was sometimes observed visually for the steeper experiments. From the sources of dissipation that we can estimate using 2.15, damping from surface contamination was by far the most important contribution followed by sidewall and bottom boundary dissipation, in order of importance. The expression 2.15 assumes a smooth bottom boundary. The channel used had a mown grass bottom which should significantly increase the dissipation. The theoretical predicted values of the decay rate are somewhat less than the values calculated from the observations for the lowest three wave steepnesses (Table 2.3). They are somewhat larger than those for the experiments with the two highest steepnesses. In all cases, the largest discrepancy between the two values was less than an order of magnitude.

Also shown in Table 2.3 are three time scales: the wave period, the modulational time scale, and the viscous time scale. The modulational time scale is given by 2.4 to be:

$$T_M = T / (ak)^2 \quad (2.16)$$

where T is the wave period. The viscous time scale is defined

Segur [1981], in estimating the viscous decay of envelope solitons using the energy equation 2.10, finds that envelope solitons can be expected to decay at twice the rate of a uniform wavetrain provided that the viscous decay time is much longer than a wave period and much faster than the modulational time scale. This implies that the soliton formation time is fast enough that the soliton can continually readjust to maintain the proper shape as its energy is dissipated.

To theoretically estimate the amount of dissipation that we can expect in our experiments we used the following relation taken from Segur [1981]. (γ is the theoretical estimate of α).:

$$\gamma = \frac{(k\delta)k [1 + K \cosh^2(kh) + (\sinh(2kh)/kb)]}{[2kh + \sinh(2kh)]} \quad (2.15)$$

$\delta = (\frac{a^2}{\omega})^{1/2}$ represents a viscous boundary layer thickness. (k, ω) are the inviscid wavenumber and frequency, respectively. ν is the kinematic viscosity ($\nu = .01$ cm²/sec). h is the mean depth in the channel ($h = 72$ cm), and b is the channel width ($b = 366$ cm).

If $K = 0$, only dissipation at solid boundaries is considered, and we recover the result of Hunt [1952]. If $K = 1$, dissipation at a horizontally immobile surface is also included, and we recover the corrected result of Van Dorn

Table 2.3
Frictional Parameters

Experiment	α (/cm)	γ (/cm)	T (sec)	T_M (sec)	T_V (sec)
78	.00006	.00002	1.25	1389	510
79	.00007	"	"	"	"
80	.00008	"	"	"	"
75	.00006	.00004	1.04	212	313
76	.00006	"	"	"	"
77	.00005	"	"	"	"
86	.00007	.00005	1.04	104	250
87	.00007	"	"	"	"
88	.00006	"	"	"	"
61	.00004	.00010	0.83	37	156
62	.00004	"	"	"	"
63	.00005	"	"	"	"
21	.00004	.00007	0.83	32	223
22	.00006	"	"	"	"
23	.00004	"	"	"	"

as:

$$T_v = (\gamma c_{g,0})^{-1} \quad (2.17)$$

We see that for the three steepest sets of experiments the viscous time scale is much greater than the modulational time scale. Hence, we expect that the solitons can continually readjust and are thus best described as waves of quasi-permanent form. For the lowest steepness (Exp 78 - 80), the viscosity acts on shorter time scales than the modulational instability and the result is decay from the initial pulse. Exp 75 - 77 show comparable viscous and modulational time scales, with the viscous scale longer than the modulational time scale.

Some further ideas on the relation of viscosity and the phenomenon of frequency downshifting will be elaborated on in the discussion.

2.3.4 Modulations

We assume the following model for our wavegauge observations:

$$g(x_i, t) = \text{Re} (a(x_i, t) \exp[i (\omega_0 t + \theta(x_i, t))]), \quad (2.18)$$

where $g(x_i, t)$ is the measurement of surface displacement at

fixed location x_i and ω_0 is the initial carrier frequency. This models the surface displacement signal as the product of a rapidly varying carrier wave

$$\exp[i (\omega_0 t)] \quad (2.19)$$

and a slowly varying complex envelope

$$a(x_i, t) \exp[i \Theta(x_i, t)] \quad (2.20)$$

The amplitude modulation $a(x_i, t)$ and the phase modulation $\Theta(x_i, t)$ are obtained using the Hilbert transform of the signal. The frequency modulation is defined as

$$f(x_i, t) = \omega_0 + \frac{\partial}{\partial t} \Theta(x_i, t) \quad (2.21)$$

The method and its assumptions are documented in Appendix 2.A.

Figures 2.24 to 2.41 show the amplitude, phase and frequency modulations at 6 different wavegauge locations for 3 different experiments with varying group length and wave steepness. Figures 2.24 to 2.29 show the modulations for a group of 10 waves with wave steepness $ak = .03$ (Exp 78). Figures 2.30 to 2.35 show the modulations for a group of 15 waves with steepness $ak = .10$ (Exp 87). Figures 2.36 to 2.41 show the modulations for a group of 25 waves with steepness $ak = .16$ (Exp 23).

The amplitude modulation is superimposed on the filtered wave group. Notice the excellent fit. The phase modulation is defined with the carrier trend removed and has been

unwrapped (see Appendix 2.A). There is very little phase variation within the group. Most of the phase variation occurs outside the group where the amplitude is nearly zero. The frequency modulation is defined as the time derivative of the phase with the carrier added back in. Discontinuities (or jumps) in the frequency modulation occur where there are local reversals in phase. Again, there is little variation in the frequency of the initial group; a small amount develops with fetch. Most of the jumps in frequency (hence reversals in phase) occur outside the wave group where there are local amplitude minima (Figs 2.26, 2.33). Where jumps do occur within the wave groups, they tend to occur where there is a minimum in amplitude modulation (Figs 2.39-2.41).

This technique for demodulating the surface displacement signal was introduced from communications theory by W. K. Melville (1981). He used it to examine the evolution to breaking of nonlinear surface gravity wavetrains. He computes an instantaneous phase speed, the ratio of frequency to wavenumber modulation (wavenumber is obtained with a second space measurement), and finds small regions of very rapid, large amplitude variations in phase speed corresponding to the phase reversals. The large gradients (jumps) that he observes in the frequency, wavenumber and phase speed always occurred in the breaking region and in the neighborhood of local minima in wave amplitude.

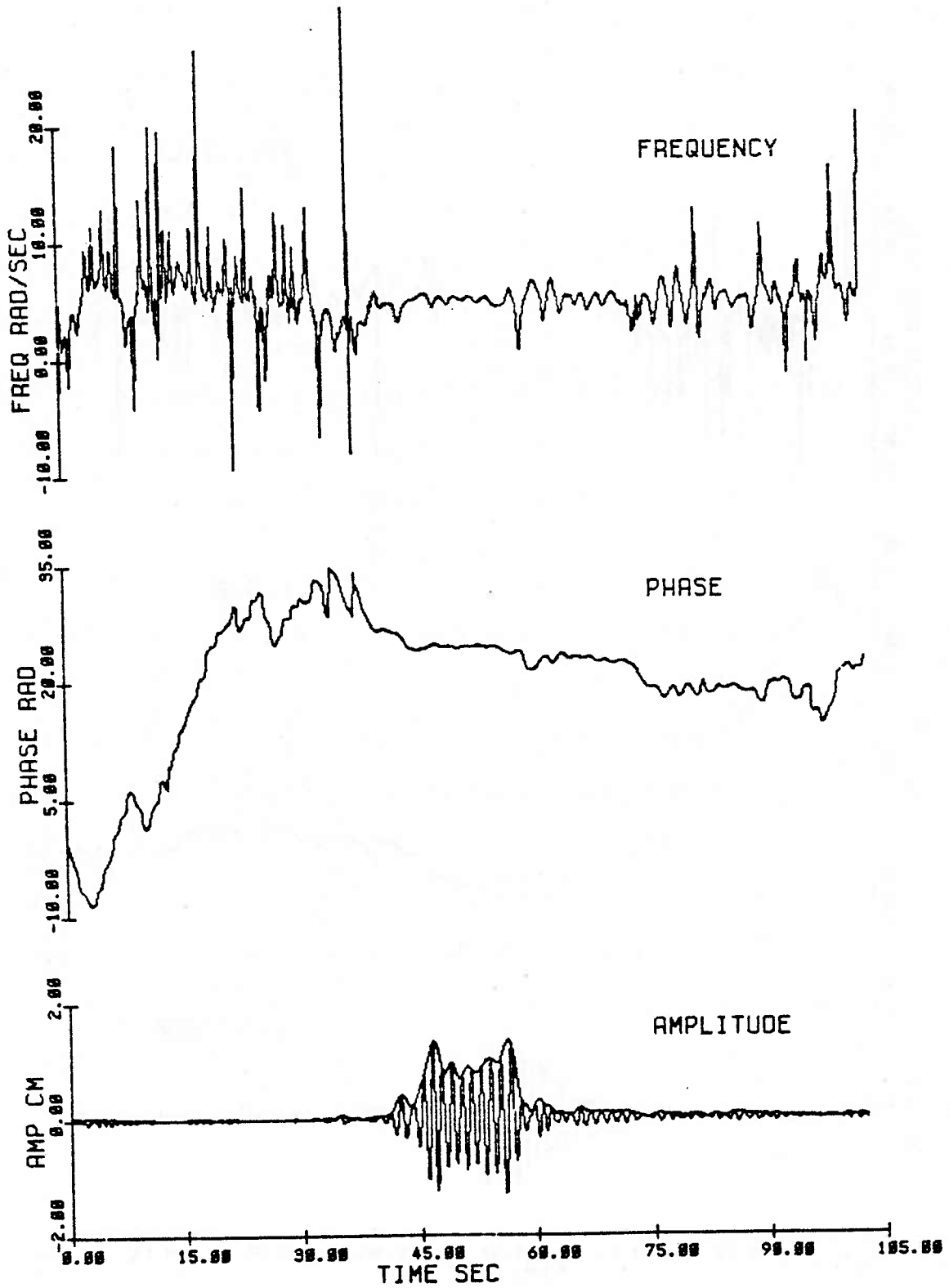


Fig. 2.24 Amplitude, phase and frequency modulations at 6.1 m for a group of 10 waves of initial steepness $ak = .03$ (Exp 78).

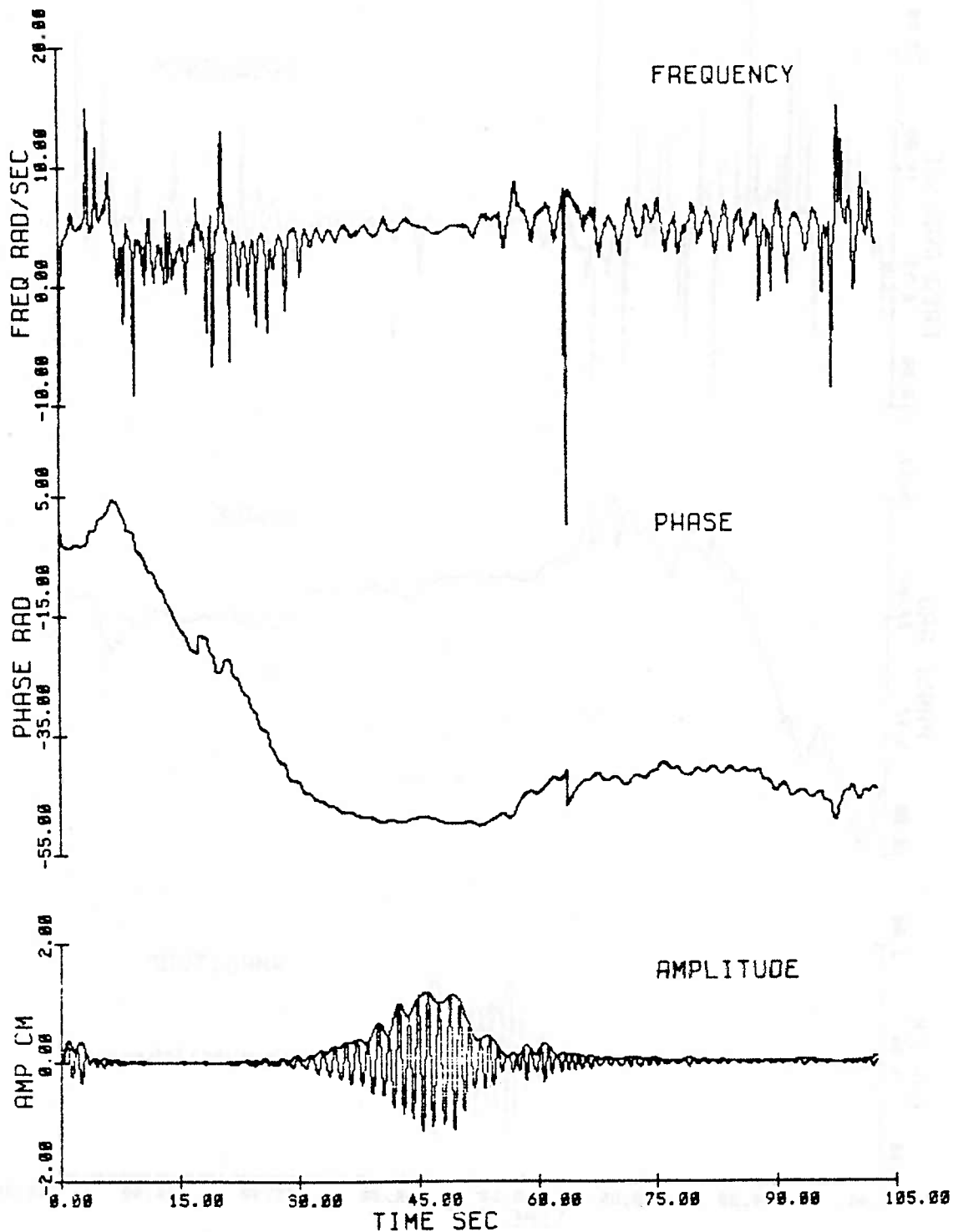


Fig. 2.25 Amplitude, phase and frequency modulations at 30.5 m for a group of 10 waves of initial steepness $ak = .03$ (Exp 78).

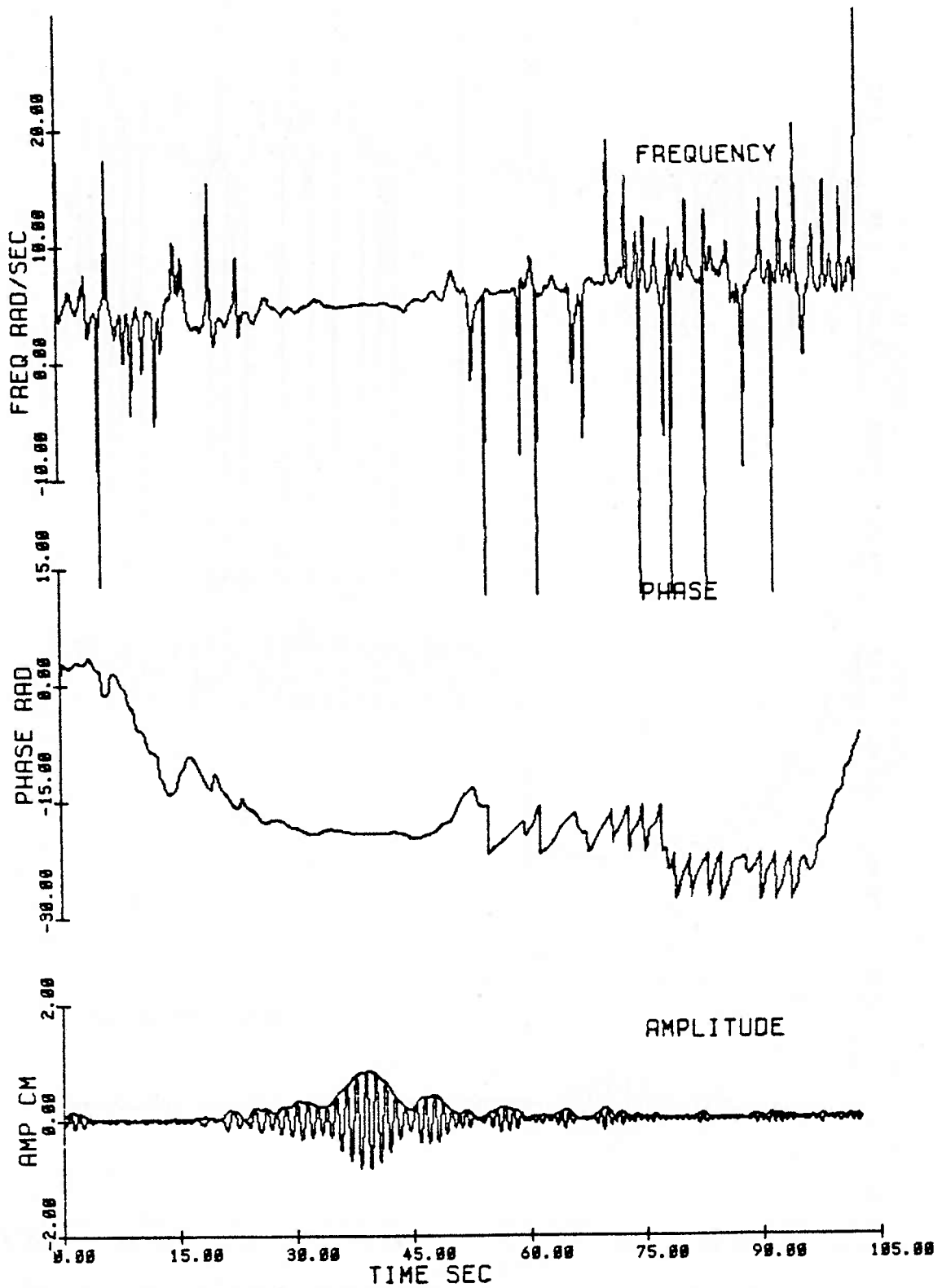


Fig. 2.26 Amplitude, phase and frequency modulations at 61.1 m for a group of 10 waves of initial steepness $ak = .03$ (Exp 78).

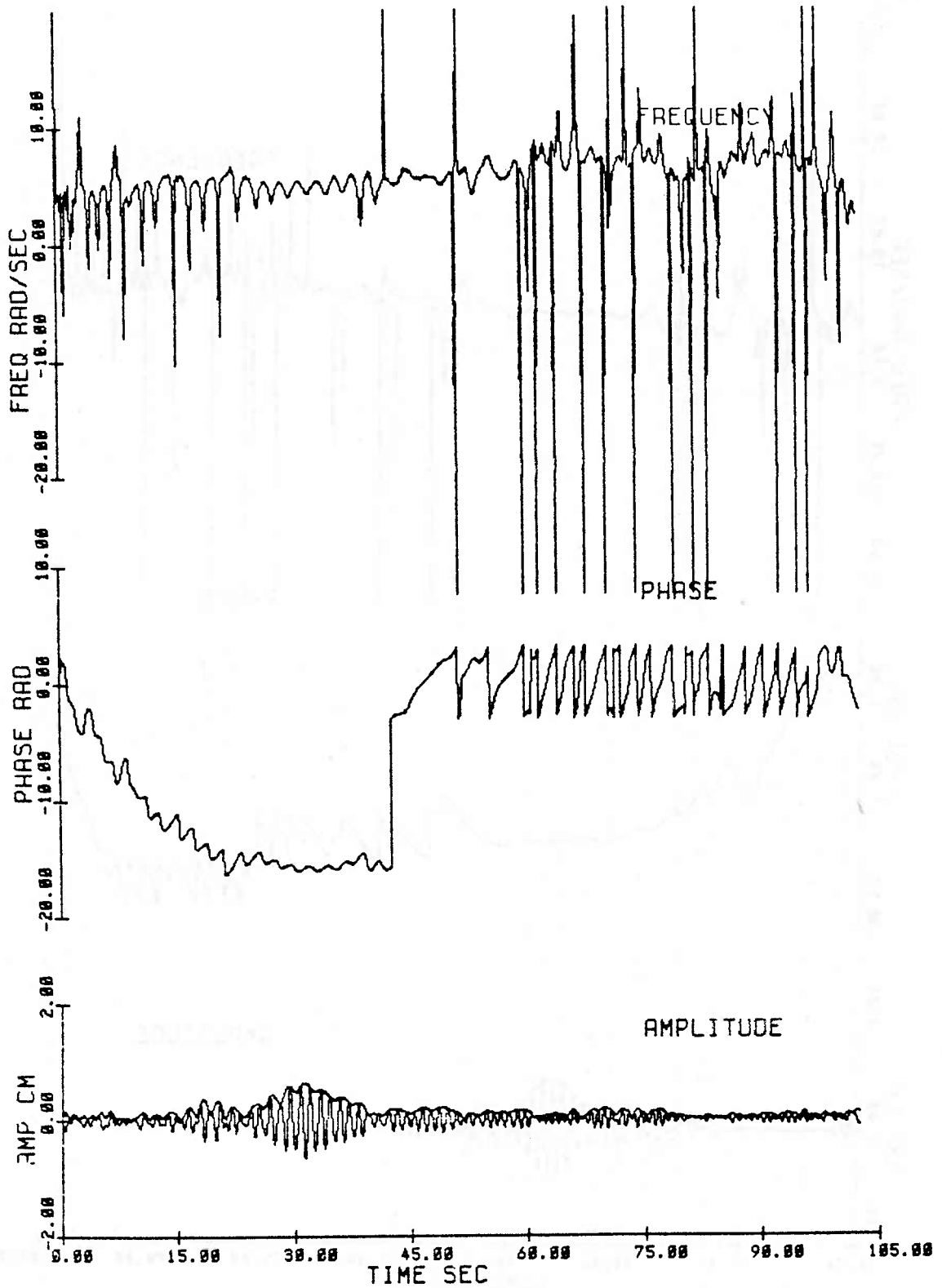


Fig. 2.27 Amplitude, phase and frequency modulations at 91.4 m for a group of 10 waves of initial steepness $ak = .03$ (Exp 78).

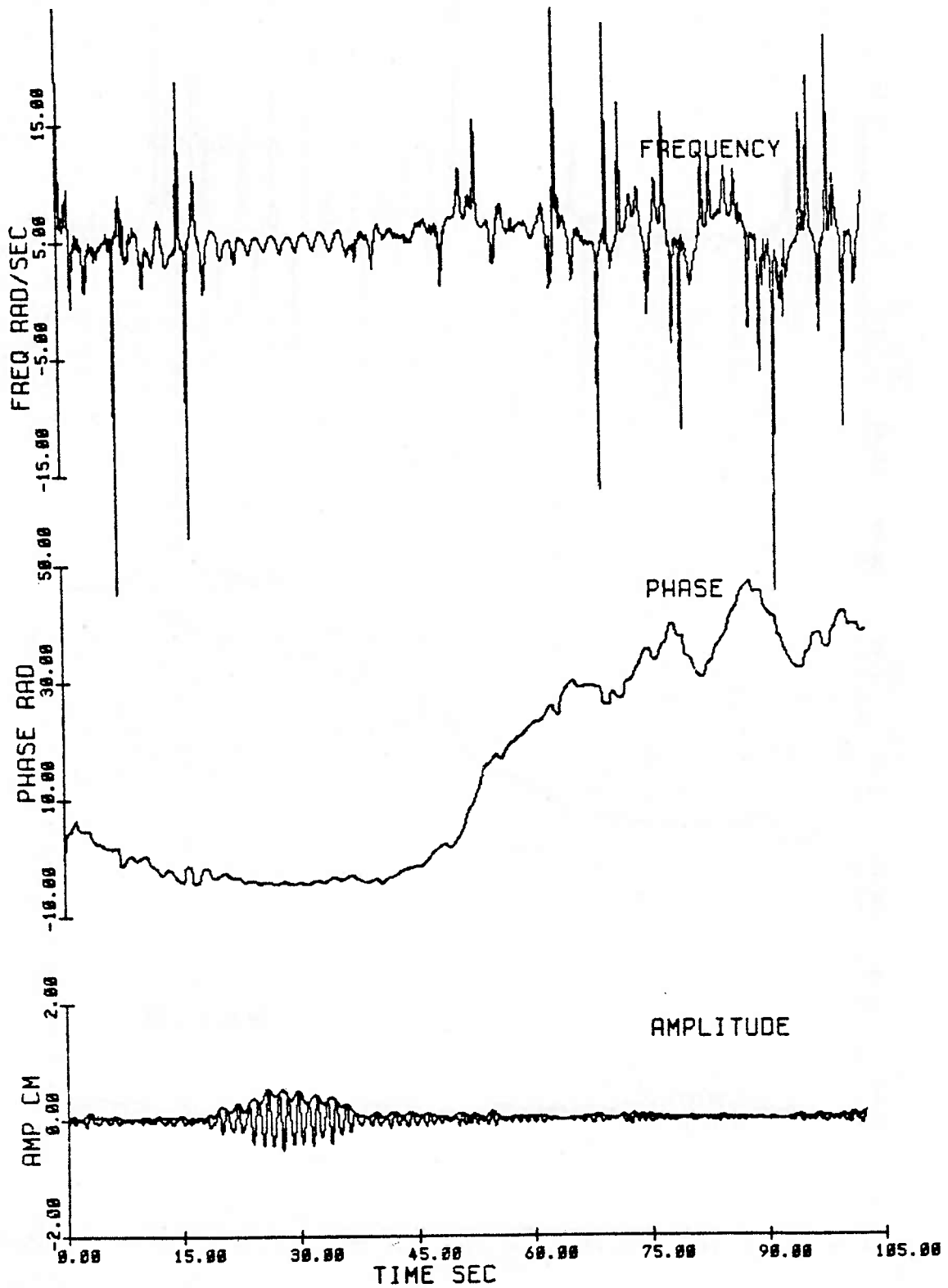


Fig. 2.28 Amplitude, phase and frequency modulations at 106.7 m for a group of 10 waves of initial steepness $ak = .03$ (Exp 78).

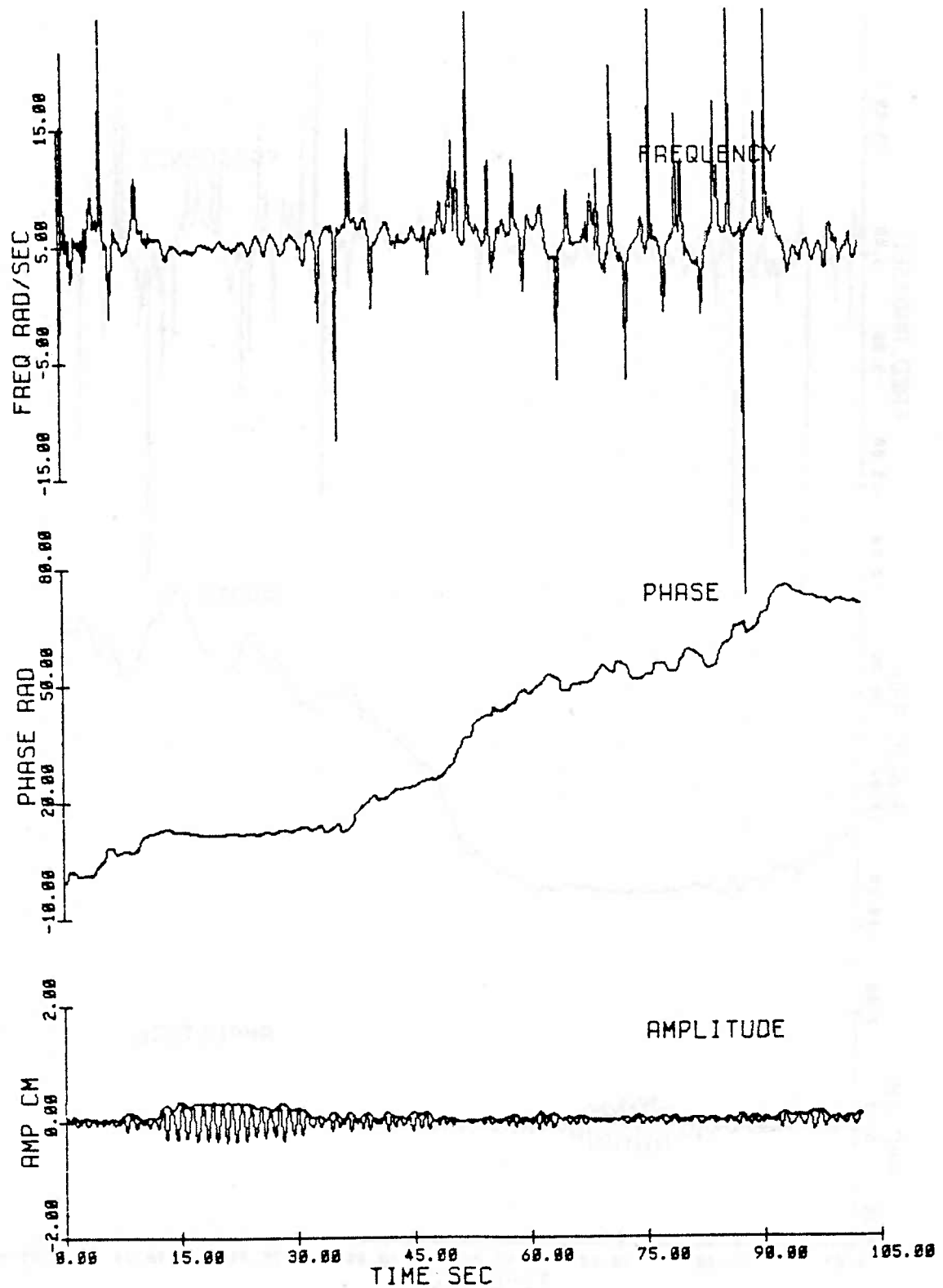


Fig. 2.29 Amplitude, phase and frequency modulations at 137.2 m for a group of 10 waves of initial steepness $ak = .03$ (Exp 78).

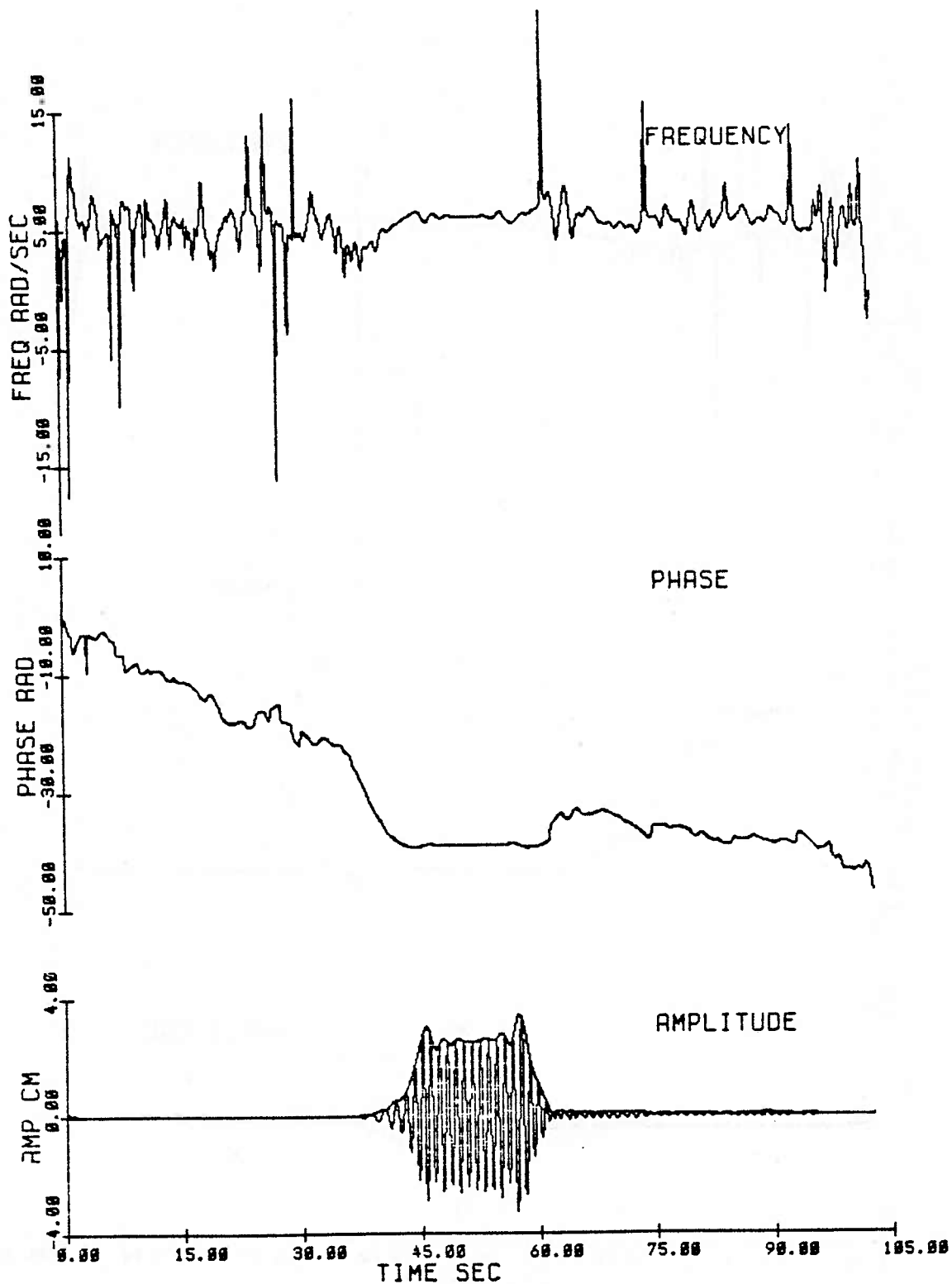


Fig. 2.30 Amplitude, phase and frequency modulations at 6.1 m for a group of 15 waves of initial steepness $ak = .10$ (Exp 87).

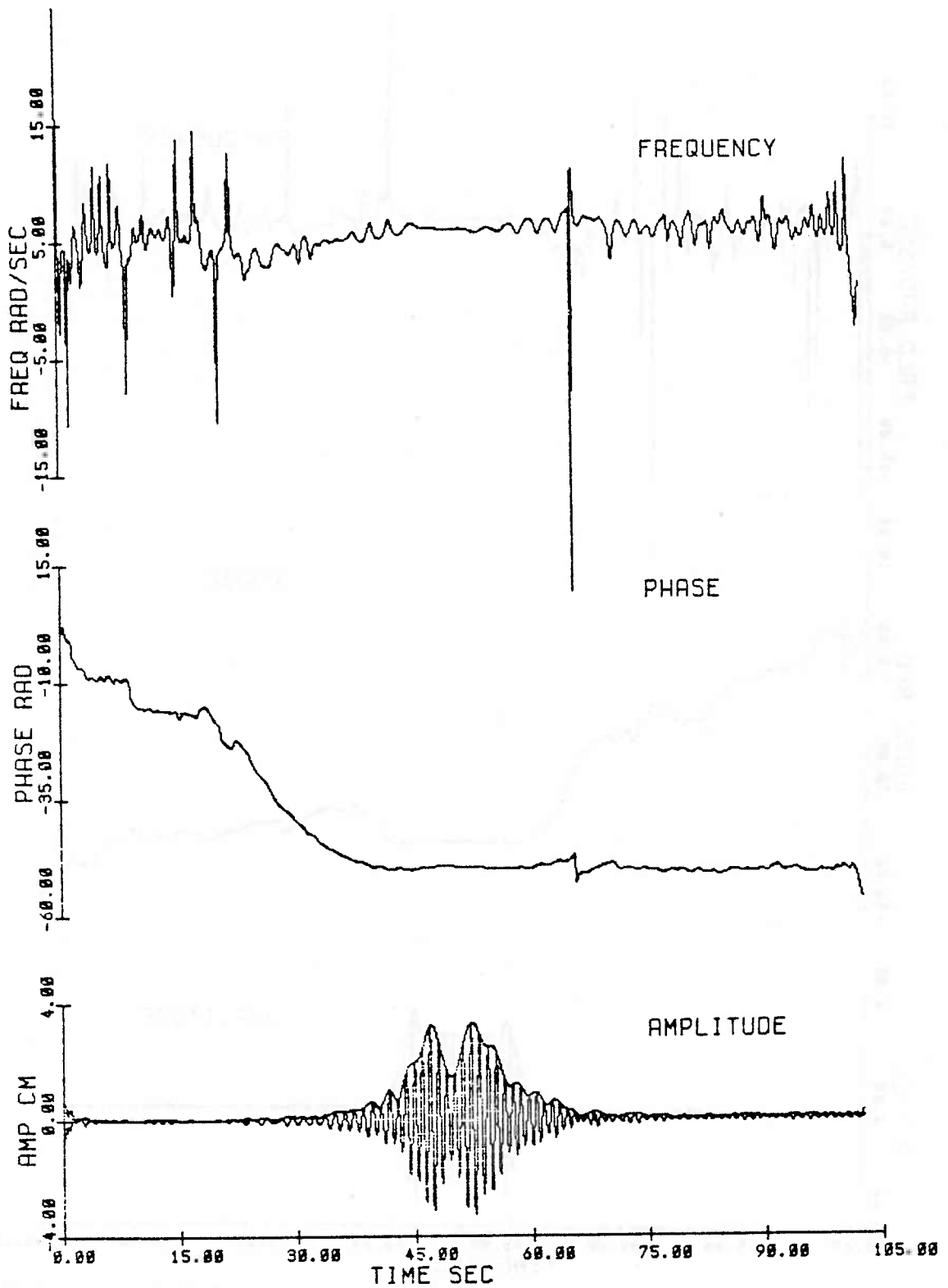


Fig. 2.31 Amplitude, phase and frequency modulations at 30.5 m for a group of 15 waves of initial steepness $ak = .10$ (Exp 87).

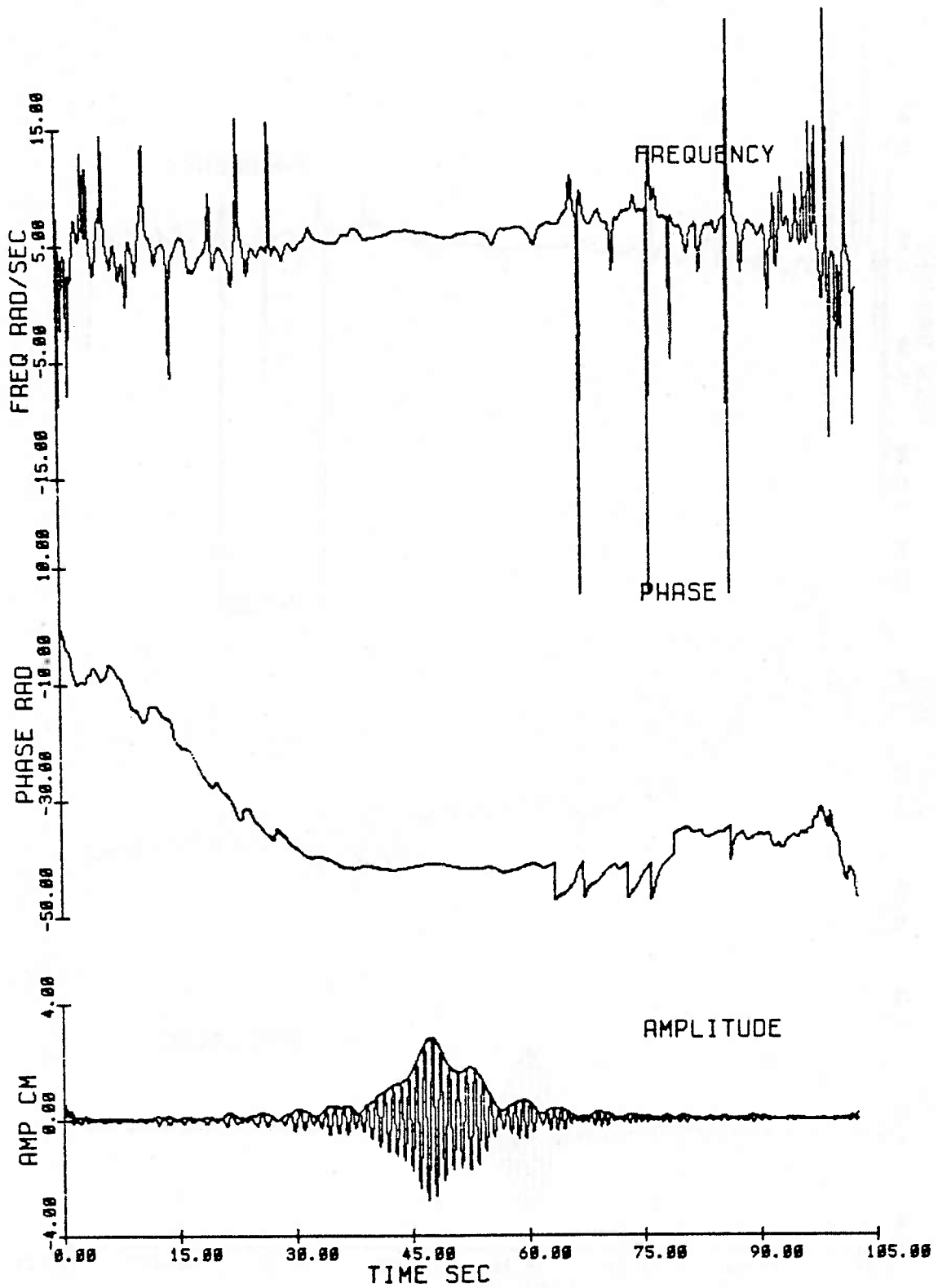


Fig. 2.32 Amplitude, phase and frequency modulations at 61.1 m for a group of 15 waves of initial steepness $ak = .10$ (Exp 87).

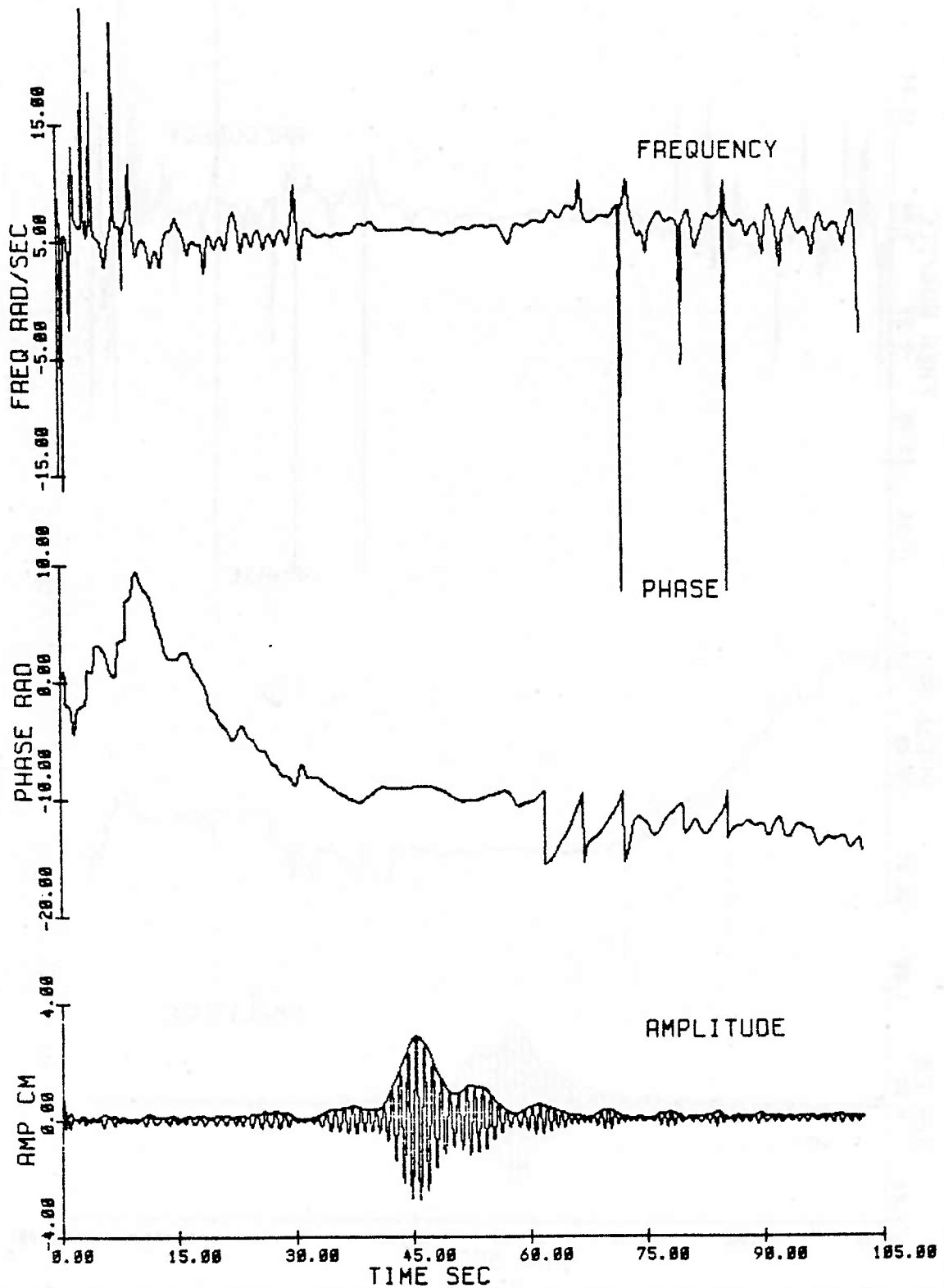


Fig. 2.33 Amplitude, phase and frequency modulations at 91.4 m for a group of 15 waves of initial steepness $ak = .10$ (Exp 87).

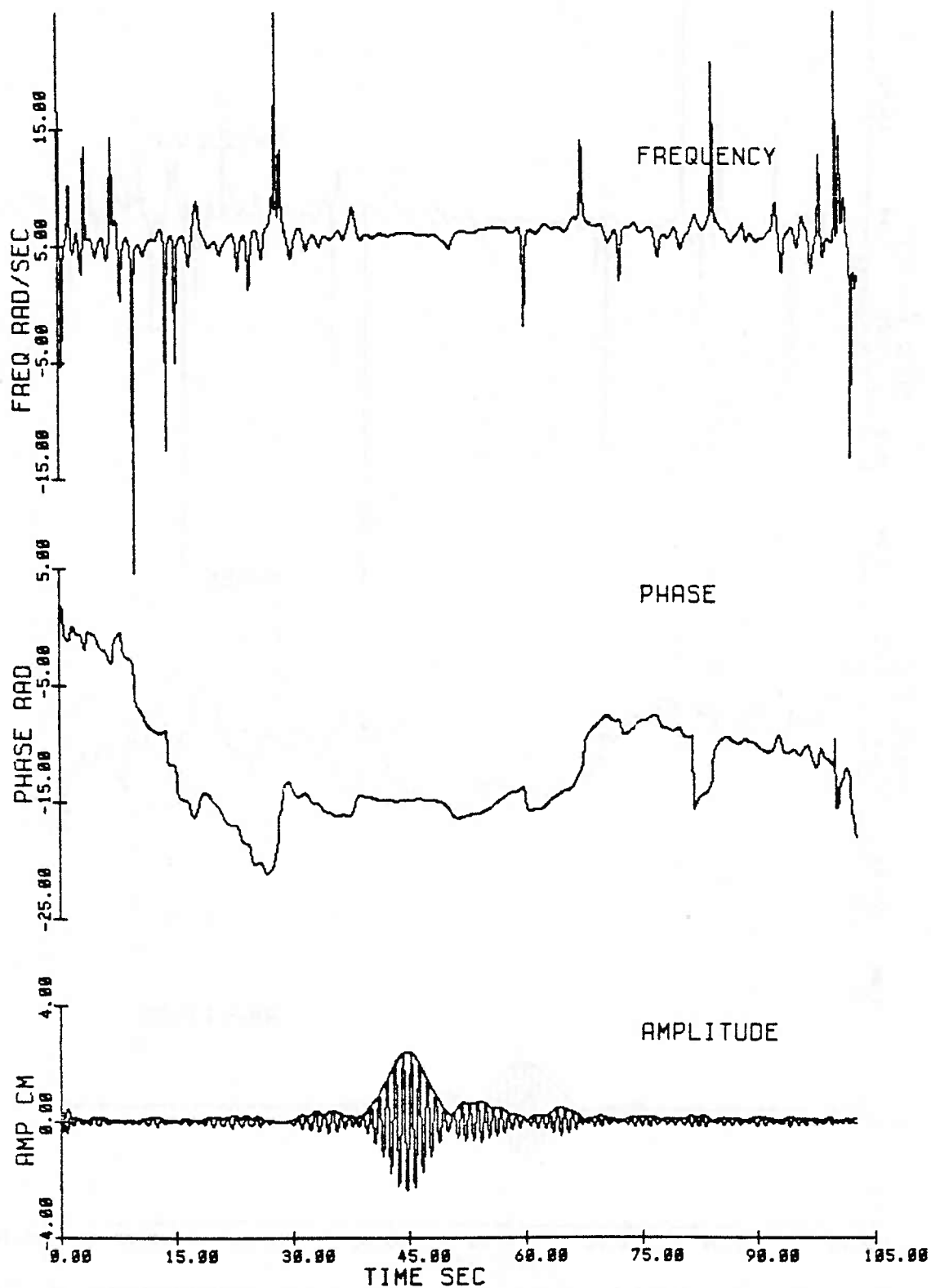


Fig. 2.34 Amplitude, phase and frequency modulations at 106.7 m for a group of 15 waves of initial steepness $ak = .10$ (Exp 87).

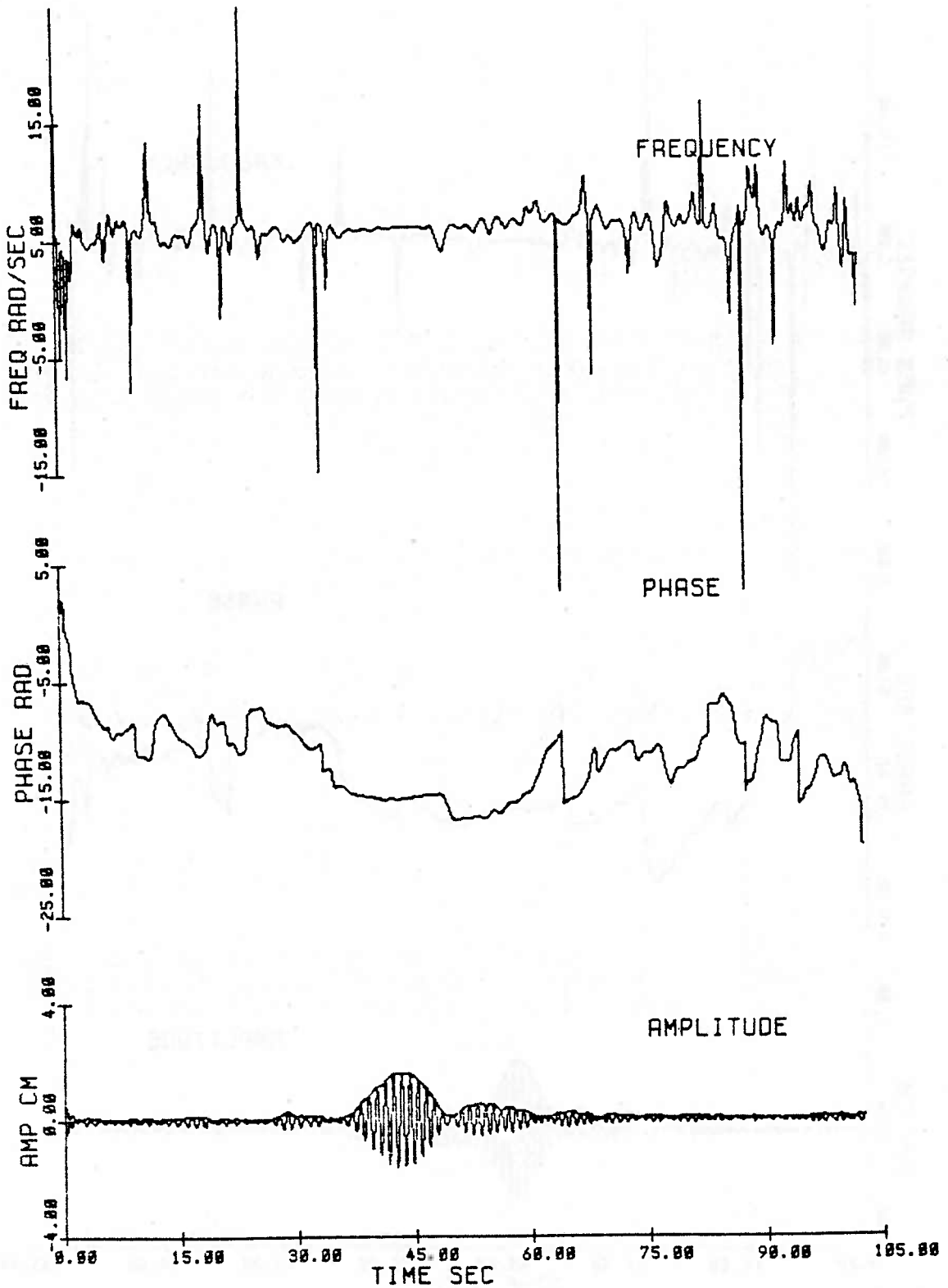


Fig. 2.35 Amplitude, phase and frequency modulations at 137.2 m for a group of 15 waves of initial steepness $ak = .10$ (Exp 87).

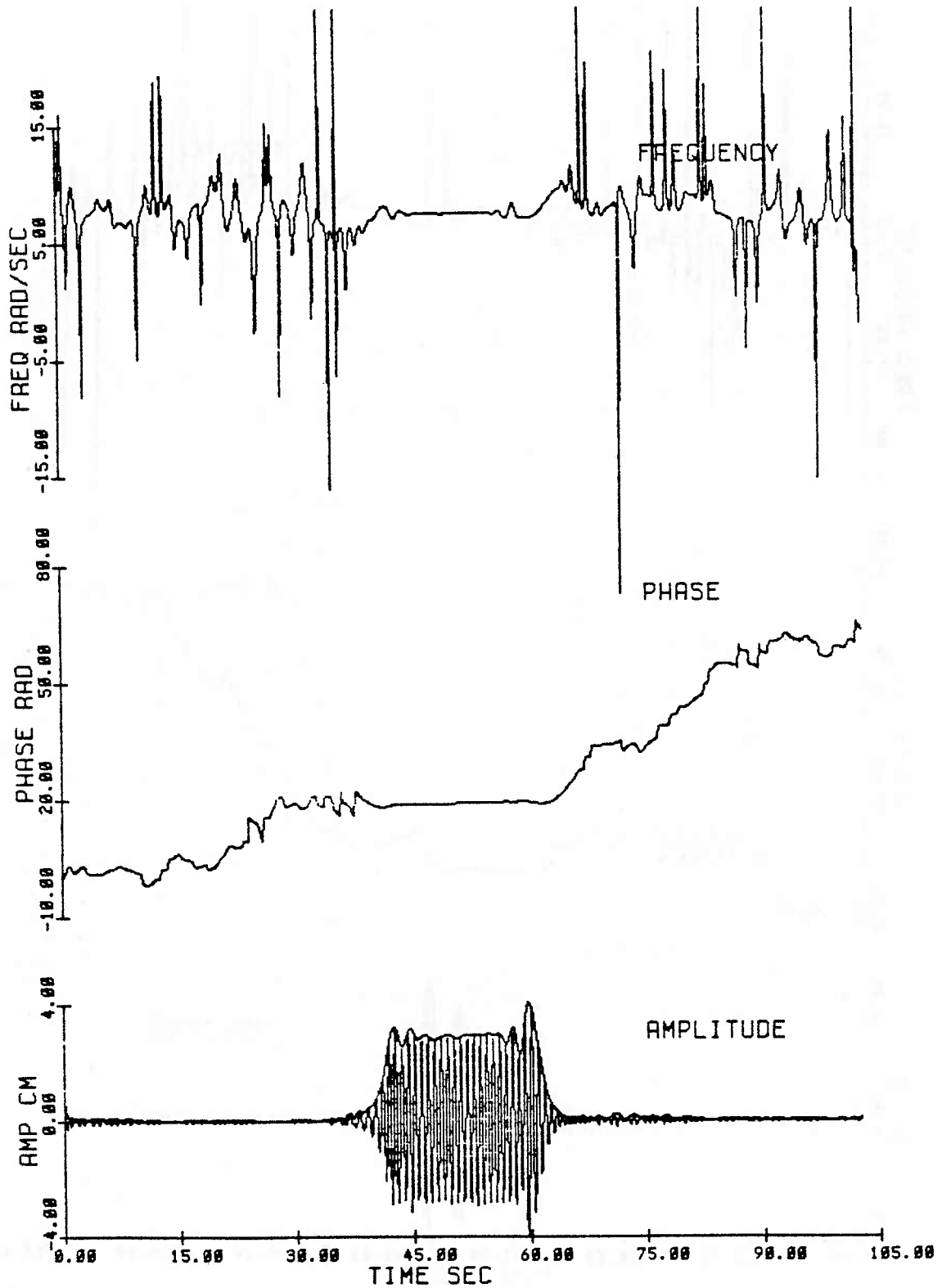


Fig. 2.36 Amplitude, phase and frequency modulations at 6.1 m for a group of 25 waves of initial steepness $ak = .16$ (Exp 23).

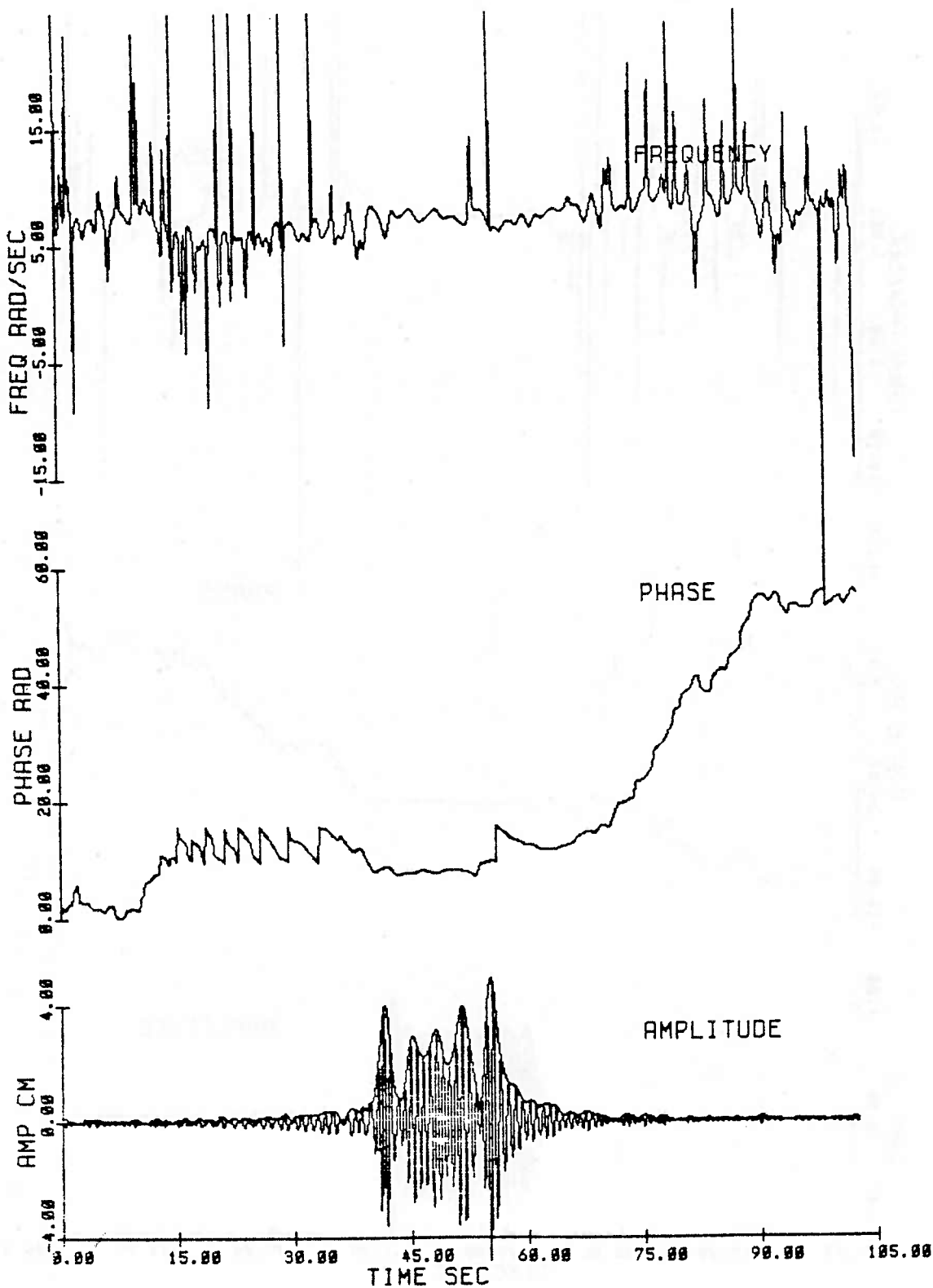


Fig. 2.37 Amplitude, phase and frequency modulations at 30.5 m for a group of 25 waves of initial steepness $ak = .16$ (Exp 23).

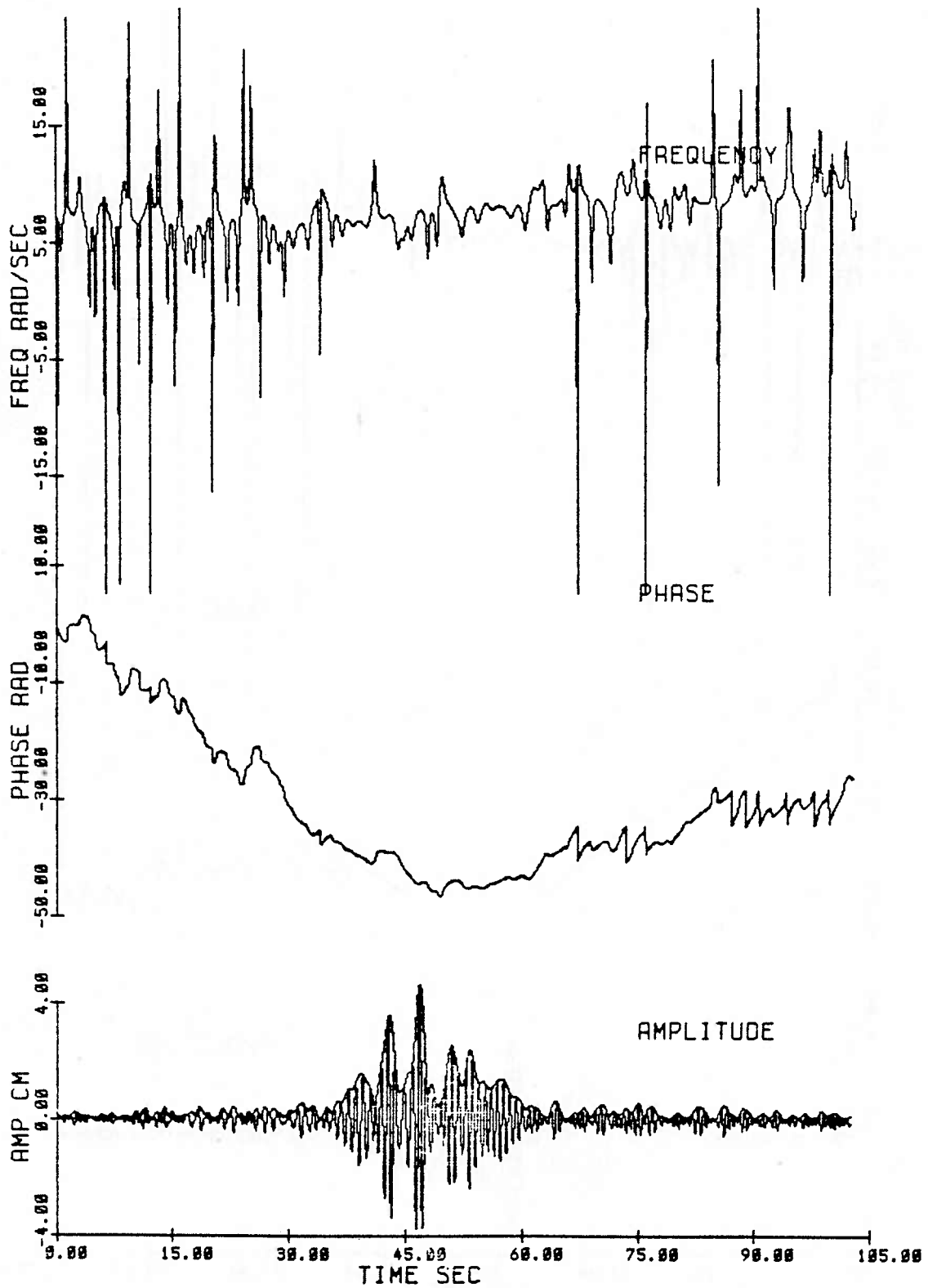


Fig. 2.30 Amplitude, phase and frequency modulations at 61.1 m for a group of 25 waves of initial steepness $ak = .16$ (Exp 23).

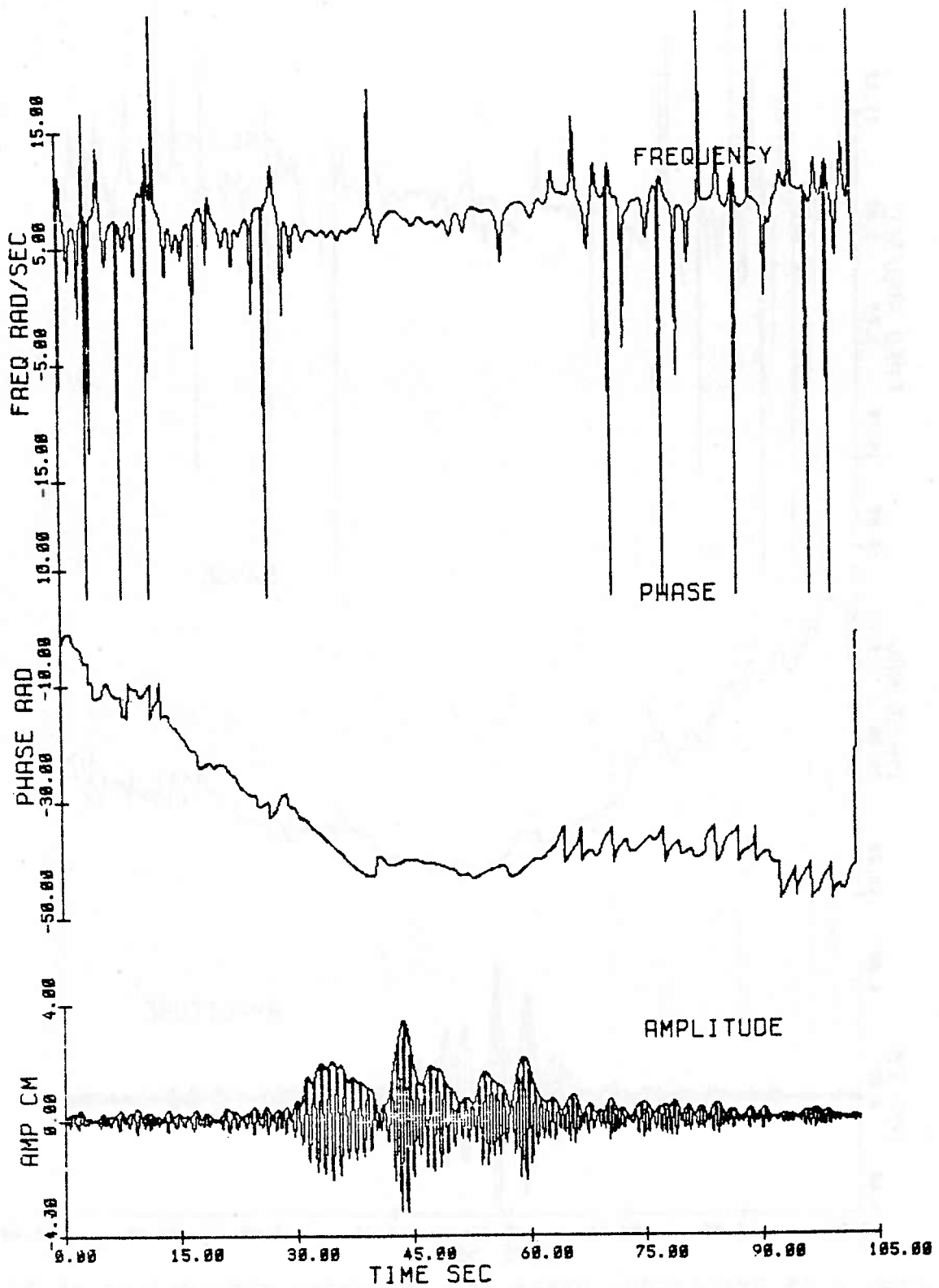


Fig. 2.39 Amplitude, phase and frequency modulations at 91.4 m for a group of 25 waves of initial steepness $ak = .16$ (Exp 23).

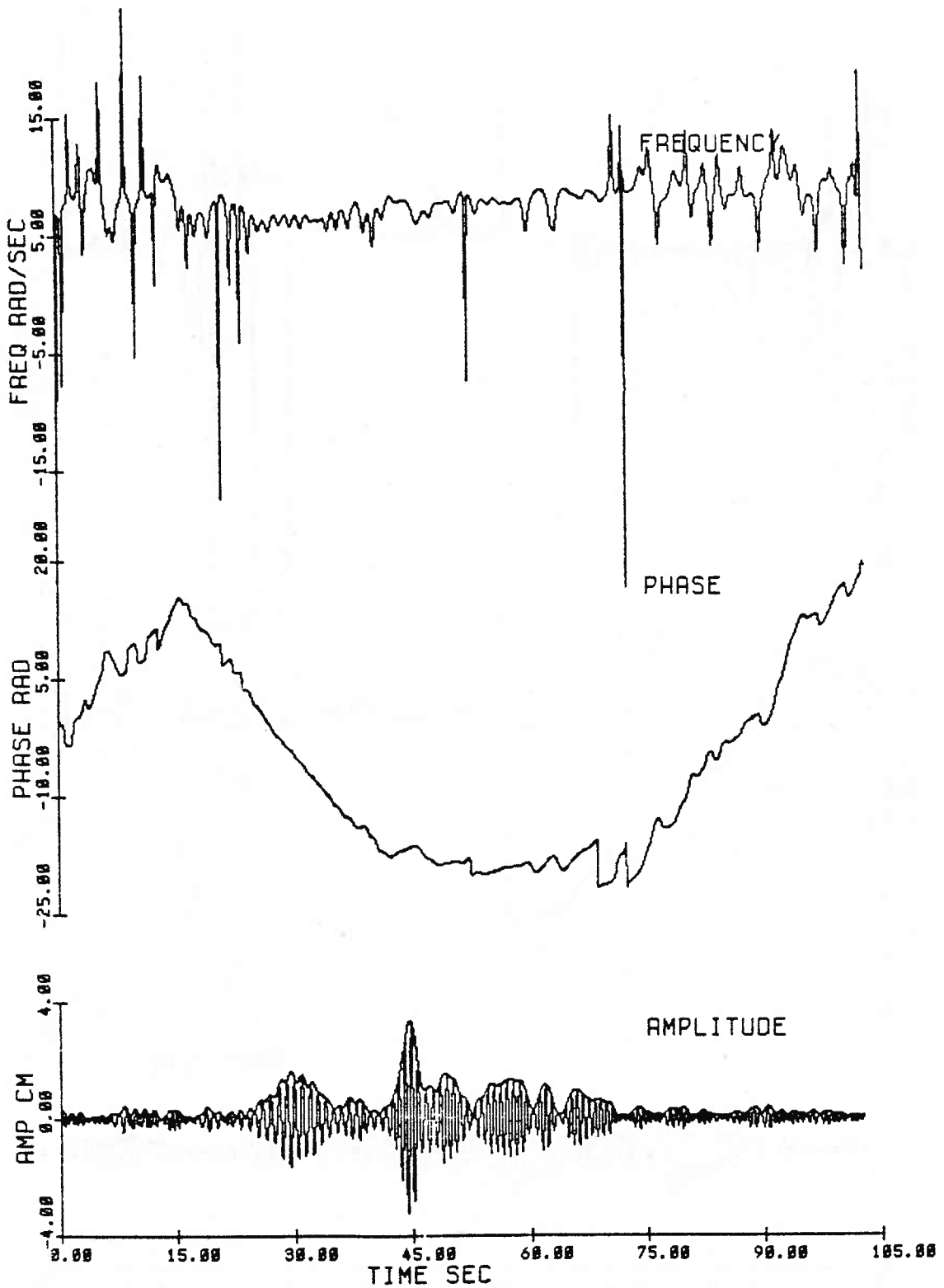


Fig. 2.40 Amplitude, phase and frequency modulations at 106.7 M for a group of 25 waves of initial steepness $ak = .16$ (Exp 23).

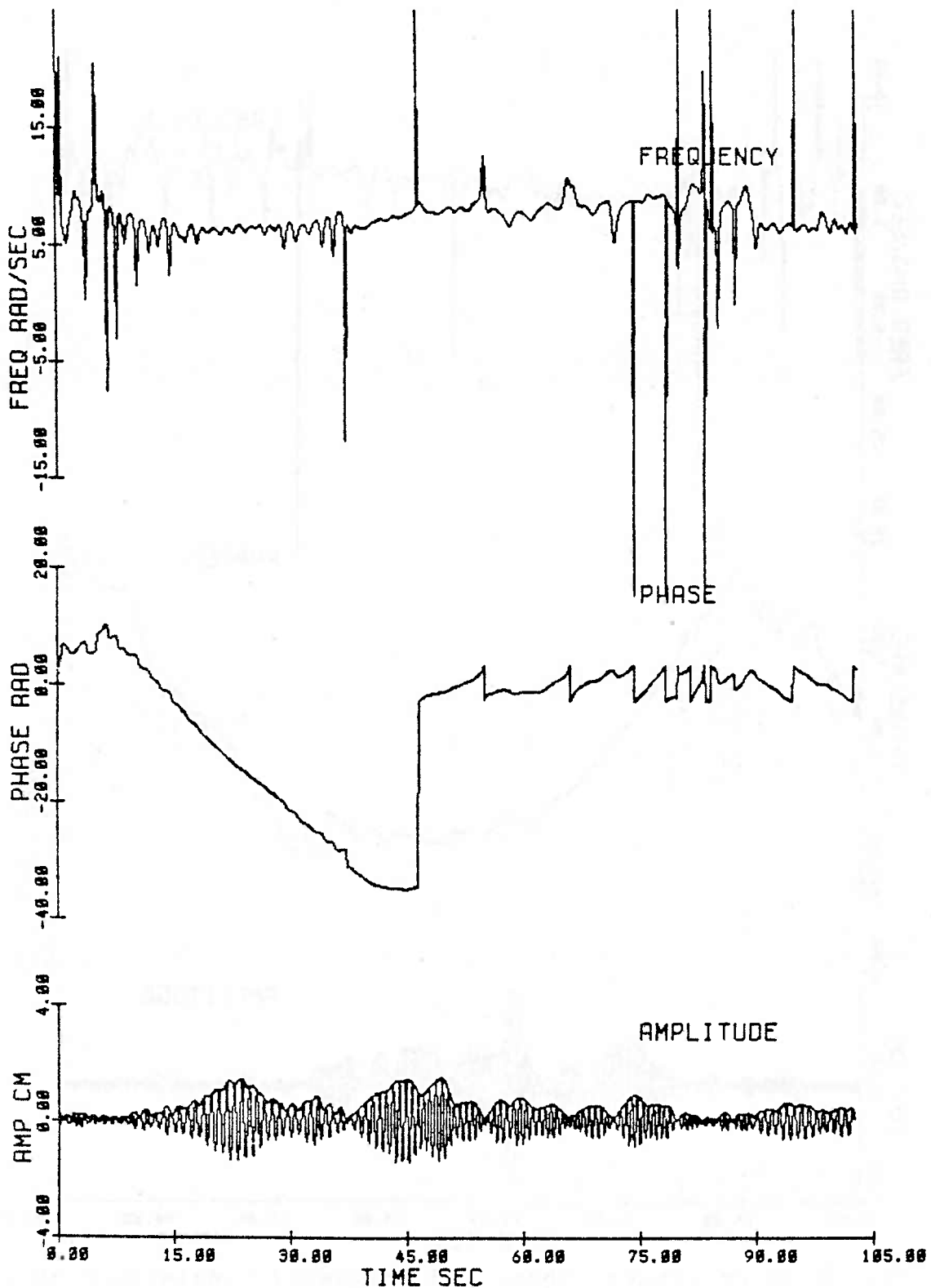


Fig. 2.41 Amplitude, phase and frequency modulations at 137.2 m for a group of 25 waves of initial steepness $ak = .16$ (Exp 23).

Our purpose in obtaining the modulations from the observations at 6.1 meters was to specify both amplitude and phase modulation as an initial condition to the cubic-nonlinear Schrodinger equation (Chapter 3). The modulations from the other observations along the wave channel were computed for comparison with those from the numerical evolution.

2.4 DISCUSSION AND SUMMARY

In the long-time evolution we see the initial group lengthen, attenuate, modulate and, for groups of sufficient length and steepness, form a succession of envelope solitons. The two most important aspects of the long-time evolution are the cumulative effect of dissipation and the phenomenon of frequency downshifting. The observations show that for wave groups of sufficient steepness ($ak \gg .10$), the downshifting that is seen in continuous wavetrains also occurs in wave groups. However, although the peak frequency of the entire modulated group is downshifted, not all the solitons or envelope modulations that develop from the initial group have downshifted. There is a sorting out into a succession of groups with the leading groups having the downshifted frequency.

Also for groups of steepness $ak \gg .10$, the viscous time

scale is seen to be much greater than the modulational time scale, indicating that the solitons or envelope modulations that develop from the initial pulse have time to adjust before they are dissipated. This suggests that groups which evolve to their final or 'asymptotic' state without being dissipated might be expected to form groups of quasi-permanent form. These groups would appear steady over the viscous time scale. However, it is likely that this energy loss prevents the groups from evolving to their asymptotic predicted state. We can think of this loss as changing the quantum state of the pulse. Both the damping and the frequency downshift are seen to be irreversible processes.

These effects cannot be modelled by a frictionless unforced cubic NLS equation, but by specifying the observations as an initial condition and comparing the wavetank and numerical evolution, we can test the time scale of validity of the cubic NLS model. We can also try to incorporate the effects of dissipation and downshifting into the model.

We have used the Hilbert transform to demodulate the amplitude and phase of the waves. Previous studies have ignored the phase modulation and determined the amplitude modulation by rectification and low pass filtering. The rectification process introduces sidebands. Loss of energy to

the sidebands and choice of a cutoff frequency can result in a significant loss of modulation energy (Sahar 1981). There is no study, to our knowledge, that determines phase modulation from observations as an initial condition to the cubic NLS equation. This was primarily due to lack of a method for determining the continuous time series of phase. Theoretical predictions of the exact solution of the cubic NLS equation based on the phase of the initial condition (Satsuma and Yajima 1974) suggested that the determination of the phase modulation was important for the evolution. In particular, it is important for predicting the occurrence of the bound state. There is almost no variation in the initial phase or frequency modulation, although small variation is seen to develop with fetch as well as small regions of quite large variation.

Small regions of phase reversal result in discontinuities or jumps in the frequency. Melville (1981) suggests these jumps may be the mechanism of 'crest pairing' (one crest overtakes another and disappears) observed by Ramamonjiarisoa and Mollo-Christensen (1979). Crest pairing may be the visual manifestation of the frequency downshift. The jumps in frequency correspond to similar large variations in wavenumber and phase speed. Local large phase speed variations in the vicinity of amplitude minima may act to merge crests or troughs (local instability) and to decrease the frequency.

A satisfactory explanation of the frequency downshift has not been obtained. Nor has the effect that dissipation may have on wave phase been examined. We proposed that the surface damping effect (which introduces variations in surface tension) might act to change the phase of the waves, thus resulting in local phase reversals and frequency downshifting. It will be shown in the next chapter that for the linear dissipative balances that were attempted, no effect on phase which could account for anything other than amplitude attenuation could be arrived at. It seems likely that if dissipation affects phase, it is through a nonlinear coupling. This is supported in part from observations; only the steeper experiments exhibit downshifting.

Appendix 2.A Data Processing Methods

The data processing was done on a Digital Equipment Corporation PDP-11/60 computer. Most of the software was generously provided by G. Sahar. Figure 2.A1 is a block diagram of the processing sequence.

2.A.1 Filtering

The filter is a finite impulse response linear phase digital filter, designed by a special program written by J. H. McClellan and documented in McClellan et al. (1973). The design algorithm uses the Remez exchange method to design a filter with minimum weighted Chebyshev error in approximating a desired ideal frequency response.

The impulse response was made causal by shifting to the right in the time domain. This translates into a linear phase in the frequency domain. This linear phase in the output of the filter is eliminated by shifting it to the left. The filtering program uses an overlap-add algorithm (Oppenheim and Schaffer 1975).

2.A.2 Spectral estimation

The spectral estimator is of the nonlinear adaptive kind.

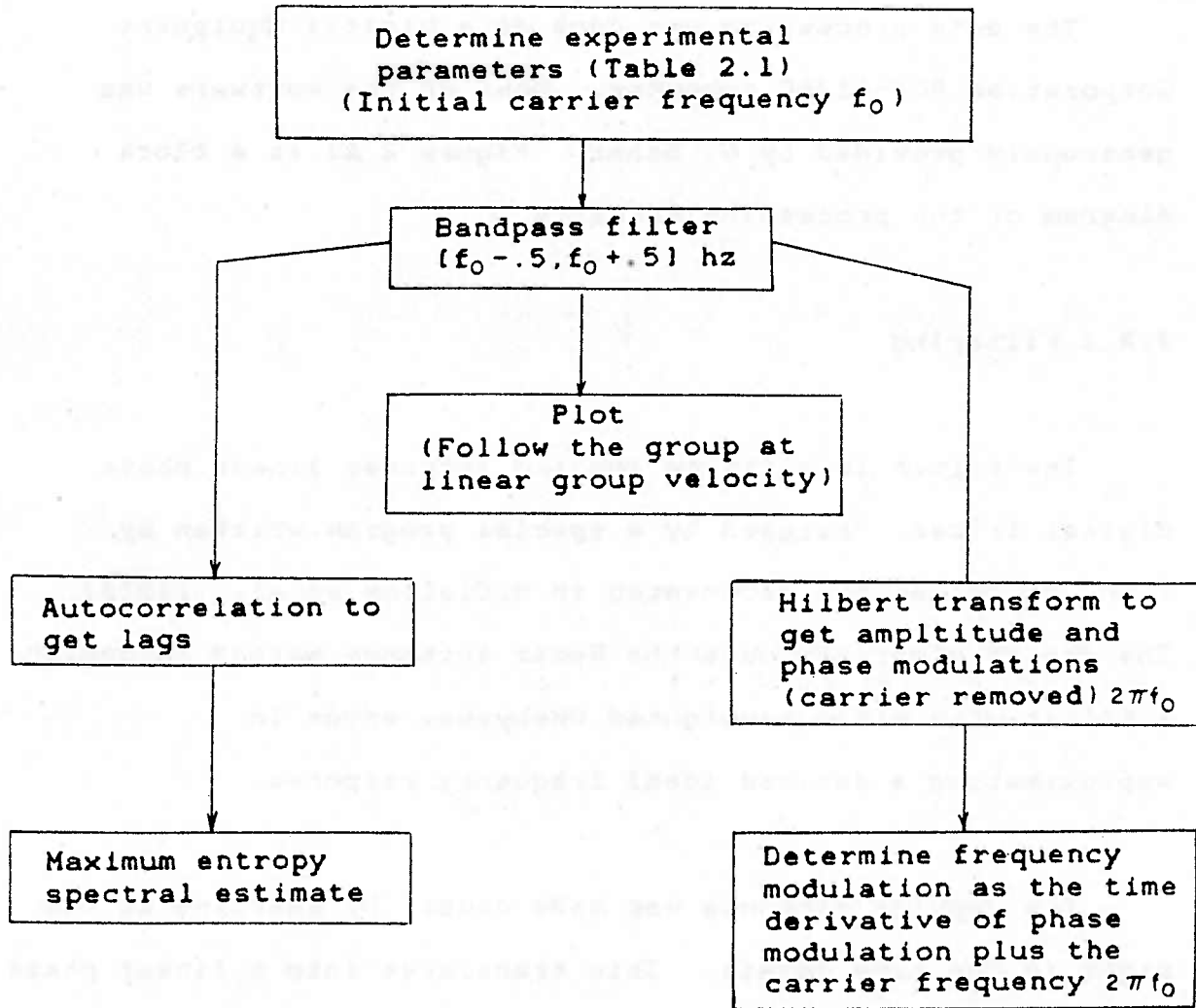


Fig. 2.A1 Sequence of processing

APPENDIX 2.A

using the maximum entropy (MEM) or autoregressive (AR) method. A brief outline of the method is given below. The computer code was written by Dr. B. Campbell, Dr. B. Dunwoody, and M. Briggs. The required input is the autocorrelation of the signal. It is computed using Rader's algorithm [1970] and a code written by Dr. B. Campbell.

Kay and Marple [1981] give a good overview of new techniques developed in the last two decades for spectrum analysis. The summary given below follows their discussion.

We model our (discretized) process as a rational transfer function which produces the output sequence $(x_n(t))$ from an input driving sequence $(w_n(t))$ assumed to be a white noise sequence of zero mean and variance σ^2 .

The spectrum, $S(f)$, of our data is then:

$$S_x(f) = |H(f)|^2 S_w(f) = |H(f)|^2 \sigma^2 \quad (2.A1)$$

If autoregression is a reasonable model for our process, we write $x_n(t)$ as an order p linear regression on itself. The error is represented by $w_n(t)$.

$$x_n(t) = w_n(t) - \sum_{k=1}^p a_k x_{n-k} \quad (2.A2)$$

If $A(f)$ is the inverse filter with z -transform $A(z)$, i.e.,

$$A(z) = 1/H(z) , \quad (2.A3)$$

APPENDIX 2.A

where $z = \exp (i2\pi f\Delta t)$, then the relation between the autoregressive model and the linear filter with rational transfer function is :

$$A(z) = z\text{-transform of } \left\{ - \sum_{k=1}^P a_k x_{n-k} \right\} = \sum_{m=0}^P a_m z^{-m} \quad (2.A4)$$

Without loss of generality we assume $a_0 = 1$ and incorporate any filter gain into σ^2 .

$$|A(z)|^2 = \left| 1 + \sum_{m=1}^P a_m z^{-m} \right|^2 \quad (2.A5)$$

Specifying the autoregressive (AR) coefficients (a_k) and σ^2 is equivalent to specifying the spectrum of our process ($x_n(t)$).

$$S_x(f) = \frac{\sigma^2}{\left| 1 + \sum_{m=1}^P a_m z^{-m} \right|^2} \quad (2.A6)$$

The AR parameters are obtained using the relation between them and the autocorrelation function which we estimate from the data. We write the k th autocorrelation lag as

$$\begin{aligned} R_{xx}(k) &= E(x_{n+k} x_n^*) = E\left(x_n^* \left(w_{n+k} - \sum_{m=1}^P a_m x_{n-m+k} \right) \right) \\ &= - \sum_{m=1}^P a_m R_{xx}(k-m) + E(w_{n+k} x_n^*) \end{aligned} \quad (2.A7)$$

where $E[\]$ denotes the expected value. Since $H(z)$ is assumed to be a stable, causal filter we have that

$$\begin{aligned}
 E(w_{n+k} x_n^*) &= E\left(w_{n+k} \sum_{m=0}^{\infty} h_m^* w_{n-m}^*\right) \\
 &= \sum_{m=0}^{\infty} h_m^* \sigma^2 \delta_{k+m} \\
 &= \sigma^2 h_{-k}^* \\
 &= \begin{cases} 0 & , k > 0 \\ h_0^* \sigma^2 & , k = 0 \end{cases} \quad (2.A8)
 \end{aligned}$$

where δ_m is Kronecker's delta. Using $h_0 = \lim_{z \rightarrow \infty} H(z) = 1$, we find

$$R_{xx}(k) = \begin{cases} - \sum_{m=1}^p (a_m R_{xx}(k-m)) & , k > 0 \\ - \sum_{m=1}^p (a_m R_{xx}(-m)) & , k = 0 \end{cases} \quad (2.A9)$$

These are the Yule-Walker equations. The AR parameters are determined by choosing p equations, $k > 0$, and solving for (a_k) , $k = 1, \dots, p$. σ^2 is determined from the equation for $k = 0$. The set of equations that requires the fewest lags is for $k = 1, \dots, p$. We formulate the following set of matrix equations, equivalent to (2.A9).

$$\begin{bmatrix} R_{xx}(0) & R_{xx}(-1) & \dots & R_{xx}(-p) \\ R_{xx}(1) & R_{xx}(0) & \dots & R_{xx}(-p+1) \\ \vdots & & & \vdots \\ R_{xx}(p) & R_{xx}(p-1) & \dots & R_{xx}(0) \end{bmatrix} \begin{bmatrix} 1 \\ a_1 \\ \vdots \\ a_p \end{bmatrix} = \begin{bmatrix} \sigma^2 \\ 0 \\ \vdots \\ 0 \end{bmatrix} \quad (2.A10)$$

The above autocorrelation matrix is Hermitian, Toeplitz (all diagonal elements identical) and positive definite. The system can be solved efficiently using the Levinson-Durbin

algorithm. The actual algorithms used can be found in Kay and Marple (1981).

2.A.3 Hilbert transform

The wave modulation fields were obtained using the Hilbert transform. Use of this technique was suggested by Dr. W. K. Melville, who has used the method to study breaking waves. Although the technique is well known in communications theory, its application to the study of surface waves is quite new. Therefore, we give a brief outline of the method and its assumptions, following the discussion in Melville (1981). The reader is referred to his paper and to a thesis by G. Sahar (1981). The actual computation of the transform can be done quite efficiently by using a Fast Fourier Transform (FFT). This exploits the relation between the Hilbert transform of a function and its Fourier transform. The computer code was a modification of a program written by G. Sahar. The method assumes that the data is causal and weakly narrow-banded.

If $g(t)$ is a real function of time, $-\infty < t < \infty$, then define the analytic function

$$h(t) = g(t) - i \hat{g}(t) \quad (2.A11)$$

$$\text{where } \hat{g}(t) = \text{H.T.}[g(t)] =: \frac{1}{\pi} \int_{-\infty}^{\infty} \frac{g(t') dt'}{t-t'} \quad (2.A12)$$

(H. T. [] denotes Hilbert transform of . . .). We use the

following properties of the Hilbert transform:

1. H. T. [$\cos(at + b)$] = - $\sin(at + b)$
2. H. T. [$\sin(at + b)$] = $\cos(at + b)$
3. F. T. [$\hat{g}(t)$] = $i \operatorname{sgn}(s)$ F. T. [$g(t)$]

(F. T. [] denotes Fourier transform of . . .).

$$\text{F.T.}[g(t)] =: \int_{-\infty}^{\infty} g(t) e^{-i2\pi st} dt$$

4. F.T.[$h(t)$] = $2 \text{F.T.}[g(t)]$, $s > 0$ or $s = 0$
 0 , $s < 0$

5. The Hilbert transform is a linear functional of g .

If we represent our real measured time series $g(t)$ as a Fourier series

$$g(t) = \operatorname{Re} \left(\sum_{n=0}^{\infty} a_n \exp[i \phi_n] \right) \quad (2.A13)$$

where a_n and ϕ_n are the amplitude and phase of the n th Fourier component, respectively, then by properties 1) and 5):

$$\text{H.T.}[g(t)] = - \operatorname{Im} \left(\sum_{n=0}^{\infty} a_n \exp[i \phi_n] \right) \quad (2.A14)$$

In general, if our data is given as

$$g(t) = \operatorname{Re} \left(a(t) \exp[i \phi(t)] \right) \quad (2.A15)$$

We define the analytic function $h(t)$

$$h(t) =: g(t) - i \hat{g}(t) = a(t) \exp[i \phi(t)] \quad (2.A16)$$

The amplitude $a(t)$ is given by

$$a(t) = [g^2 + \hat{g}^2]^{1/2} \quad (2.A17)$$

and the phase $\phi(t)$ is given by

APPENDIX 2.A

$$-\phi(t) = \arctan(\hat{g}/g) \quad (2.A18)$$

For our observations we assume the following model:

$$g(x_i, t) = \text{Re} (a(x_i, t) \exp[i (\omega_0 t + \Theta(x_i, t))]) , \quad (2.A19)$$

where x_i corresponds to a fixed wavegauge location and ω_0 is the wave carrier frequency. The analytic function $h(x_i, t)$ is defined as:

$$\begin{aligned} h(x_i, t) &= g(x_i, t) - i \hat{g}(x_i, t) \\ &= a(x_i, t) \exp[i (\omega_0 t + \Theta(x_i, t))] \end{aligned} \quad (2.A20)$$

If we think of the signal (in time) as the product of a rapidly varying carrier wave and a slowly varying modulation, then the complex envelope is described by

$$A(x_i, t) = a(x_i, t) \exp[i \Theta(x_i, t)] \quad (2.A21)$$

where $a(x_i, t)$ is the amplitude modulation which we determine using 2.A17. The phase modulation, $\Theta(x_i, t)$, is given by

$$\begin{aligned} \Theta(x_i, t) &= \phi(x_i, t) - \omega_0 t \\ &= \arctan(-\hat{g}/g) - \omega_0 t \end{aligned} \quad (2.A22)$$

using 2.A18. However, the phase modulation is a continuous function of time whereas the arctangent is restricted to the interval $[-\pi/2, +\pi/2]$. Instead of using the arctangent, we actually solve for the cosine and sine of ϕ which extends our interval to $[-\pi, \pi]$. Both the principal value of the phase and an 'unwrapped' phase are calculated. The unwrapping

APPENDIX 2.A

technique looks for discontinuities in the principal value and adds in a multiple of 2π to get the continuous phase function. The carrier frequency ω_0 was determined from MEM spectra at the most upstream observation. This initial carrier frequency was removed from the phase modulation for all the wavegauge signals for a given experiment. This was done in order to specify a real data initial condition to the cubic-nonlinear Schrodinger (NLS) equation (Chapter 3). This equation governs the slowly varying complex modulation envelope $A(x_i, t)$ (carrier removed) of surface gravity waves on deep water. The further fetches were transformed for comparison with the numerical evolution. All the data was bandpass filtered in a band of width one hertz centered on the carrier. Both the transform method and the cubic NLS equation imply a weakly narrow-banded assumption. (The Hilbert transform requires the bandwidth of the spectrum to be less than or equal to $2f_0$; Melville refers to Schwartz et al. (1966)). The carrier frequency is added back in to the frequency modulation which is calculated as

$$f(x_i, t) = \omega_0 + \frac{\theta(x_i, t+\Delta t) - \theta(x_i, t-\Delta t)}{2\Delta t} \quad (2.A23)$$

CHAPTER 3

MODELLING OF SURFACE WAVE GROUP DEVELOPMENT

3.1 INTRODUCTION

The wave group development described in chapter 2 was modelled numerically using the cubic nonlinear Schrodinger (NLS) equation. The amplitude and phase modulations from the most upstream wavegauge observation (6.1 meters) were obtained using the Hilbert transform and specified as an initial condition for the numerical model. The transformation from a spatial evolution in the wave channel frame of reference to a temporal evolution in the numerical frame was accomplished using the linear group velocity. This transformation has been employed by Benjamin and Feir [1967], Benjamin [1967], Chu and Mei [1970, 1971], and Lake et al [1977] to make comparisons between theory and experiment. Further details on the assumptions made in both the modelling and the comparisons will be discussed below and at greater length in the appropriate sections.

The cubic NLS equation, which we derive in the next section, describes the slowly varying complex envelope of gravity waves on deep water. The theory is weakly nonlinear, narrow-banded and inviscid. By narrow-banded we mean that the wavenumber and frequency are assumed to be slowly varying about their mean (constant) values. For continuous wavetrains the cubic NLS equation recovers the modulational instability of Benjamin and Feir (the growth of perturbations whose frequencies are sidebands to the carrier wave frequency). However, the sideband growth remains symmetric about the carrier, and the equation can not describe a frequency downshift such as that observed for steep wavetrains (Lake et al 1977) and as seen in chapter 2 in wave groups.

The modulational instability does not, however, lead to thermalization and disintegration of the wavetrain. If dissipation were present, the growth could perhaps be balanced and result in steady, limit cycle behavior. However, when dissipation is absent, as in the inviscid model, recurrence of the linearly unstable mode is observed. That is, after reaching a maximum modulation, the wavetrain demodulates and eventually returns to its initial state. There is neither a steady end-state nor thermalization of the wavetrain. Instead we find a long-time periodic behavior that is characteristic of other undamped nonlinear systems and known as the Fermi-Pasta-Ulam recurrence phenomenon. There have been no

long-time observations to verify FPU-recurrence for wavetrains due to restrictions of wave tank length. However, observations [Lake et al 1977] indicate that an initially uniform wavetrain, after modulating, demodulates and reforms into a nearly uniform wavetrain of slightly lower frequency (frequency downshift).

So far, we have cited results of the model for continuous wavetrains. For pulse-like initial conditions (i.e. wave groups), the cubic NLS equation can be solved exactly using the inverse scattering transform developed by Gardner et al [1967]. The inverse scattering method does not apply to continuous wavetrains. The recurrence phenomenon in wave groups is related to the bound state of solitons predicted by Zakharov and Shabat [1972] from the inverse scattering solution of the cubic NLS equation. The bound state is a long-time periodic behavior with eventual recurrence of the initial condition. The recurrence cycle does not result from a sideband instability but rather from a strong interaction between solitons with identical velocities which remain superposed. Yuen and Lake [1976] mention that there is no straightforward physical interpretation of the bound state (it was predicted when the eigenvalues of the related scattering problem are purely imaginary). They also suggest that dissipation may rule out the possibility of recurrence in wave groups. They did not think that they had observed the bound

state in their wave group experiments although they mention that the component soliton speed differences were very small [Lake et al 1977]. Satsuma and Yajima [1974] did a theoretical and numerical study in which they predicted the occurrence of the bound state from properties of the initial condition. There has not been an observational study which tested their predictions.

Thus, in using the inviscid cubic NLS equation to model the wave group evolution, there are two important effects which we can not expect to describe: the observed frequency downshifting of the steeper experiments and the cumulative effect of dissipation. However, we can use the model in comparison with the observations to answer several important questions. What is the limit of validity of the cubic NLS model? On what time scale does dissipation act? In the presence of dissipation, is recurrence physically realizable?

We propose to describe in detail this recurrence phenomenon (bound state) for wave groups. From amplitude modulation alone, it is difficult to determine the type of wave interaction that is taking place: linear dispersion (radiation), soliton or bound soliton. However, the differences in the phase modulations of the above types of behavior seem to be quite distinct. First, we analyze the phase modulation of exact solutions of the cubic NLS equation

to see how the phase evolves for different types of behavior. Using this as a guide, we can interpret and compare the development of the phase modulation in the numerical model and in the observations.

In an attempt to include dissipation in the model, we have tried various linear balances of dissipative terms with complex constant coefficients. Admittedly, this is an arbitrary procedure. We examine the possible effect that dissipation might have on the phase, in particular, the role dissipation might play in frequency downshifting. At least for the linear balances that were attempted, dissipation was shown to affect only amplitude. A decay rate estimated from the observations (Table 2.3) was included to model the amplitude damping. These viscous numerical evolutions are also compared to the observations and the inviscid solutions. Although there is no direct effect on the phase, by changing the 'quantum' of the soliton the long-time behavior of the dissipated solution was sometimes altered from that of the inviscid solution and this was reflected in the phase modulation development.

In the next two sections we derive the cubic NLS equation and the numerical model. Section 3.4 examines the evolution from initial conditions for which we have exact analytic solutions. In section 3.5 we include the effect of

dissipation. This is followed by a comparison between observations and numerical solutions, both inviscid and viscous. Section 3.7 presents a discussion and summary.

3.2 FORMULATION OF THE SCHRÖDINGER MODEL

3.2.1 Background

Zakharov [1968] was the first to derive the two-dimensional Schrödinger equation in the context of deep water waves using a van der Pohl (multiple scales) method. Zakharov and Shabat [1972] then solved the one-dimensional cubic NLS equation exactly for pulse-like initial conditions using the inverse scattering transform. They showed that an arbitrary pulse evolved into a number of solitons and a relatively unimportant linearly dispersive tail. Unlike the soliton solutions of the KdV equation, the velocity and amplitude of these solitons are independent of each other. The KdV equation has long been known to describe shallow water waves of permanent form. It can also be solved exactly for pulse-like initial conditions using the inverse scattering method. Zakharov and Shabat examined the stability of the soliton solutions of the one-dimensional NLS equation. They found them to be stable in the sense that the solitons survive pairwise collisions with no permanent change except for a

possible shift in position and phase. The amplitudes and velocities of the solitons remain unaltered. They are also stable or neutrally stable to one-dimensional perturbations (neutral in the sense stable but tending asymptotically to a soliton of slightly different parameters).

What is principally new compared to KdV solitons is the possibility of the formation of a 'bound' state of a finite number of solitons having identical velocities. The simplest case of two solitons is a periodic-in-time solution characterized by a single frequency. In the case of N -solitons it is an arbitrarily periodic solution characterized by $N(N-1)/2$ frequencies.

Proceeding along somewhat different lines, Chu and Mei (1970, 1971) applied a WKB-perturbation technique to study the slow modulation of a deep water Stokes wavetrain. They found that new dispersive terms representing the modulation rate and of the same order as the nonlinear correction were needed to extend the scope of validity of Whitham's theory based on an averaged Lagrangian. Differences between the Chu-Mei equations and the Schrodinger equation were resolved by Davey (1972). Yuen and Lake (1975) showed the equivalence of the Schrodinger equation to a higher order theory of Whitham's method. Thus all existing theories yield the same equation to the order considered, and earlier discrepancies have been

accounted for due to expansions to different orders.

Chu and Mei found that the dispersive term removed the singularity encountered in the application of Whitham's theory. They likened Whitham's theory to the Airy equation where amplitude dispersion causes the wave to continue to steepen until shocks occur. To extend this analogy they likened their equations to those of Boussinesq. The presence of frequency dispersion counteracts the effect of amplitude dispersion thus eliminating the early occurrence of shocks. Hence there is the possibility for waves of permanent form where amplitude dispersion exactly balances frequency dispersion (soliton solutions).

They proceeded to study the nonlinear evolution of wave envelope on deep water numerically. One of their equations contains the envelope amplitude in the denominator; hence their calculations break down at the first occurrence of a node in wave envelope. Based on their calculations they conjectured that the envelope disintegrates to multiple groups of waves each of which approaches a stable permanent envelope with dynamical equilibrium between amplitude and frequency dispersion. In actuality, the analytic initial condition that they chose to study numerically was the exact 2-soliton solution (a hyperbolic secant with width to height ratio twice that of a soliton). They cannot follow the evolution after

the first node occurs, at time T , but what actually happens is that the initial condition reconstructs itself at time $2T$ (and at $2nT$, $n = 1, 2, 3 \dots$). This was pointed out in a comment by Roskes [1976] who did the numerical evolution using the Schrodinger equation rather than the equivalent Chu-Mei equations and hence was able to observe much longer evolution. He points out that the initial condition used in the laboratory experiments of Yuen and Lake [1975] is also that of a 2-soliton. He suggests that the expected evolution would be a periodic (period T) nondiverging bound state.

In a reply to Roskes comment, Yuen and Lake [1976] mention that there is no straightforward interpretation of the occurrence of a bound state. Hence it would be difficult, based only on this information, to try to produce the correct profiles experimentally. Although they attempted to vary the initial state (sech, sin, etc.), they did not see the bound state phenomenon, i.e., they did not see the initial condition reconstruct itself. They attribute their observations to several possible explanations. First, the initial condition required may be very sensitive. Secondly, the cumulative effect of dissipation may become important, perhaps on the scale of $T =$ recurrence period. This would prevent recurrence from being observed even when initial conditions are favorable.

Although Yuen and Lake do not see recurrence in their experiments in the sense that the initial pulse reconstructs, the solitons do not seem to separate. Lake et al [1977] mention that the component soliton phase speed differences are quite small. This may be due to the observation period not being long enough. However, it remains open to question whether they have observed the bound state (solitons do not separate) where recurrence can not take place due to dissipation, or whether they have solitons that diverge (although not observed for long enough time). They do not describe the phase of their observations. As we see next, the phase of the initial condition can be used to predict the occurrence of the bound state (in some cases). Besides considering the initial phase, the evolution of the phase in the cases of linear dispersion, divergent solitons and the bound state is different.

Satsuma and Yajima [1974] did a theoretical study of the nonlinear Schrodinger equation as an initial value problem. They managed to classify certain initial conditions as yielding nondivergent bound states and certain others as yielding the divergent soliton states. They confirmed their predictions using numerically computed solutions to the various types of initial conditions. We summarize their main results in section 3.2.3 after first deriving the governing equation in the next section.

3.2.2 Simple derivation

The derivation given in this section follows the rather elegant variational approach used by Yuen and Lake [1975].

We use x, z, t to denote the horizontal coordinate, vertical coordinate (positive upwards) and the time. $\nabla^2 = \left(\frac{\partial^2}{\partial x^2} + \frac{\partial^2}{\partial z^2}\right)$ is the two-dimensional Laplacian operator, and $\nabla = \left(\frac{\partial}{\partial x}, \frac{\partial}{\partial z}\right)$ is the two-dimensional gradient operator.

The basic governing equation for inviscid surface gravity waves on deep water is Laplace's equation within the fluid:

$$\nabla^2 \phi = 0, \quad -\infty < z < \eta(x, t) \quad (3.1)$$

$\eta(x, t)$ is the free surface elevation. The velocity \vec{u} is the gradient of the potential:

$$\vec{u} = \nabla \phi \quad (3.2)$$

The bottom boundary condition for a fluid of infinite depth is:

$$\phi_z \rightarrow 0, \quad z \rightarrow -\infty \quad (3.3)$$

The nonlinear surface boundary condition is:

$$\phi_{tt} + g \phi_z + \left(\frac{\partial}{\partial t} + \frac{1}{2} \vec{u} \cdot \nabla\right) |\vec{u}|^2 = 0, \quad z = \eta(x, t) \quad (3.4)$$

The surface boundary condition is evaluated on the unknown free surface η . The free surface is related to the potential by:

$$\eta = -\frac{1}{g} \left\{ \phi_t + \frac{1}{2} |\vec{u}|^2 \right\}, \quad z = \eta(x, t) \quad (3.5)$$

For small amplitude waves, we can expand the surface boundary conditions (3.4) and (3.5) in Taylor series about $z = 0$. If we expand the velocity potential ϕ and the surface elevation η in a perturbation series in the wave steepness parameter $\epsilon = ak$ (amplitude \times wavenumber) we find Stokes series solution (1847).

Instead we follow the variational approach given in Yuen and Lake (1975). If we can find a Lagrangian $L(x, t)$ to describe our system, then the evolution of the system is described by the variation of the averaged Lagrangian:

$$\delta \iint \mathcal{L} dx dt = 0 \quad (3.6)$$

where
$$\mathcal{L}(x, t) = \frac{1}{2\pi} \int_0^{2\pi} L(x, t) d\theta \quad (3.7)$$

if a phase function θ exists. The characteristic frequency ω and wavenumber k are given by

$$\omega = -\frac{\partial}{\partial t} \theta \quad ; \quad k = \frac{\partial}{\partial x} \theta \quad (3.8)$$

The Lagrangian for deep water waves has been shown to be

$$L(x, t) = \int_{-\infty}^{\eta} \left\{ \phi_t + \frac{1}{2} |\vec{u}|^2 + gz \right\} dz \quad (3.9)$$

For a weakly nonlinear, slowly varying, modulated wavetrain we expand η and ϕ as an amplitude modulated Stokes wavetrain

$$\eta = a(x, t) \cos \theta + \frac{1}{2} k a^2(x, t) \cos 2\theta + \dots \quad (3.10)$$

$$\phi = \frac{\omega a(x, t)}{k} \sin \theta e^{kz} + \left\{ \frac{a_t}{k} \cos \theta + \frac{\omega a_x}{k^2} (1 - k_z) \cos \theta \right\} e^{kz} + \frac{\omega a^2}{2} \sin 2\theta e^{2kz} + \dots \quad (3.11)$$

where $\theta = kx - \omega t$ is the phase function. If we substitute (3.10) and (3.11) into (3.9) and average we find from (3.7)

$$\begin{aligned} \mathcal{L} = & -\frac{\omega^2 a^2}{4k} + \frac{g a^2}{4} + \frac{a_t^2}{4k} + \frac{\omega a_x a_t}{4k^2} + \frac{\omega^2 a_x^2}{8k^3} + \frac{a a_{tt}}{2k} \\ & + \frac{3}{4} \frac{\omega a a_{xt}}{k^2} + \frac{3}{8} \frac{\omega^2 a a_{xx}}{k^3} + \frac{g k^2 a^4}{8} \end{aligned} \quad (3.12)$$

Variations with respect to θ and a yield, respectively,

$$(a^2)_t + (c_g a^2)_x = 0 \quad (3.13)$$

$$\omega = \sqrt{gk} \left\{ 1 + \frac{1}{2} k^2 a^2 + \left(\frac{a_{xx}}{8ak^2} \right) \right\} \quad (3.14)$$

(3.13) is the energy equation, and c_g is the linear group velocity.

$$c_g = \frac{1}{2} \sqrt{\frac{g}{k}} \quad (3.15)$$

(3.14) is the dispersion relation. The curvature or modulation rate term $(\frac{a_{xx}}{8ak^2})$ is the additional term first derived by Chu and Mei (1970, 1971). (3.14) is obtained using (3.13). These equations are valid to $O(\epsilon^2, a^2 k^2)$. The system is closed with a consistency or conservation of wave crest equation

$$k_t + \omega_x = 0 \quad (3.16)$$

To derive the NLS equation, we perturb the phase function

$$\theta = \theta_0 + \tilde{\theta} \quad (3.17)$$

where $\theta_0 = k_0 x - \omega_0 t$; $\tilde{\theta}_t = -\tilde{\omega}$, $\tilde{\theta}_x = \tilde{k}$

Equivalently, $\omega = \omega_0 + \tilde{\omega}$, $k = k_0 + \tilde{k}$ (3.18)

This assumes a constant carrier wave of wavenumber k_0 and frequency ω_0 . We assume the variations of ω and

k are small compared with variations of a and are slowly varying.

$$|\tilde{k}|/k \ll 1 \quad ; \quad |\tilde{\omega}|/\omega \ll 1$$

If we substitute (3.17) and (3.18) into (3.13), (3.14) and (3.16) we obtain

$$a_t + \frac{1}{2} \left(\frac{\omega_0}{k_0} \right) a_x - \left(\frac{\omega_0}{8k_0^2} \right) (\tilde{\theta}_{xx} + 2\tilde{\theta}_x a_x) = 0 \quad (3.19)$$

$$\begin{aligned} \tilde{\theta}_t + \frac{1}{2} \left(\frac{\omega_0}{k_0} \right) \tilde{\theta}_x - \left(\frac{\omega_0}{8k_0^2} \right) \{ \tilde{\theta}_x^2 - (a_{xx}/a) \} \\ + \frac{1}{2} \omega_0 k_0^2 a^2 = 0 \end{aligned} \quad (3.20)$$

Introducing the complex variable $A = a e^{i\tilde{\theta}}$ (3.19) and (3.20) combine to become the cubic NLS equation

$$i \{ A_t + \frac{1}{2} \left(\frac{\omega_0}{k_0} \right) A_x \} - \left(\frac{\omega_0}{8k_0^2} \right) A_{xx} - \frac{1}{2} \omega_0 k_0^2 |A|^2 A = 0 \quad (3.21)$$

If we scale the equation as follows

$$\bar{t} = \epsilon^2 \omega_0 t \quad ; \quad \bar{\xi} = \epsilon k_0 (x - \frac{\omega_0}{2k_0} t) \quad ; \quad \bar{A} = A/A_{max} \quad (3.22)$$

(3.21) becomes

$$i \bar{A}_{\bar{t}} - \frac{1}{8} \bar{A}_{\bar{\xi}\bar{\xi}} - \frac{1}{2} |\bar{A}|^2 \bar{A} = 0 \quad (3.23)$$

(3.23) is the dimensionless form in a frame which propagates

at linear group velocity $\frac{1}{2} \frac{\omega_0}{k_0}$.

3.2.3 Properties of the Schrodinger equation

Zakharov and Shabat (1972) have demonstrated the existence of an infinite number of conservation laws for the Schrodinger equation. An enumerable set of these which conserve certain spatial integrals of A and its derivatives are called polynomial laws. A similar set of laws has been found for the KdV equation. We list the first five:

$$C_1 \sim \int_{-\infty}^{\infty} |A|^2 d\xi \quad (3.24a)$$

$$C_2 \sim \int_{-\infty}^{\infty} (A^* A_\xi - A_\xi^* A) d\xi \quad (3.24b)$$

$$C_3 \sim \int_{-\infty}^{\infty} (|A_\xi|^2 - \frac{1}{4} |A|^4) d\xi \quad (3.24c)$$

$$C_4 \sim \int_{-\infty}^{\infty} (AA^*_{\xi\xi\xi} + \frac{3}{4} AA^*_\xi |A|^2) d\xi \quad (3.24d)$$

$$C_5 \sim \int_{-\infty}^{\infty} \left\{ |A_{\xi\xi}|^2 + \frac{1}{8} |A|^6 - \frac{1}{4} (|A|^2_\xi)^2 - \frac{1}{2} |A_\xi|^2 |A|^2 \right\} d\xi \quad (3.24e)$$

The first three conserved quantities have a physical meaning in the context of the nonlinear Schrodinger equation. They correspond to conservation of the number of particles (mass), conservation of momentum, and conservation of energy, respectively. This interpretation is correct to first order for the mass and momentum of the wave motion (Yue, 1980).

Equation (3.23) has exact solutions, called solitons, which are progressive envelope pulses of permanent form whose heights and widths are inversely proportional to each other but are unrelated to their speed U relative to the linear group velocity. The soliton solution to equation (3.23) is given by

$$A(\xi, \tau) = a \operatorname{sech} \left\{ \sqrt{2} a (\xi - U\tau) \right\} e^{-\frac{1}{4} \frac{a^2}{\tau} - i 4U\xi + 2iU^2\tau} \quad (3.25a)$$

or for equation (3.21) in dimensional form in coordinates fixed in space:

$$A(x, t) = a \operatorname{sech} \left\{ \sqrt{2} k_0^2 a \left[x - \left(\frac{\omega_0}{2k_0} + U \right) t \right] \right\} \cdot \exp \left\{ -i \frac{k_0^2 a^2 \omega_0 t}{4} - i \frac{4k_0^2 U}{\omega_0} \left[x - \left(\frac{\omega_0}{2k_0} + \frac{U}{a} \right) t \right] \right\} \quad (3.25b)$$

Equation (3.23) also has similarity solutions for decaying oscillations (radiation) which decay like linear dispersion as $1/\sqrt{\tau}$ and contain two arbitrary constants A_0 and θ_0 in amplitude and phase respectively.

$$A(\xi, \tau) = \frac{A_0}{\sqrt{\tau}} \exp \left\{ -i \left[\frac{\xi^2}{\tau} + A_0^2 \ln \tau + \theta_0 \right] / 2 \right\} \quad (3.26)$$

In section 2.3.1 of chapter 2 we have already discussed properties of the inverse scattering solution of (3.23) for pulse initial conditions.

We can put the NLS equation (3.21) in standard form using the following scaling

$$\tau = \omega t \quad ; \quad \xi = 2k_0 \left(x - \frac{\omega_0}{2k_0} t \right) \quad ; \quad \bar{A} = \frac{k_0 A}{\sqrt{2}} \quad (3.27)$$

to find, in accordance with Satsuma and Yajima [1974],

$$i \bar{A}_{\tau} - \frac{1}{2} \bar{A}_{\xi\xi} - |\bar{A}|^2 \bar{A} = 0 \quad (3.28)$$

The soliton solution in the new variables is

$$\bar{A}(\xi, \tau) = a \operatorname{sech}(a\xi) e^{-i\alpha^2 \tau / 2} \quad (3.29)$$

Satsuma and Yajima show that the equation is both Galilean and gauge invariant. By Galilean invariant we mean invariant under the transformation

$$\begin{aligned} \xi' &= \xi - v\tau \quad ; \quad \tau' = \tau \\ A'(\xi', \tau') &= \exp [i v \xi - i v^2 \tau / 2] \bar{A}(\xi, \tau) \end{aligned} \quad (3.30)$$

By gauge invariant, we mean that it is invariant to constant phase shifts

$$A' = \bar{A}(\xi, \tau) e^{i\alpha} \quad (3.31)$$

An arbitrary pulse evolves into a number of solitons and an oscillatory tail. The solitons are bound if their velocities are the same. This occurs if the eigenvalues of the associated scattering problem have common real parts. Satsuma and Yajima [1974] tried to relate this eigenvalue condition to the initial value problem. We summarize their

main results as follows. Write the solution as

$$A(\xi, \tau) = |A| e^{ip(\xi, \tau)} = R e^{ip} \quad (3.32)$$

where R is the amplitude modulation and p is the phase modulation. Then they showed that

1.) If the initial condition is real and not antisymmetric

$$p(\xi, 0) \equiv 0, \quad A(-\xi, 0) \neq -A(\xi, 0)$$

then the solution A is the bound state. The eigenvalues of the related scattering problem have zero (common) real part.

2.) If the initial value takes the form

$$p(\xi, 0) = \sqrt{\xi}, \quad A(-\xi, 0) \neq -A(\xi, 0)$$

then all the eigenvalues have the same common real part and the solution is a bound state.

3.) If A is a solution to (3.28) and A is real and not antisymmetric

$$p(\xi, 0) \equiv 0, \quad A(-\xi, 0) \neq -A(\xi, 0)$$

then we perturb A such that $A = A + dA$ where $\text{Im}(dA)$ is nonzero (i.e. small random phase perturbation). Then the eigenvalues have noncoinciding real parts and the perturbed solution should break up into moving (divergent) solitons.

4.) If A antisymmetric

$$A(-\xi, 0) = -A(\xi, 0)$$

then the solution breaks up into divergent solitons.

Our wave group data has nearly zero initial phase. Using the Hilbert transform, we have a method for examining the phase evolution with propagation distance. We can also, from exact asymptotic analytic solutions with known initial conditions, examine the phase evolution of radiation, solitons and bound state. These characteristic phase evolutions are then used to classify the observations and the numerical evolutions of the NLS model. We next derive the numerical model and then proceed to study the evolution of model solutions from a variety of initial conditions (real data and analytic functions) with comparison to observations.

3.3 NUMERICAL MODEL

We solve the cubic NLS equation using a modified Crank-Nicholson implicit scheme with second-order centered spatial finite differencing. The scheme and computer code were taken from a thesis by Yue (1980). For completeness, we include the details of the numerical scheme here.

Prior to modelling, data from the most upstream (6.1 m) observation were converted from wavetank (\bar{x}, \bar{t}) to numerical model (x, t) coordinates using the linear group velocity.

$$(x, t) = (c_g \bar{t}, \bar{x} / c_g) \quad (3.33)$$

The data were then scaled appropriately using (3.22). Data

from the further fetches were also transformed and scaled like the initial condition for comparison.

The finite difference form of (3.23) is

$$A_j^{n+1} = A_j^n - \frac{\Delta\tau}{2} \left\{ \left(\frac{i}{8} \frac{A_{j+1}^{n+1} - 2A_j^{n+1} + A_{j-1}^{n+1}}{(\Delta\zeta)^2} + \frac{i}{2} |\tilde{A}_j^{n+1}|^2 A_j^{n+1} \right) + \left(\frac{i}{8} \frac{A_{j+1}^n - 2A_j^n + A_{j-1}^n}{(\Delta\zeta)^2} + \frac{i}{2} |A_j^n|^2 A_j^n \right) \right\} + \mathcal{O}(\Delta\tau^3, \Delta\zeta^2) \quad (3.34)$$

where $A_j^n = A(j\Delta\zeta, n\Delta\tau)$

The implicit nonlinear term is estimated using an Euler scheme that maintains a local truncation error of $\mathcal{O}(\Delta\tau^3)$.

$$\tilde{A}_j^{n+1} = A_j^n - \Delta\tau \left(\frac{i}{8} \frac{A_{j+1}^n - 2A_j^n + A_{j-1}^n}{(\Delta\zeta)^2} + \frac{i}{2} |A_j^n|^2 A_j^n + \mathcal{O}(\Delta\tau^2, \Delta\zeta^2) \right) \quad (3.35)$$

Equation (3.34) is convergent with global truncation error $\mathcal{O}(\Delta\tau^2, \Delta\zeta^2)$. The cubic nonlinear term complicates the stability analysis. However, the Crank-Nicholson scheme is unconditionally stable for the linear Schrodinger equation. Yue [1980] provides the details of the linear Neumann stability analysis. Numerical solutions for reasonable choices of $\Delta\tau$ and $\Delta\zeta$ gave quite good results. The first conservation law (3.24a) was computed at each time step as a check on the error

$$\text{Error} = \frac{C_1(\tau) - C_1(0)}{C_1(0)} \quad (3.36)$$

The largest final error was five percent. Typically, the error was less than one tenth of one percent.

The boundary condition used was

$$|A| \rightarrow 0, \quad \zeta \rightarrow \pm \infty \quad (3.37)$$

3.4 EXACT SOLUTIONS

In this section we examine the evolution of exact asymptotic solutions of the Schrodinger equation for initial conditions specified from analytic functions. We try to characterize the types of behavior thus modelled to use in classifying the evolution from actual observations discussed later on in section 3.6.

The nondimensionalized equation that we solve is (3.23). The scales for the variables are given by (3.22). The initial condition is

$$A(\zeta, 0) = f(\zeta) \quad (3.38)$$

where $\max f(\zeta) = 1$ due to normalization. We solve for A using the numerical scheme of the previous section. We write

$$\begin{aligned}
 A(\xi, \tau) &= R(\xi, \tau) e^{i\theta(\xi, \tau)} \\
 &= R e^{i\pi p}
 \end{aligned}
 \tag{3.39}$$

where R represents the amplitude modulation and p represents the phase modulation normalized by π .

The first five cases that we consider are for spatially compact initial profiles of symmetric sech form:

$$f(\xi) = \text{sech}(\sqrt{\sigma} \xi / \sigma) \tag{3.40}$$

This form of initial condition is purely real ($p \equiv 0$). Hence we use the formula (2.7) to estimate the number of solitons in the asymptotic state.

$$N_s = \frac{\sqrt{\sigma}}{\pi} \int_{-\infty}^{\infty} f(\xi) d\xi = \sigma \tag{3.41}$$

For integer values of σ we get an exact number of solitons. For noninteger σ we get solitons plus radiation. When $\sigma < 1$, only radiation (linear dispersion) is present. Since the initial condition is real and symmetric, the results of Satsuma and Yajima cited in 3.2.3 predict the bound state of solitons when $\sigma \gg 2$.

As a final example we look at the evolution of an antisymmetric initial condition which yields divergent solitons.

3.4.1 Radiation

We consider a steeper-than-soliton profile of form (3.40) with $\sigma = 1/2$.

$$f(\xi) = \operatorname{sech}(2\sqrt{\sigma} \xi) \quad (3.42)$$

The asymptotic state contains no permanent soliton and the evolution is dominated by linear dispersion. The dispersion or radiation is considered as a slowly varying modulation of form (3.26) where A_0, θ_0 are now functions of (ξ/τ) . The amplitude and phase are given by:

$$R(\xi, \tau) = A_0 \sqrt{\tau} \quad (3.43a)$$

$$p(\xi, \tau) = -\frac{1}{2\pi} \left[\frac{\xi^2}{\tau} + A_0^2 \ln \tau + \theta_0 \right] \quad (3.43b)$$

The full solution (magnitude of complex envelope) is plotted in figure 3.1 for $-12.5 < \xi < 12.5$ and $0 < \tau < 10$. The percent error calculated from the first conservation law (3.36) is .003 percent. By comparing the centerline ($\xi = 0$) amplitude decay to the asymptotic rate (3.43a) we find that the deviation is small for $\tau > 5$, and at $\tau = 18$ the asymptotic state is fully achieved. From the first conserved quantity (mass)

$$C_1 = \int_{-\infty}^{\infty} R^2 d\xi = \frac{A_0^2}{\tau} L(\tau) \quad (3.44)$$

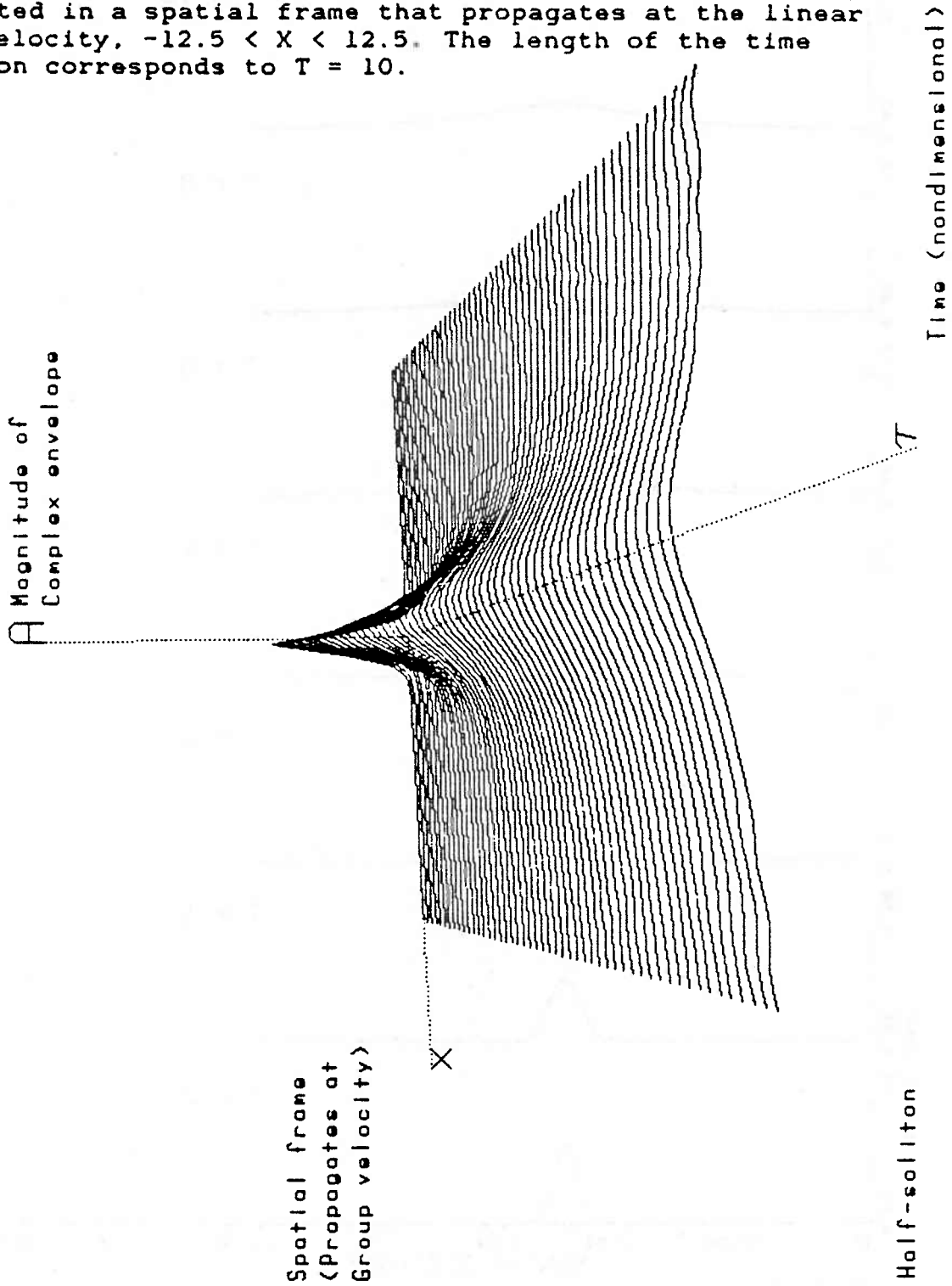
We see that the length scale L of the envelope increases

linearly with time.

Figures 3.2a and 3.2b show the amplitude and phase modulation at various times. The amplitude decays like $1/\sqrt{\tau}$ for $\tau > 5$. The initial phase modulation is zero. The phase evolution for radiation behaves like (3.43b). The phase appears discontinuous in fig. 3.2b because it is 'wrapped' (Appendix 2.A). It is actually a smooth continuous function, and the jumps of 2π occur from using the principal value of the arctangent which is defined on the (expanded) interval $(-\pi, \pi]$. The initial group is centered at $\xi = 0$ in a frame that propagates at linear group velocity. The center value of the phase decreases with time and exhibits a smooth and symmetric spatial decay from the origin like $(-\xi^2)$. This represents the dispersion of wavenumber components in the moving reference frame.

Figures 3.3a and 3.3b show the amplitude and phase modulations at four different times ($\tau = 0, 2, 6, 10$) superposed. Notice that as the centerline amplitude decreases, and the envelope length scale increases, that the off-center amplitude increases initially as the group spreads (radiates).

Fig. 3.1 Numerical evolution of a steeper-than-soliton initial profile (1/2-soliton). The magnitude of the complex envelope is plotted in a spatial frame that propagates at the linear group velocity, $-12.5 < X < 12.5$. The length of the time evolution corresponds to $T = 10$.



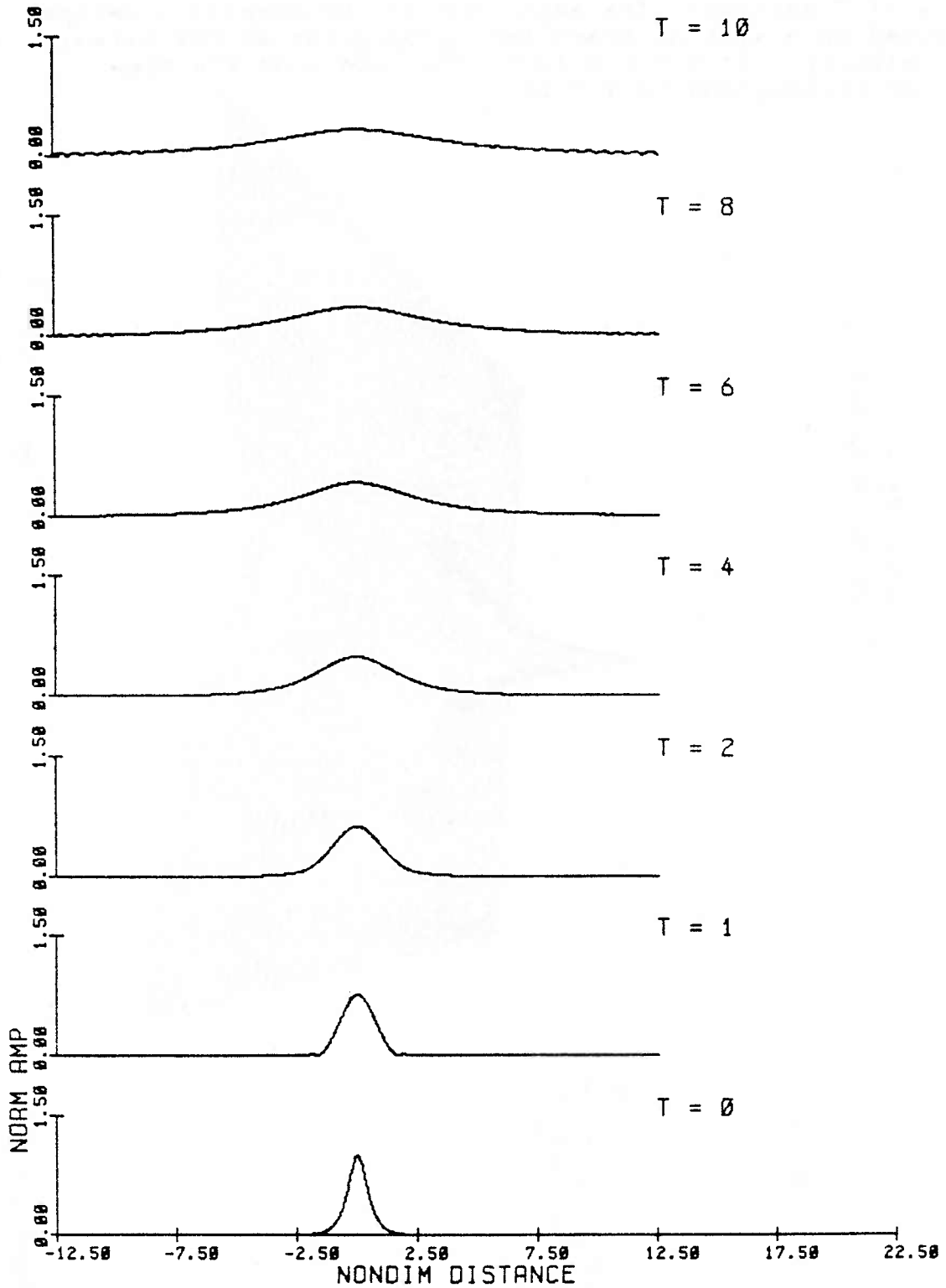


Fig. 3.2a Evolution of the magnitude of the complex envelope plotted at 7 successive time steps (time increases upwards) for the 1/2-soliton initial condition.

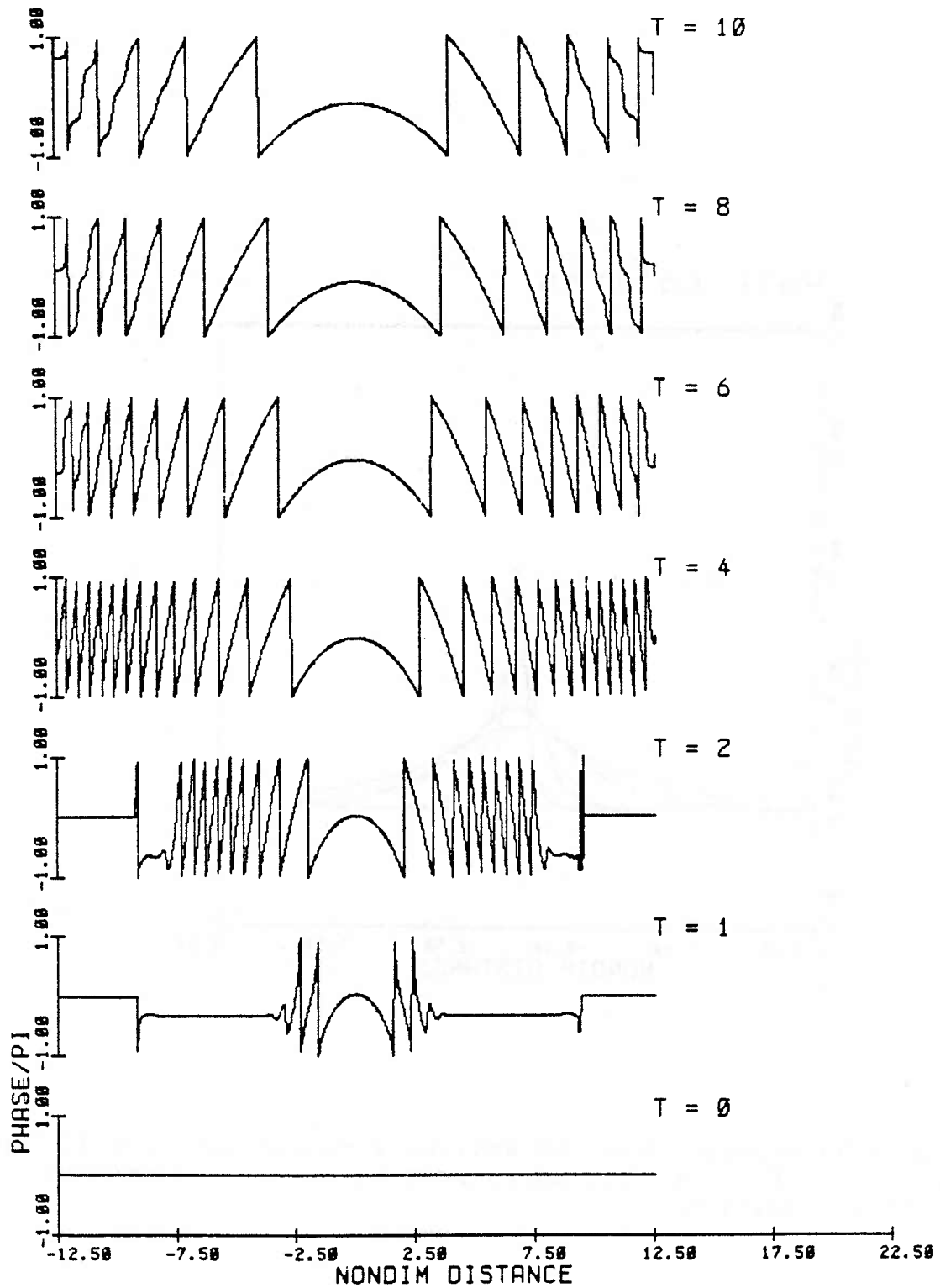


Fig. 3.2b Evolution of the principal value of the phase modulation, normalized by pi, at 7 successive time steps corresponding to the amplitude modulation of fig. 3.2a.

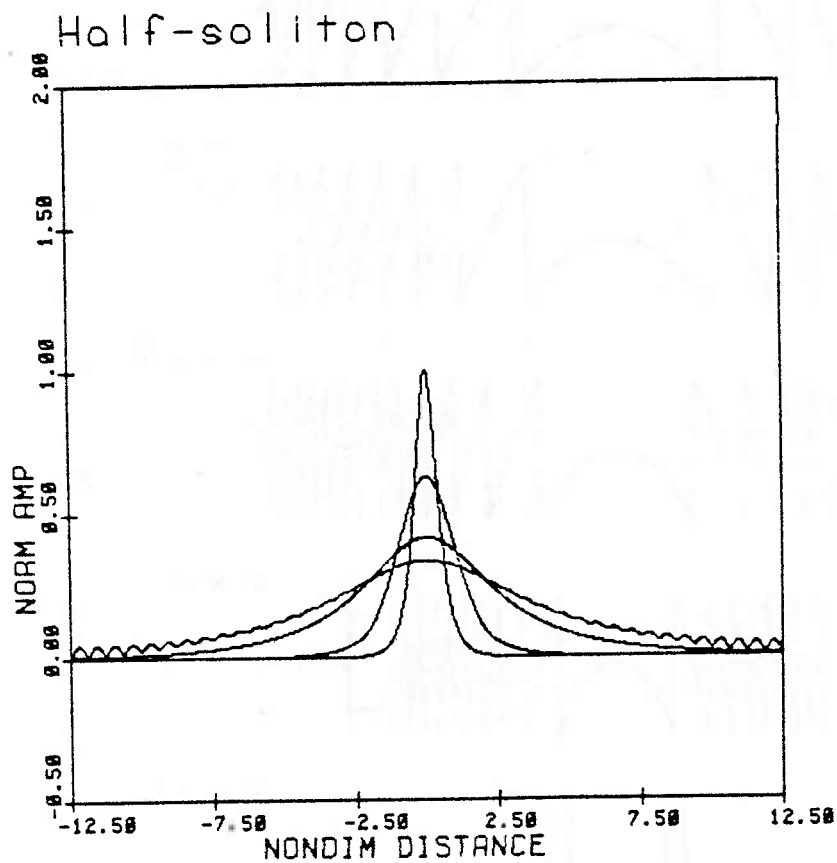


Fig. 3.3a Superposition of amplitude modulation at 4 different times, $T = 0, 2, 6, 10$, corresponding to the $1/2$ -soliton initial condition.

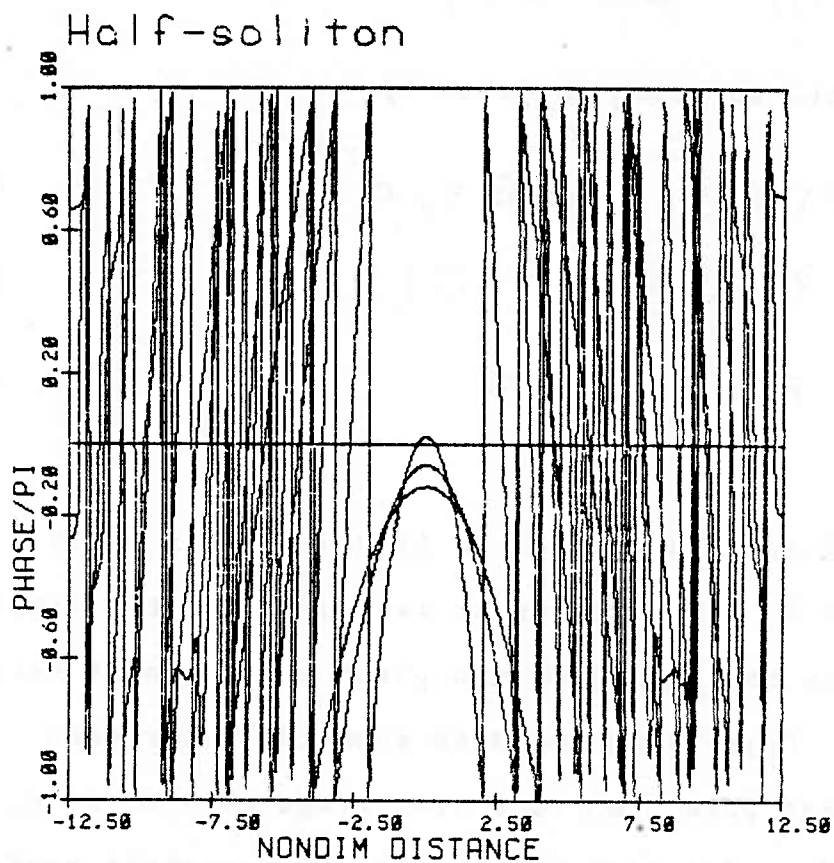


Fig. 3.3b Superposition of phase modulation at 4 different times, $T = 0, 2, 6, 10$, corresponding to the amplitude modulation superposition of fig. 3.3a.

3.4.2 Soliton

The next example is for an exact one-soliton ($\sigma = 1$) solution. The initial condition is

$$f(\xi) = \operatorname{sech}(\sqrt{2} \xi) \quad (3.45)$$

The asymptotic solution is given by

$$A(\xi, \tau) = \operatorname{sech}(\sqrt{2} \xi) e^{-i\tau/4} \quad (3.46a)$$

with
$$R(\xi, \tau) = \operatorname{sech}(\sqrt{2} \xi) \quad (3.46b)$$

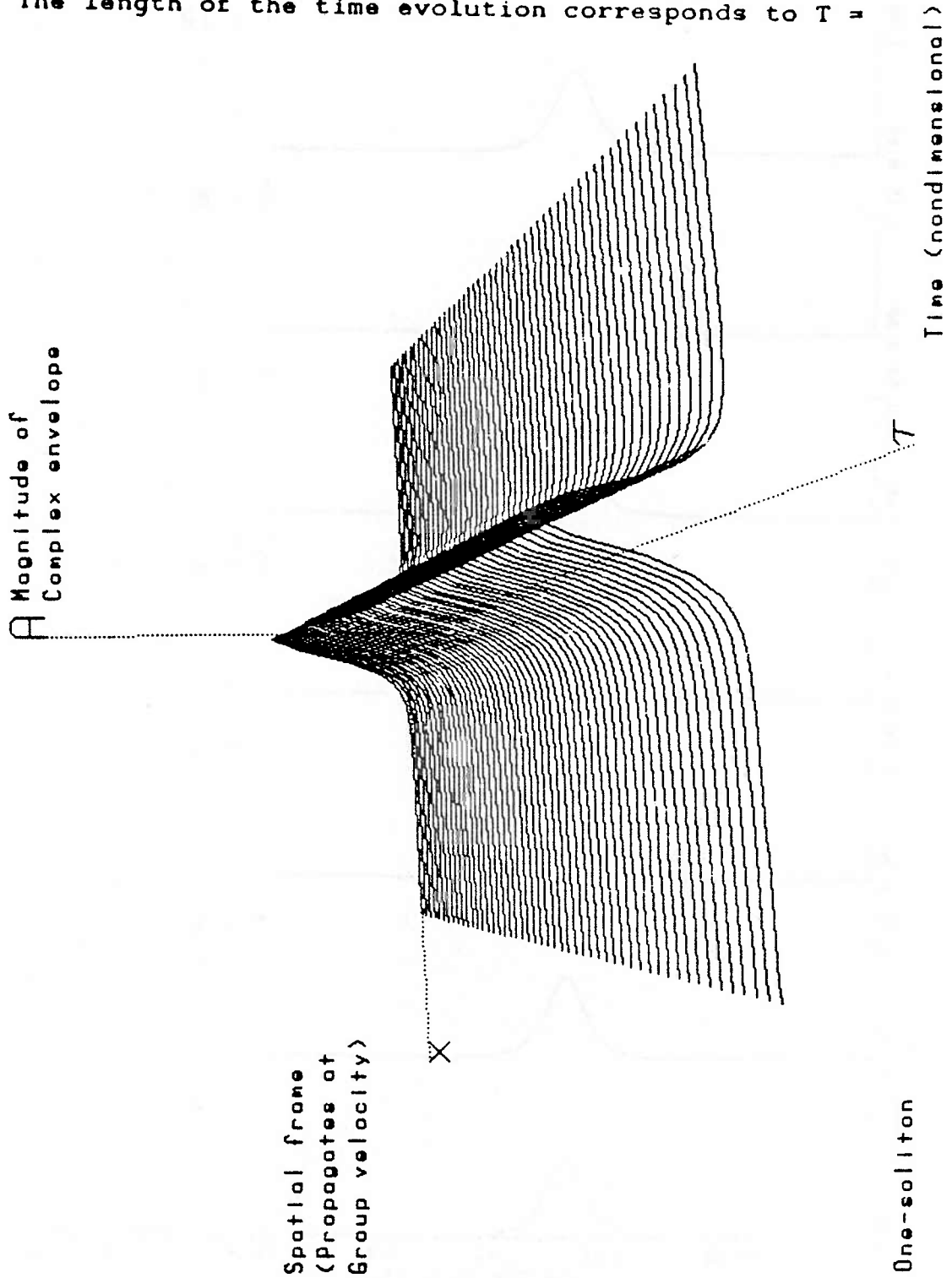
$$p(\xi, \tau) = -\tau/4\pi \quad (3.46c)$$

The solution is plotted in figure 3.4 for $-12.5 < \xi < 12.5$ and $0 < \tau < 10$. The error is .001 percent. Figures 3.5a and 3.5b show the amplitude and phase evolution at various time steps. Figs. 3.6a and 3.6b show the superposed amplitudes and phases at four time steps ($T = 0, 2, 6, 10$). The amplitude modulation shows a steady permanent profile. The phase modulation shows a constant downward shift in time. We see some linear dispersion in phase (with zero amplitude) at the edges due to numerical noise.

3.4.3 Bound state

The initial condition is that for the simplest bound

Fig. 3.4 Numerical evolution of a one-soliton initial profile. The magnitude of the complex envelope is plotted in a spatial frame that propagates at the linear group velocity, $-12.5 < X < 12.5$. The length of the time evolution corresponds to $T = 10$.



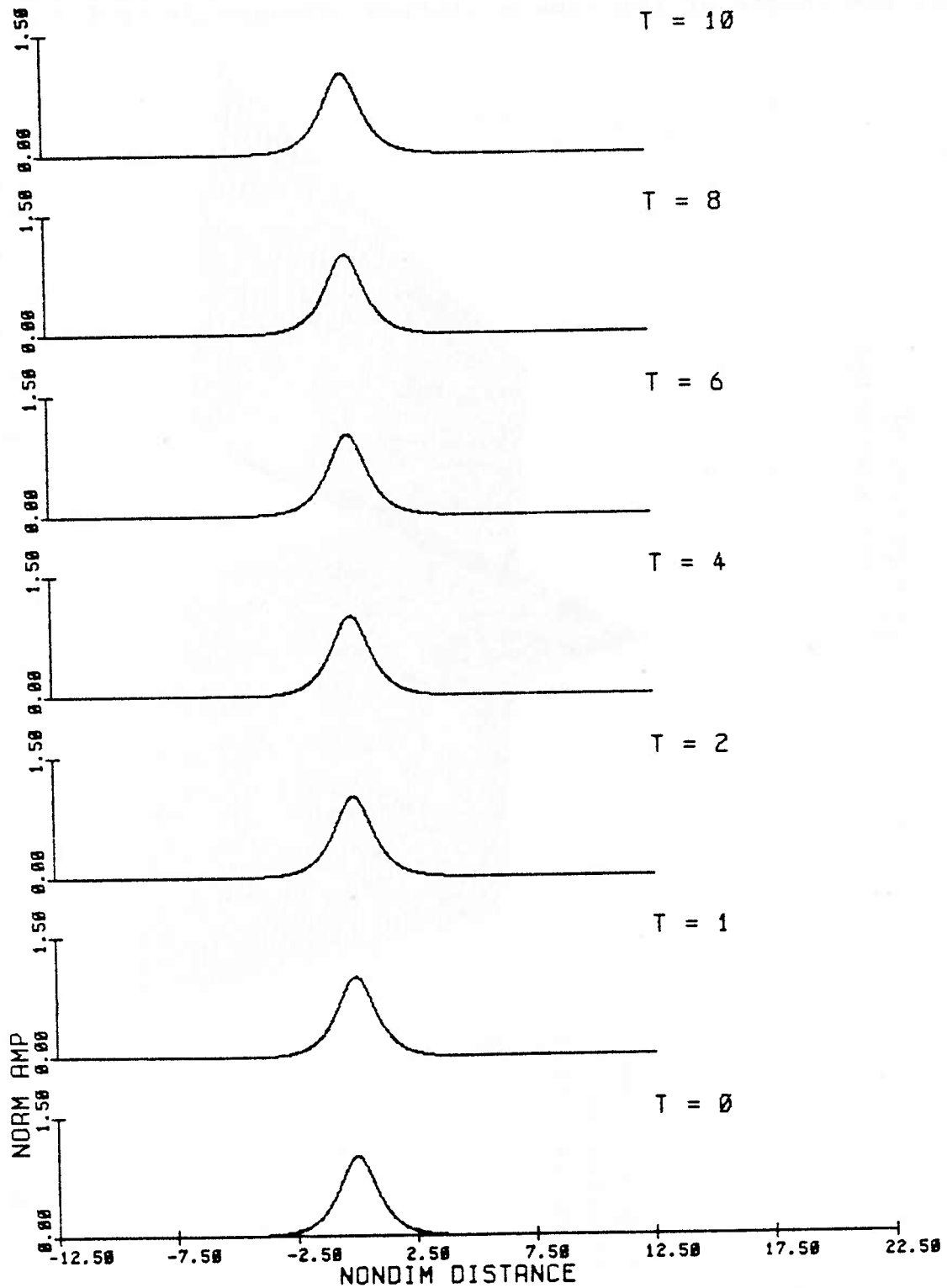


Fig. 3.5a Evolution of the magnitude of the complex envelope plotted at 7 successive time steps (time increases upwards) for the 1-soliton initial condition.

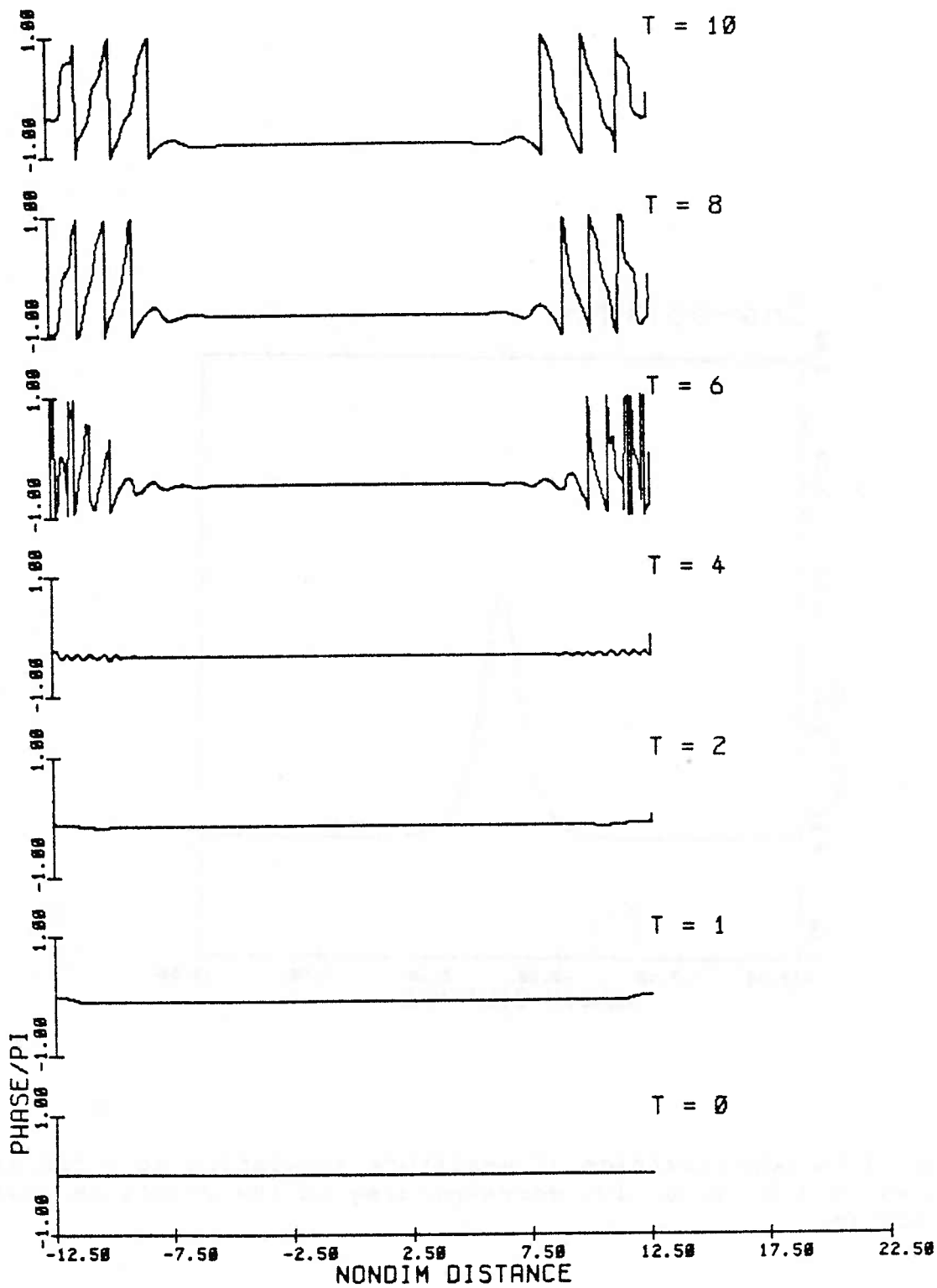


Fig. 3.5b Evolution of the principal value of the phase modulation, normalized by pi, at 7 successive time steps corresponding to the amplitude modulation of fig. 3.5a.

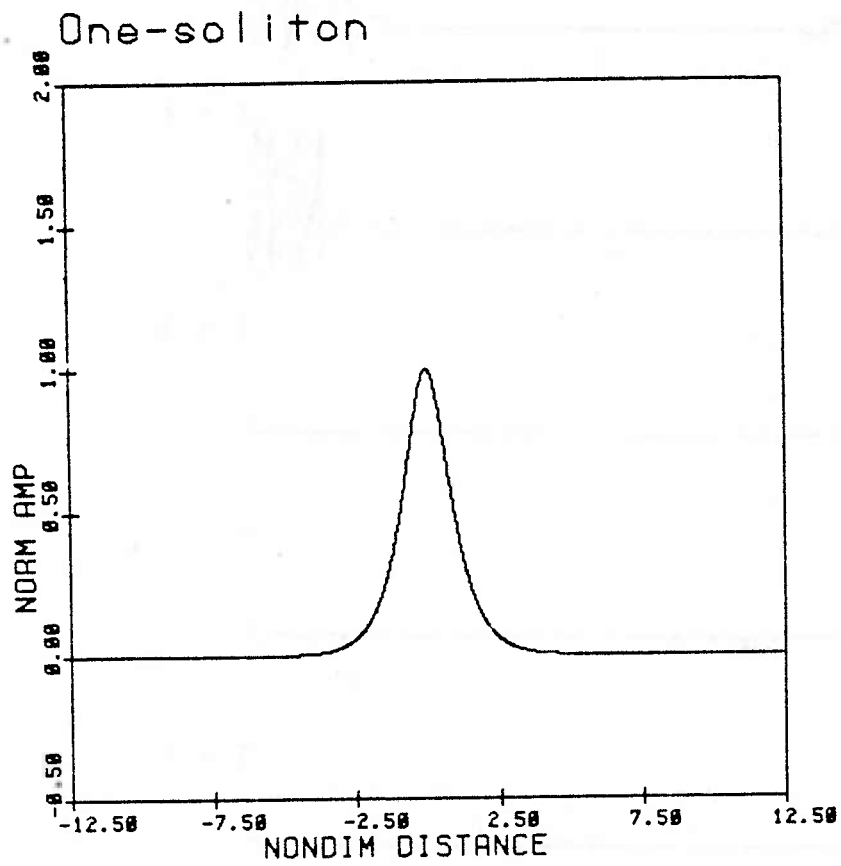


Fig. 3.6a Superposition of amplitude modulation at 4 different times, $T = 0, 2, 6, 10$, corresponding to the 1-soliton initial condition.

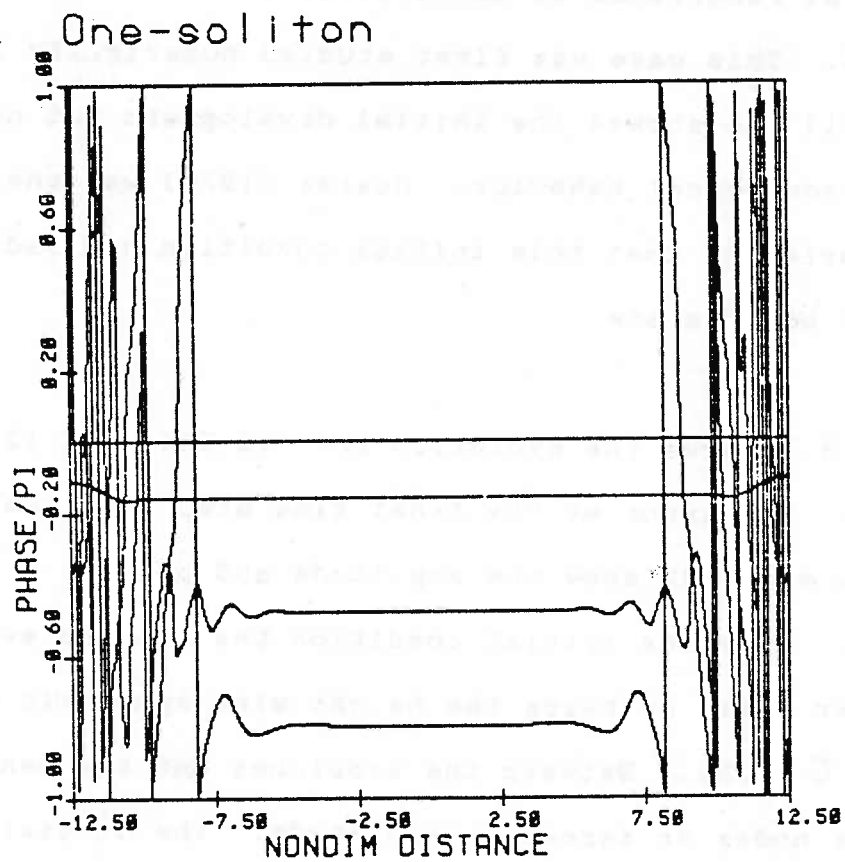


Fig. 3.6b Superposition of phase modulation at 4 different times, $T = 0, 2, 6, 10$, corresponding to the amplitude modulation superposition of fig. 3.6a.

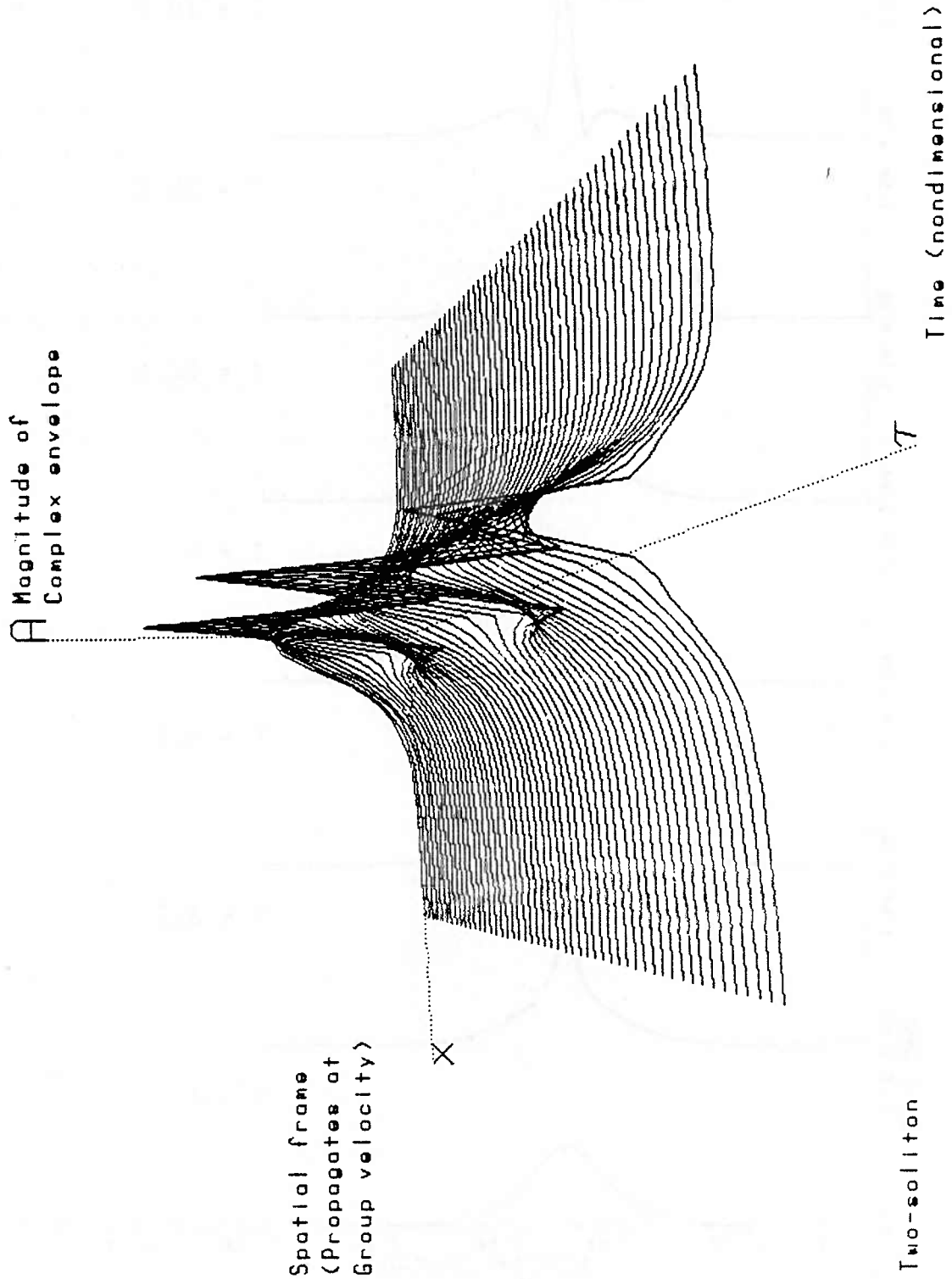
state containing two interacting solitons and one recurrence frequency. The initial condition, with $\sigma = 2$, is

$$f(\xi) = \operatorname{sech}(\sqrt{2} \xi / 2) \quad (3.47)$$

The first recurrence of the initial condition takes place at $\bar{t} = 12.6$. This case was first studied numerically by Chu and Mei [1971] who showed the initial development but not the long-time (recurrence) behavior. Roskes [1976] was the first to show numerically that this initial condition evolved into a nondivergent bound state.

Figure 3.7 shows the evolution for $-12.5 < \xi < 12.5$ and $0 < \bar{t} < 30$. The error at the final time step is .3 percent. Figures 3.8a and 3.8b show the amplitude and phase modulations. From the initial condition the soliton evolves to a narrower pulse of twice the height with symmetric sidelobes ($\bar{t} = 6.3$). Between the sidelobes and the central pulse we see nodes or zeroes in amplitude. The initial phase is uniform and zero. It is seen to modulate ($\bar{t} = 3.2$) and then return to uniform except for 2 discontinuities: a jump of π connects 2 sides of nearly constant phase. The jumps occur in ξ at the location of the amplitude nodes. In the complex plane this means that A has constant phase angle and passes through the origin so that there is no discontinuity in derivative across the node.

Fig. 3.7 Numerical evolution of a two-soliton initial profile. The magnitude of the complex envelope is plotted in a spatial frame that propagates at the linear group velocity, $-12.5 < X < 12.5$. The length of the time evolution corresponds to $T = 30$.



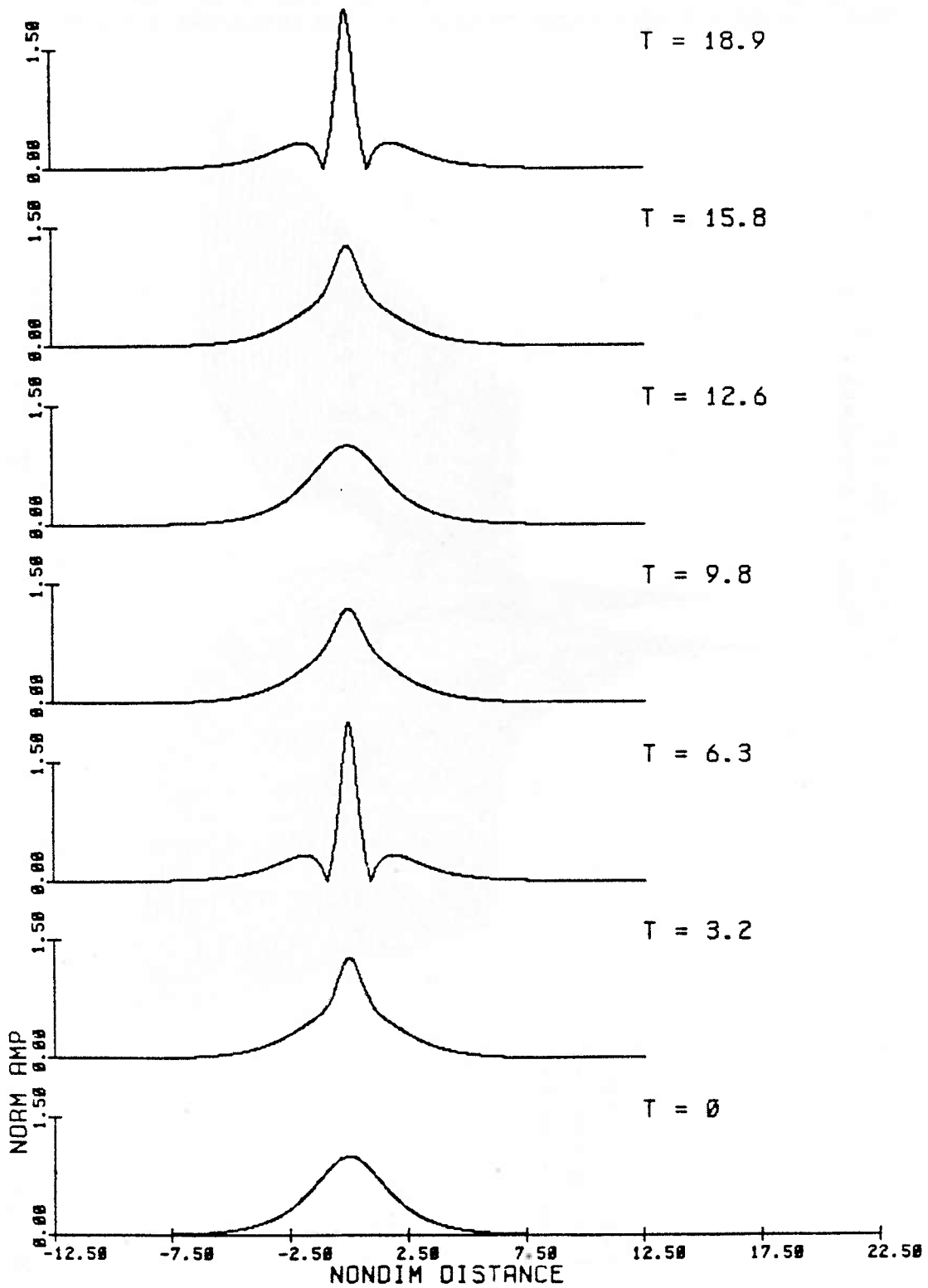


Fig. 3.8a Evolution of the magnitude of the complex envelope plotted at 7 successive time steps (time increases upwards) for the 2-soliton initial condition.

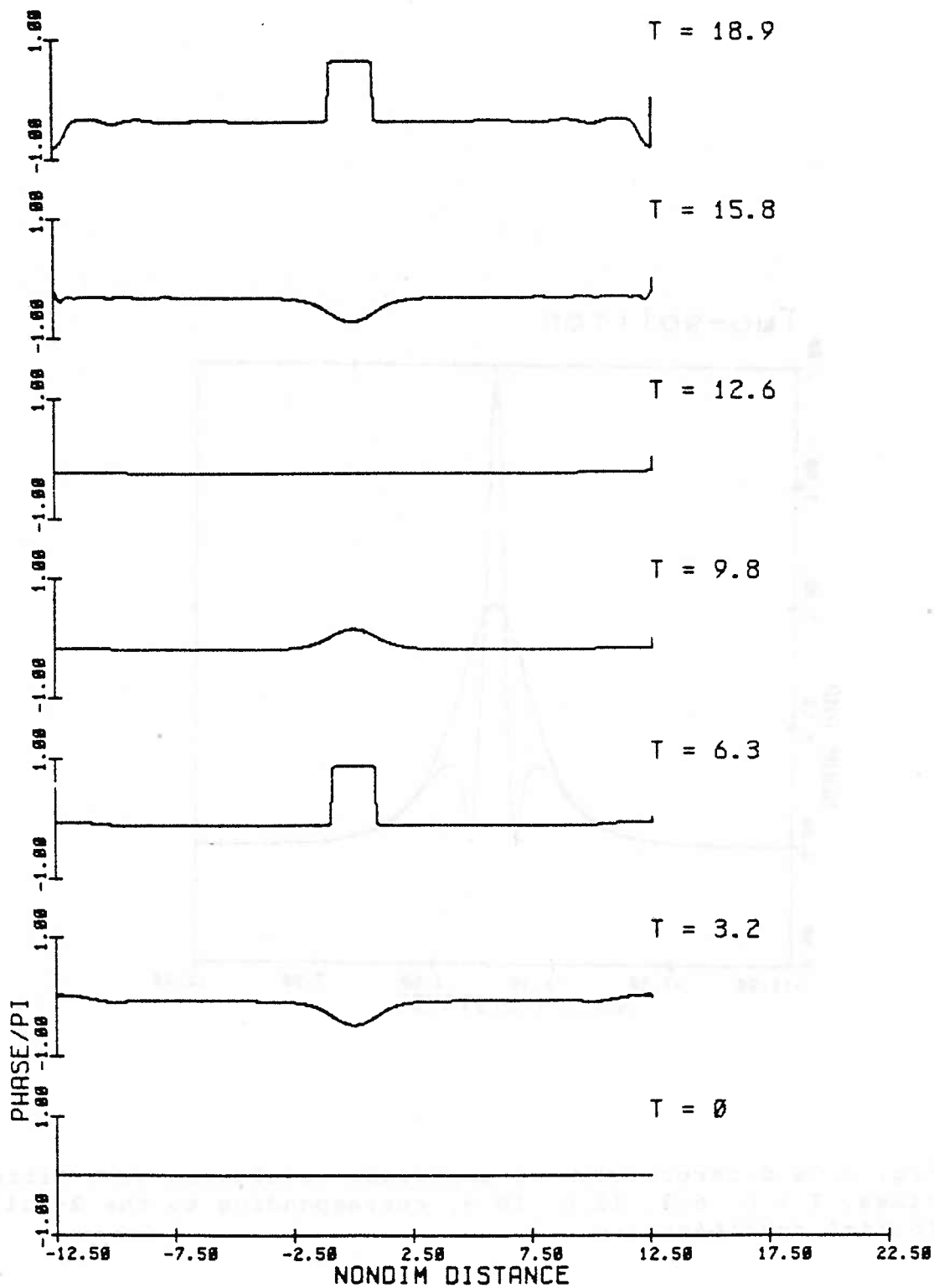


Fig. 3.8b Evolution of the principal value of the phase modulation, normalized by π , at 7 successive time steps corresponding to the amplitude modulation of fig. 3.8a.

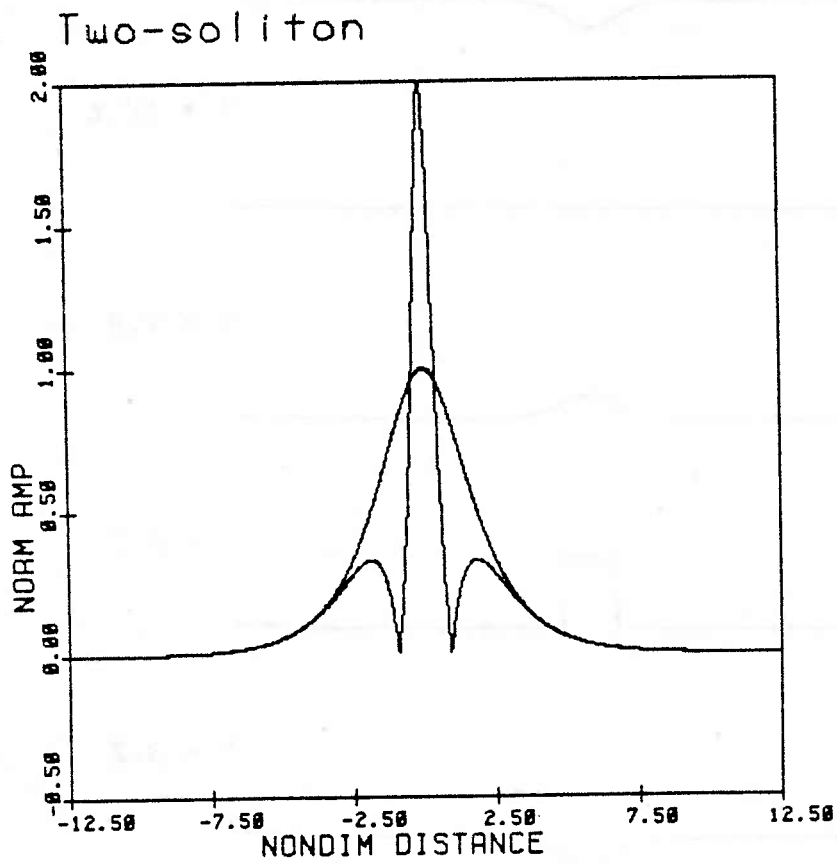


Fig. 3.9a Superposition of amplitude modulation at 4 different times, $T = 0, 6.3, 12.6, 18.9$, corresponding to the 2-soliton initial condition.

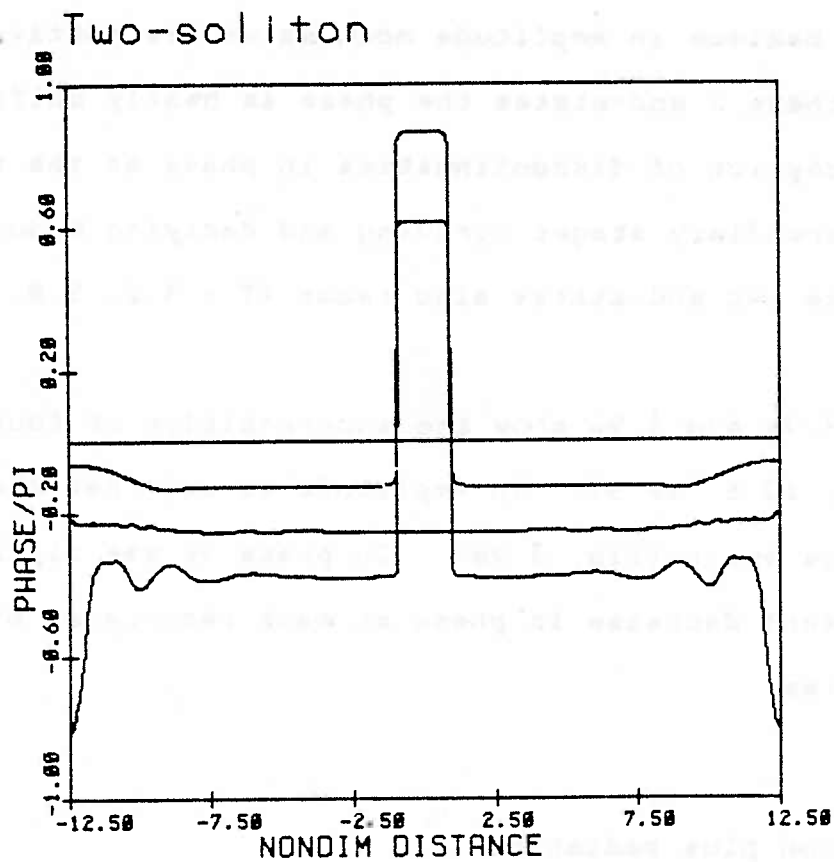


Fig. 3.9b Superposition of phase modulation at 4 different times, $T = 0, 6.3, 12.6, 18.9$, corresponding to the amplitude modulation superposition of fig. 3.9a.

The phase modulates again ($\tau = 9.8$) as the solitons interact to reconstruct the initial condition at $\tau = 12.6$. The phase is again uniform but with a small constant phase shift as in the evolution of the one-soliton. The oscillation is seen to go back and forth between two end-states: the initial condition and the narrower, steeper pulse with sidelobes (the minimum and maximum in amplitude modulation, respectively). At each of these 2 end-states the phase is nearly uniform, with the exception of discontinuities in phase at the nodes of A. The intermediary stages (growing and decaying modulation) between these two end-states also recur ($T = 3.2, 9.8, 15.8$).

Figs. 3.9a and 3.9b show the superposition of four times ($T = 0, 6.3, 12.6, 18.9$). In amplitude we see that the recurrence is exact (fig. 3.9a). In phase we see clearly the small, constant decrease in phase at each recurrence of the two end-states.

3.4.4 Soliton plus radiation

The next example is for an initial condition that represents a soliton plus radiation. The initial condition takes the form ($\sigma = 3/2$):

$$f(\xi) = \operatorname{sech}(2\sqrt{2}\xi/3) \quad (3.48)$$

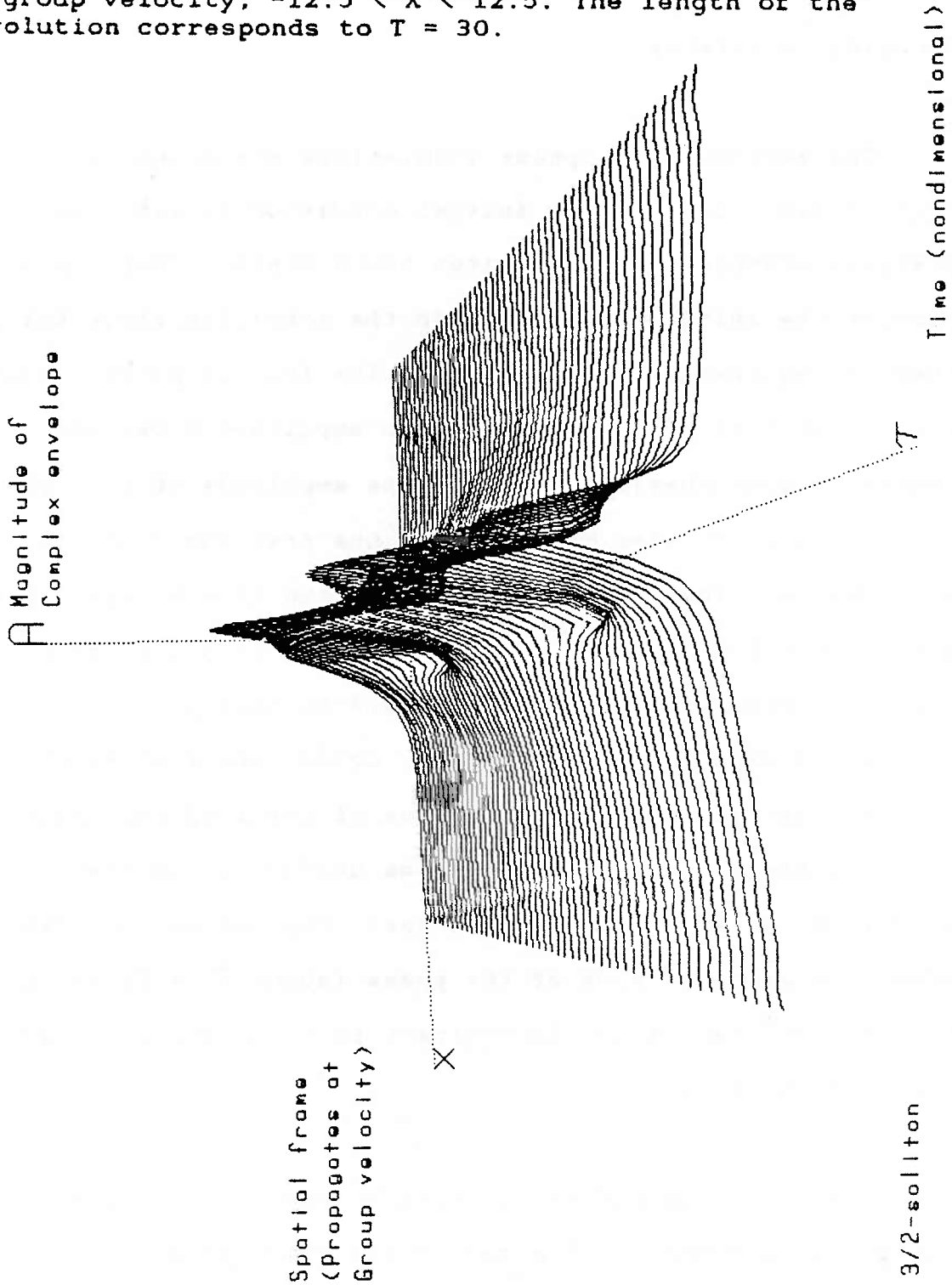
The full solution can be seen for $-12.5 < \xi < 12.5$ and $0 <$

$T < 30$ in figure 3.10. The overall picture shows a slowly decaying recurrence.

The amplitude and phase modulations are shown in figs. 3.11a - 3.11d. The initial condition is like the previous example for a 2-soliton bound state. There is more mass in the initial pulse than in the 1-soliton state but less than is required for a 2-soliton. The initial pulse evolves into a narrower, steeper pulse with amplitude nodes and symmetric sidelobes at $T = 6.3$. The amplitude of this steeper pulse is 1.5, smaller than that of the previous 2-soliton which was 2. The initial phase evolution is also similar to that of the 2-soliton. The phase evolves from initially uniform (zero) to modulated at $T = 3.2$ to nearly uniform again at $T = 6.3$ except for jumps of π connecting 2 sides of nearly equal phase at the locations of the amplitude nodes. However, the phase is not nearly as uniform as in the 2-soliton case; we clearly see small ripples in the phase. Also, the central value of the phase (about $\xi = 0$) is lower than the initial value, in contrast to the 2-soliton case where it is higher.

There is a damped oscillation between the 2 end-states of the previous example. The center amplitude decays slowly with time, approaching its asymptotic 1-soliton state of nearly uniform phase. The decay is not monotone. We see evidence of

Fig. 3.10 Numerical evolution of a soliton plus radiation (3/2-soliton) initial profile. The magnitude of the complex envelope is plotted in a spatial frame that propagates at the linear group velocity, $-12.5 < X < 12.5$. The length of the time evolution corresponds to $T = 30$.



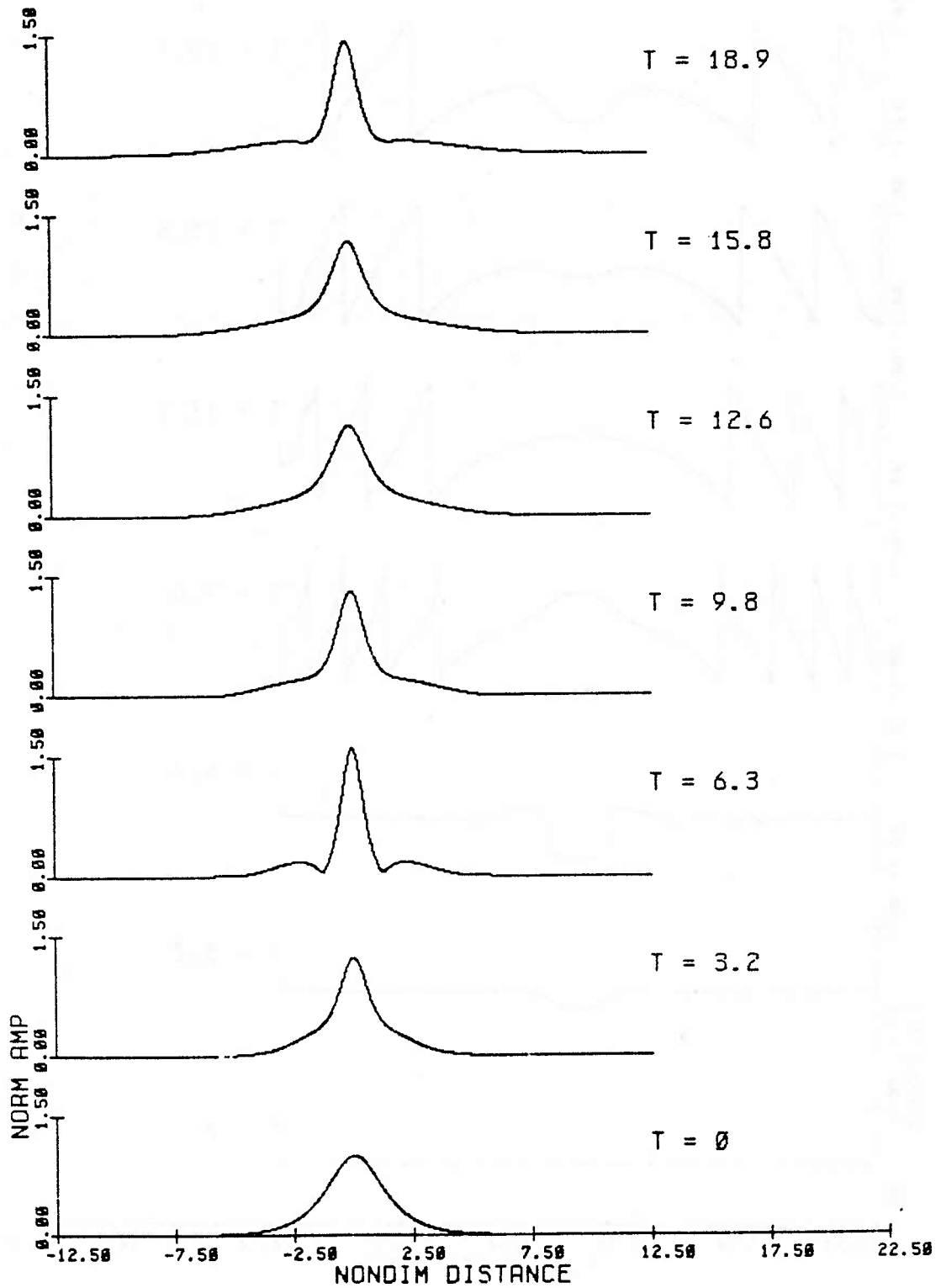


Fig. 3.11a Evolution of the magnitude of the complex envelope plotted at 7 successive time steps (time increases upwards) for the 3/2-soliton initial condition.

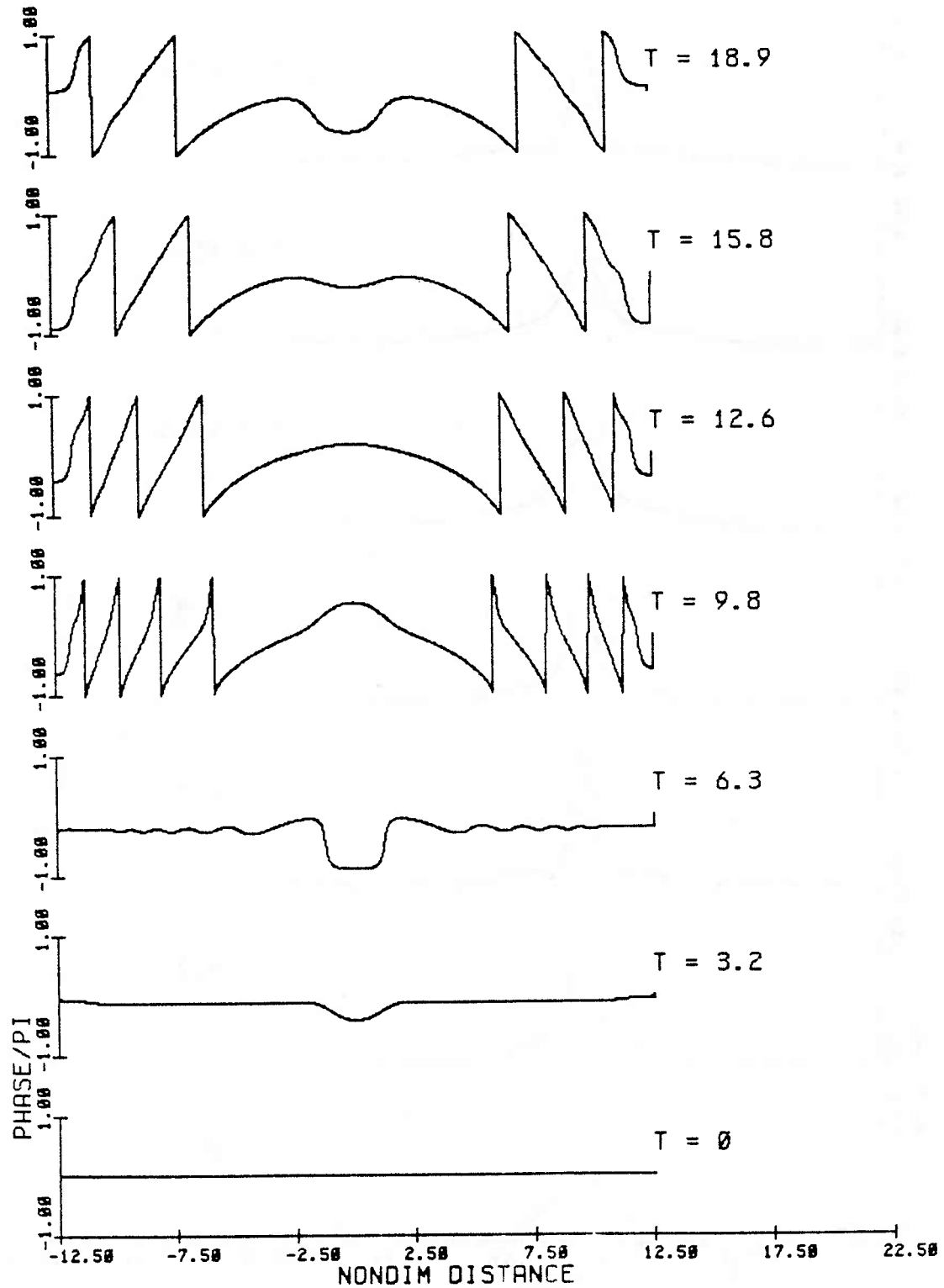


Fig. 3.11b Evolution of the principal value of the phase modulation, normalized by pi, at 7 successive time steps corresponding to the amplitude modulation of fig. 3.11a.

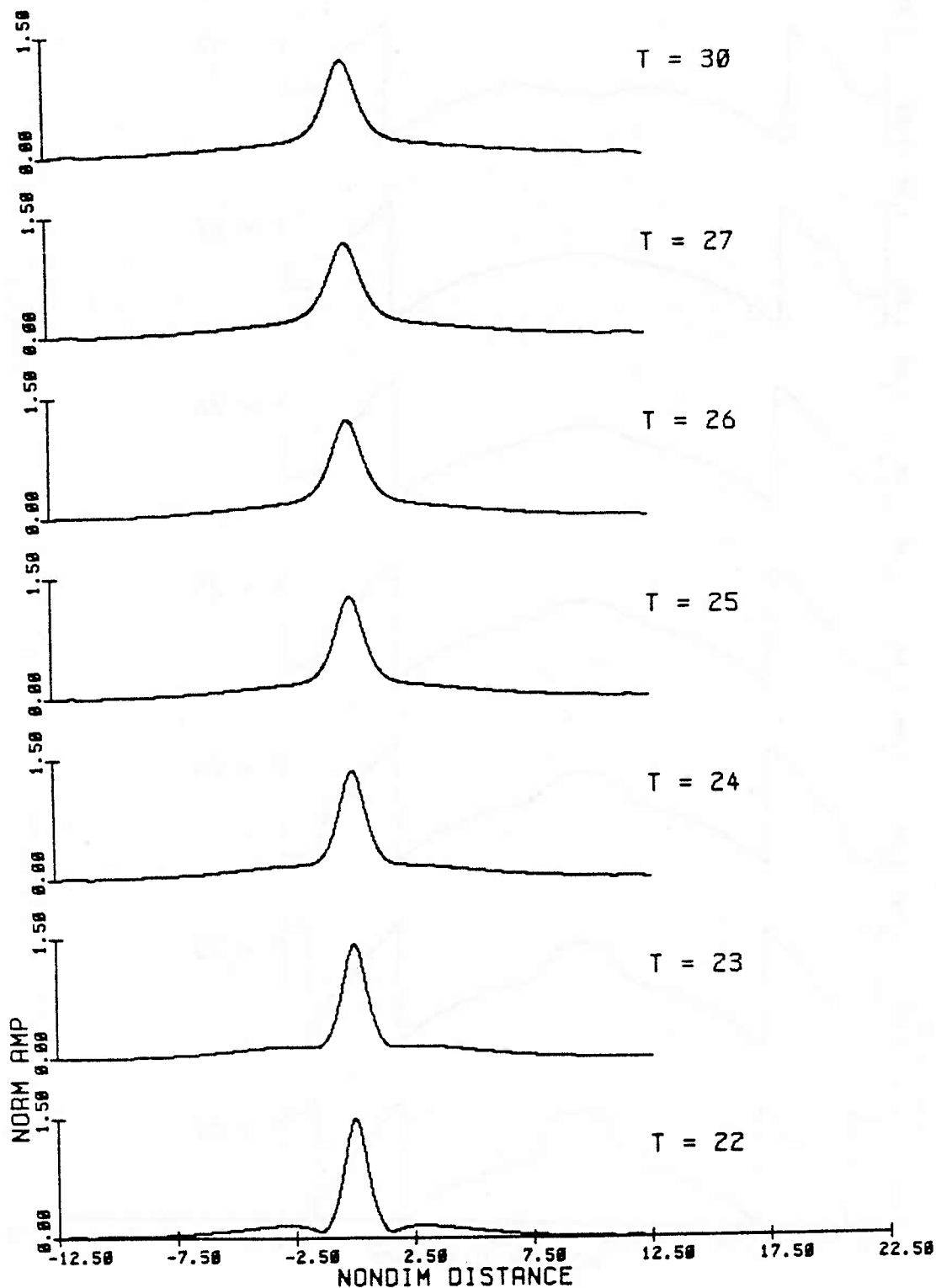


Fig. 3.11c Further evolution of the magnitude of the complex envelope plotted at 7 successive time steps (time increases upwards) for the 3/2-soliton initial condition.

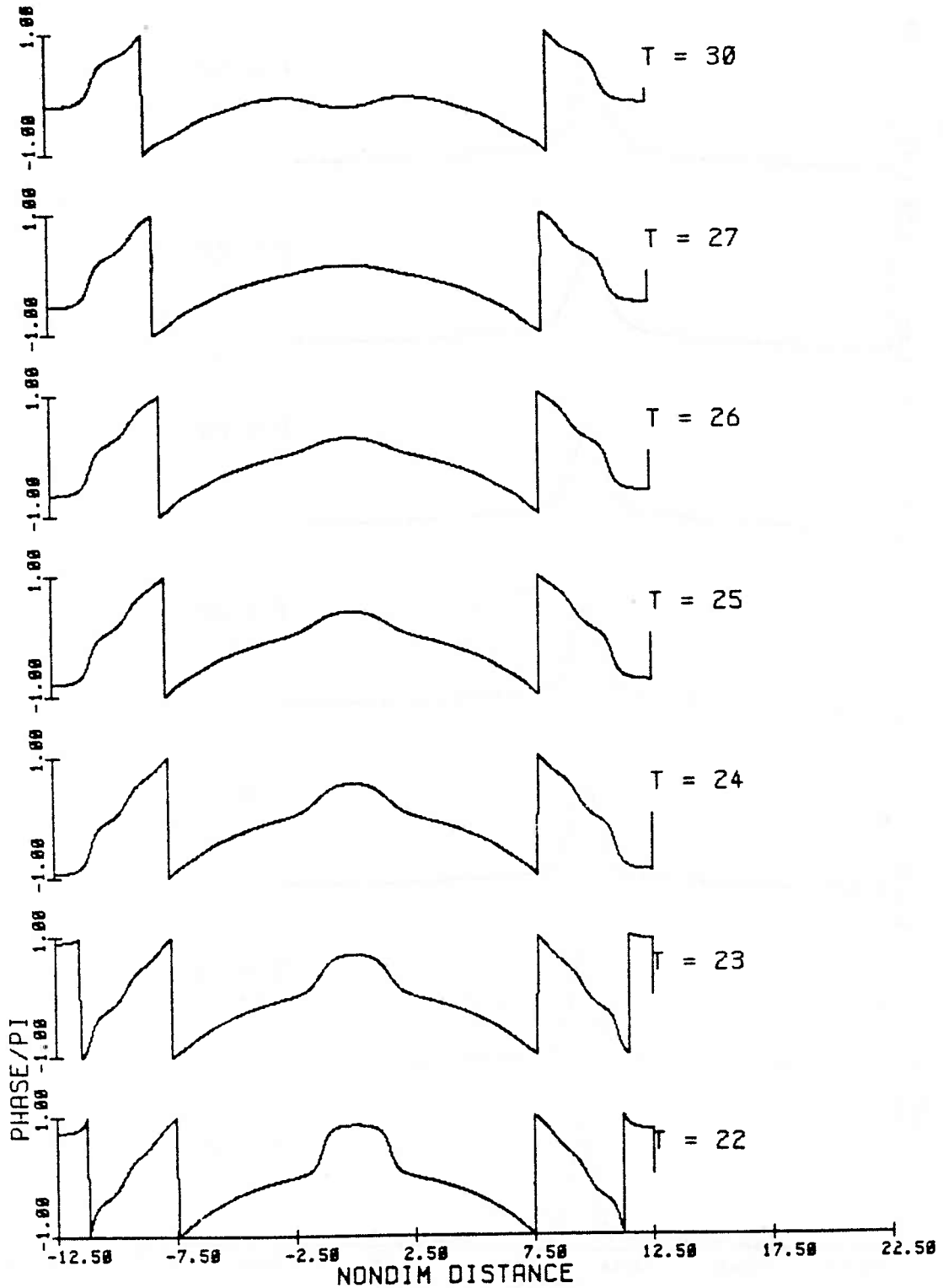


Fig. 3.11d Further evolution of the principal value of the phase modulation, normalized by pi, at 7 successive time steps corresponding to the amplitude modulation of fig. 3.11c.

another partial recurrence of the steep narrow pulse in fig. 3.10 and in figs. 3.11c and 3.11d at $T = 22$. The center amplitude is slightly less than at $T = 6.3$, and the sidelobes are more spread due to the dispersive tail. The phase has jumps at the locations of the amplitude nodes. The time scale for this first quasi-recurrence is longer than in the previous example. At $T = 30$ which is the last time shown (fig. 3.11c), the asymptotic state has not yet been reached. The maximum amplitude is about 1.17, and the amplitude of the tail ($\xi \rightarrow \pm\infty$) is still larger than that of a 1-soliton. The radiation can best be seen in this growth in amplitude of the tail at a distance from the origin as in the case of pure radiation (fig. 3.3a). In contrast, the amplitude of the tail of the exact soliton solutions is constant and steady (figs. 3.6a and 3.9a).

In the phase modulation the central region of the phase (about $\xi = 0$), where the soliton behavior dominates, remains fairly uniform (slight curvature) with small constant shifts at successive times. There is a background of linear dispersion as seen from the symmetric decay (strong curvature) in the phase which dominates in the tail ($\xi \rightarrow \pm\infty$). With time, the phase modulation is seen to flatten as the linearly dispersive components radiate away, and the soliton asymptotically approaches the uniform phase of the 1-soliton.

3.4.5 Bound state plus radiation

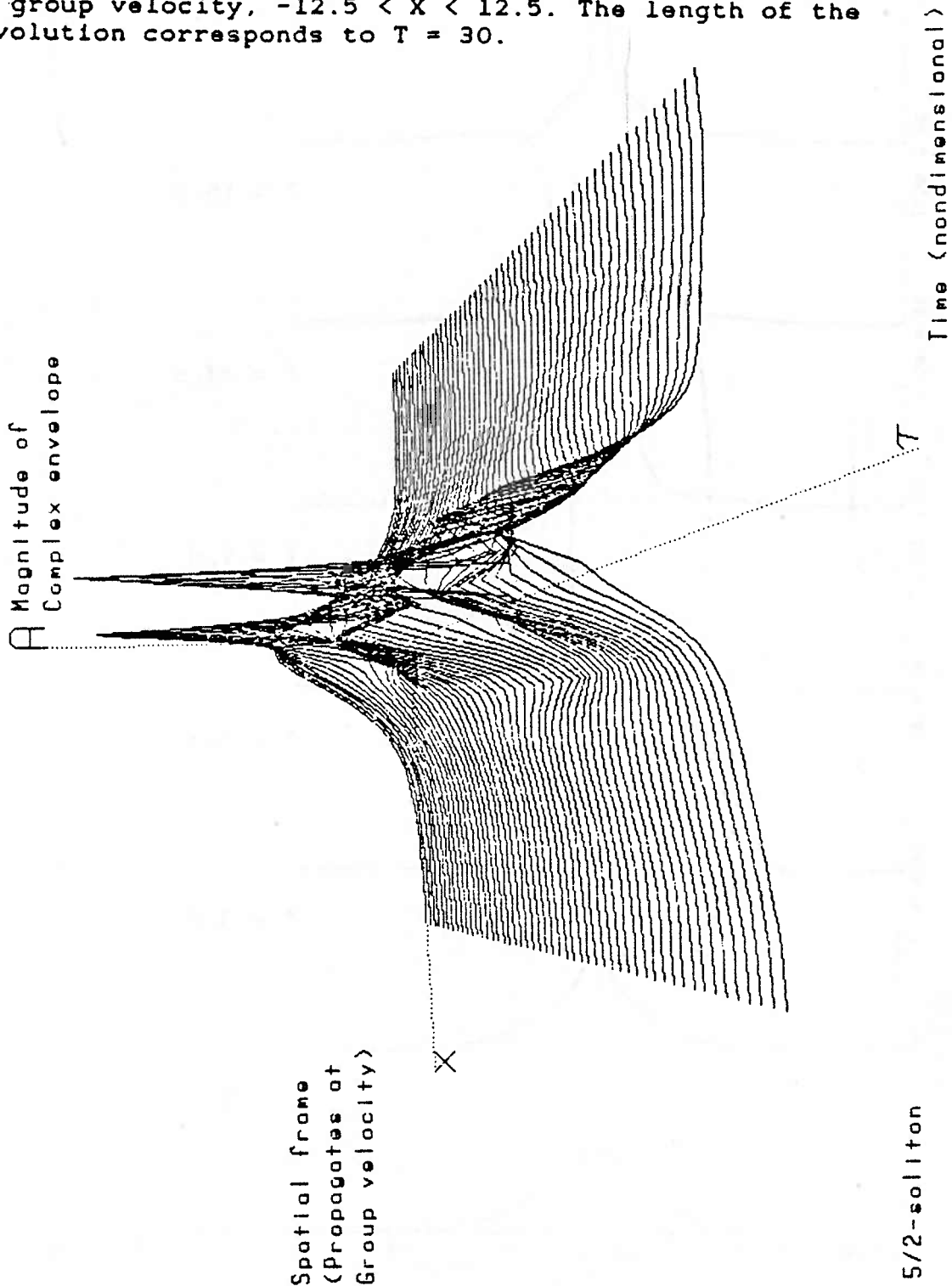
The next example is for an initial condition that yields a bound state plus radiation. The initial condition is ($\sigma = 5/2$):

$$f(\zeta) = \operatorname{sech}(2\sqrt{2} \zeta/5) \quad (3.49)$$

The overall evolution is shown in figure 3.12 where we see approximately two recurrence cycles. The evolution is similar to the previous two examples of 2-soliton and 3/2-soliton. The recurrence time scales are slightly different in each of the three cases. This can be seen from the full solutions and from comparing them at fixed times (the amplitude and phase modulations for the 5/2-soliton are shown in fig. 3.13). The times chosen are optimal for seeing the recurrence of the 2 end-states of the 2-soliton bound state.

The evolution is best distinguished by the phase (figs. 3.13b, 3.13d). The large jumps of 2π result from using the principal value of the arctangent; the phase is continuous at these points. We still see the jump of π at the node locations when $T = 6.3$ (figs. 3.13a, 3.13b). The background of linear dispersion is evidenced by the symmetric decay (strong curvature in the phase) that dominates in the tail.

Fig. 3.12 Numerical evolution of a bound state plus radiation (5/2-soliton) initial profile. The magnitude of the complex envelope is plotted in a spatial frame that propagates at the linear group velocity, $-12.5 < X < 12.5$. The length of the time evolution corresponds to $T = 30$.



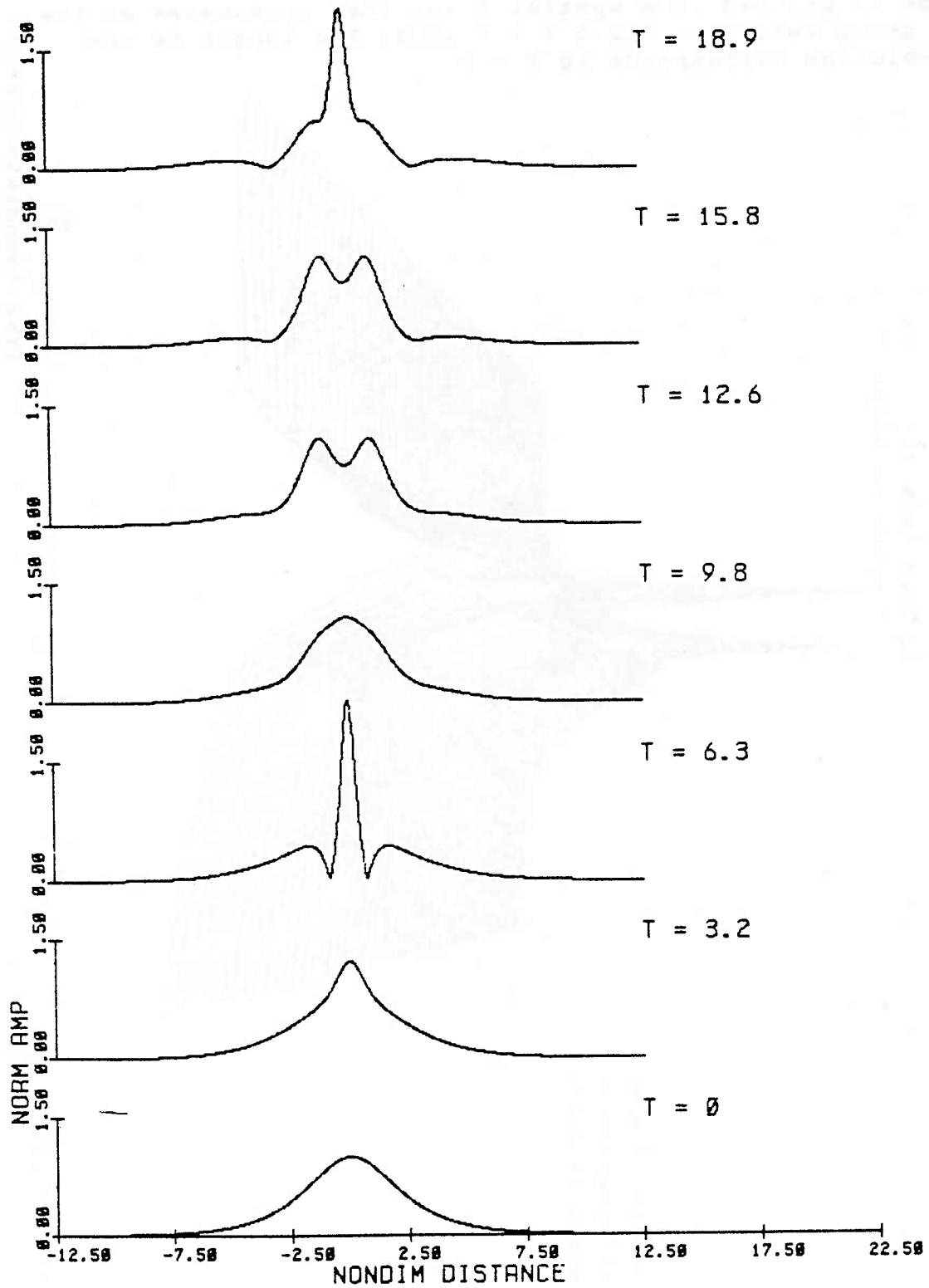


Fig. 3.13a Evolution of the magnitude of the complex envelope plotted at 7 successive time steps (time increases upwards) for the 5/2-soliton initial condition.

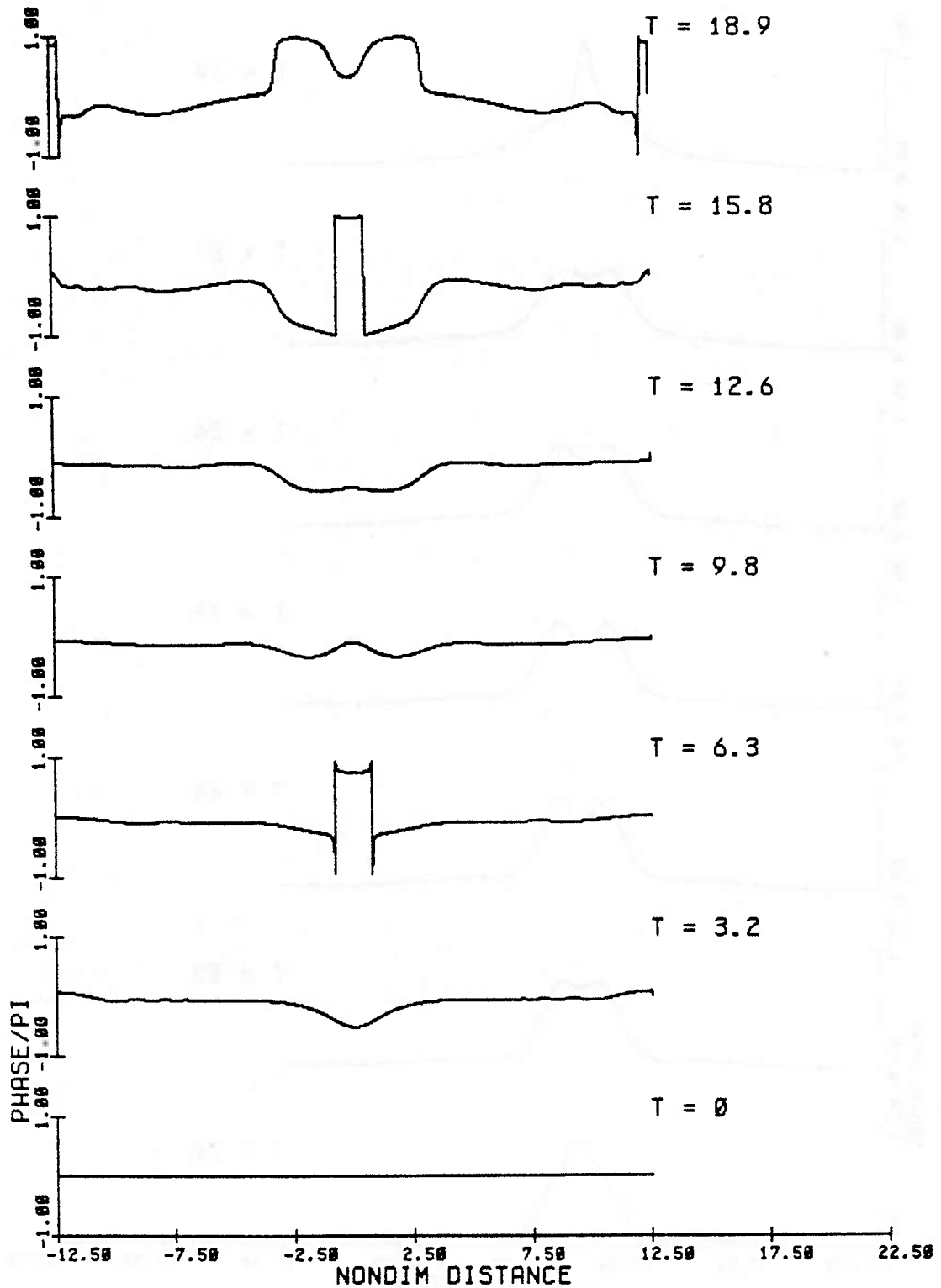


Fig. 3.13b Evolution of the principal value of the phase modulation, normalized by pi, at 7 successive time steps corresponding to the amplitude modulation of fig. 3.13a.

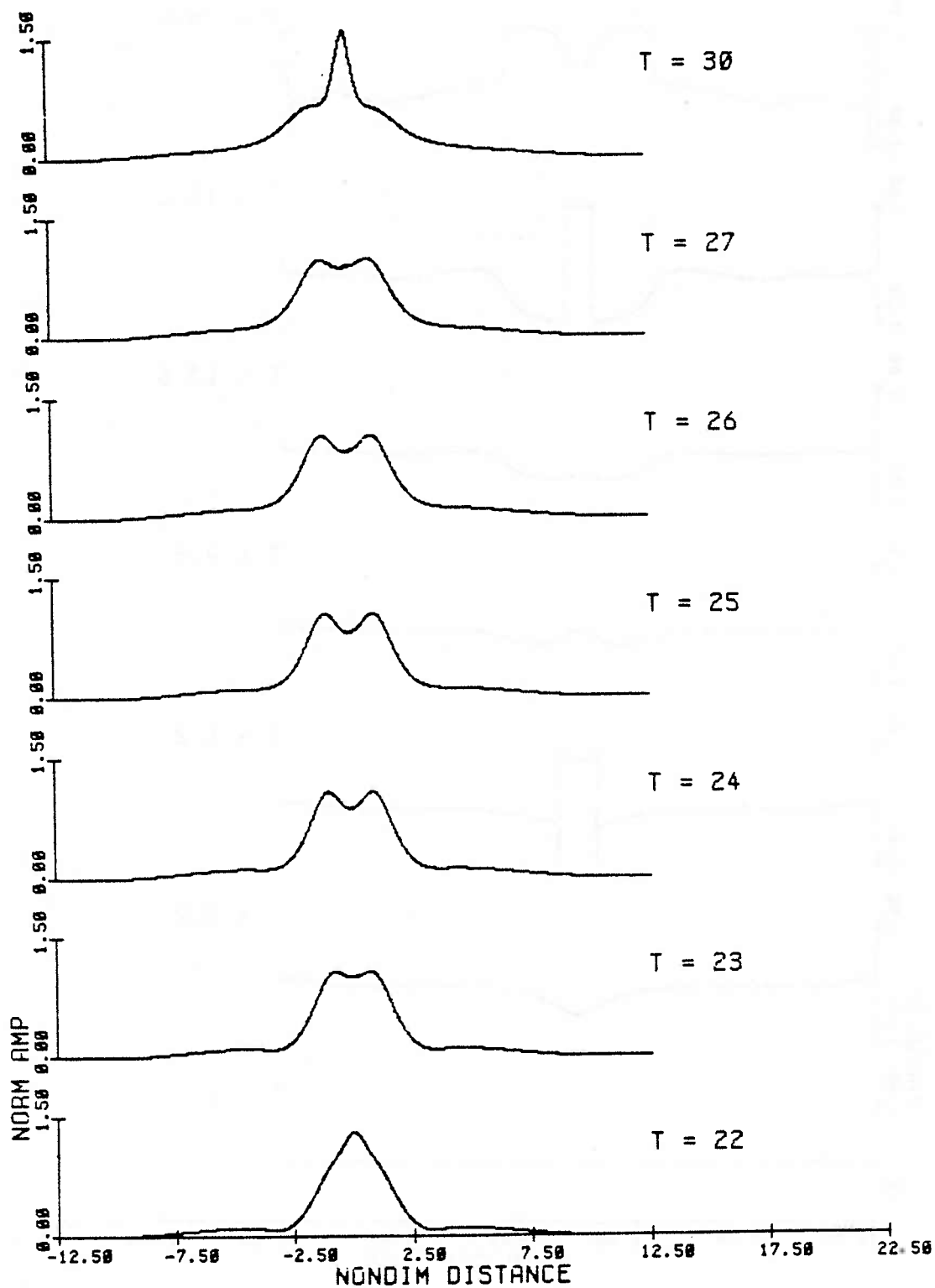


Fig. 3.13c Further evolution of the magnitude of the complex envelope plotted at 7 successive time steps (time increases upwards) for the 5/2-soliton initial condition.

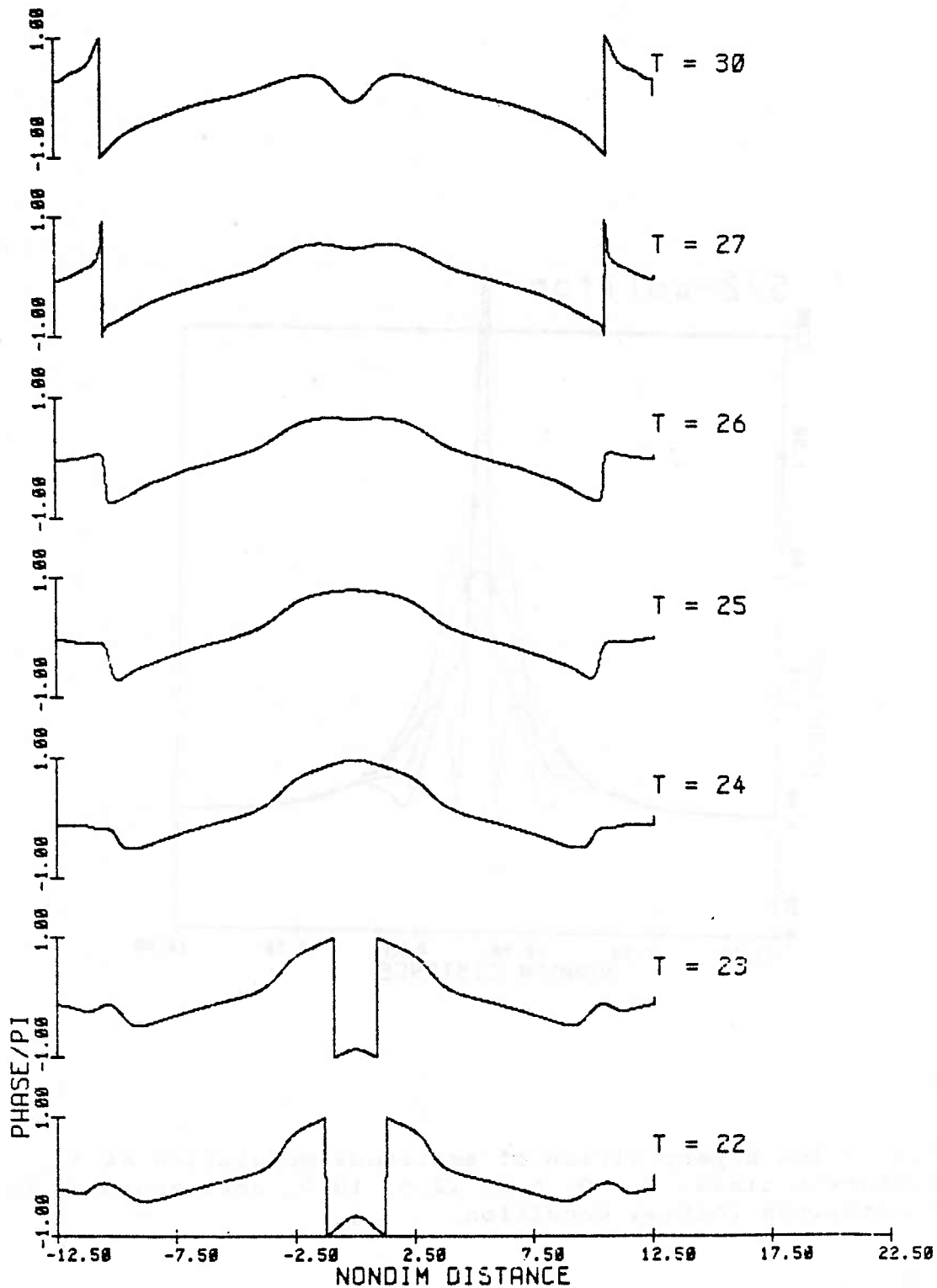


Fig. 3.13d Further evolution of the principal value of the phase modulation, normalized by pi, at 7 successive time steps corresponding to the amplitude modulation of fig. 3.13c.

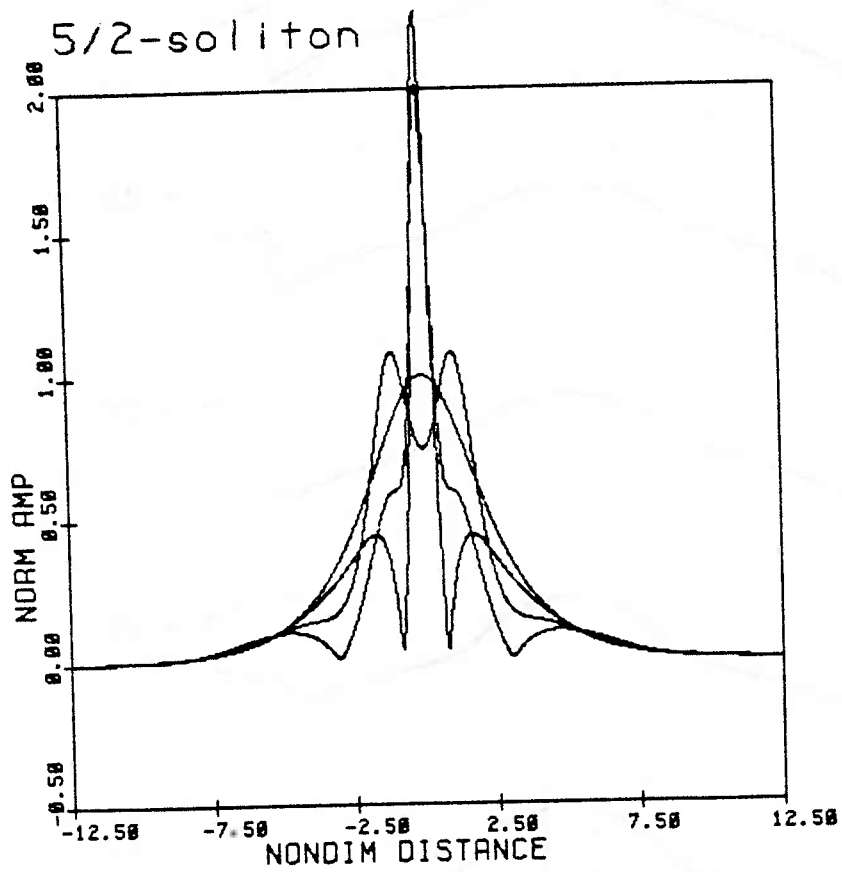


Fig. 3.14a Superposition of amplitude modulation at 4 different times, $T = 0, 6.3, 12.6, 18.9$, corresponding to the 5/2-soliton initial condition.

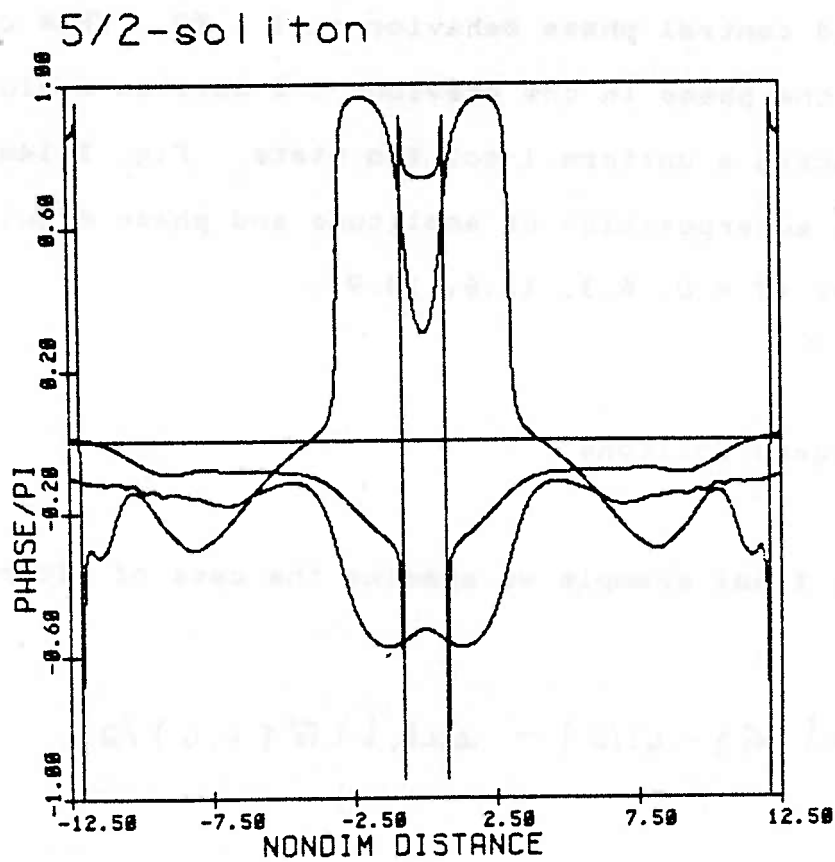


Fig. 3.14b Superposition of phase modulation at 4 different times, $T = 0, 6.3, 12.6, 18.9$, corresponding to the amplitude modulation superposition of fig. 3.14a.

The bound state interaction is characterized, as in fig. 3.8b, by an oscillation between 2 end-states of maximum and minimum amplitude modulation. The phase is nearly uniform at the extremes of amplitude modulation ($T = 0, 6.3, 23$) and is modulated during the transitions ($T = 3.2, 18.9, 30$). That the 2-soliton interaction is still occurring is evidenced in the modulated central phase behavior at $T = 30$. This can be compared to the phase in the previous 3/2-soliton evolution which approached a uniform 1-soliton state. Fig. 3.14a and 3.14b show a superposition of amplitude and phase modulations at four times ($T = 0, 6.3, 12.6, 18.9$).

3.4.6 Divergent solitons

For our final example we examine the case of divergent solitons

$$f(\xi) = \operatorname{sech}[(\sqrt{2}\xi - .6)/2] - \operatorname{sech}[(\sqrt{2}\xi + .6)/2] \quad (3.50)$$

This case was first examined numerically by Satsuma and Yajima (1974) and is shown in fig. 5 of their paper. The initial condition is antisymmetric and yields two divergent solitons of equal amplitude and equal but opposite velocities. Figure 3.15 shows the evolution. Figures 3.16a-3.16d show the amplitude and phase evolution at various times.

Fig. 3.15 Numerical evolution of divergent solitons from an antisymmetric initial profile corresponding to figure 5 of Satsuma and Yajima (1974). The magnitude of the complex envelope is plotted in a spatial frame that propagates at the linear group velocity, $-12.5 < X < 12.5$. The length of the time evolution corresponds to $T = 30$.

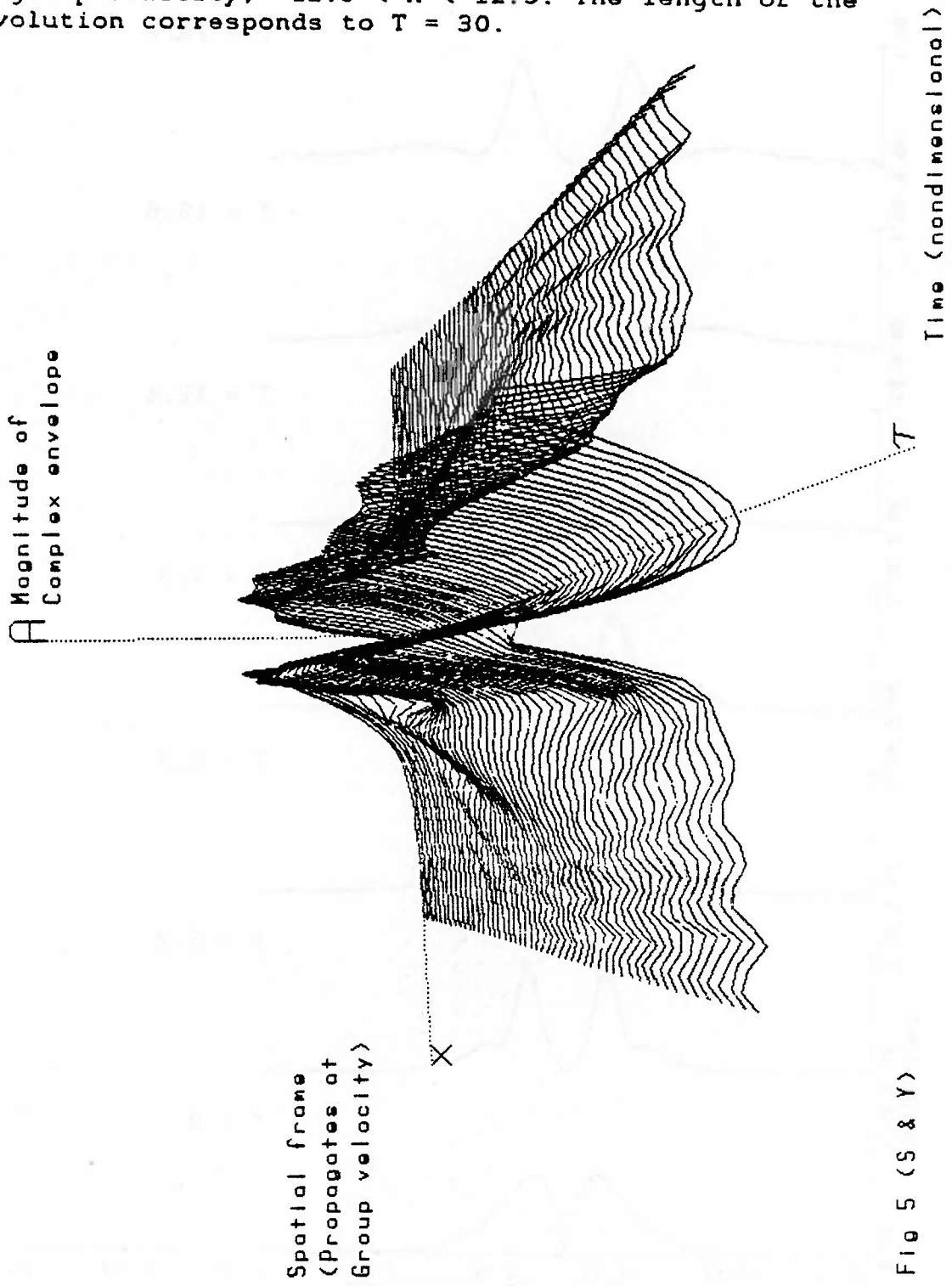


Fig 5 (S & Y)

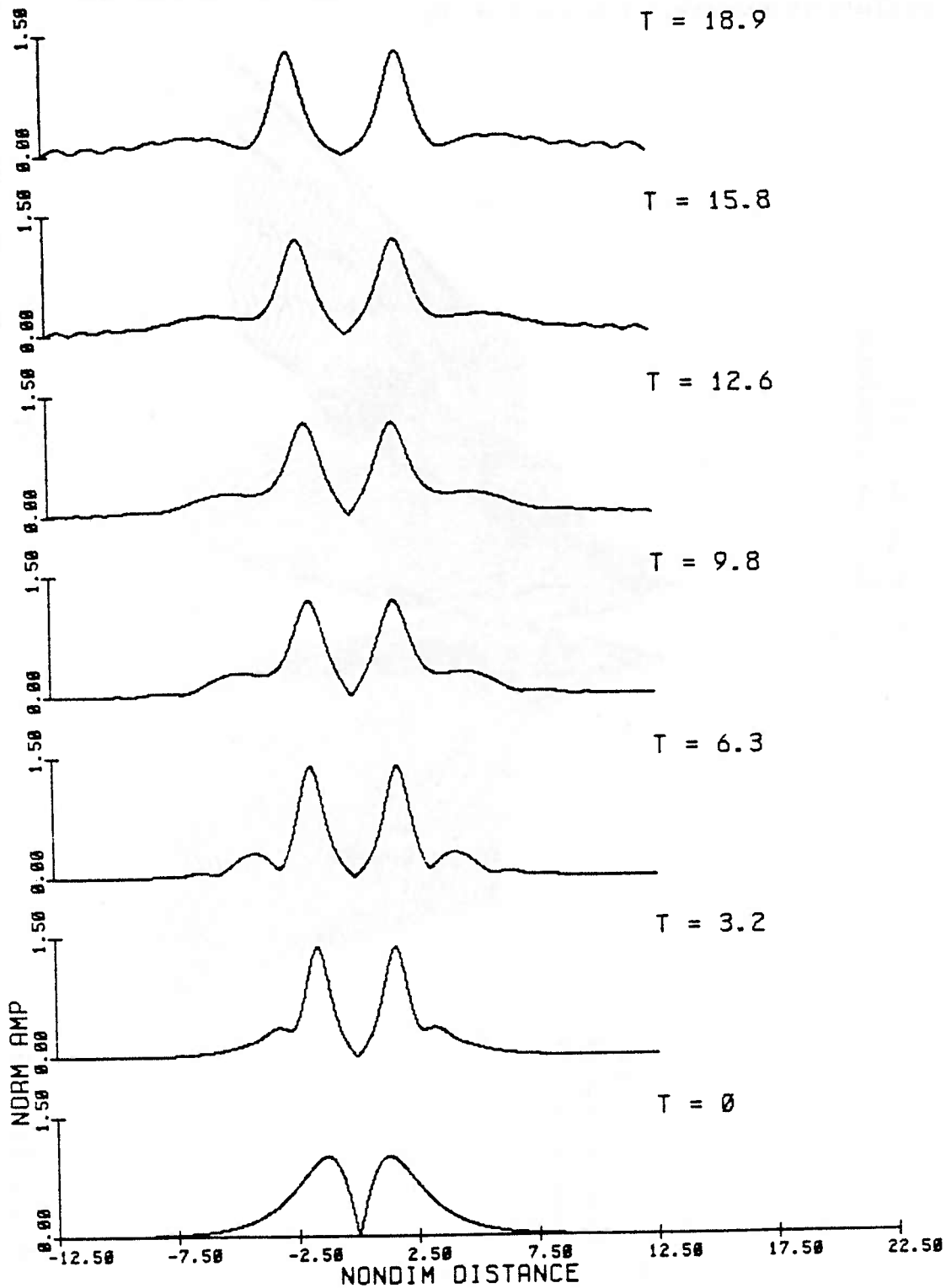


Fig. 3.16a Evolution of the magnitude of the complex envelope plotted at 7 successive time steps (time increases upwards) for the divergent soliton initial condition.

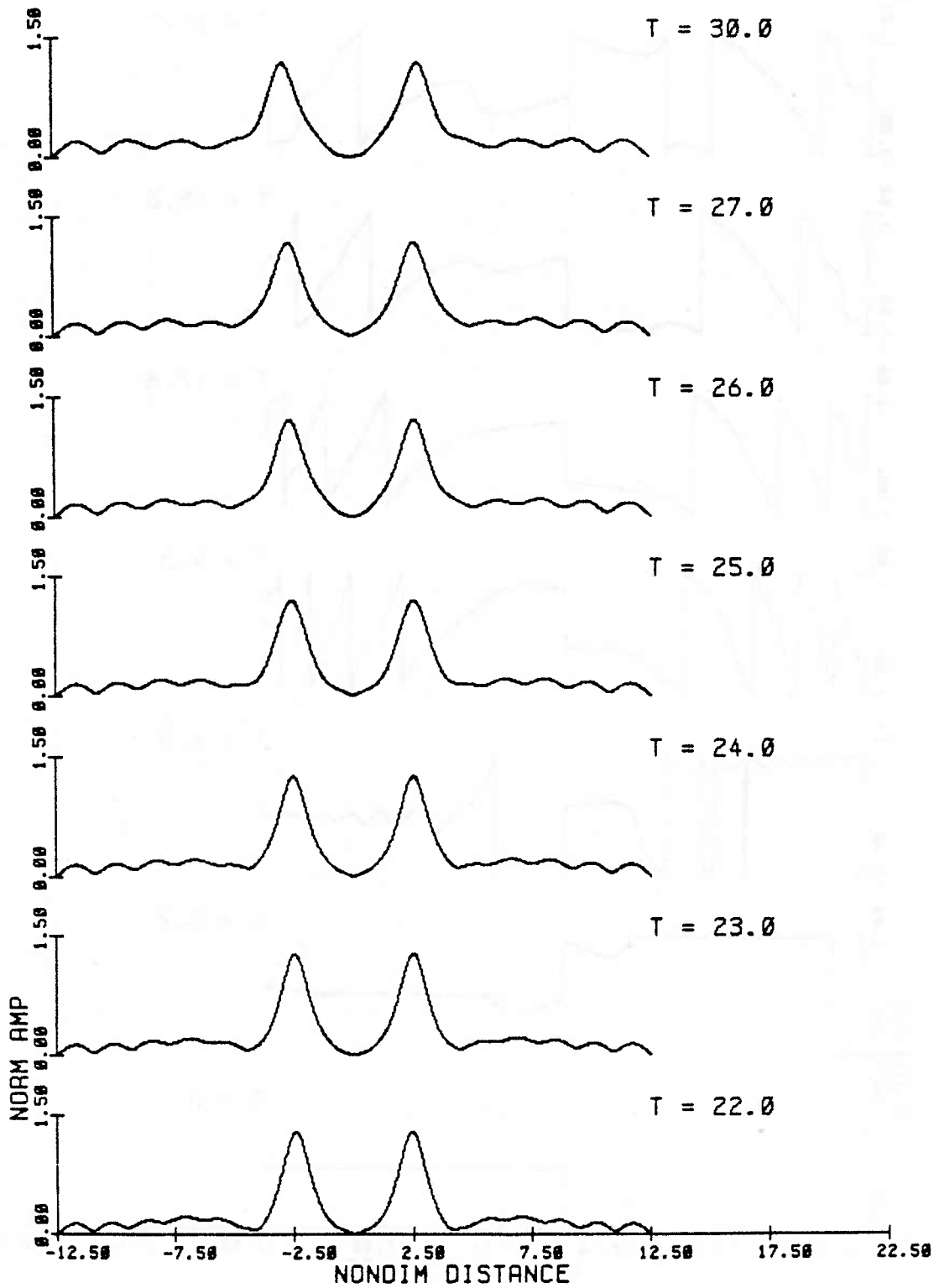


Fig. 3.16b Further evolution of the magnitude of the complex envelope plotted at 7 successive time steps (time increases upwards) for the divergent soliton initial condition.

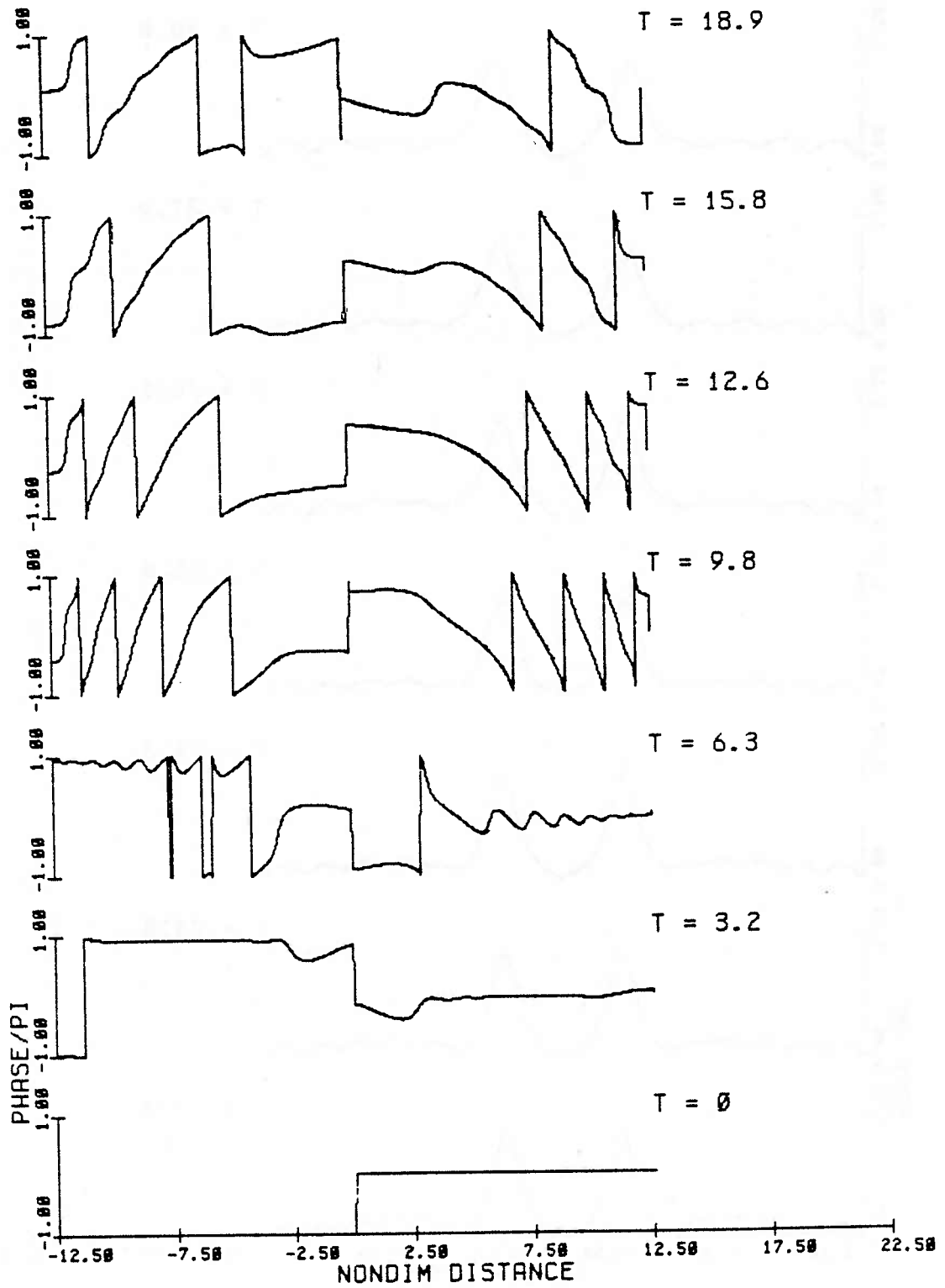


Fig. 3.16c Evolution of the principal value of the phase modulation, normalized by pi, at 7 successive time steps corresponding to the amplitude modulation of fig. 3.16a.

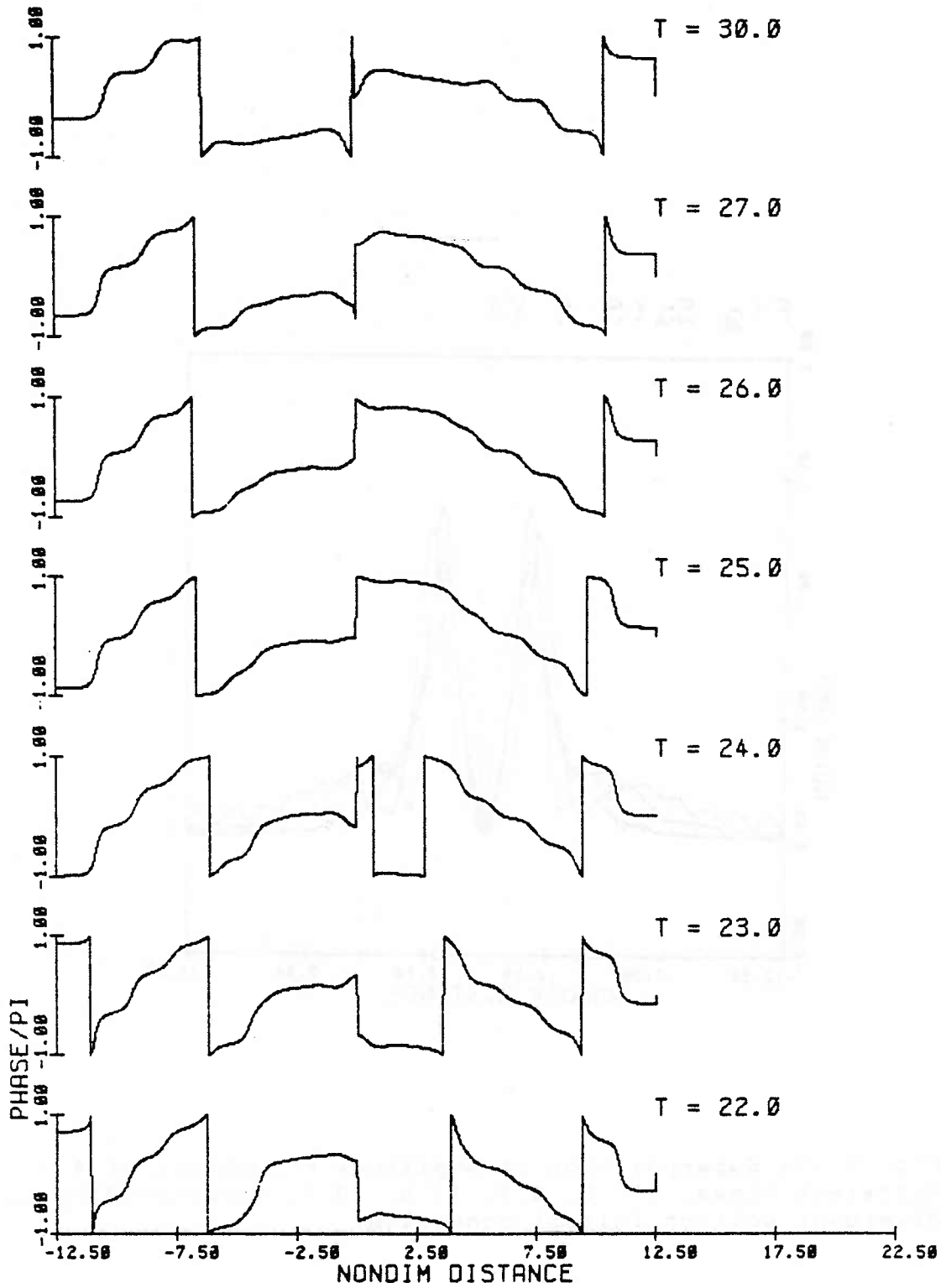


Fig. 3.16d Further evolution of the principal value of the phase modulation, normalized by pi, at 7 successive time steps corresponding to the amplitude modulation of fig. 3.16b.

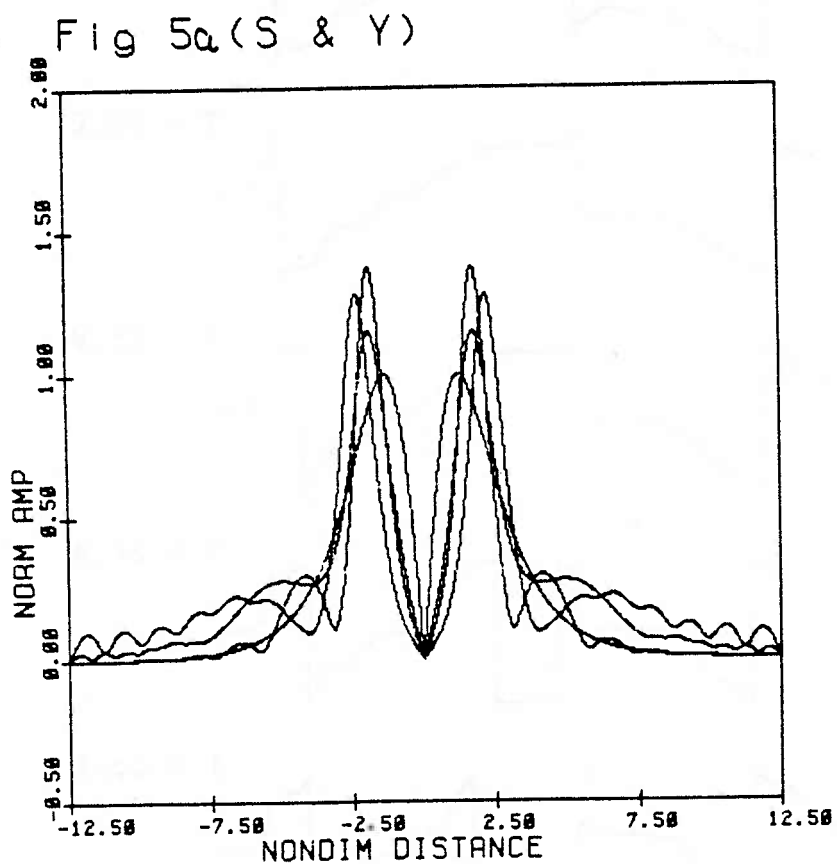


Fig. 3.17a Superposition of amplitude modulation at 4 different times, $T = 0, 6.3, 12.6, 18.9$, corresponding to the divergent soliton initial condition.

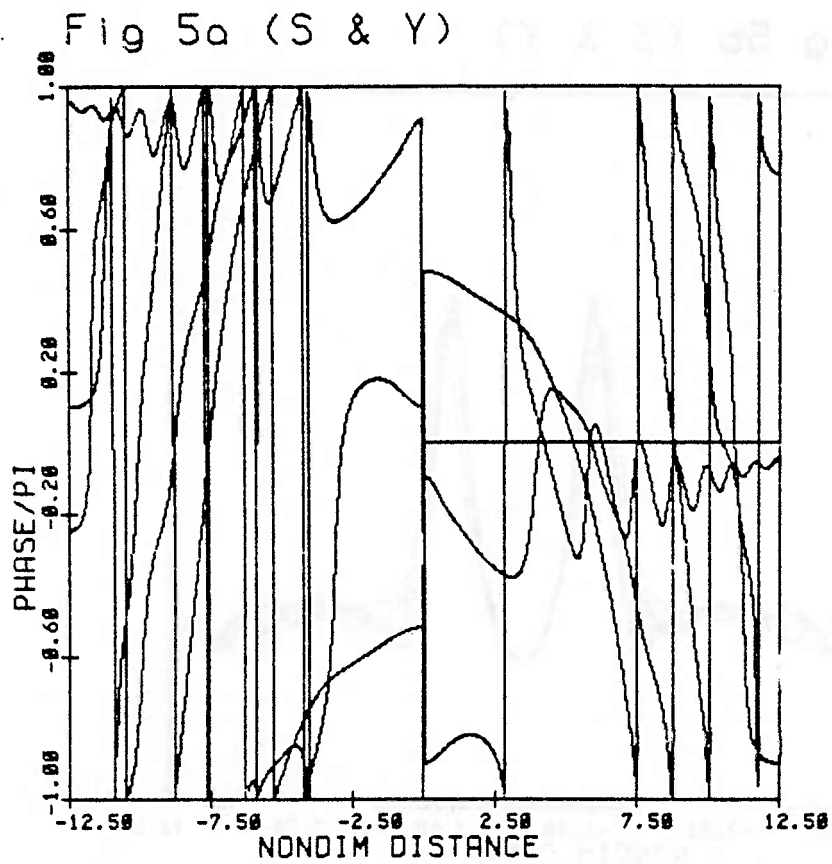


Fig. 3.17b Superposition of phase modulation at 4 different times, $T = 0, 6.3, 12.6, 18.9$, corresponding to the amplitude modulation superposition of fig. 3.17a.

Fig 5b (S & Y)

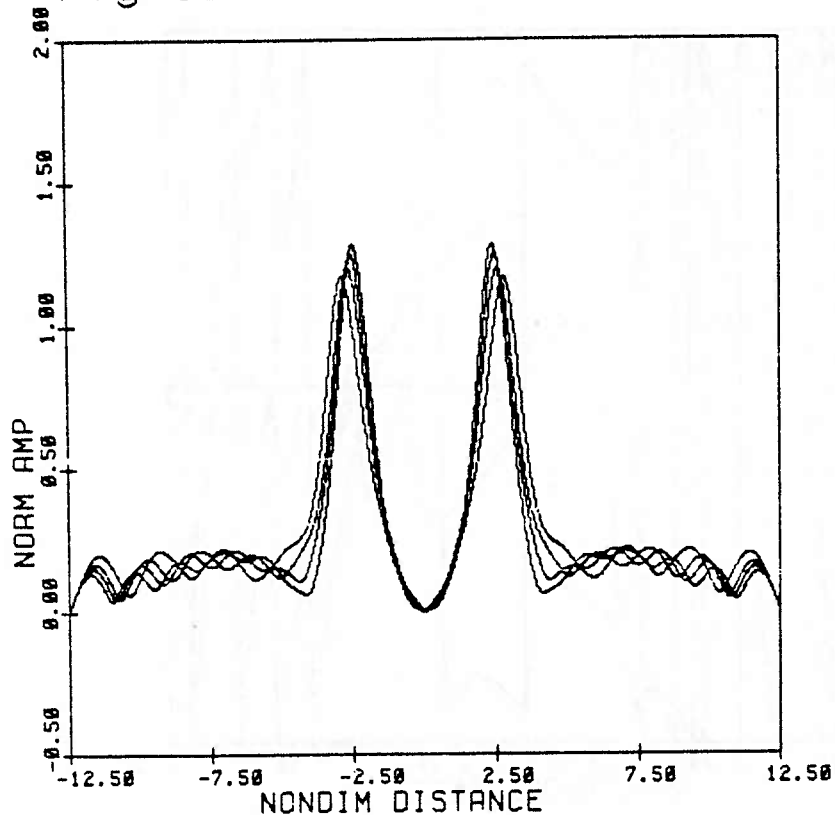


Fig. 3.17c Superposition of amplitude modulation at 4 different times, $T = 22, 24, 26, 30$, corresponding to the divergent soliton initial condition.

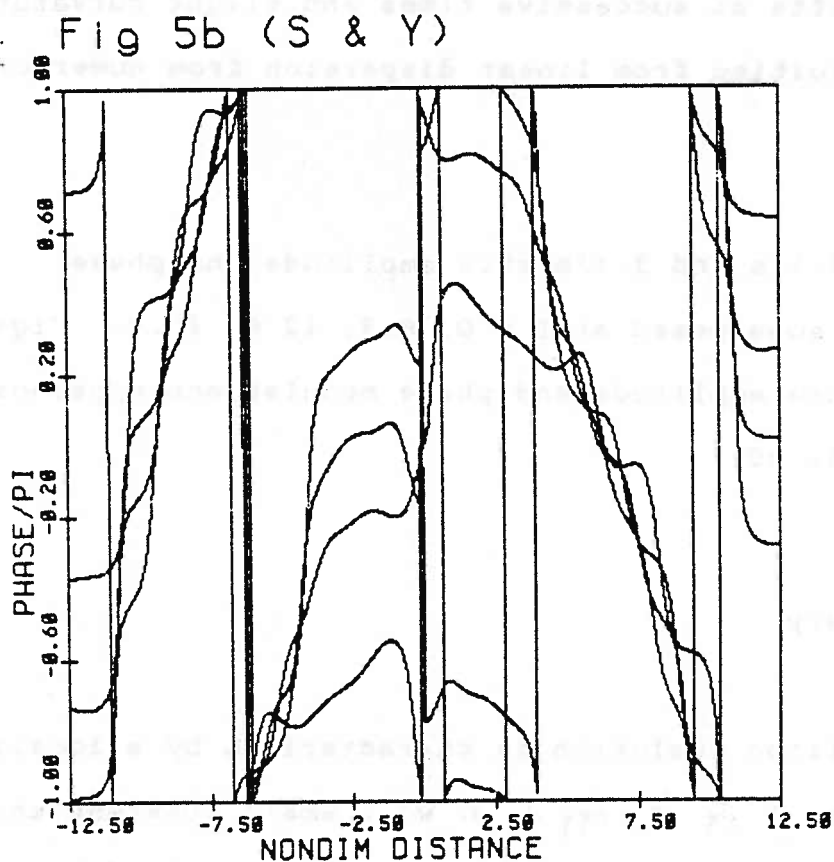


Fig. 3.17d Superposition of phase modulation at 4 different times, $T = 22, 24, 26, 30$, corresponding to the amplitude modulation superposition of fig. 3.17c.

The phase evolution shows 2 uniform regions of phase corresponding to the 2 pulses with a jump of π connecting the 2 regions where the amplitude node occurs. The solitons do not interact, as evidenced by the amplitude modulation which is fairly steady and by the lack of phase modulation. The phase remains uniform in each of the two regions, with slight constant shifts at successive times and slight curvature at the edge resulting from linear dispersion from numerical noise.

Figs. 3.17a and 3.17b show amplitude and phase modulations superposed at $T = 0, 6.3, 12.6, 18.9$. Figs. 3.17c and 3.17d show amplitude and phase modulations superposed at $T = 22, 24, 26, 30$.

3.4.7 Summary

The soliton evolution is characterized by a locally uniform phase ($\dot{P}_\xi = \dot{P}_{\xi\xi} = 0$) with small constant shifts in time. The bound state evolution is characterized by a locally uniform phase ($\dot{P}_\xi = 0$) at times of minimum and maximum amplitude modulation. Undulations in phase occur during the growth and decay of modulation. Radiation is characterized by a negative curvature in the phase ($\dot{P}_{\xi\xi} < 0$).

3.5 INCLUSION OF DISSIPATION

An attempt was made to include dissipation in the model, and in particular to examine the effect that dissipation might have on the phase. The motivation behind this was to account for both frequency downshifting and dissipation, neither of which can be modelled using the inviscid NLS equation. Because the observed downshifting seems to be an irreversible process, dissipation seemed a strong candidate to account for it. Also, an examination of the effect of dissipation on phase did not appear to have been investigated.

In this section we look at two types of dissipative terms. One is the usual linear drag normally used to account for amplitude decay, but with a complex coefficient so that it can affect the phase. The second type of term is wavenumber dependent. A frequency downshift in the wave channel frame of reference corresponds to a wavenumber shift in the NLS frame of reference. A dissipation which acted preferentially on higher wavenumbers could account for a downshift.

This examination is, admittedly, arbitrary. There are other processes, such as a selective instability, which could cause a downshift. The most we can hope to point out is whether dissipation could have such an effect, but not to determine if it is dominant. The conclusion is rather

interesting in that it seems these linear dissipative balances have no cumulative effect on the phase. In each case we are able to transform back to the NLS equation with real coefficients.

We summarize as follows. We consider the following form of the NLS equation:

$$A_t + \frac{i}{8} A_{xx} + \frac{i}{2} |A|^2 A = -\mu A + \eta A_x \quad (3.51)$$

Case 1.) Consider

$$\begin{aligned} \eta &= 0 \\ \mu &= \alpha + i\beta ; \quad \alpha, \beta \in \mathbb{R}, \quad \alpha, \beta \ll 1 \end{aligned} \quad (3.52)$$

We make the transformation

$$\begin{aligned} B &= A e^{i\beta t} = R e^{i\theta + i\beta t} \\ \phi &= \theta + \beta t \end{aligned} \quad (3.53)$$

Then (3.51) becomes

$$B_t + \frac{i}{8} B_{xx} + \frac{i}{2} |B|^2 B = -\alpha B \quad (3.54)$$

where α is real. We arrive at the NLS equation for B with real damping coefficient. The modulation frequency and wavenumber are defined as

$$\begin{aligned} \omega &= -\frac{\partial}{\partial t} \phi = -\theta_t - \beta \\ k &= \frac{\partial}{\partial x} \phi = \theta_x \end{aligned} \quad (3.55)$$

We see that there is a small, constant frequency shift

from the complex dissipation, but not a mechanism for a downshift with evolution.

Case 2.) We consider a wavenumber dependent dissipation

$$\begin{aligned} \mu &= 0 \\ \eta &\neq 0 \end{aligned} \tag{3.56}$$

We make the transformation

$$\begin{aligned} B &= A e^{i(4\eta x) + i(2\eta^2 t)} \\ \phi &= \theta + 4\eta x + 2\eta^2 t \end{aligned} \tag{3.57}$$

Then B satisfies

$$B_t + \frac{\nu}{8} B_{xx} + \frac{i}{2} |B|^2 B = 0 \tag{3.58}$$

The modulation frequency and wavenumber are

$$\begin{aligned} \omega &= -\theta_t - 2\eta^2 \\ k &= \theta_x + 4\eta \end{aligned} \tag{3.59}$$

Again there is a small, constant shift in both wavenumber and frequency but no time-dependent downshift.

To model the effects of the amplitude damping the numerical code was modified to the form (3.51) with $\eta = 0$ and μ purely real. This is equivalent to damping of the form included in the energy equation (2.10). The real coefficient, α , was estimated from the observations as described in section 2.3.3 and tabulated in Table 2.3

3.6 COMPARISON OF MODEL AND OBSERVATIONS

In this section we make comparisons between observations and numerical solutions for 7 experiments of varying steepness and group length. In each case we show a 3-D plot of the overall numerical solution of the inviscid equation (3.23) and the viscous model (3.51). These are only intended to give a qualitative picture of the evolution since the details are somewhat obscured.

We then compare the amplitude and phase modulations of the observations at fixed fetches to the numerical solutions at times corresponding to those fetches. The initial condition specified from the observation at 6.1 meters is exactly the same for the observations and the numerical model. The amplitude and phase modulations were obtained using the Hilbert transform. They were nondimensionalized by equation (3.22) using the scaling of the initial condition. The carrier frequency was removed. The time series were centered based on propagating the initial observation down the channel at the linear group velocity as described in chp 2 (section 2.3.1). This optimizes comparison with the NLS model which describes the evolution of the group envelope (carrier removed) in a frame that propagates at linear group velocity.

The spatial grid was chosen subject to three conditions:

maximize the amount of data used, obtain a reasonable mesh size and have a sufficient distance between the end of the group and the grid edges so that the first conservation law is satisfied within reason. The Hilbert transformed data files are 4096 points long. The initial condition and subsequent comparisons typically use twice that many points. Therefore, the beginning and end are padded by the same constant value that matches to the start of the group. The first and last eleven points are tapered to zero to exactly match the boundary conditions. The length of the (nondimensional) time evolution was chosen to correspond to the length of evolution in the wave channel. The steepest experiments have, thus, the longest evolution times.

The phase modulation in this section is defined with the opposite sign of the phase in chapter 2, as determined from the Hilbert transform, to be consistent with the definition in the NLS model. The phase we show here is also wrapped. (I.E., it has jumps of 2π from principal value of the arc sine and cosine functions).

The comparisons at each fetch are not exact. First, there is an error introduced in using the linear group velocity. Secondly, the time chosen is taken to be the closest grid point to the exact time calculated using linear group velocity. The phase evolutions of the exact solutions

(section 3.4) show how different the time evolution of the phase appears for slightly different behavior at the same times (2-soliton, 5/2-soliton, 3/2-soliton) as well as for one solution at different times.

What we hope to illustrate here is the overall character of the phase evolution based on insight gained from the exact solutions. We compare the overall phase behavior between observations and numerical solutions. From amplitude modulation we can estimate the time scale on which dissipation becomes important. The effect of dissipation can also be seen in the change in character of the phase evolution between viscous and inviscid numerical results.

Figures 3.18 and 3.19 show the full inviscid and viscous solutions, respectively, for a group of 10 waves of small wave steepness $ak = .03$ (Exp 78). The observations have been discussed previously in chapter 2. The numerical evolution was done for $-9.0 < \xi < 9.0$ and $0 < \tau < 2.5$.

This group evolution is dominated by linear dispersion (radiation). In figure 3.18 we can clearly see the radiating components along lines of constant ξ/τ , indicative of linear dispersion. The lengthening of the group, as estimated by eq. (3.44), is linear in τ .

Fig. 3.18 Inviscid NLS numerical evolution for a wave group of 10 waves, initial steepness $ak = .03$ (Exp 78). Spatial frame $-9 < X < 9$ and time interval $0 < T < 2.5$.

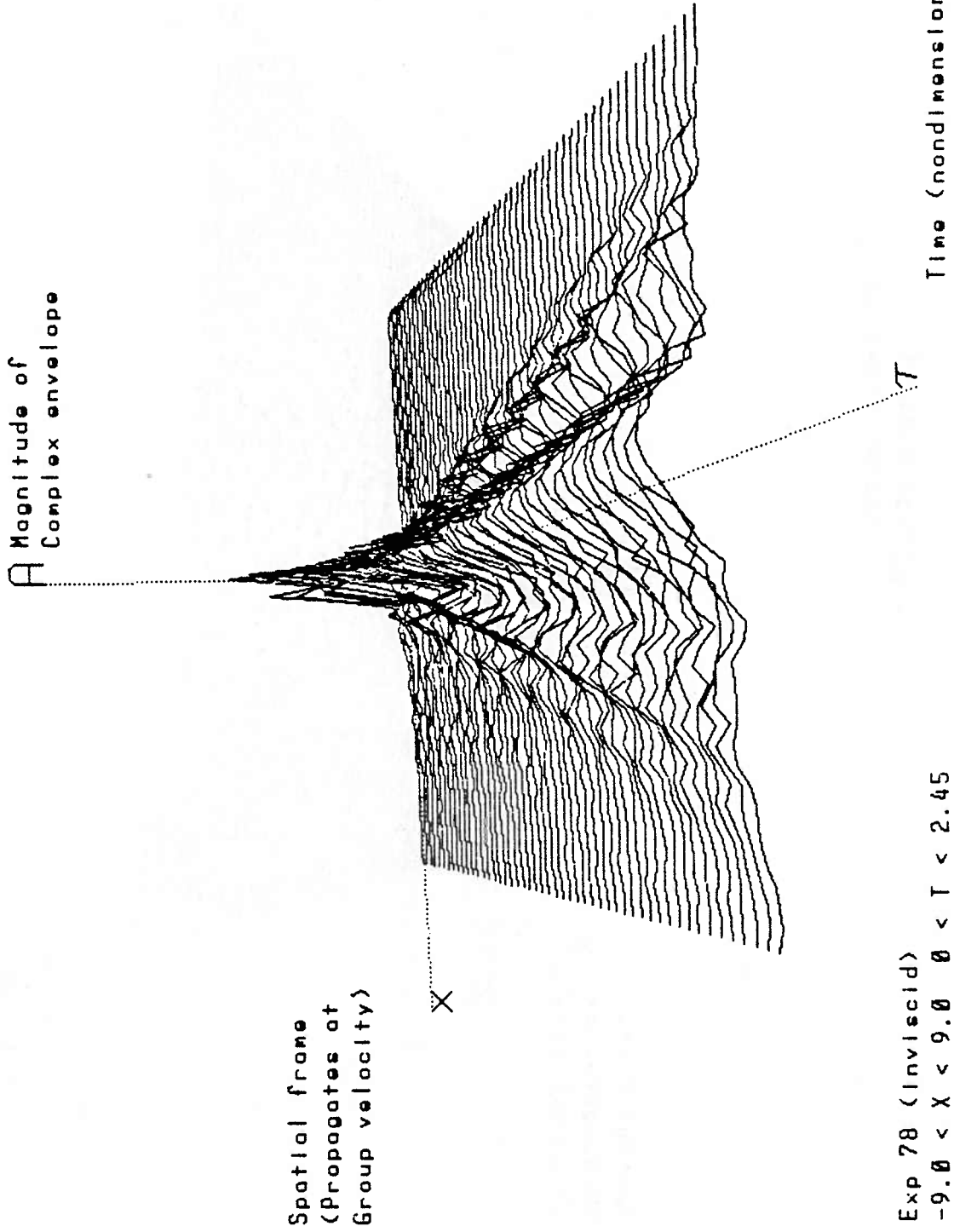
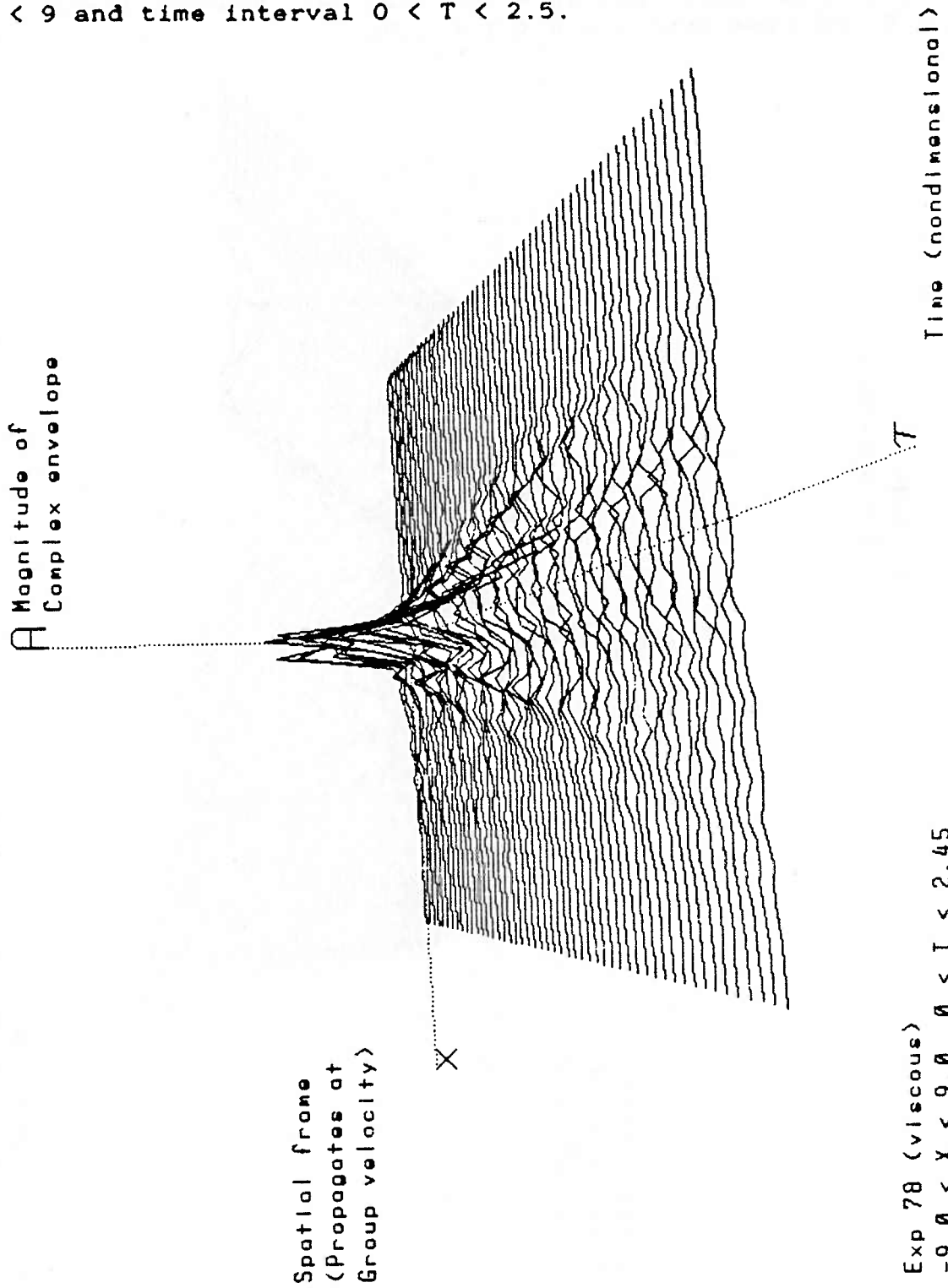


Fig. 3.19 Viscous NLS numerical evolution for a wave group of 10 waves, initial steepness $ak = .03$ (Exp 78). Spatial frame $-9 < X < 9$ and time interval $0 < T < 2.5$.



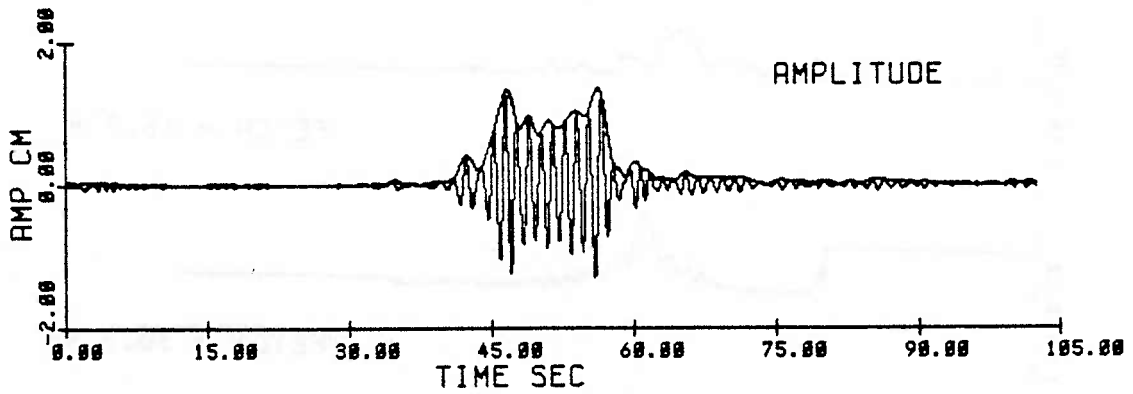
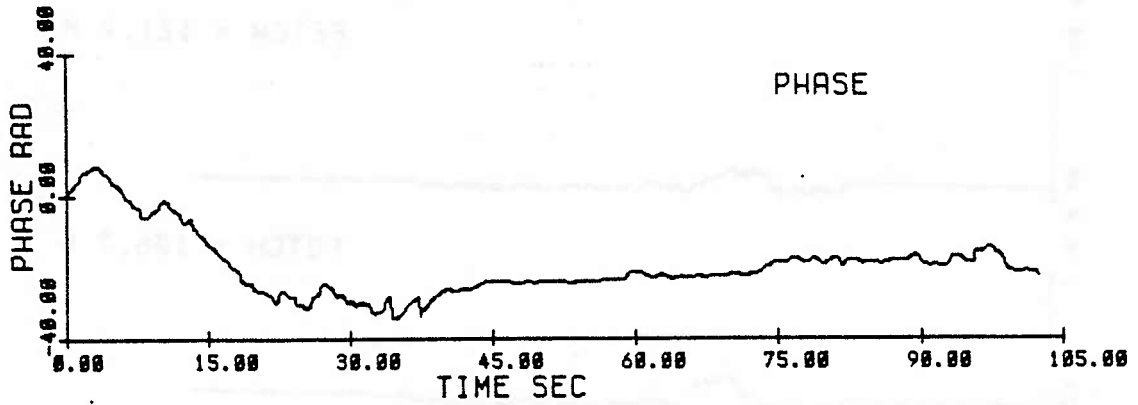


Fig 3.20 Initial condition at 6.1 m (E78)
ak = .03, N = 10

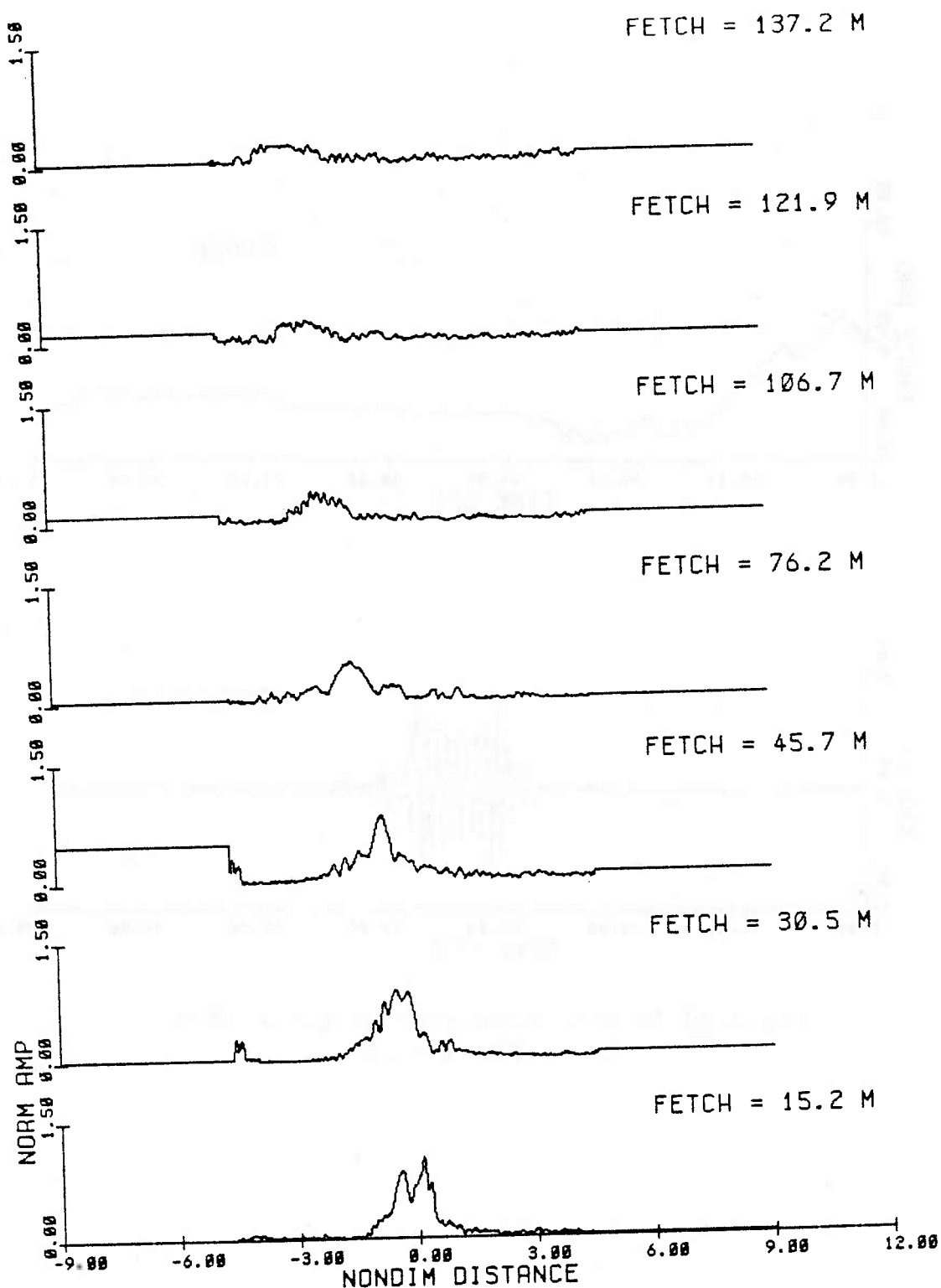


Fig. 3.21a Amplitude modulations from observations, nondimensionalized at each fetch by the initial condition scaling, for the evolution of a group of 10 waves, initial steepness $ak = .03$ (Exp 78).

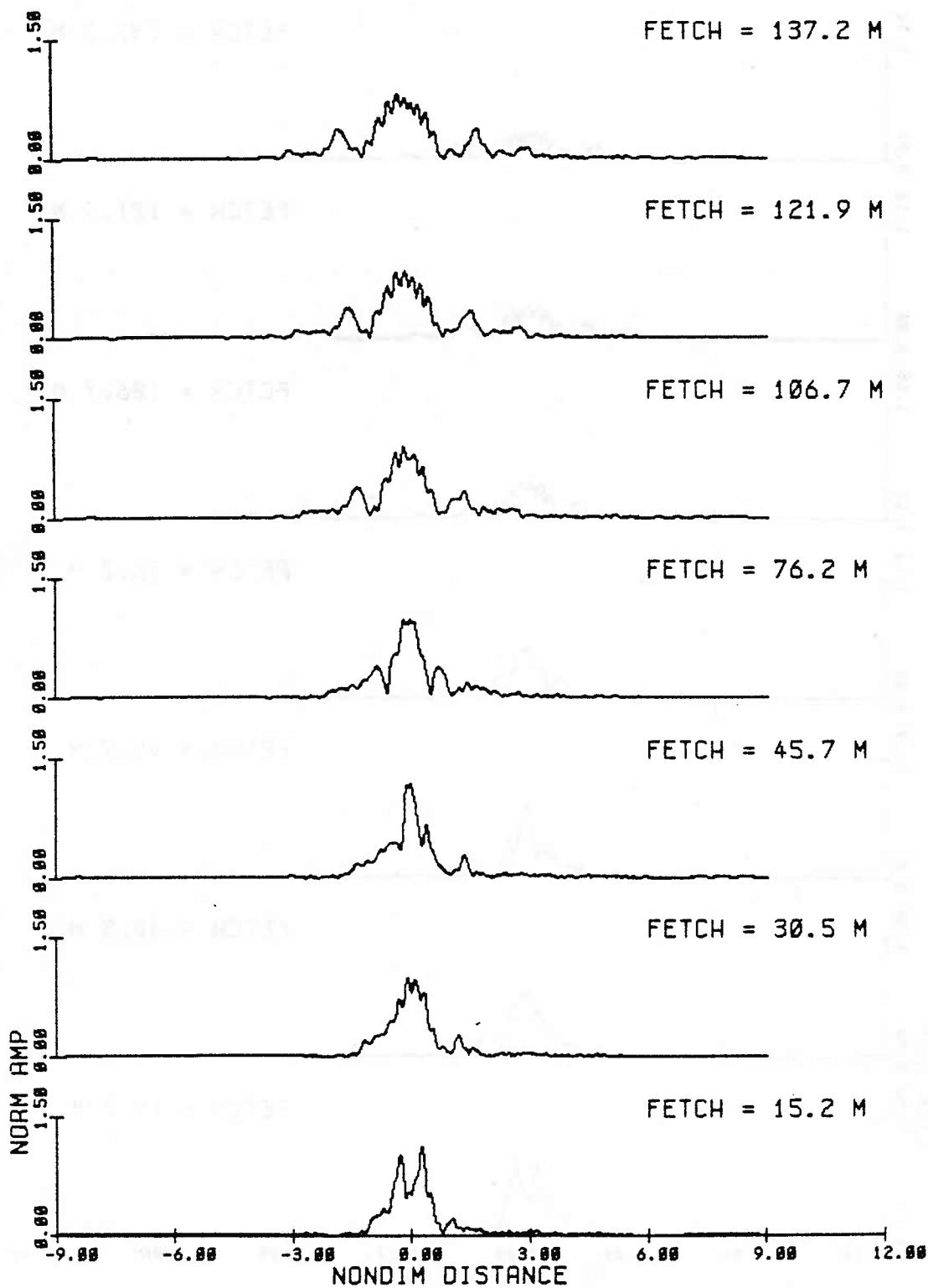


Fig. 3.21b Amplitude modulations from the inviscid NLS solution, at times corresponding to the fetches in (a), for the evolution of a group of 10 waves, initial steepness $ak = .03$ (Exp 78).

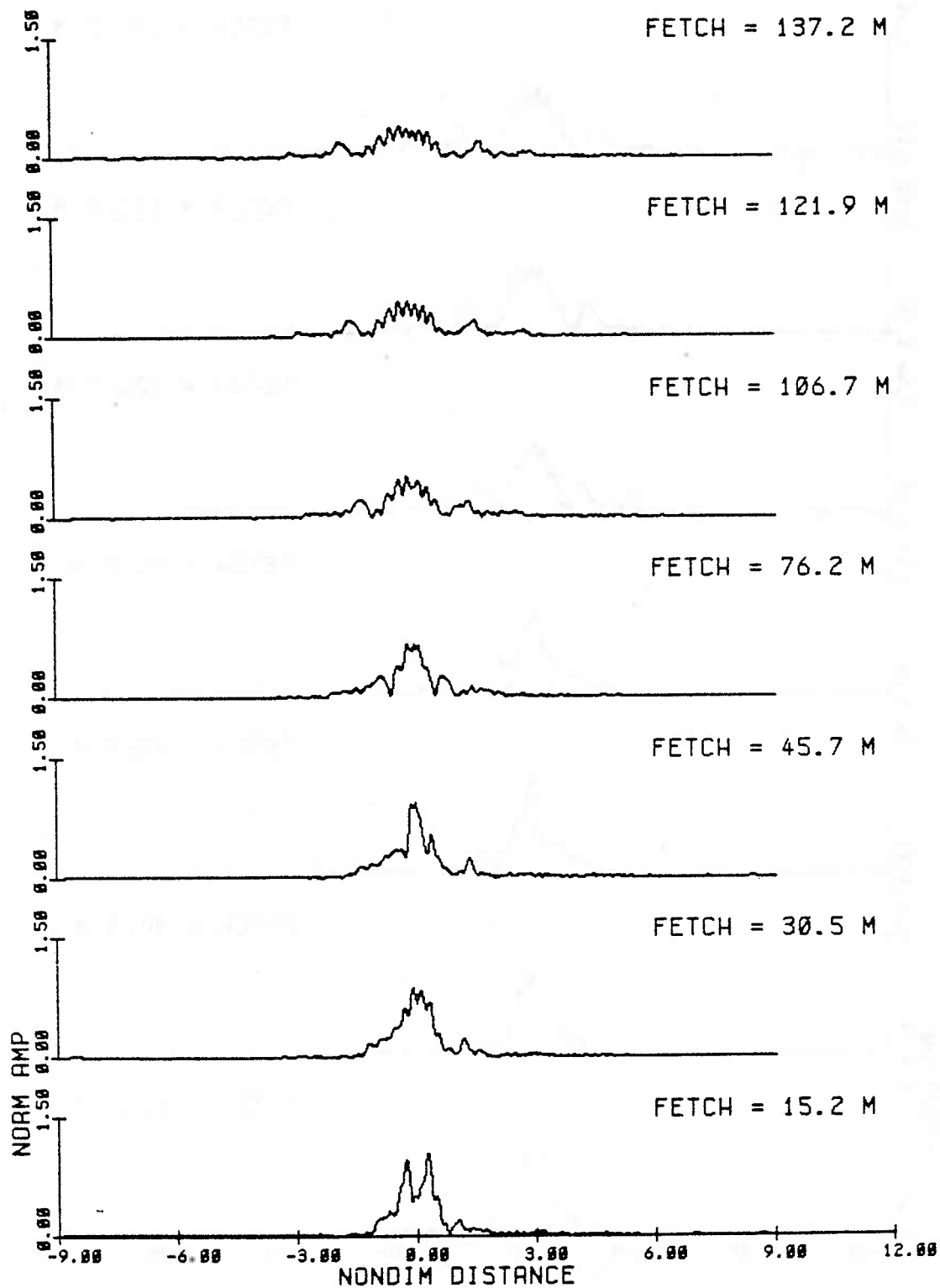


Fig. 3.21c Amplitude modulations from the viscous NLS solution, at times corresponding to the fetches in (a), for the evolution of a group of 10 waves, initial steepness $ak = .03$ (Exp 78).

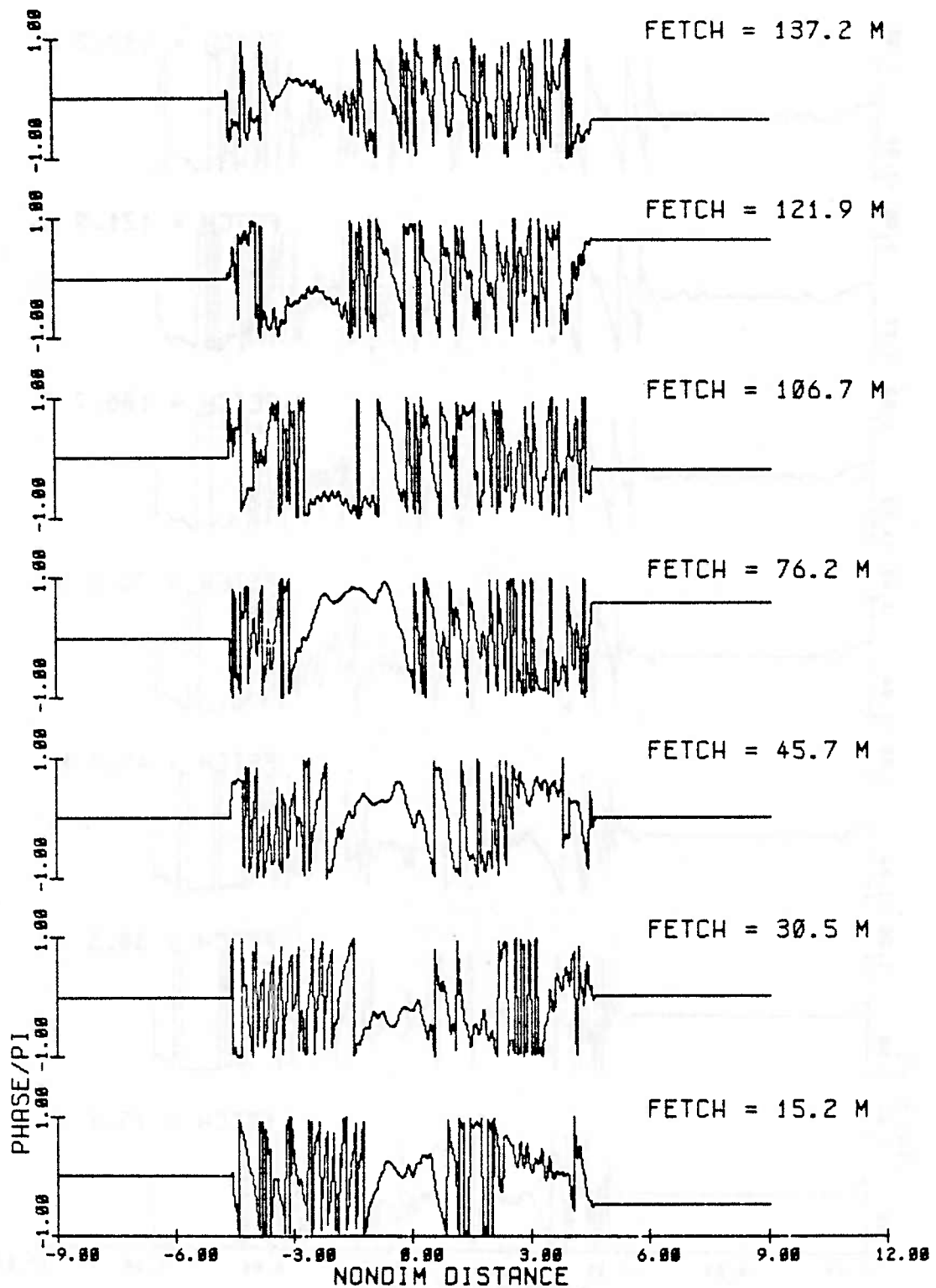


Fig. 3.22a Phase modulations from observations, principal value and normalized by pi, for successive fetches for the evolution of a group of 10 waves, initial steepness $ak = .03$ (Exp 78).

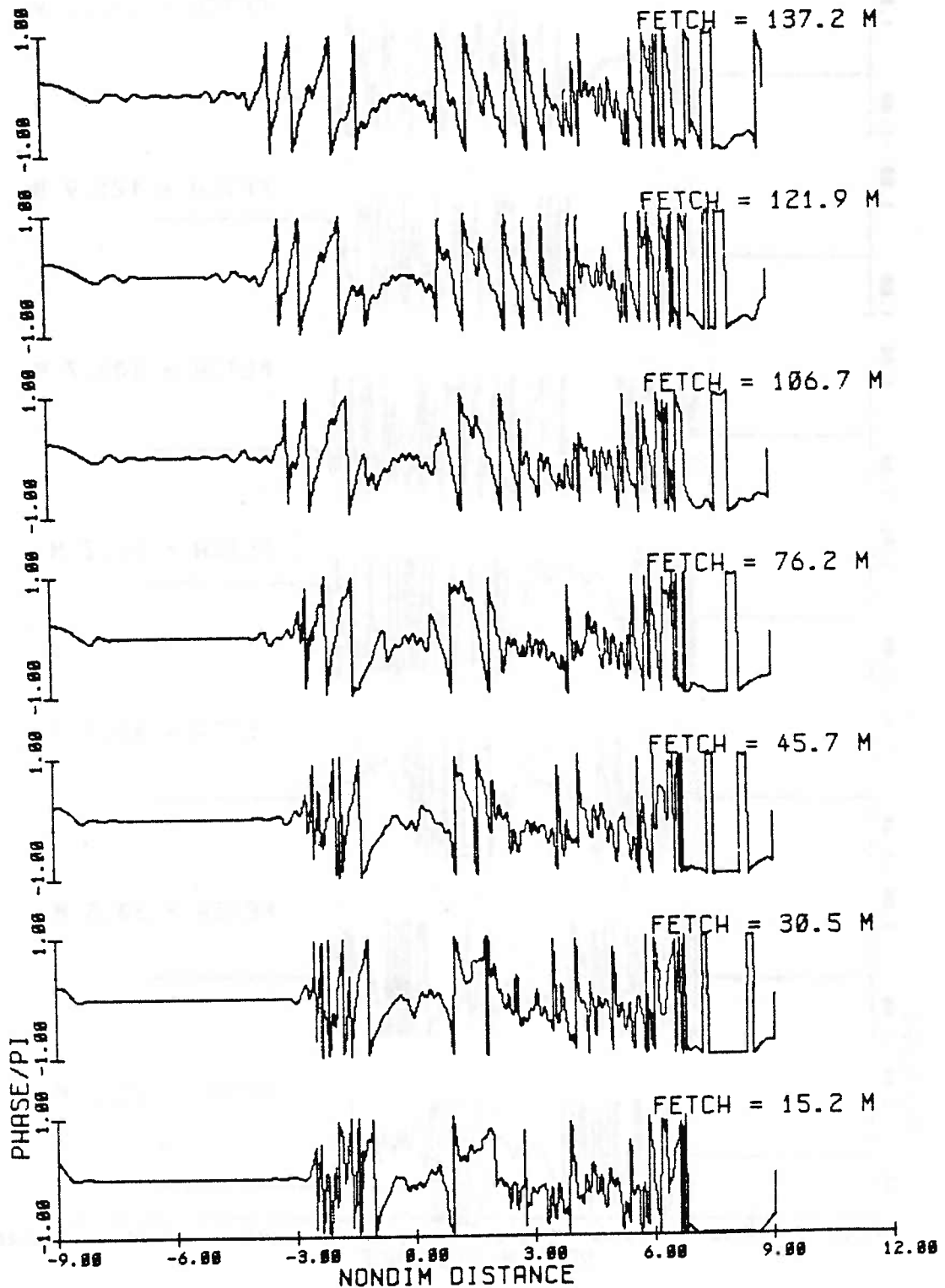


Fig. 3.22b Phase modulations from the inviscid NLS solution, at times corresponding to the fetches in (a), for the evolution of a group of 10 waves, initial steepness $ak = .03$ (Exp 78).

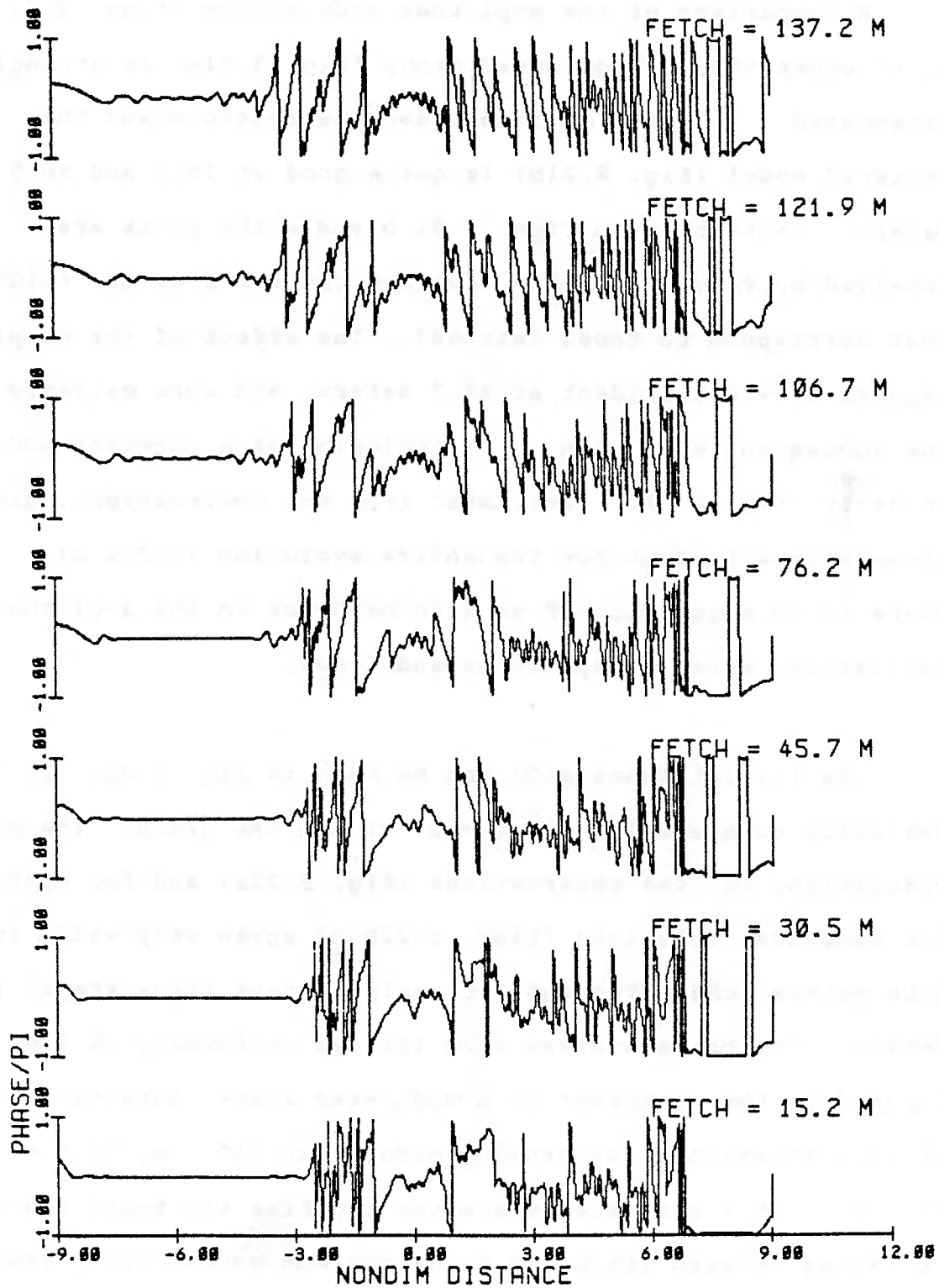


Fig. 3.22c Phase modulations from the viscous NLS solution, at times corresponding to the fetches in (a), for the evolution of a group of 10 waves, initial steepness $ak = .03$ (Exp 78).

A comparison of the amplitude modulations (figs. 3.21 a, b, c) shows that the observed group (fig. 3.21a) is strongly attenuated. The comparison between observations and the inviscid model (fig. 3.21b) is quite good at 15.2 and 30.5 meters. (Note that in figs. 3.21 b and c the plots are labelled by fetch, actually they are the times of the solution that correspond to those fetches). The effect of the damping becomes somewhat evident at 45.7 meters, and more markedly in the subsequent evolution. The inclusion of a constant modulus of decay (fig. 3.21c), estimated from the observations, gives remarkable agreement for the entire evolution (137.2 m). There is no suggestion of soliton behavior in the amplitude modulation, merely a spreading and decay.

The initial phase $p(0)$ can be seen in fig. 3.20. It is basically constant ($P_{\xi} = P_{\eta} = 0$) within the group. The phase modulations for the observations (fig. 3.22a) and for both of the numerical solutions (figs. 3.22b,c) agree very well, in both general character and, at early fetches (time steps) in detail. The phase evolves from initial uniformity (6.1 m) imposed by the wavemaker to a modulated state characteristic of wave interaction or growing modulation (15.2 m, 30.5 m, 45.7 m). This modulated character typifies the bound state as it passes between its minimum and maximum modulation. The final state shows the strong negative curvature ($P_{\xi} < 0$) characteristic of radiation. The evolution thus seems to

consist of an initial forced pulse that disperses linearly. We start from an imposed uniform phase characteristic of a soliton or bound state, followed by modulation and radiation.

The next example is for a group of 25 waves of wave steepness $ak = .07$ (Exp 77). The full inviscid and frictional numerical solutions are shown in fig. 3.23 and 3.24. The numerical evolutions were done for $-21.0 < \xi < 21.0$ and $0 < \bar{t} < 5$. The dimensional initial condition is shown in fig. 3.25.

The amplitude modulation (figs. 3.26 a,b,c) for the observations and the numerical solutions agree quite well until 106.7 m. Dissipation then becomes important. The observations (fig. 3.26a) show a steady, single envelope from 106.7 to 137.2 meters. The inviscid solution (fig. 3.26b) shows a continuation of the modulation into 2 group envelopes which became apparent in all 3 figures at 76.2 m. It looks as though the inviscid solution might evolve to a multi-soliton, as in the theoretical estimate ($N_{S,T} = 2.3$, Table 2.2). However, as we see next, the phase indicates this is not so. The frictional solution (fig. 3.26c) is not as strongly damped as the actual observations. It compares better than the inviscid solution, but it shows the same modulation to two groups, only damped, that we see in the inviscid evolution. The observations (fig. 3.26a) do not modulate further after

Fig. 3.23 Inviscid NLS numerical evolution for a wave group of 25 waves, initial steepness $ak = .07$ (Exp 77). Spatial frame $-21 < X < 21$ and time interval $0 < T < 5$.

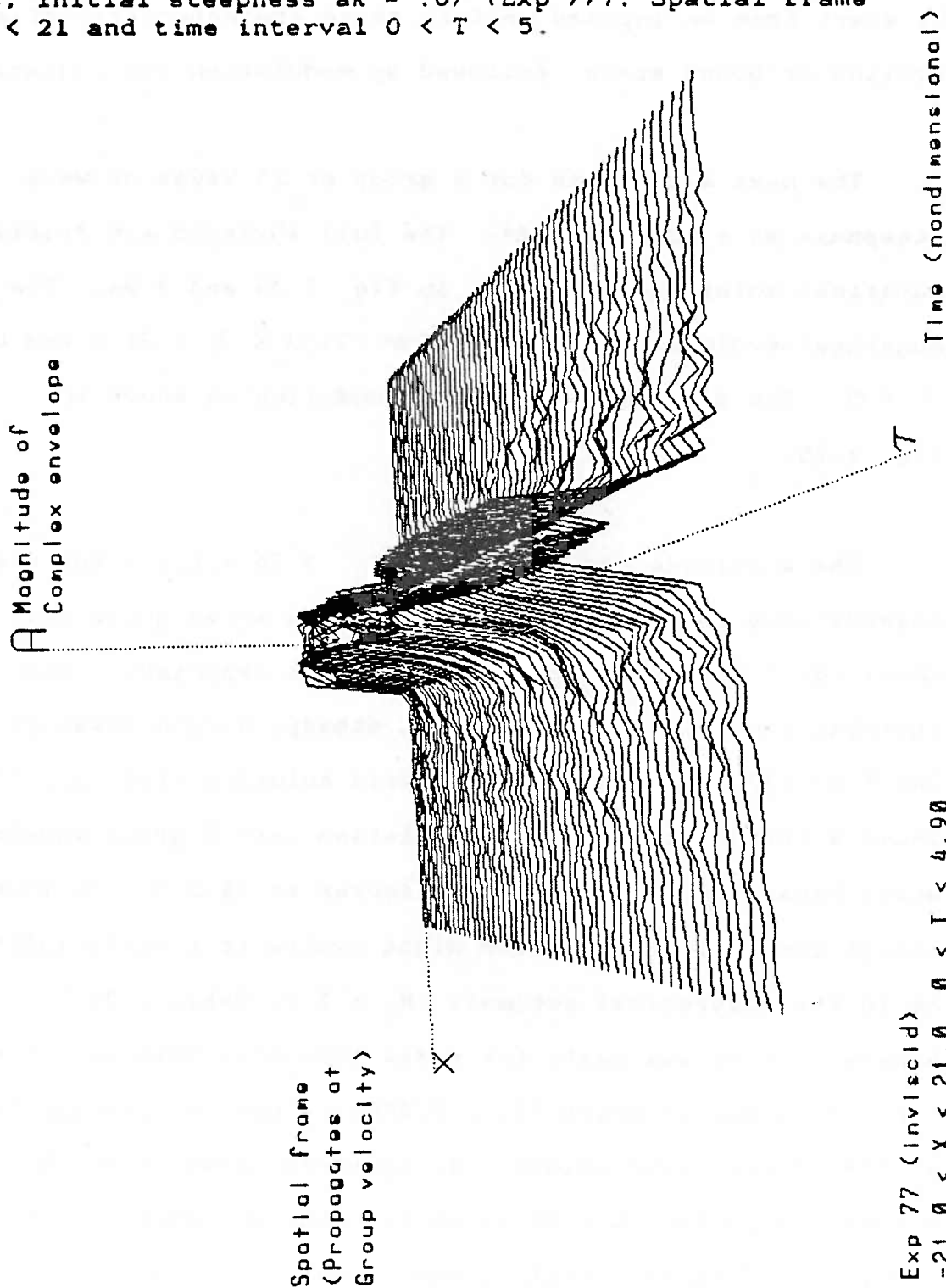
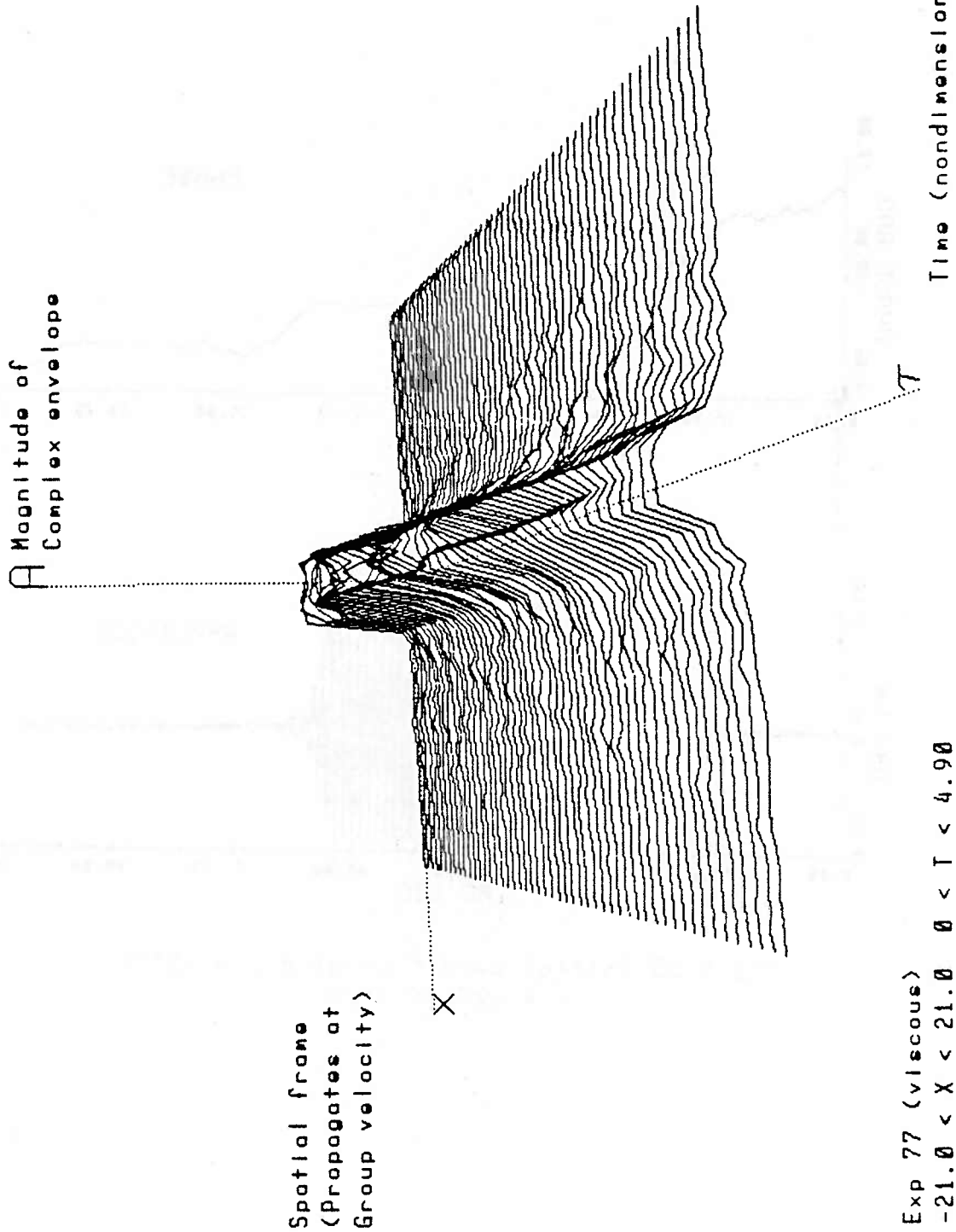


Fig. 3.24 Viscous NLS numerical evolution for a wave group of 25 waves, initial steepness $ak = .07$ (Exp 77). Spatial frame $-21 < X < 21$ and time interval $0 < T < 5$.



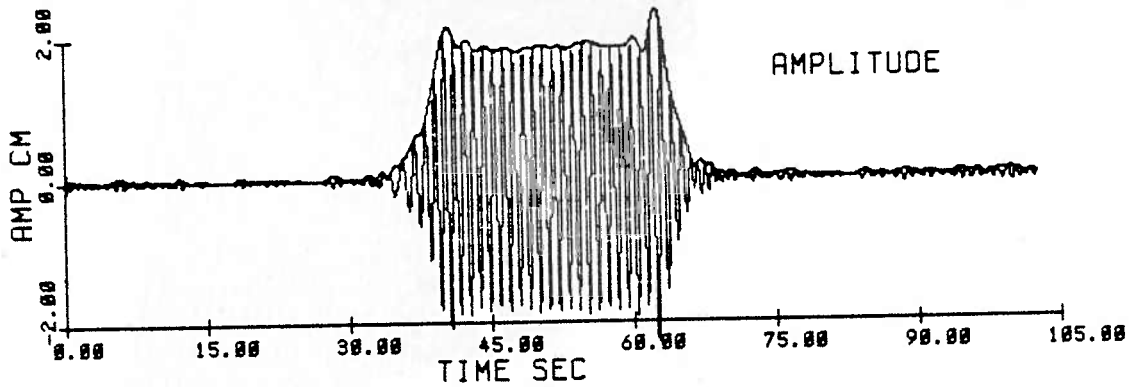
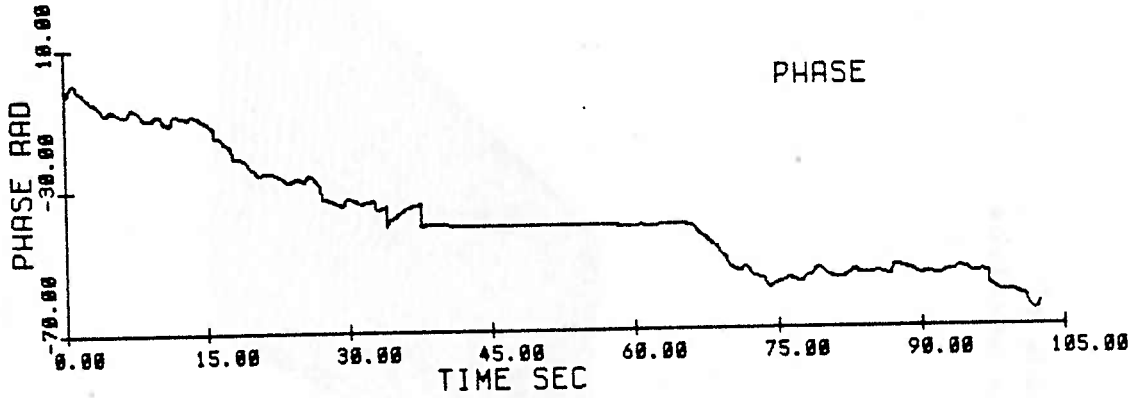


Fig 3.25 Initial condition at 6.1 m (E77)
ak = .07, N = 25

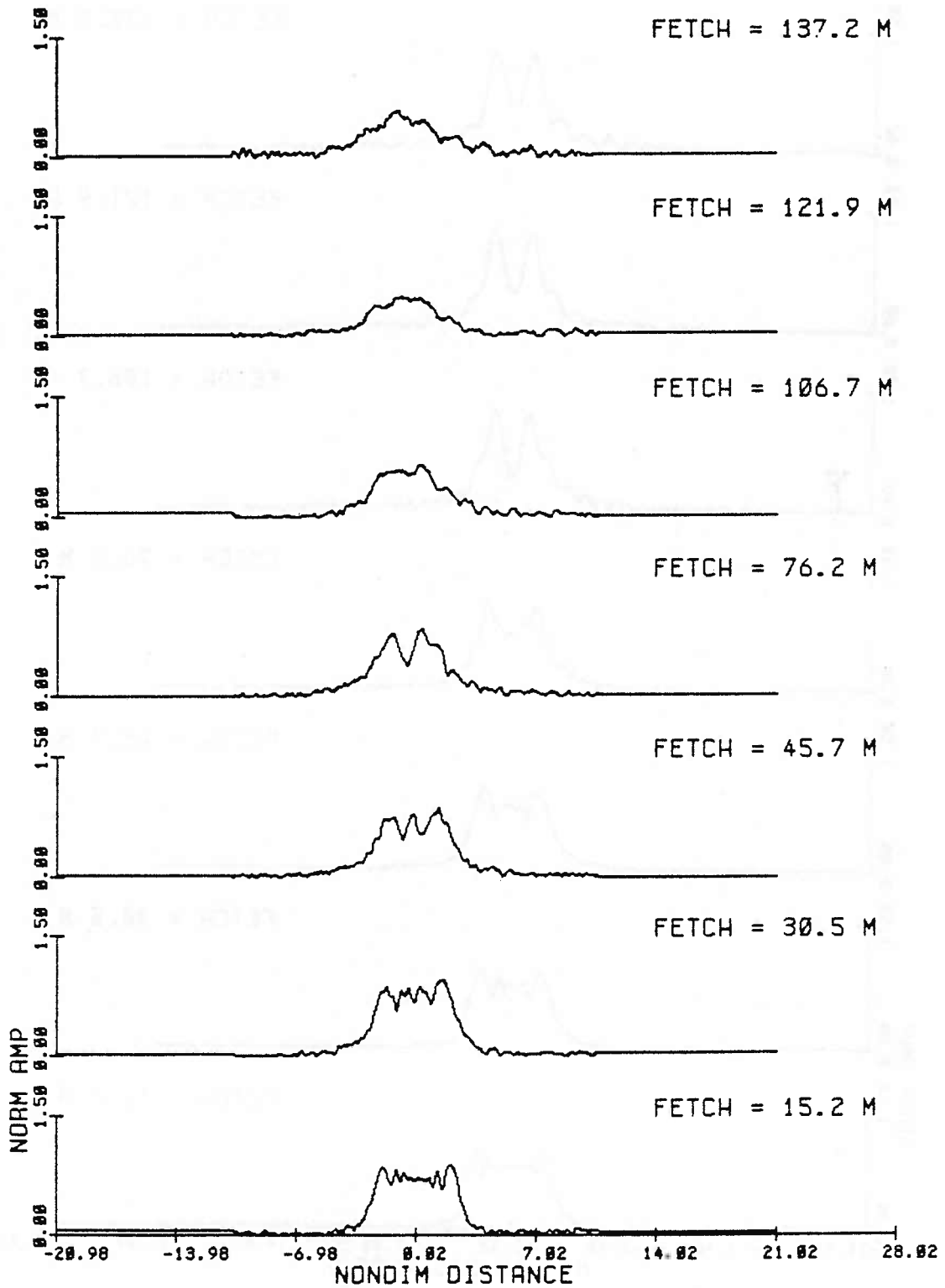


Fig. 3.26a Amplitude modulations from observations, nondimensionalized at each fetch by the initial condition scaling, for the evolution of a group of 25 waves, initial steepness $ak = .07$ (Exp 77).

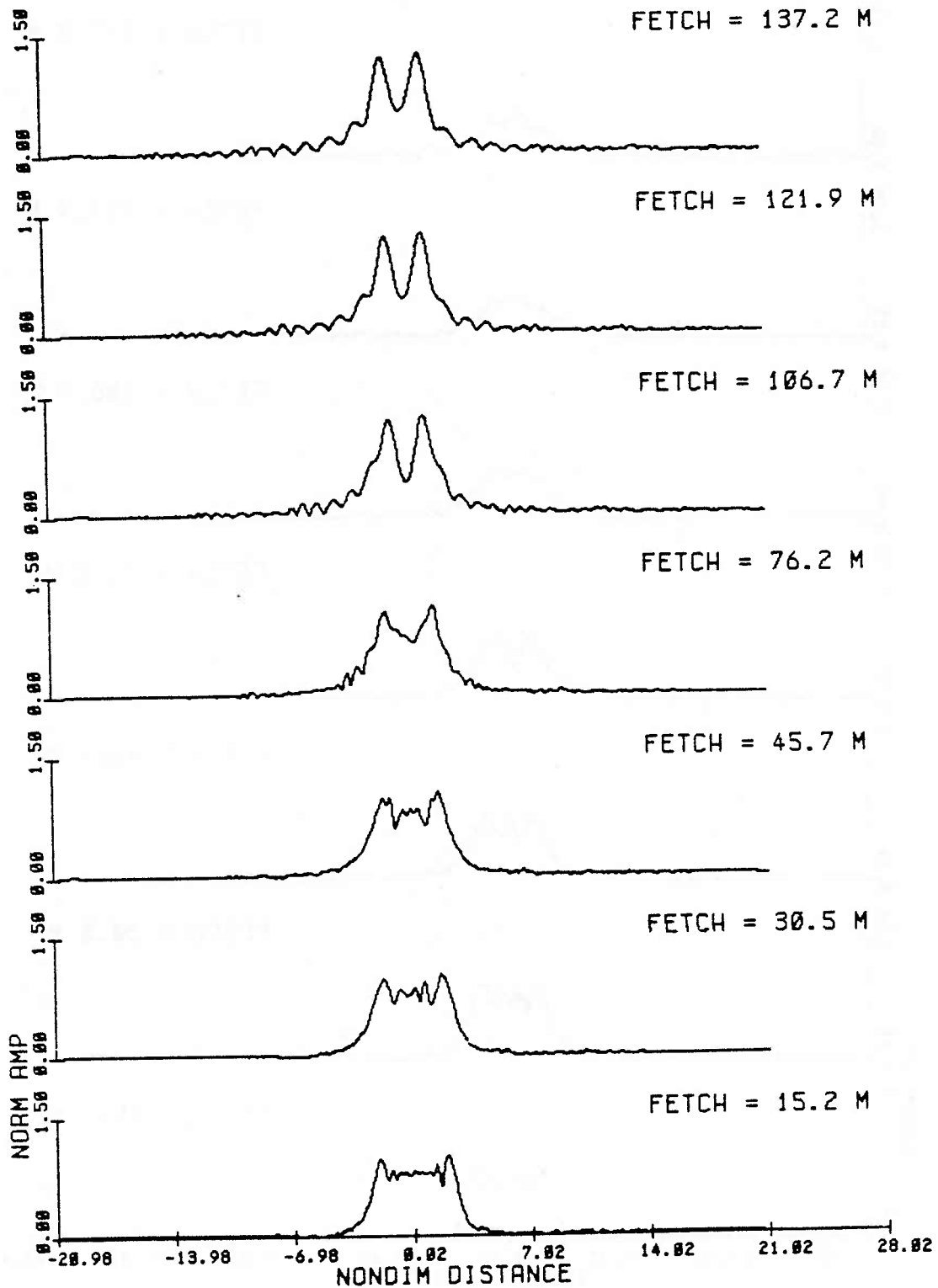


Fig. 3.26b Amplitude modulations from the inviscid NLS solution, at times corresponding to the fetches in (a), for the evolution of a group of 25 waves, initial steepness $ak = .07$ (Exp 77).

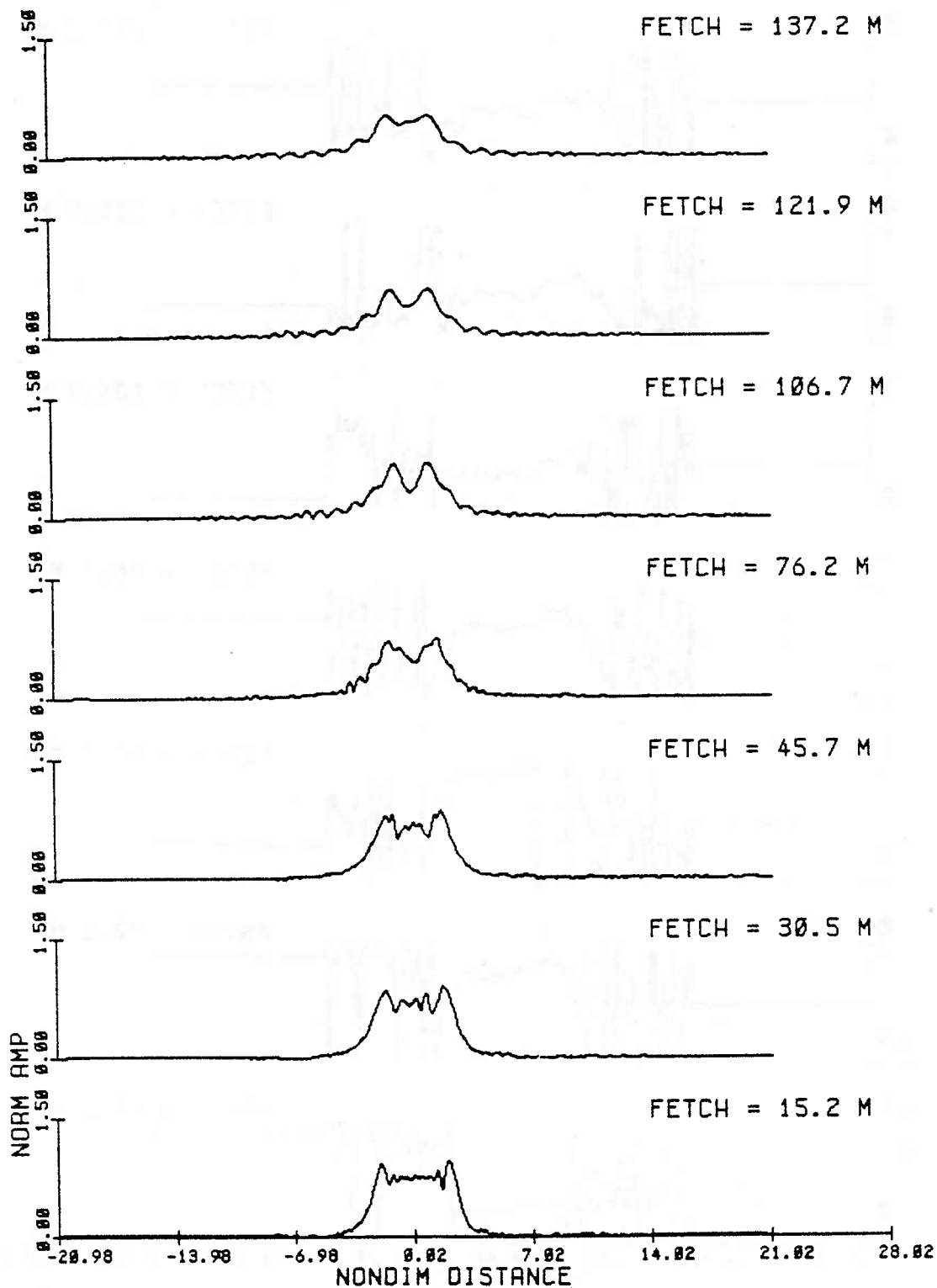


Fig. 3.26c Amplitude modulations from the viscous NLS solution, at times corresponding to the fetches in (a), for the evolution of a group of 25 waves, initial steepness $ak = .07$ (Exp 77).

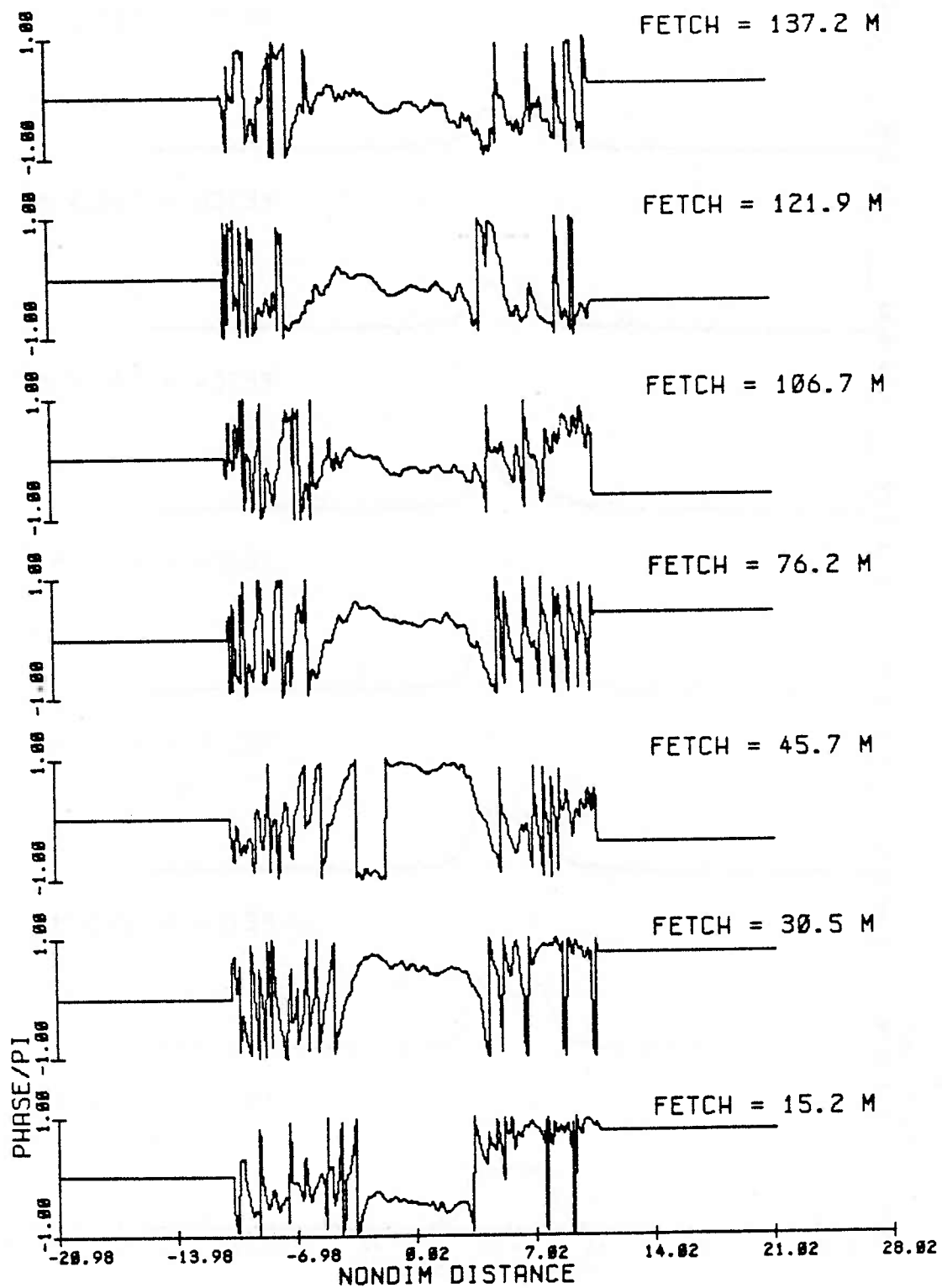


Fig. 3.27a Phase modulations from observations, principal value and normalized by pi, for successive fetches for the evolution of a group of 25 waves, initial steepness $ak = .07$ (Exp 77).

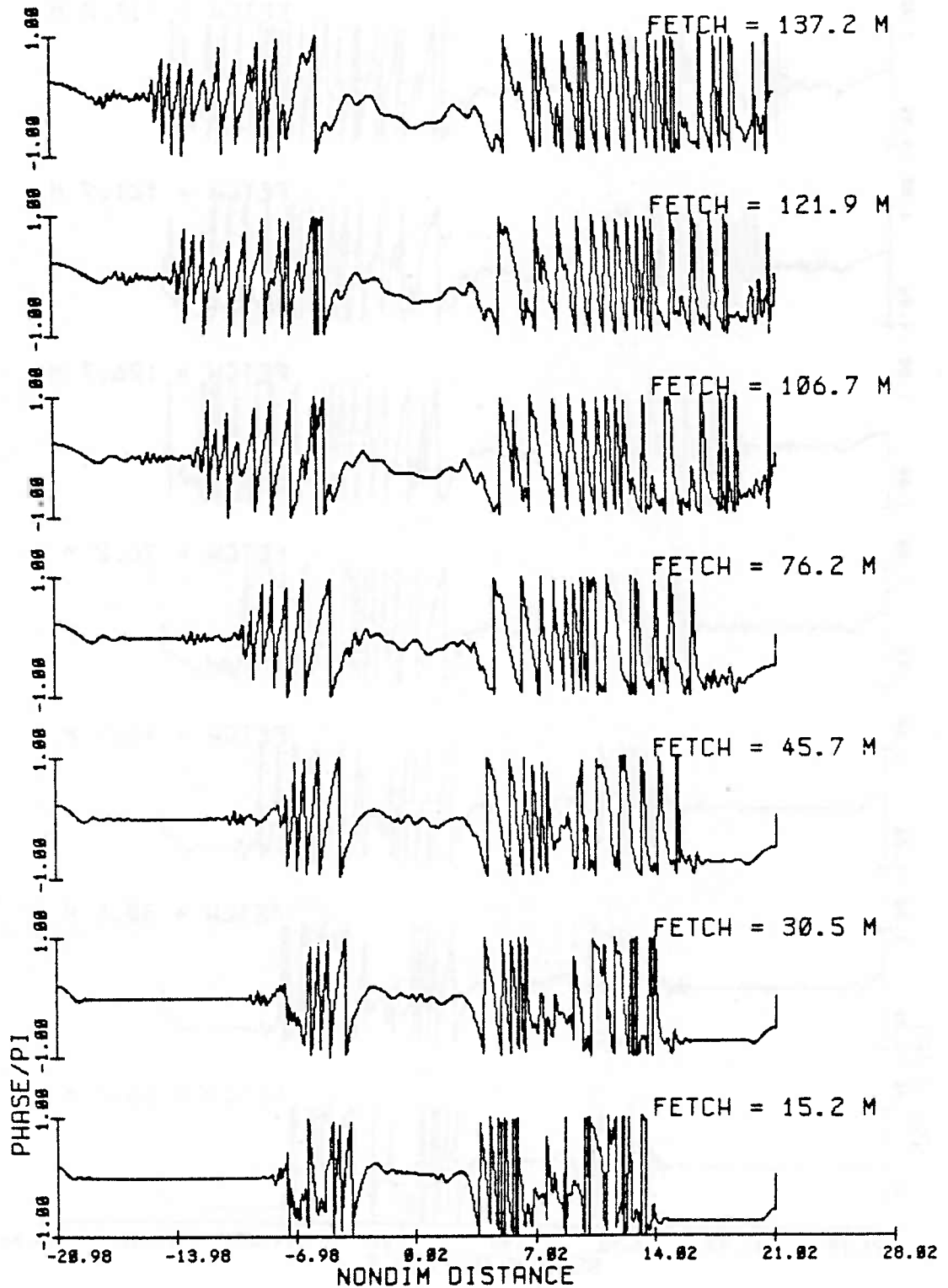


Fig. 3.27b Phase modulations from the inviscid NLS solution, at times corresponding to the fetches in (a), for the evolution of a group of 25 waves, initial steepness $ak = .07$ (Exp 77).

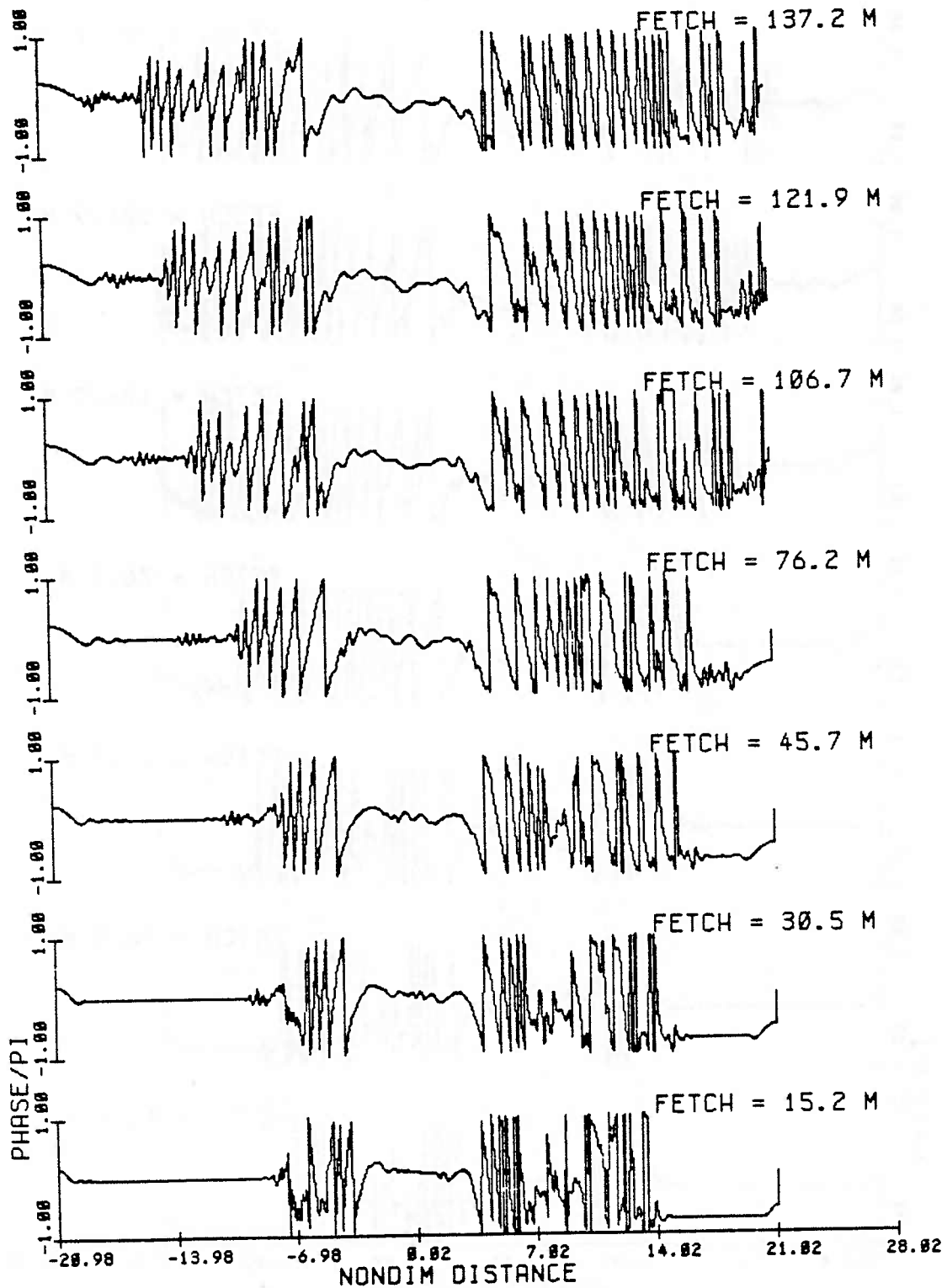


Fig. 3.27c Phase modulations from the viscous NLS solution, at times corresponding to the fetches in (a), for the evolution of a group of 25 waves, initial steepness $ak = .07$ (Exp 77).

76.2 m. At 137.2 m, in fig. 3.26c, the frictional solution modulation shows a single envelope again. Finally, we note that because of its weak nonlinearity and long group length, this group evolution should take (relative to other experiments) the longest time to reach its asymptotic state.

The phase modulations are shown in Figs. 3.27 a,b,c. They show remarkable agreement and are different from the previous phase evolution (figs. 3.22 a,b,c). There is a slight linear trend in phase within the group ($P_{\xi} = \text{constant}$) indicating that not all the carrier frequency was removed. The overall phase is very flat within the group ($P_{\xi\xi} = 0$), with quite small undulations. This uniform phase is indicative of soliton behavior or the bound state at an extremum (maximum or minimum) of modulation. Linear dispersion (radiation, $P_{\xi\xi} < 0$) can be seen at the edges of the group. Most of the discontinuities of 2π are due to principal value; however, the initial jumps in phase (moving in ξ from the center of the group at $\xi = 0$ outwards) are located at the ends of the group where amplitude minima (nodes) occur.

The next two examples are for wave groups of the same wave steepness, $ak = .10$, and different group lengths: 15 waves (Exp 87) and 25 waves (Exp 88). In order, the number of predicted solitons for each case was $N_{S,T} = 1.8$ and 2.3 (Table

2.2).

For the group of 15 waves, the full solution is shown in figs. 3.28 and 3.29 for the inviscid and viscous cases, respectively. The solution was calculated on the interval $-29.3 < \xi < 29.3$ and $0 < \tau < 10$. The dimensional initial condition is shown in fig. 3.30.

The amplitude modulation is shown in figs. 3.31 a, b, c. The agreement is good between all three until 76.2 meters. The agreement of the frictional numerical solution (fig. 3.31c) with the observations (fig. 3.31a) for the entire evolution is striking.

The initial condition for the phase is shown in fig. 3.30. It is uniform ($P_{\xi} = P_{\xi\xi} = 0$) within the group. The phase evolution in the observations (fig. 3.32a) is basically like that of the 1-soliton (uniform) with some small undulations. As one moves outward in ξ from the packet center at $\xi = 0$ we see linear dispersion ($P_{\xi\xi} < 0$). The phase evolution of the frictional solution (fig. 3.32c) agrees quite well with the observations. We notice that beyond 76.2 meters, the amplitude modulation of the observations and the inviscid model (fig. 3.31a,b) differ due to dissipation. These differences are also evident in the phase modulation (figs. 3.32a,b). The inviscid amplitude modulation

Fig. 3.28 Inviscid NLS numerical evolution for a wave group of 15 waves, initial steepness $ak = .10$ (Exp 87). Spatial frame $-29.3 < X < 29.3$ and time interval $0 < T < 10$.

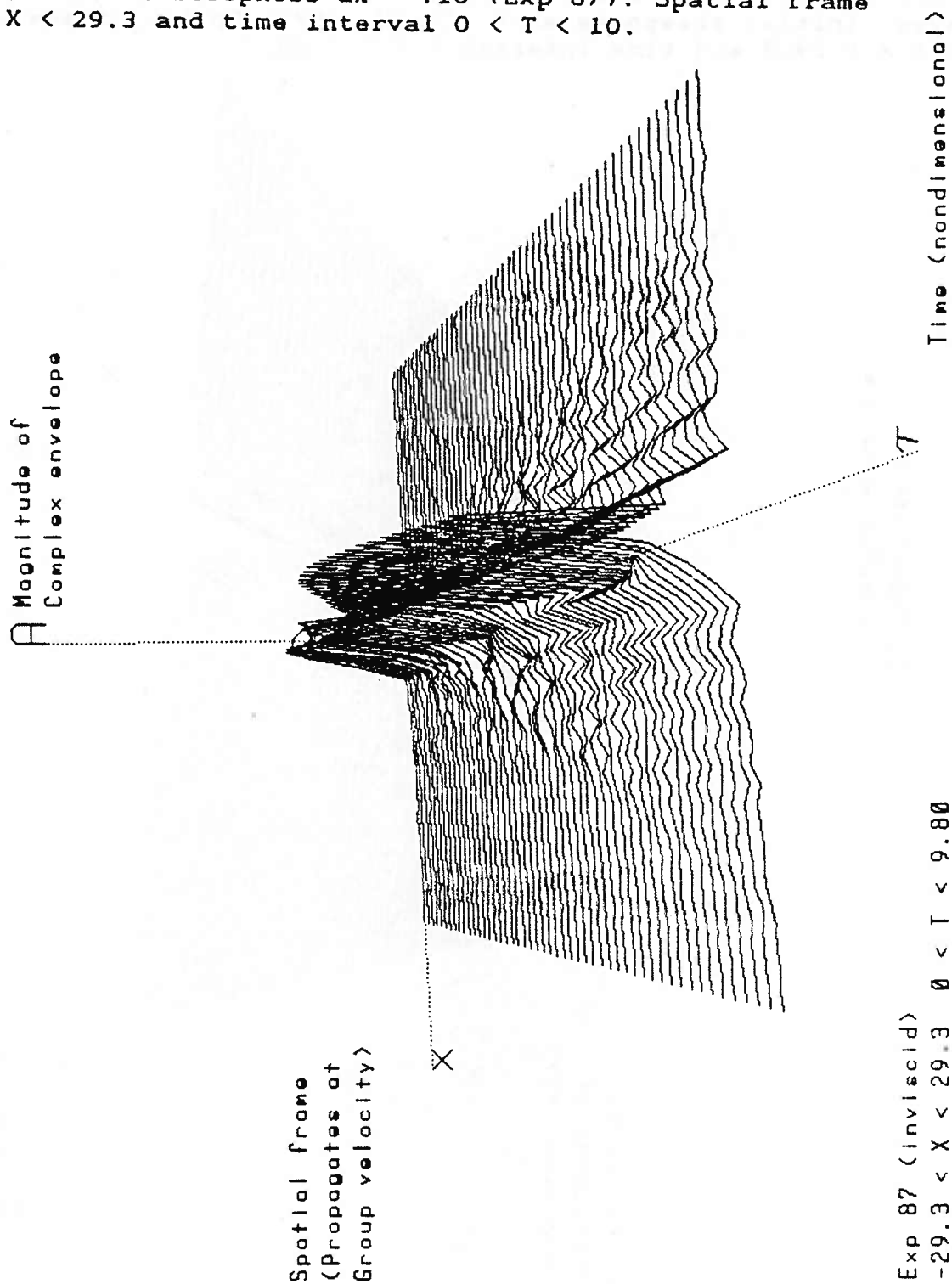
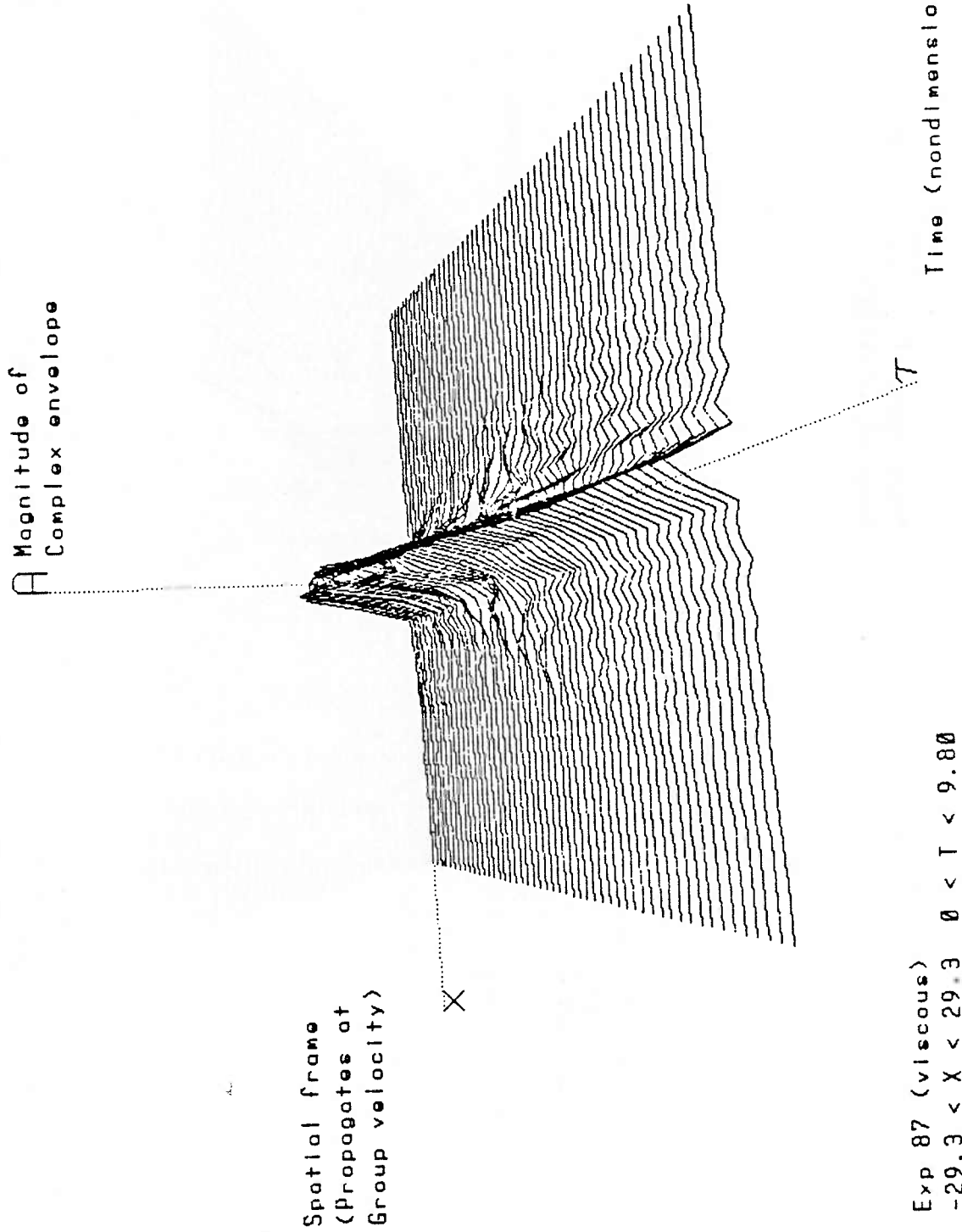


Fig. 3.29 Viscous NLS numerical evolution for a wave group of 15 waves, initial steepness $ak = .10$ (Exp 87). Spatial frame $-29.3 < X < 29.3$ and time interval $0 < T < 10$.



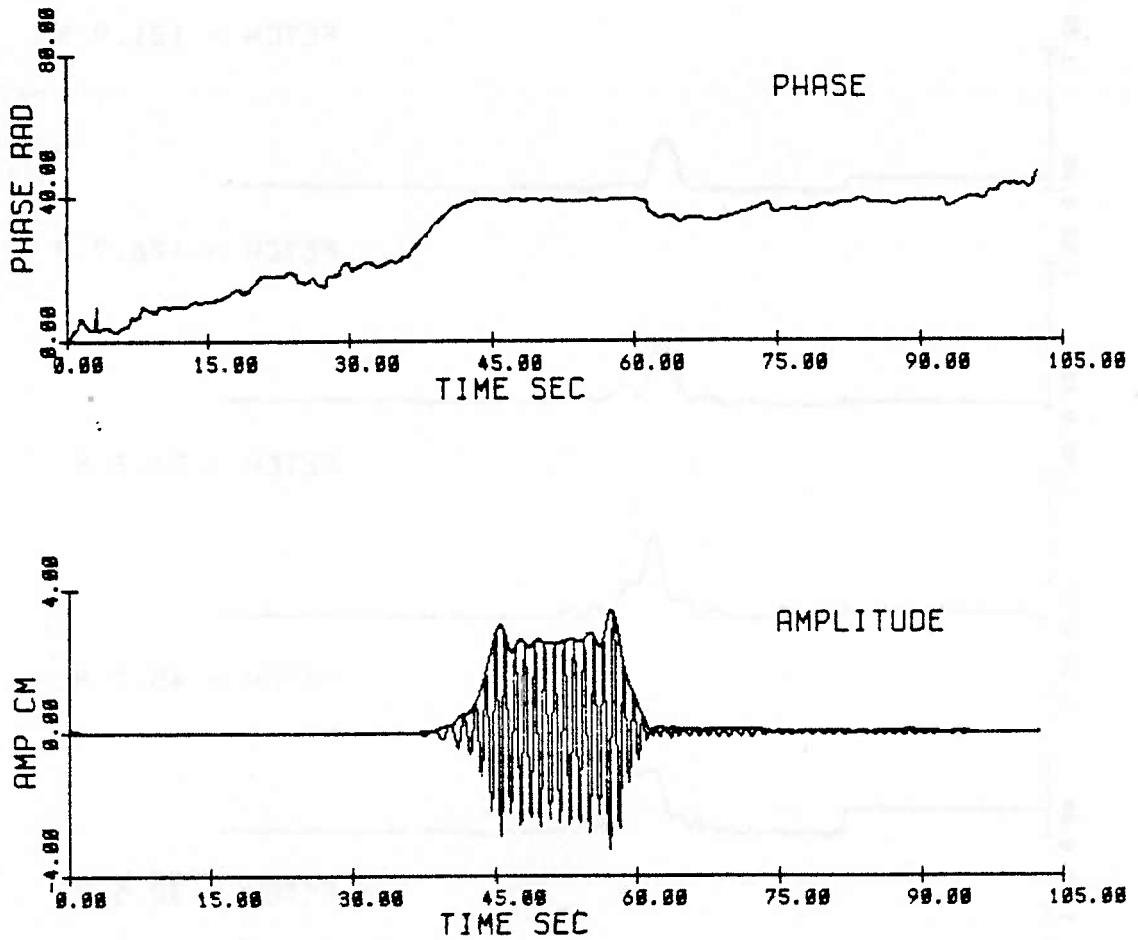


Fig 3.30 Initial condition at 6.1 m (E87)
ak = .10, N = 15

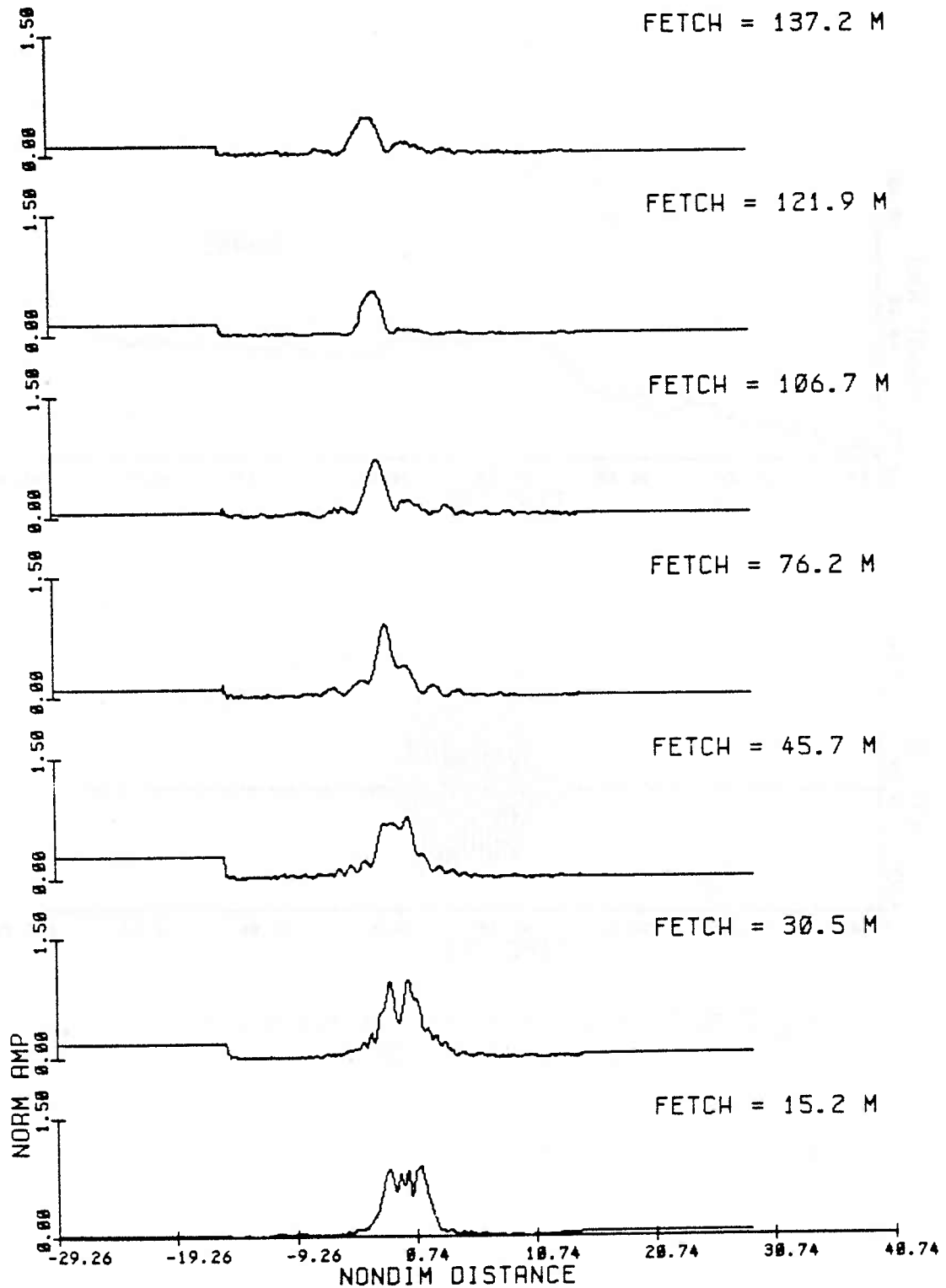


Fig. 3.31a Amplitude modulations from observations, nondimensionalized at each fetch by the initial condition scaling, for the evolution of a group of 15 waves, initial steepness $ak = .10$ (Exp 87).

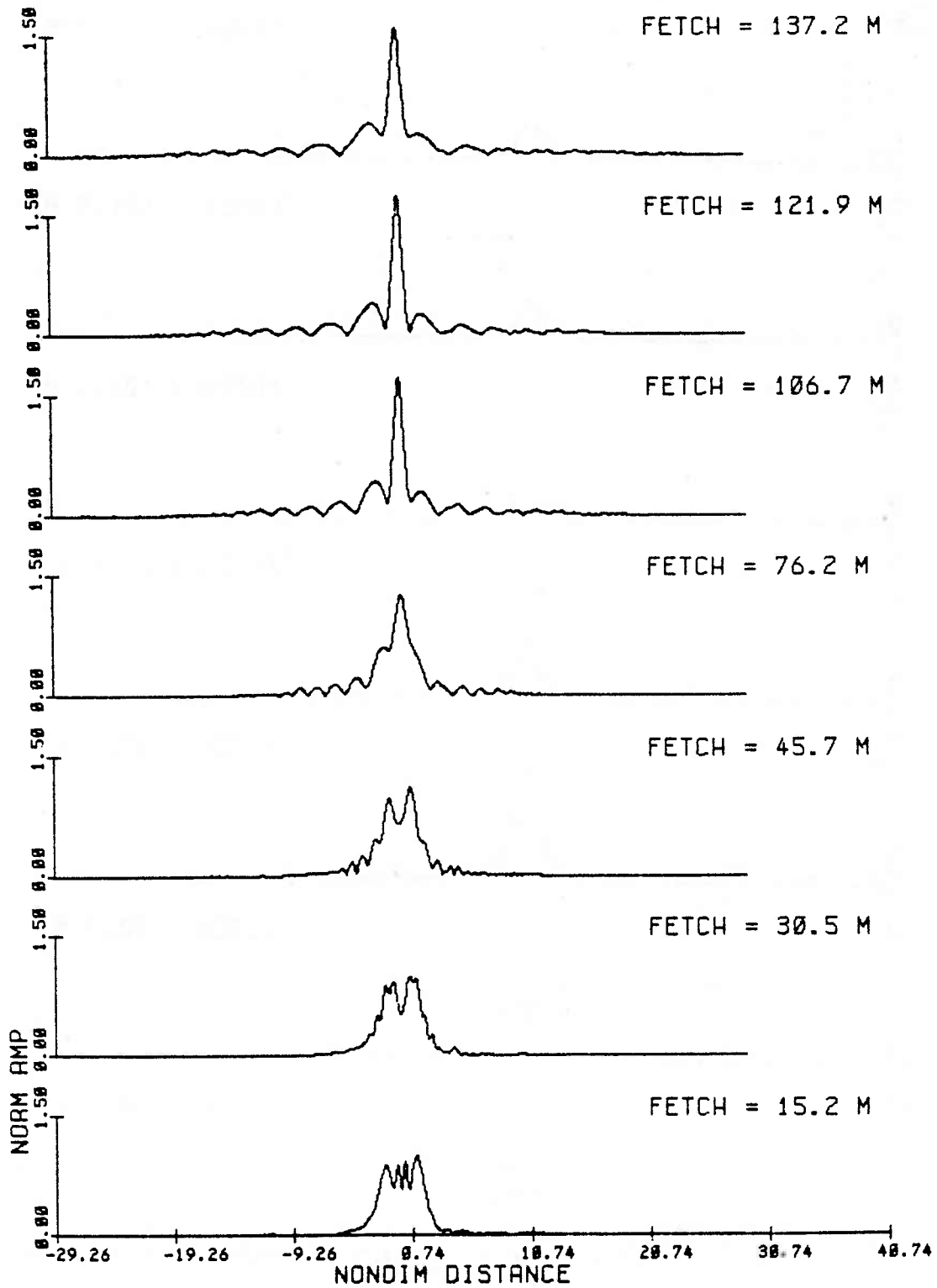


Fig. 3.31b Amplitude modulations from the inviscid NLS solution, at times corresponding to the fetches in (a), for the evolution of a group of 15 waves, initial steepness $ak = .10$ (Exp 87).

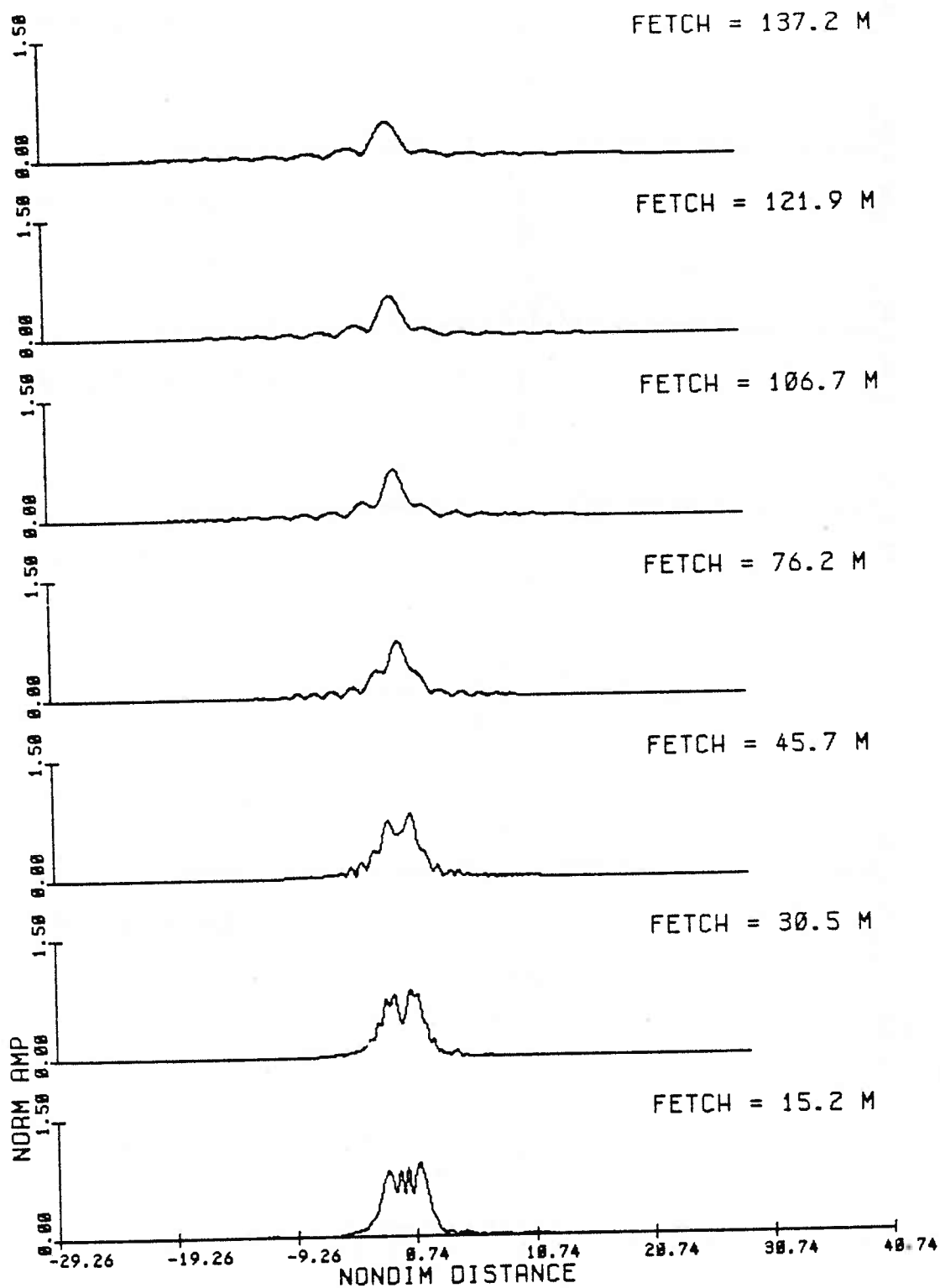


Fig. 3.31c Amplitude modulations from the viscous NLS solution, at times corresponding to the fetches in (a), for the evolution of a group of 15 waves, initial steepness $ak = .10$ (Exp 87).

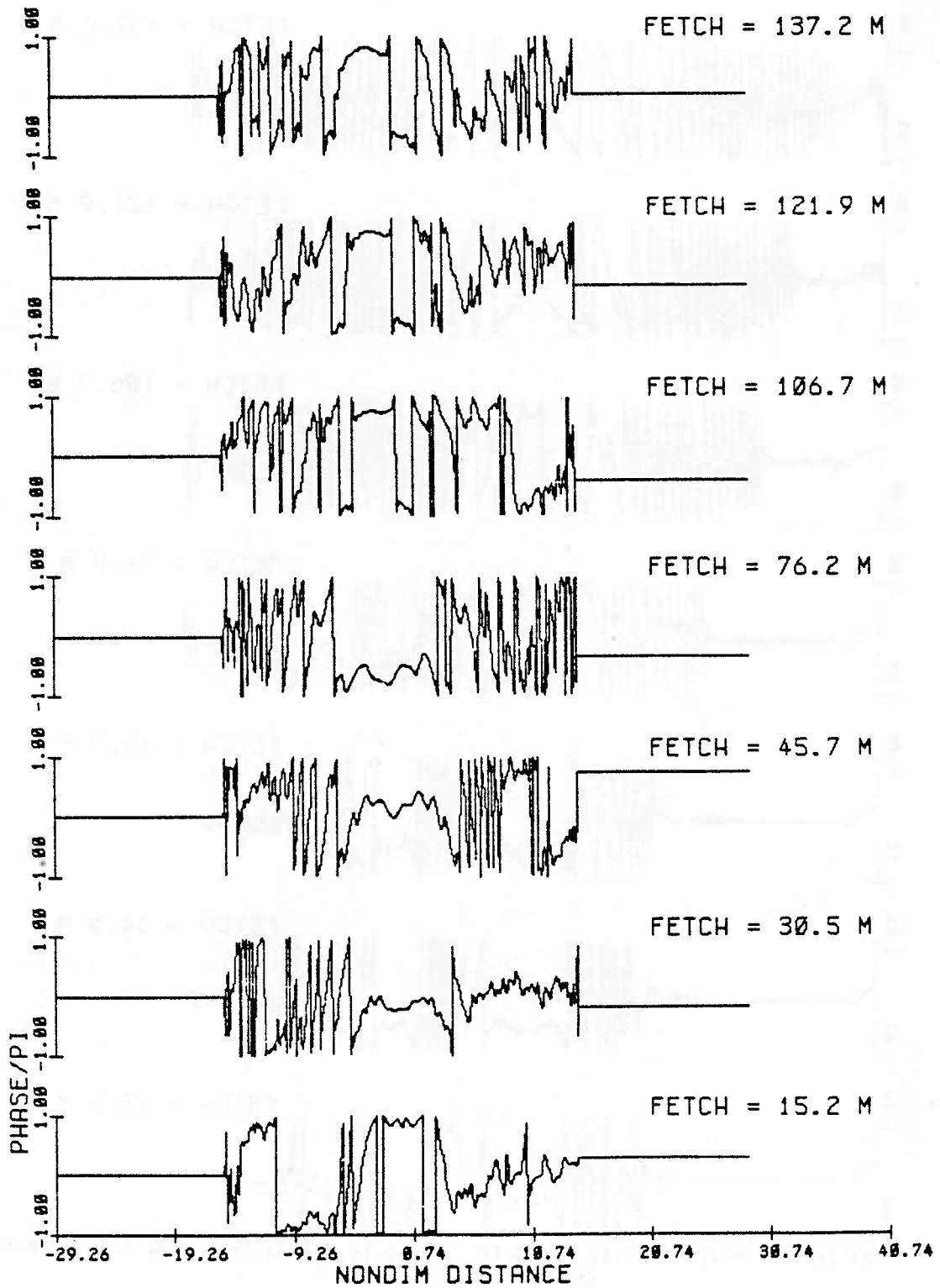


Fig. 3.32a Phase modulations from observations, principal value and normalized by pi, for successive fetches for the evolution of a group of 15 waves, initial steepness $ak = .10$ (Exp 87).

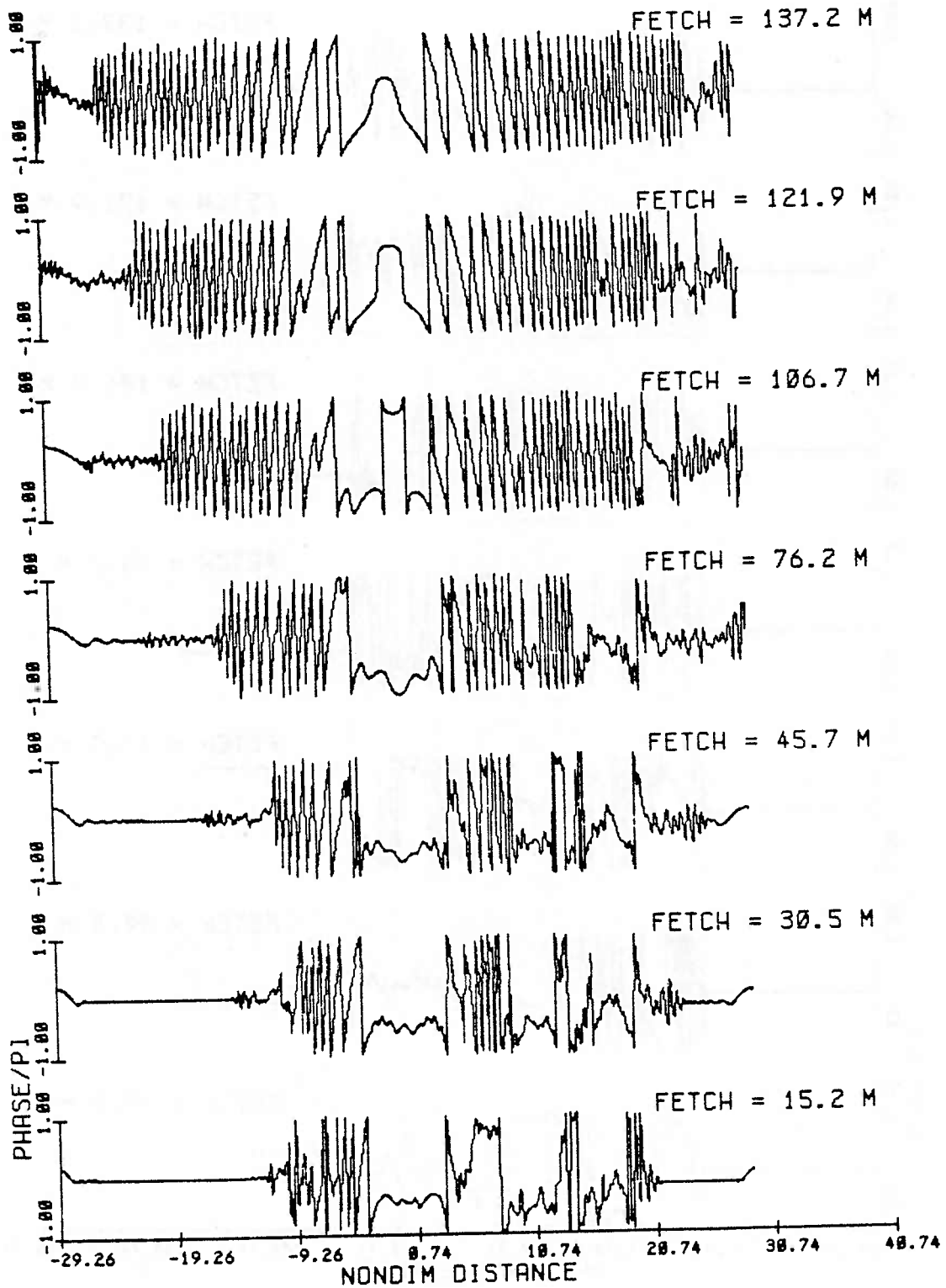


Fig. 3.32b Phase modulations from the inviscid NLS solution, at times-corresponding to the fetches in (a), for the evolution of a group of 15 waves, initial steepness $ak = .10$ (Exp 87).

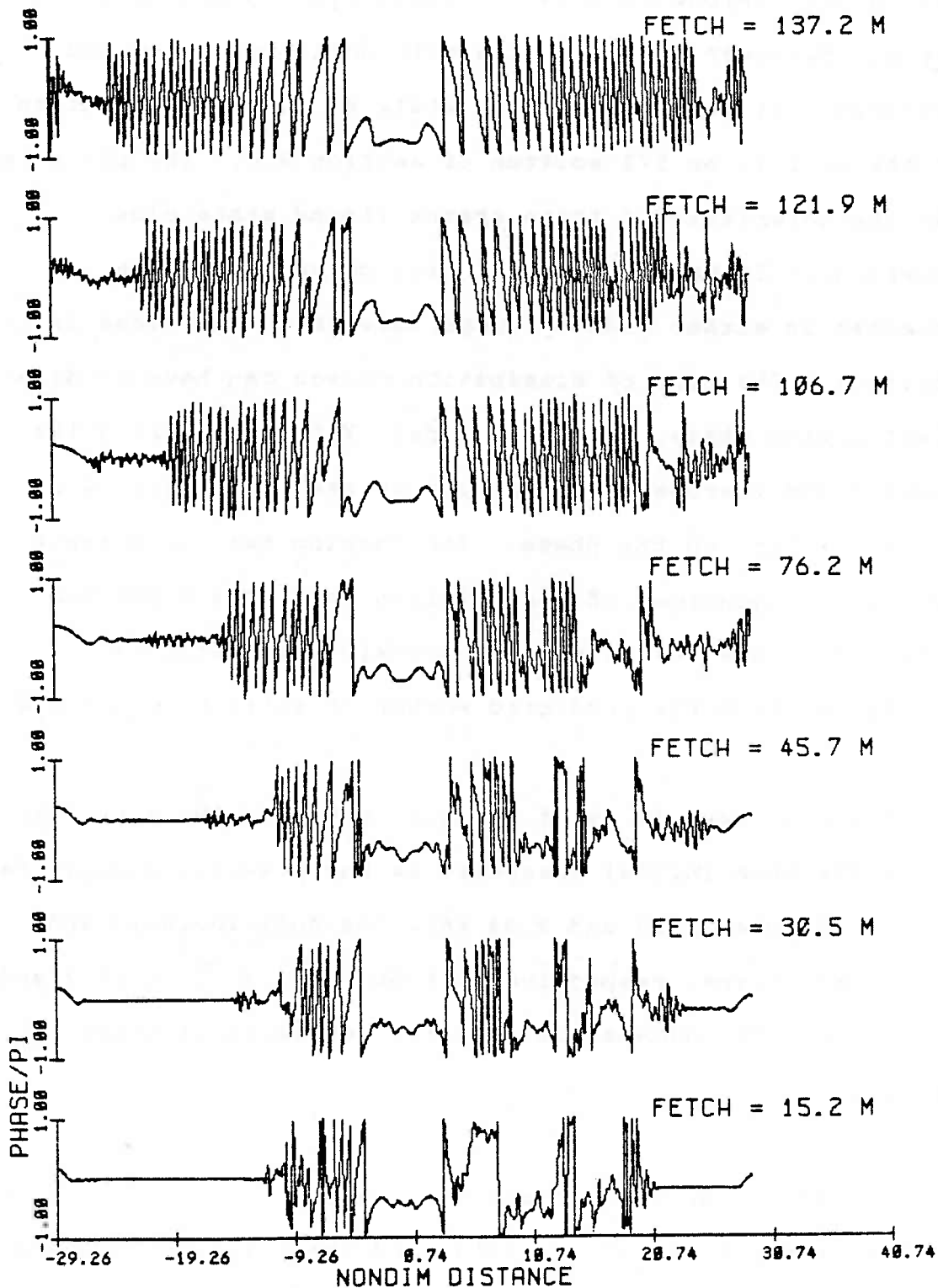


Fig. 3.32c Phase modulations from the viscous NLS solution, at times corresponding to the fetches in (a), for the evolution of a group of 15 waves, initial steepness $ak = .10$ (Exp 87).

(fig. 3.31b) beyond 76.2 meters shows growing modulation of a steeper, narrower central pulse with amplitude nodes and sidelobes. It is most like the state of maximum modulation for the 2, 3/2, or 5/2 soliton of section 3.4. The phase is also characteristic of these states (bound state plus radiation). It has a central region of uniform phase connected on either side by jumps located at the nodes in amplitude. The form of dissipation chosen can have no direct effect on the phase, only amplitude. Yet in comparing the inviscid and viscous model results we see that there is an indirect effect on the phase. The damping has, in a sense, changed the 'quantum' of the solution so that a 1-soliton asymptotic state is reached more quickly than might be anticipated from the predicted number of solitons $N_{s,T} = 1.8$.

The next example is of a longer group of 25 waves (Exp 88) of the same initial steepness as the previous example ($ak = .10$). Figures 3.33 and 3.34 show the full inviscid and viscous solutions, respectively, from $-31.3 < \xi < 31.3$ and $0 < \tau < 10$. The dimensional initial condition is shown in figure 3.35.

The amplitude modulations are plotted in fig. 3.36 a, b, c. The observations (fig. 3.36a) and the frictional numerical solution (fig. 3.36c) agree very well. Dissipation becomes important at 76.2 meters, as seen from comparison with the

Fig. 3.33 Inviscid NLS numerical evolution for a wave group of 25 waves, initial steepness $ak = .10$ (Exp 88). Spatial frame $-31.3 < X < 31.3$ and time interval $0 < T < 10$.

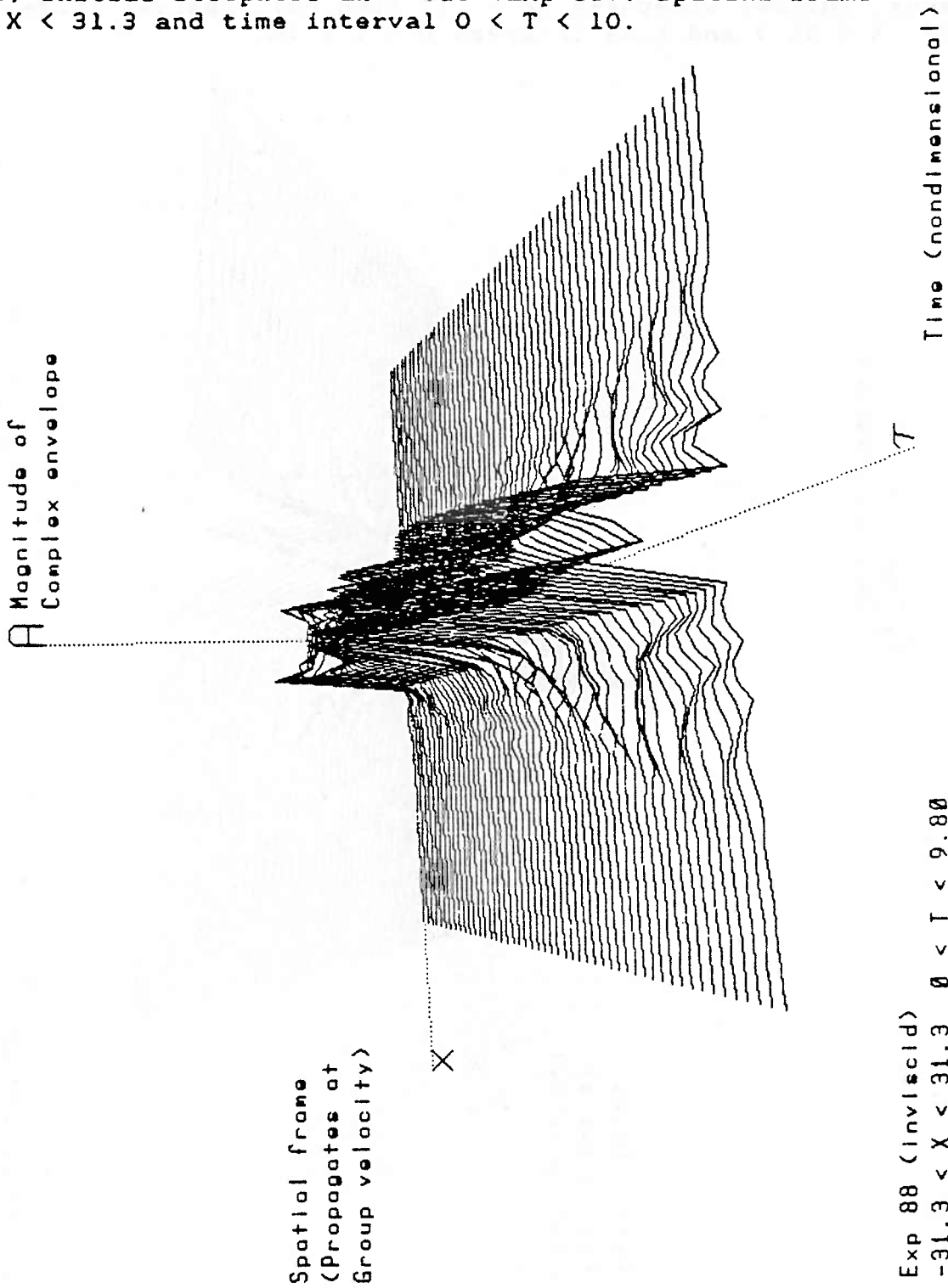
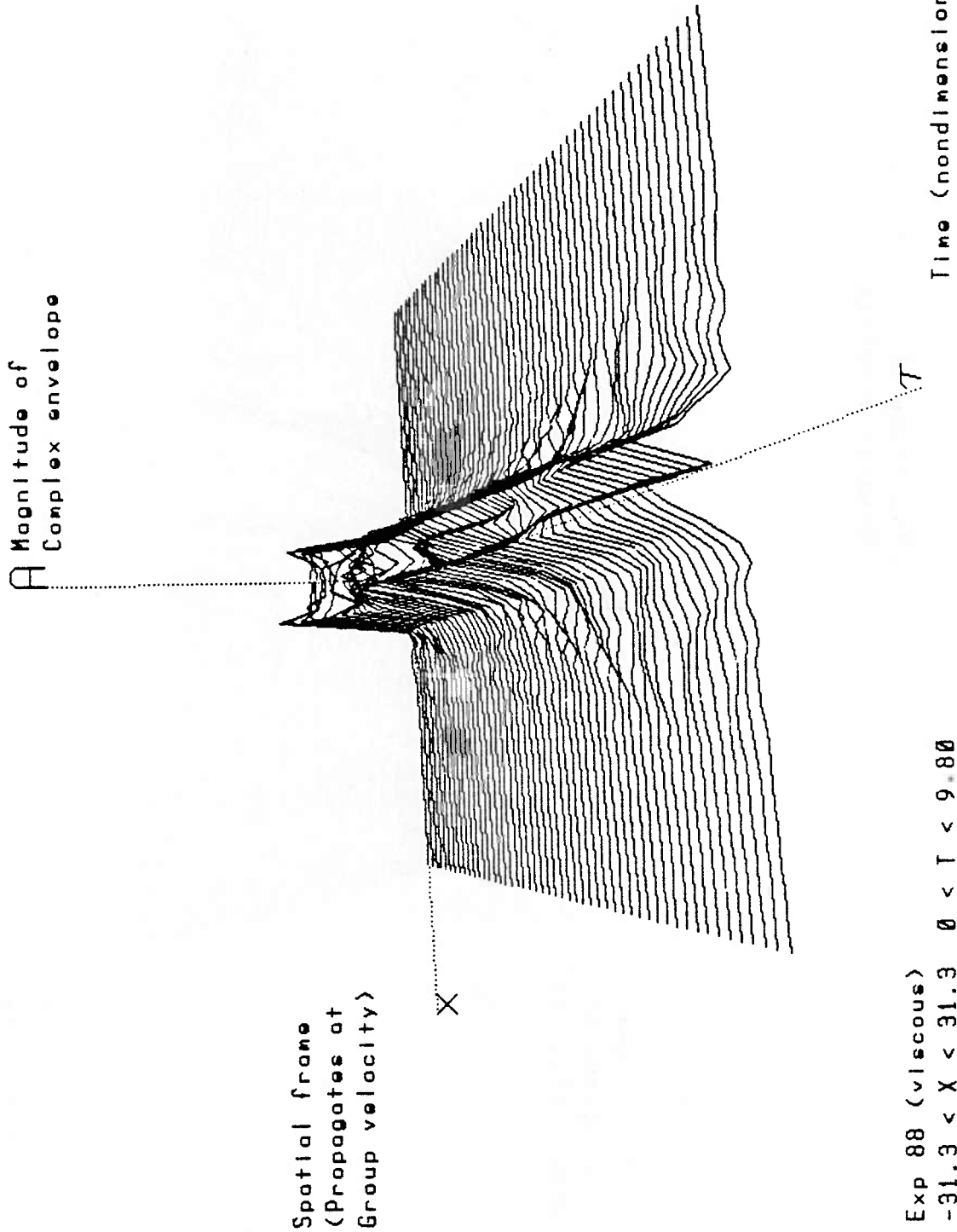


Fig. 3.34 Viscous NLS numerical evolution for a wave group of 25 waves, initial steepness $ak = .10$ (Exp 88). Spatial frame $-31.3 < X < 31.3$ and time interval $0 < T < 10$.



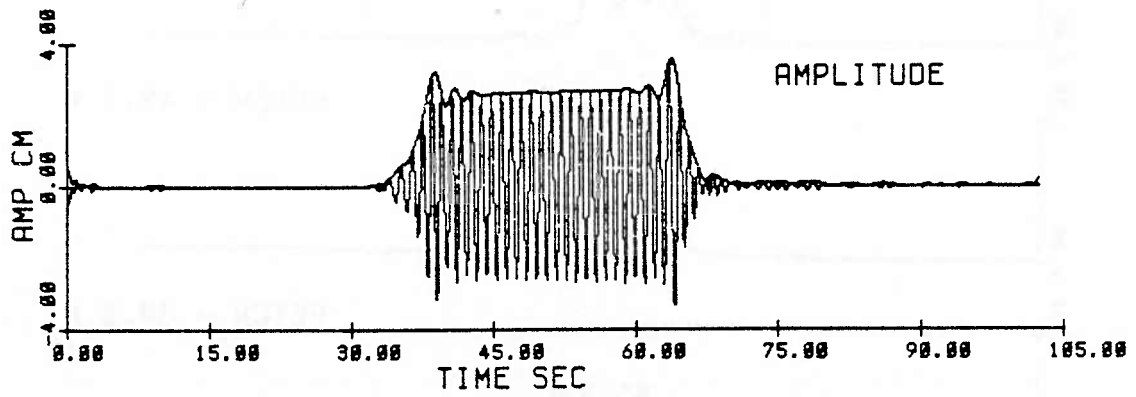
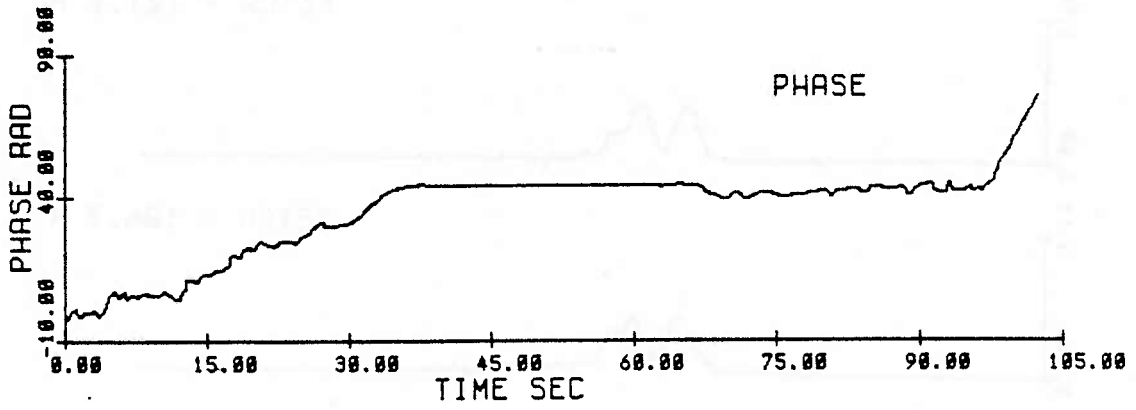


Fig 3.35 Initial condition at 6.1 m (E88)
ak = .10, N = 25

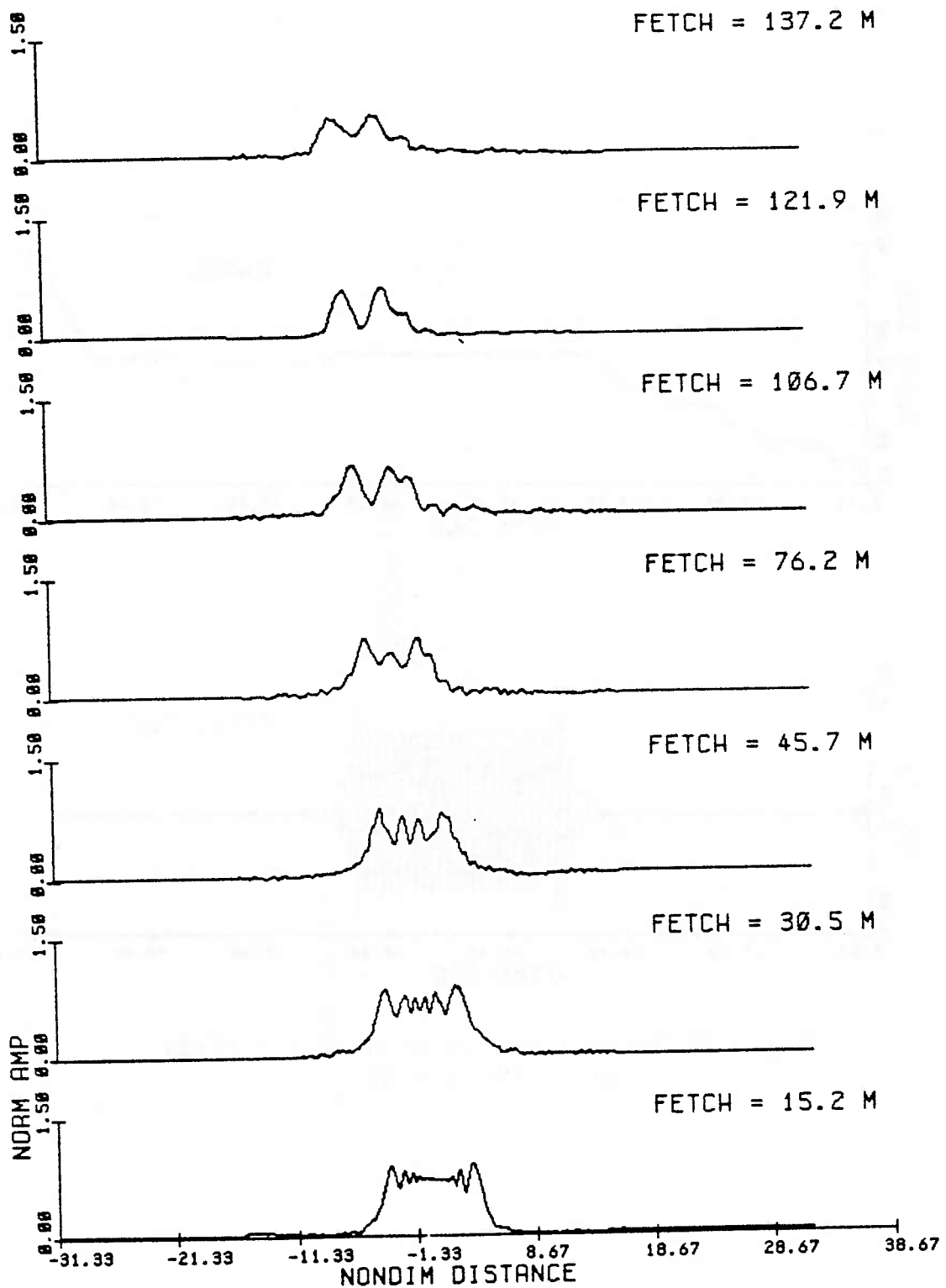


Fig. 3.36a Amplitude modulations from observations, nondimensionalized at each fetch by the initial condition scaling, for the evolution of a group of 25 waves, initial steepness $ak = .10$ (Exp 88).

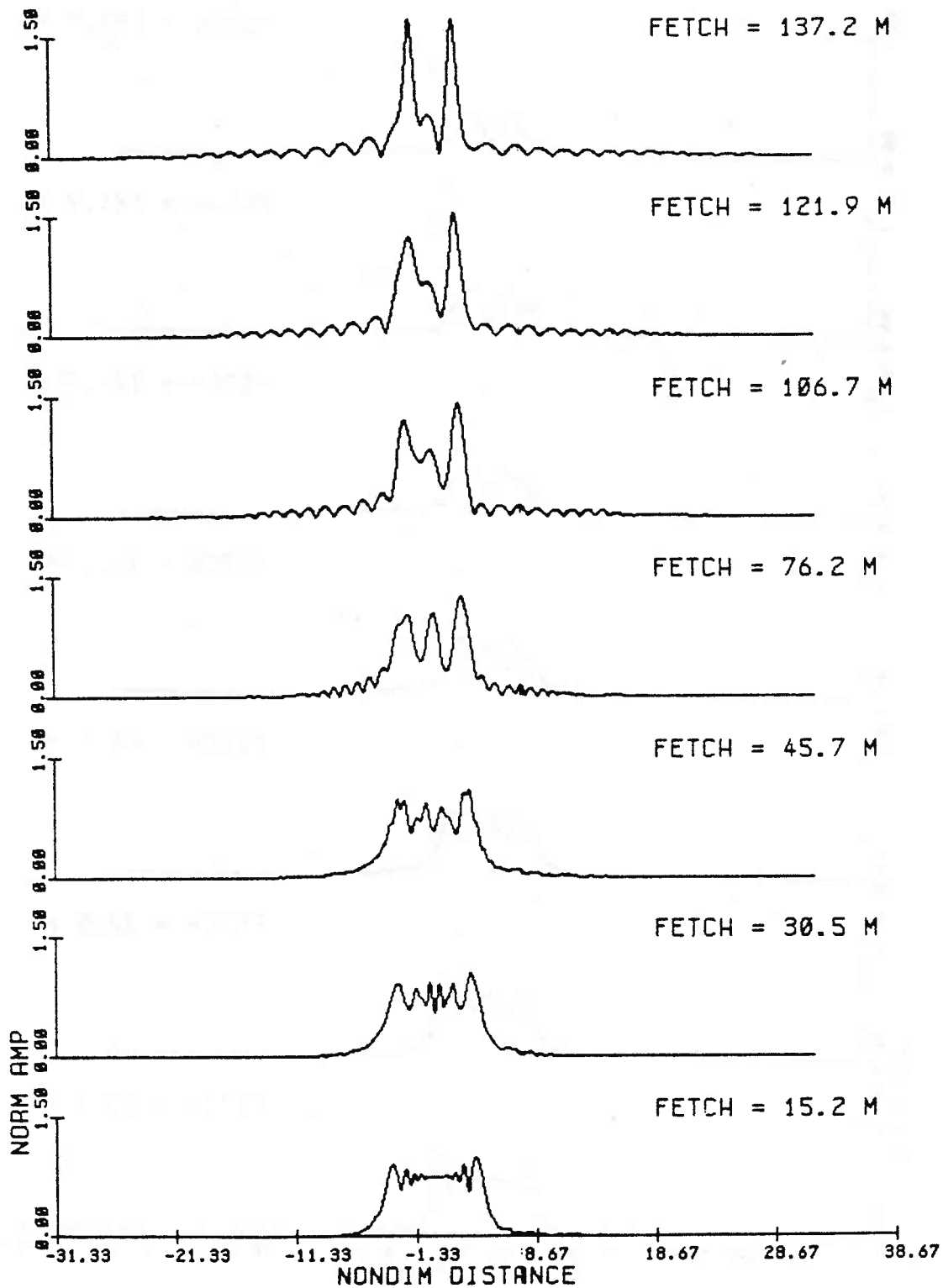


Fig. 3.36b Amplitude modulations from the inviscid NLS solution, at times corresponding to the fetches in (a), for the evolution of a group of 25 waves, initial steepness $ak = .10$ (Exp 88).

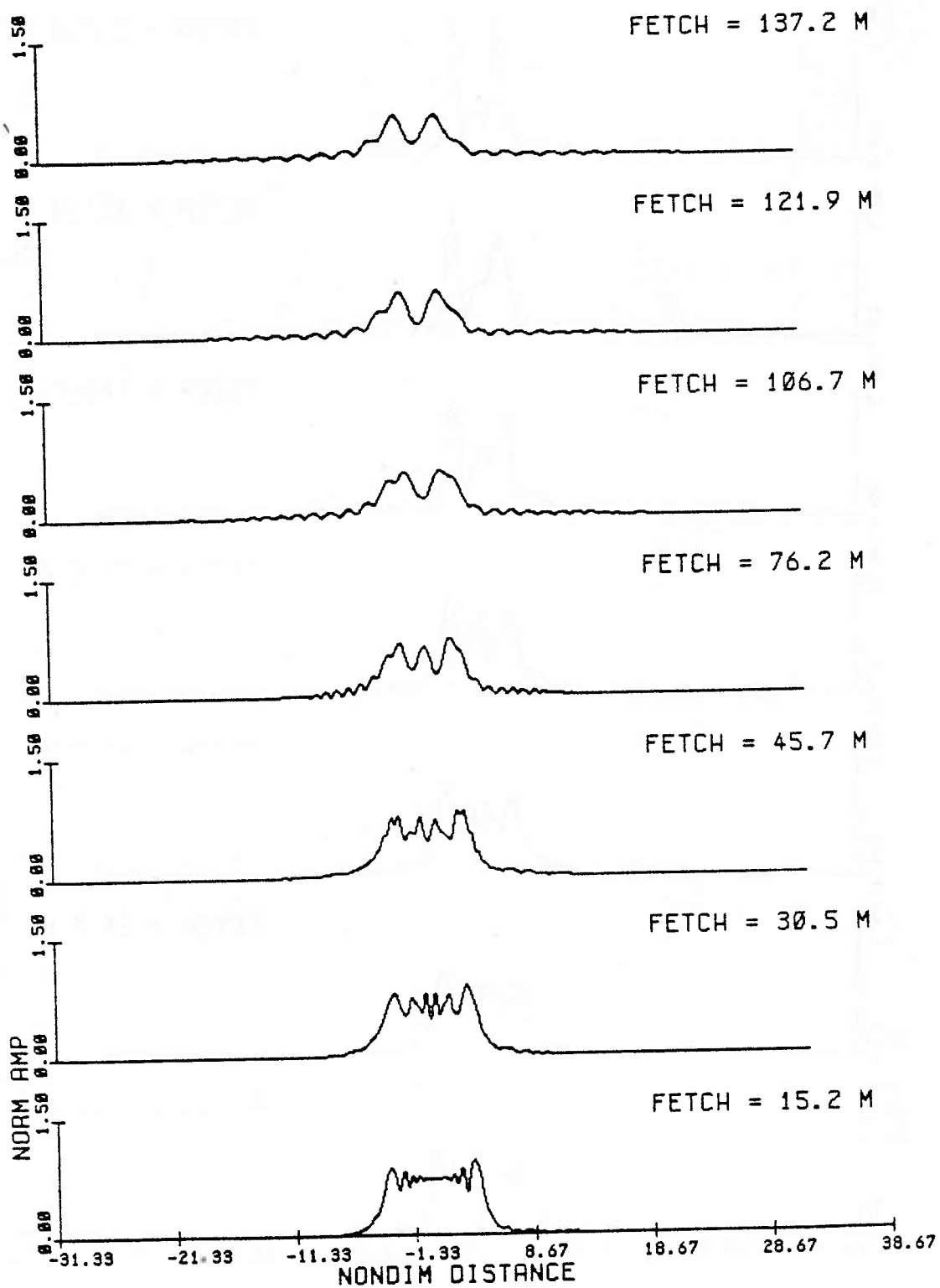


Fig. 3.36c Amplitude modulations from the viscous NLS solution, at times corresponding to the fetches in (a), for the evolution of a group of 25 waves, initial steepness $ak = .10$ (Exp 88).

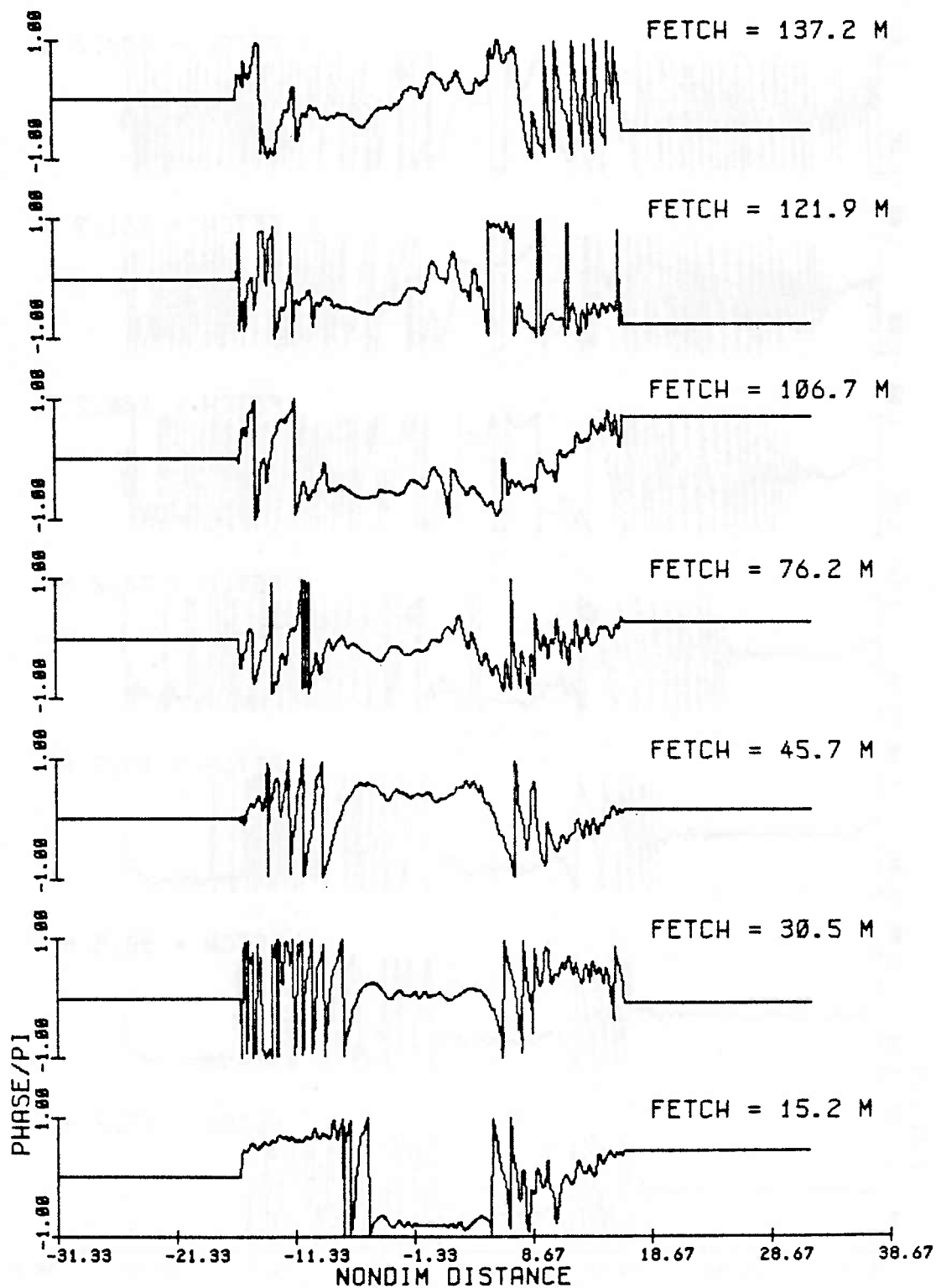


Fig. 3.37a Phase modulations from observations, principal value and normalized by pi, for successive fetches for the evolution of a group of 25 waves, initial steepness $ak = .10$ (Exp 88).

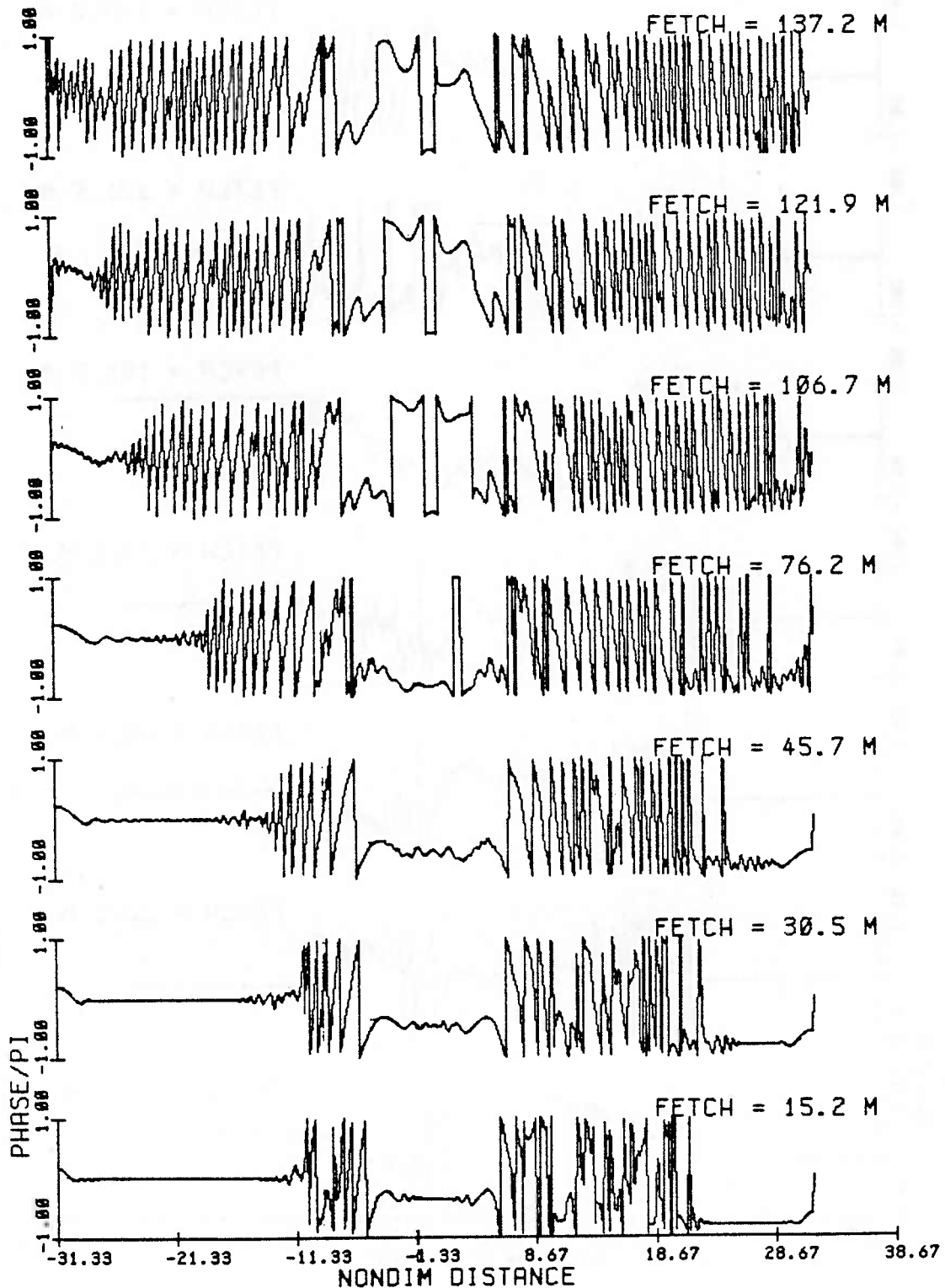


Fig. 3.37b Phase modulations from the inviscid NLS solution, at times corresponding to the fetches in (a), for the evolution of a group of 25 waves, initial steepness $ak = .10$ (Exp 88).

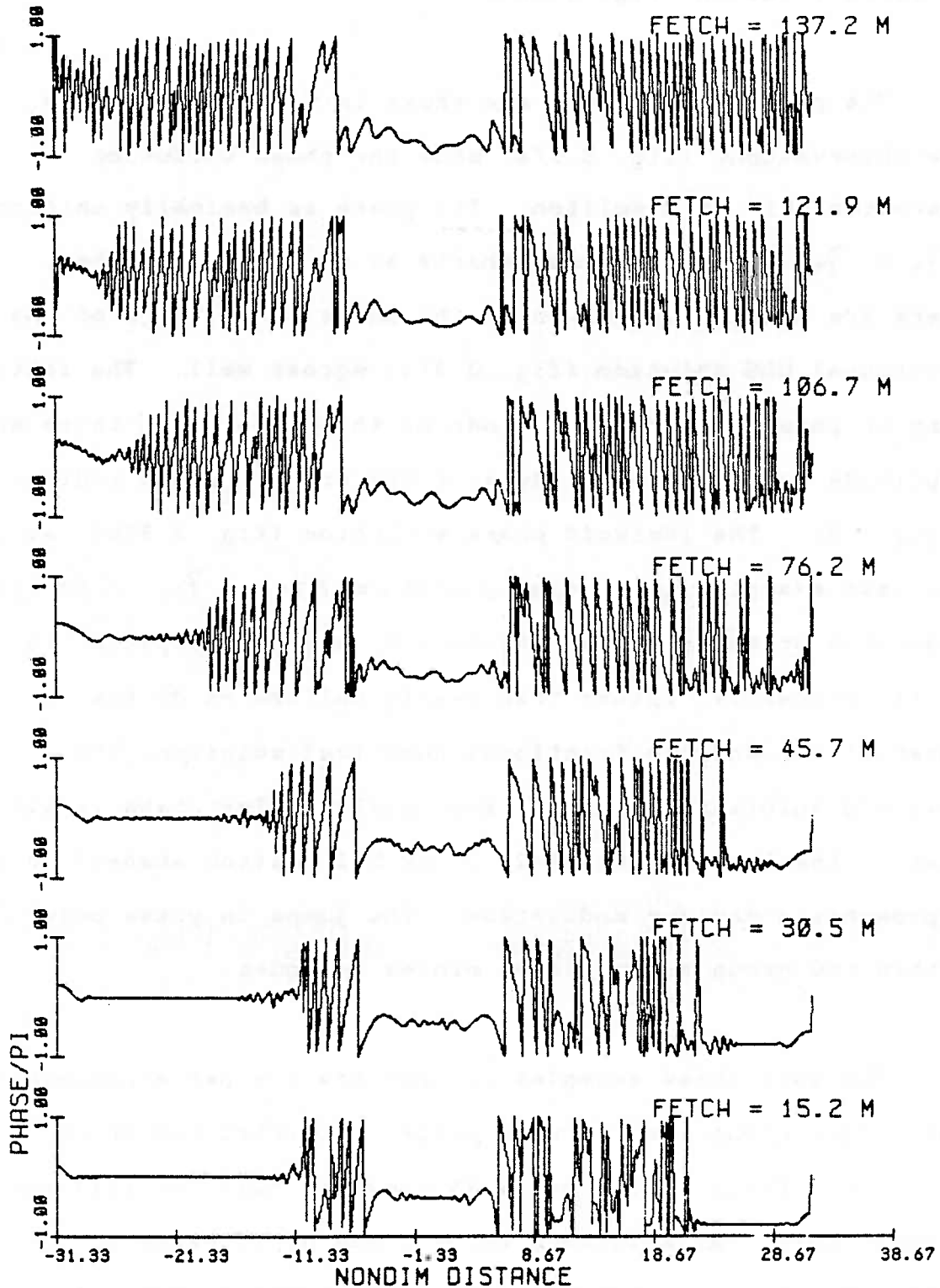


Fig. 3.37c Phase modulations from the viscous NLS solution, at times corresponding to the fetches in (a), for the evolution of a group of 25 waves, initial steepness $ak = .10$ (Exp 88).

inviscid solution (fig. 3.36b).

The phase modulations are shown in fig. 3.37 a, b, c. The observations (fig. 3.37a) show the phase evolution characteristic of a soliton. The phase is basically uniform ($P_{\xi} = P_{\xi\xi} = 0$) with small shifts at successive fetches. There are small undulations in the phase. The phase of the frictional NLS solution (fig. 3.37c) agrees well. The initial jump in phase occurs at the ends of the group where there are amplitude nodes. At the edges of the group, we see radiation ($P_{\xi\xi} < 0$). The inviscid phase evolution (fig. 3.37b), as in the last example, is initially uniform ($P_{\xi} = P_{\xi\xi} = 0$) like a soliton or bound state. At 76.2 m, where dissipation is first noticeable, rather than remain uniform as do the observations and the frictional numerical solution, the inviscid solution modulates (fig. 3.37b). The phase is like that of the bound state (3/2, 2, or 5/2 soliton states) as it approaches a maximum modulation. The jumps in phase occur within the group at amplitude minima or nodes.

The last three examples are for the steeper experiments and longer group lengths with larger estimated number of solitons. Figures 3.38 and 3.39 show the full inviscid and viscous numerical solutions for a group of 15 waves of steepness $ak = .15$ (Exp 62). They are computed for $-31.5 < \xi < 31.5$ and $0 < \tau < 40$. Figure 3.40 shows the initial

Fig. 3.39 Inviscid NLS numerical evolution for a wave group of 15 waves, initial steepness $ak = .15$ (Exp 62). Spatial frame $-31.5 < X < 31.5$ and time interval $0 < T < 40$.

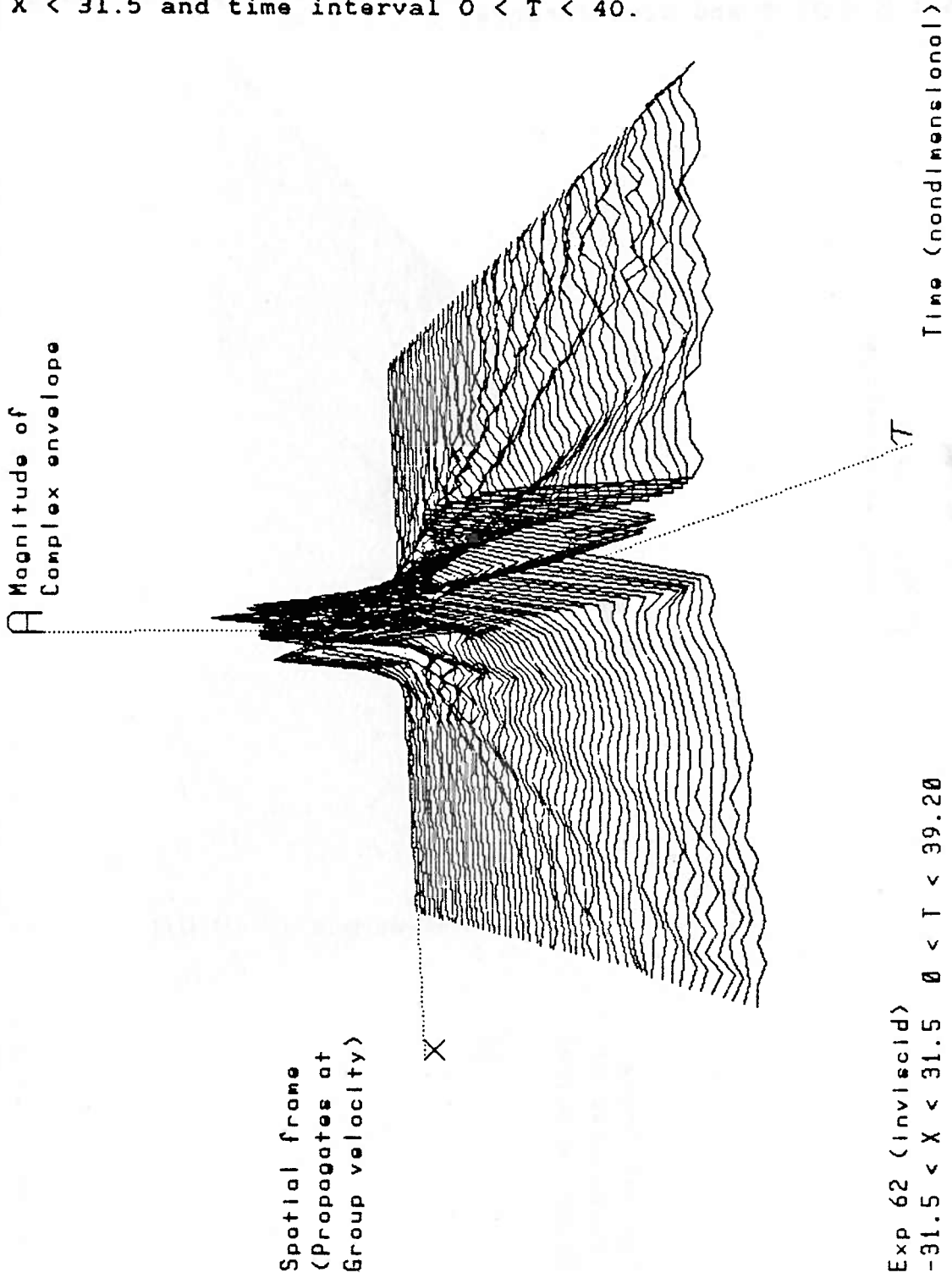
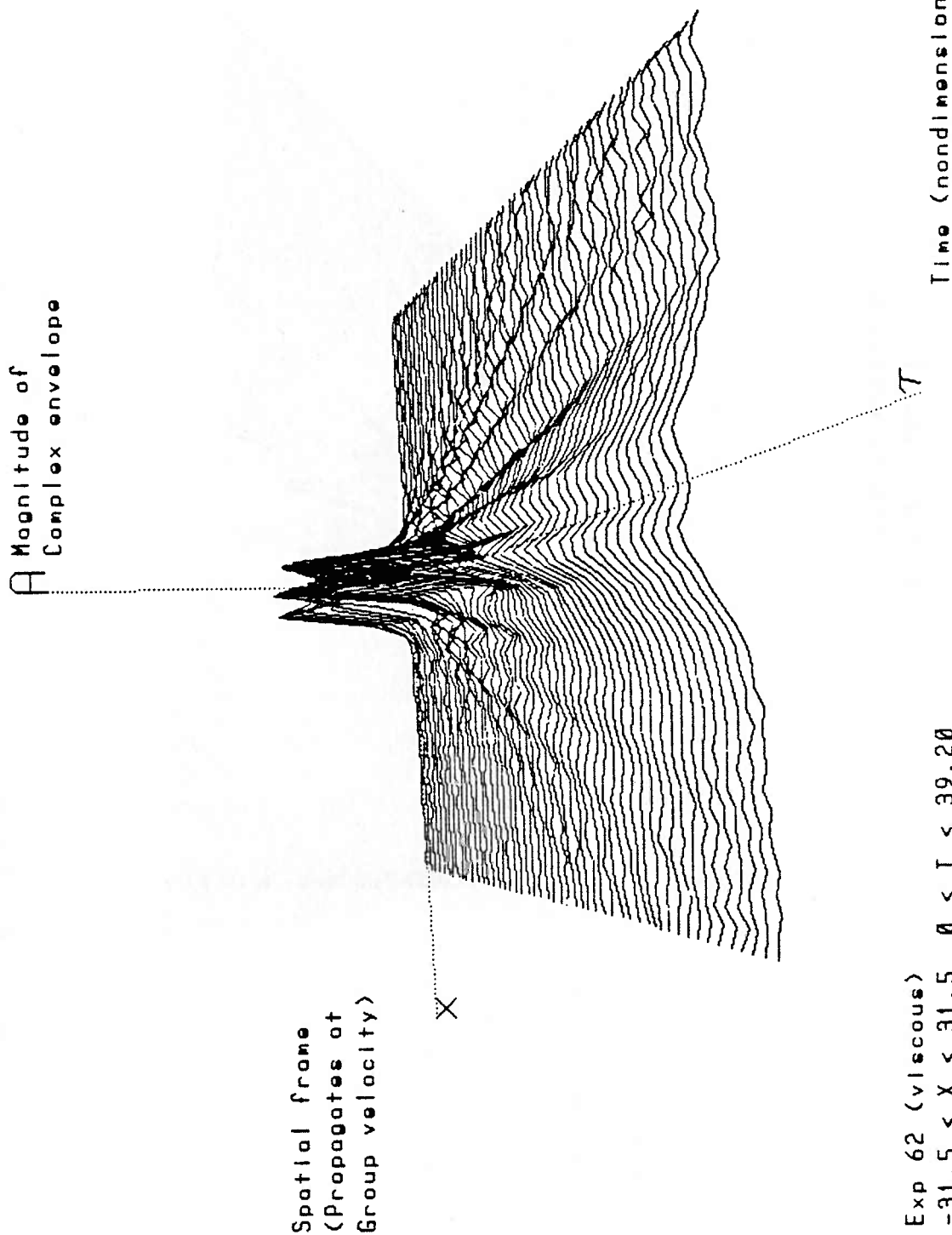


Fig. 3.39 Viscous NLS numerical evolution for a wave group of 15 waves, initial steepness $ak = .15$ (Exp 62). Spatial frame $-31.5 < X < 31.5$ and time interval $0 < T < 40$.



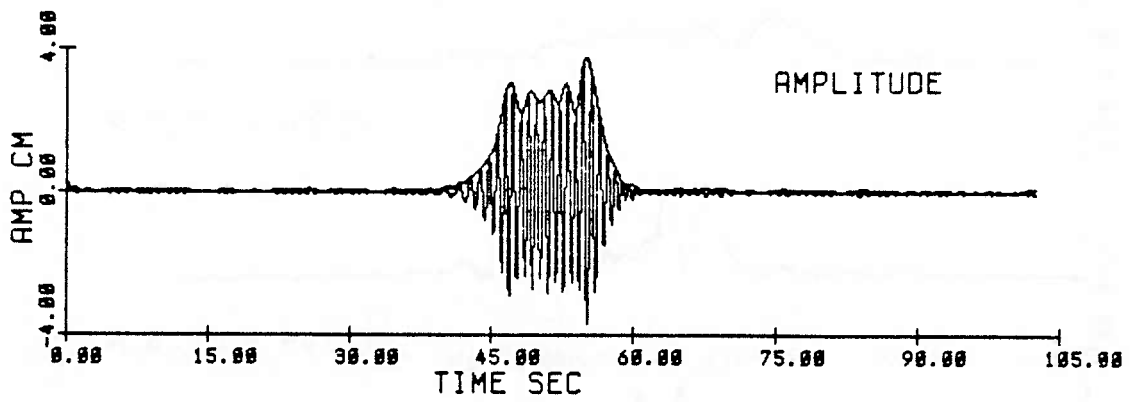
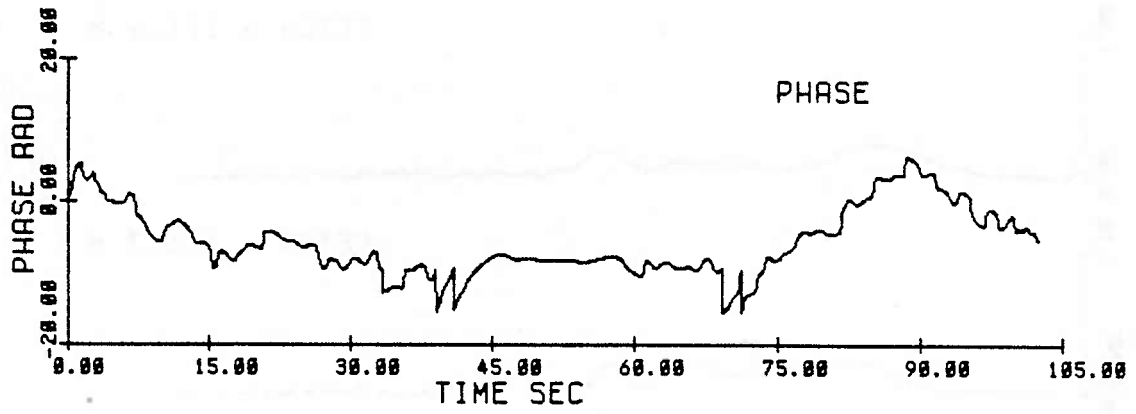


Fig 3.40 Initial condition at 6.1 m (E62)
ak = .15, N = 15

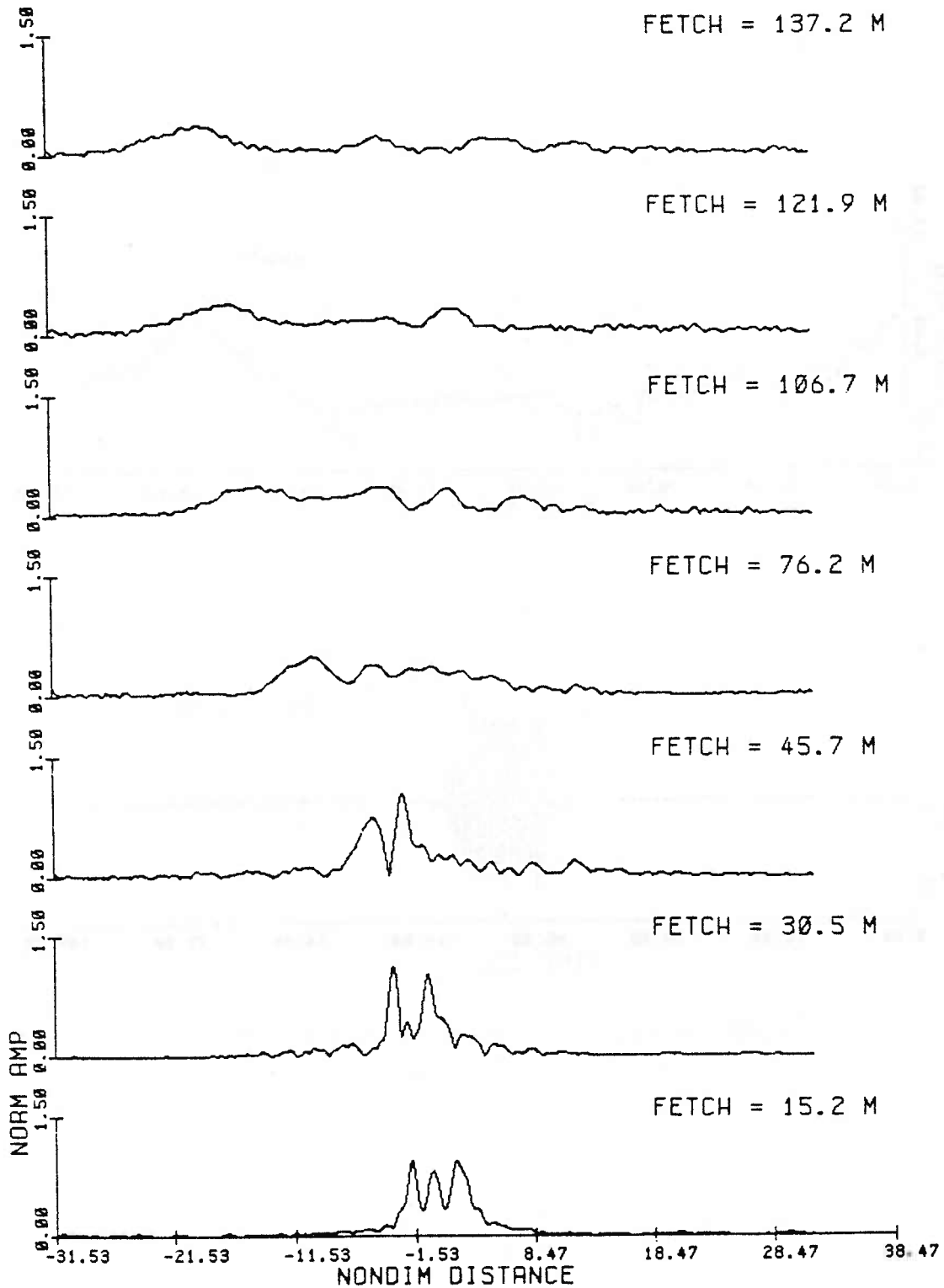


Fig. 3.41a Amplitude modulations from observations, nondimensionalized at each fetch by the initial condition scaling, for the evolution of a group of 15 waves, initial steepness $ak = .15$ (Exp 62).

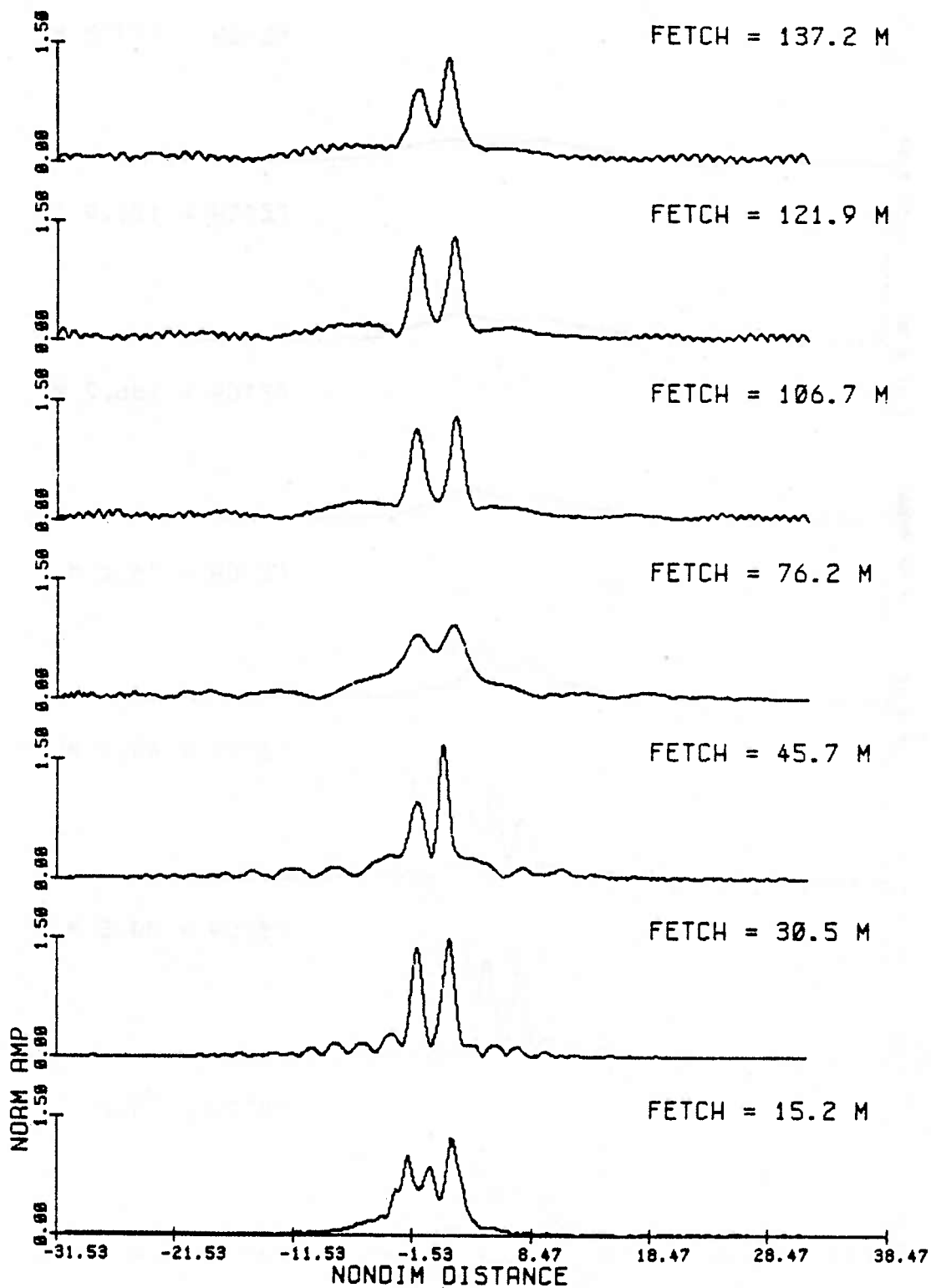


Fig. 3.41b Amplitude modulations from the inviscid NLS solution, at times corresponding to the fetches in (a), for the evolution of a group of 15 waves, initial steepness $ak = .15$ (Exp 62).

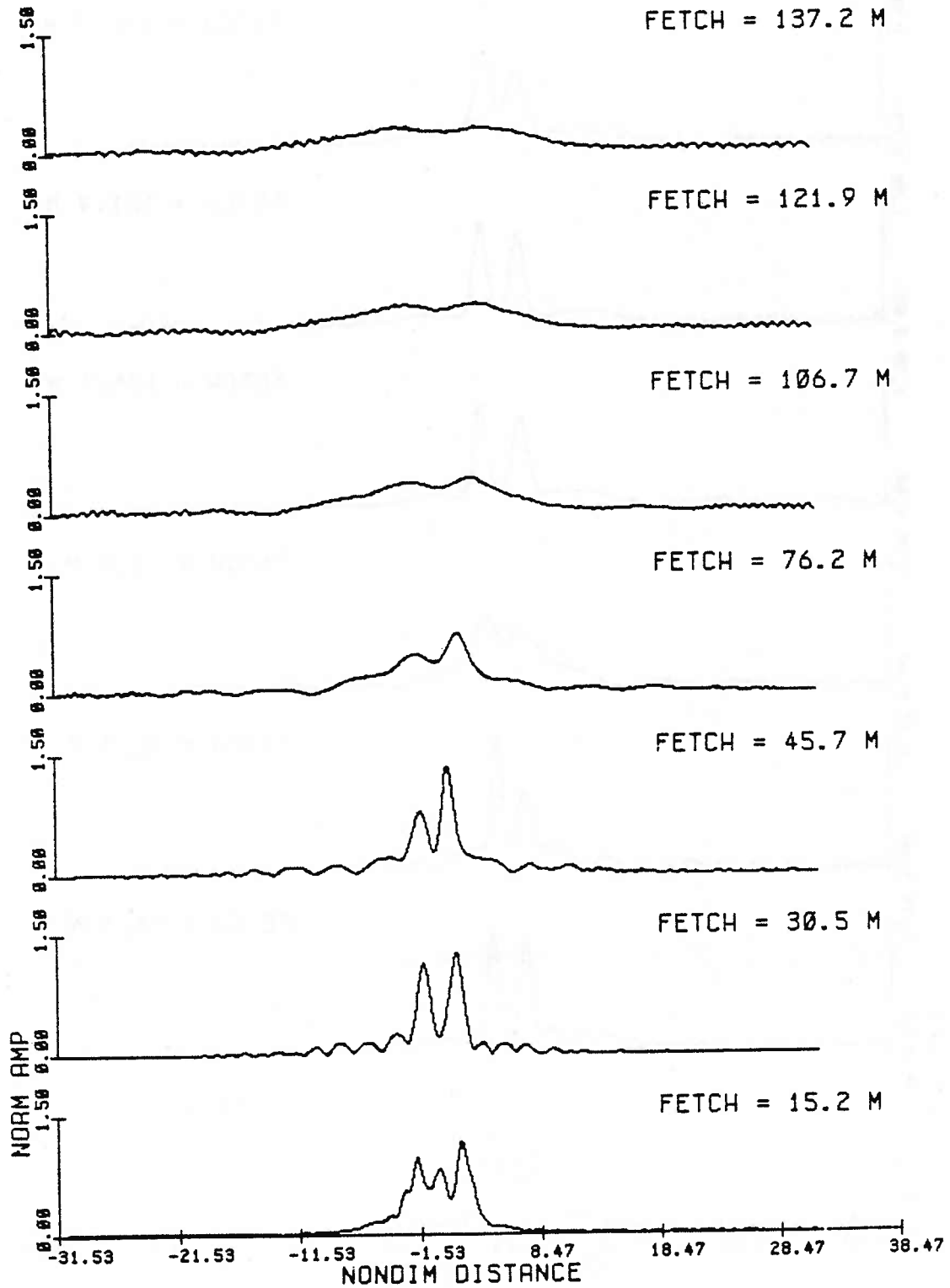


Fig. 3.41c Amplitude modulations from the viscous NLS solution, at times corresponding to the fetches in (a), for the evolution of a group of 15 waves, initial steepness $ak = .15$ (Exp 62).

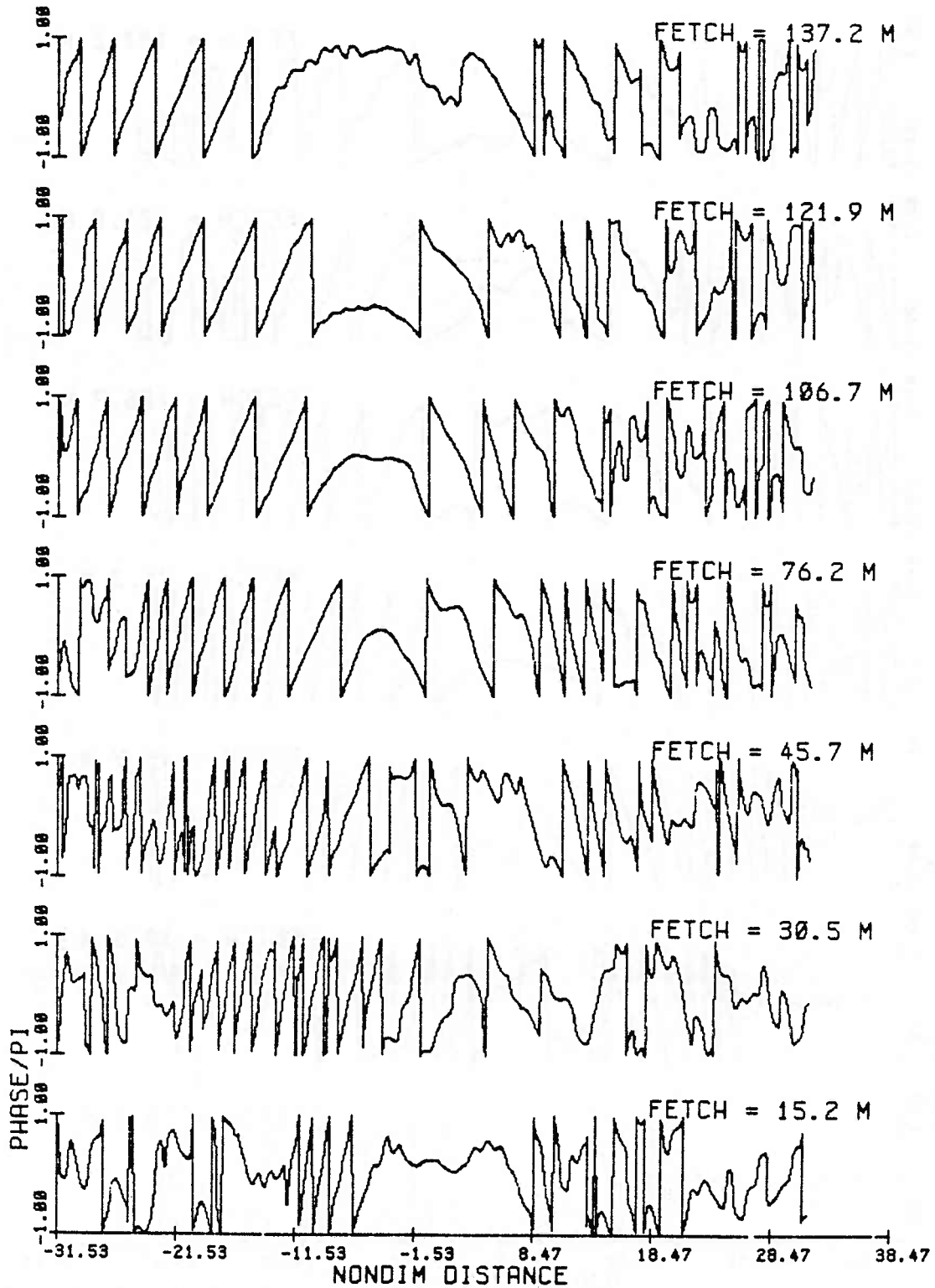


Fig. 3.42a Phase modulations from observations, principal value and normalized by pi, for successive fetches for the evolution of a group of 15 waves, initial steepness $ak = .15$ (Exp 62).

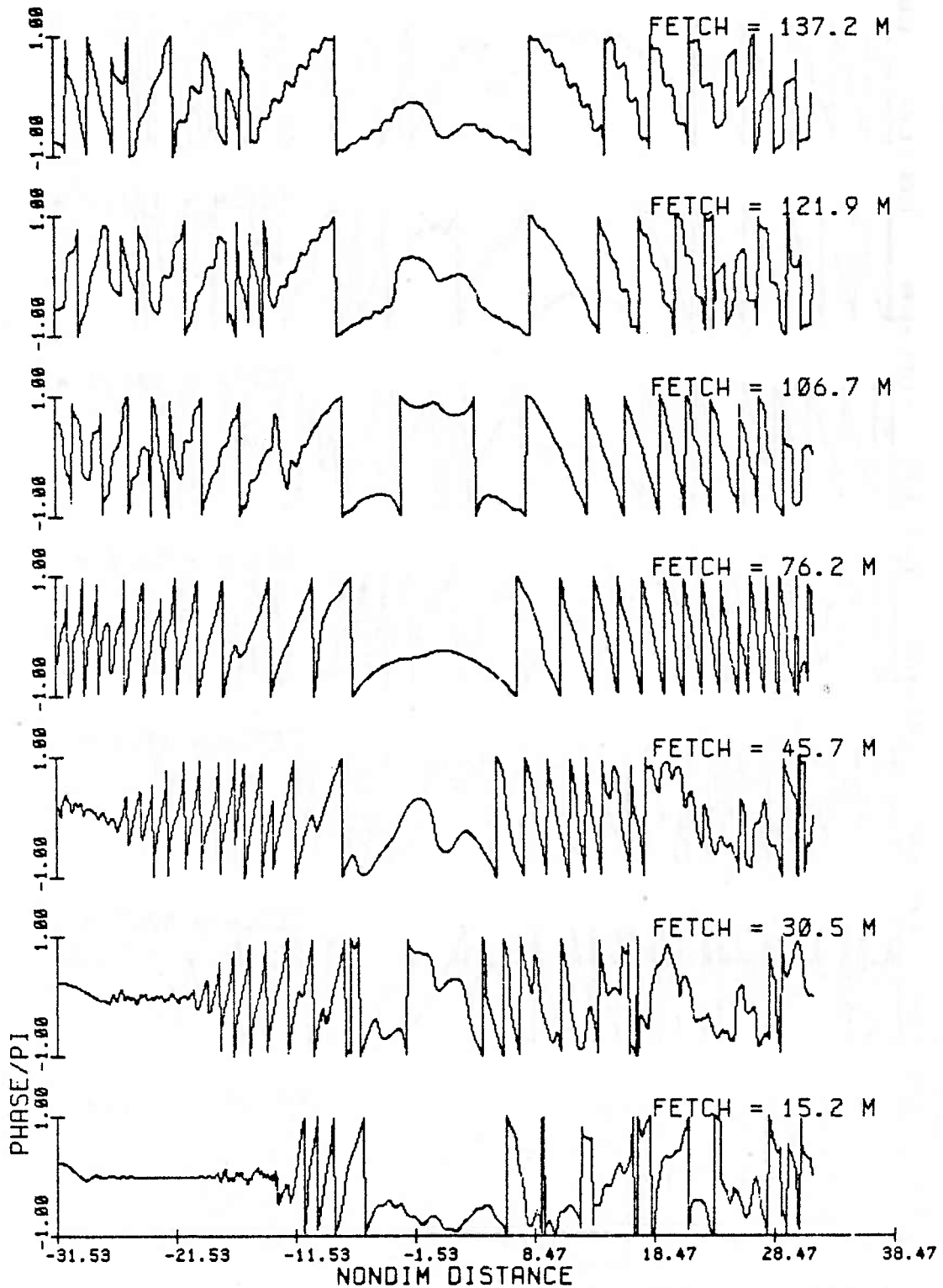


Fig. 3.42b Phase modulations from the inviscid NLS solution, at times corresponding to the fetches in (a), for the evolution of a group of 15 waves, initial steepness $ak = .15$ (Exp 62).

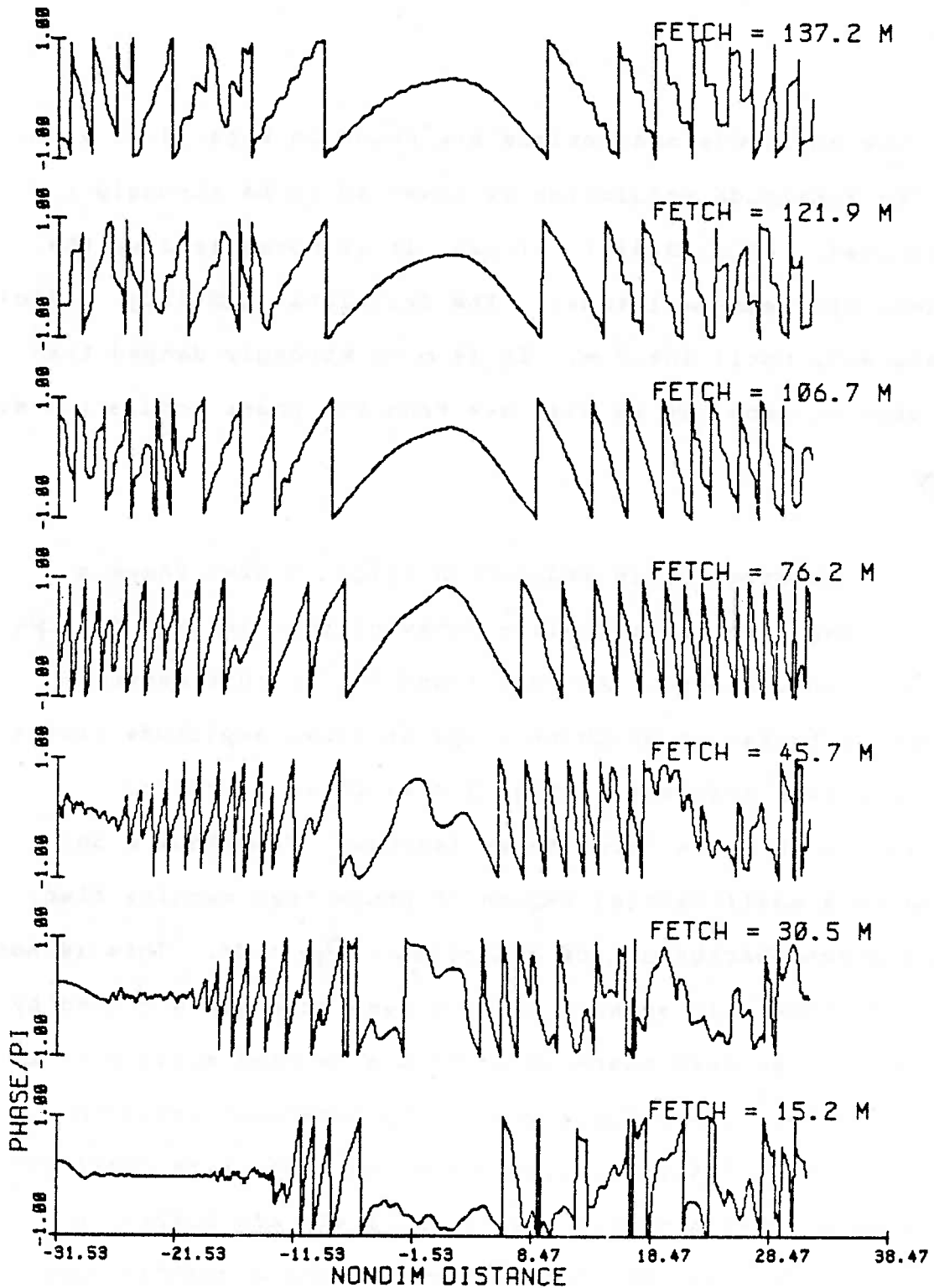


Fig. 3.42c Phase modulations from the viscous NLS solution, at times corresponding to the fetches in (a), for the evolution of a group of 15 waves, initial steepness $ak = .15$ (Exp 62).

condition. The estimated number of solitons is 2.9 (Table 2.2).

The amplitude modulations are shown in figs. 3.41 a, b, c. The amplitude modulation is observed to be strongly attenuated. (fig. 3.41a). (Also, it is normalized by the maximum upstream amplitude). The frictional NLS (fig. 3.41c) agrees well until 106.7 m. It is more strongly damped than the observations, as we will see from the phase modulation as well.

The observed phase modulation (figs. 3.42a) shows a central region of soliton-like behavior that is uniform ($P_{\gamma} = 0$), with undulations. At 30.5 m and 45.7 m this central region is broken up by phase jumps at local amplitude minima. The amplitude modulation (fig. 3.41a) shows a growing modulation at these first three fetches. From 76.2 m on, there is a small central region of phase that remains flat, and a strong background of radiation ($P_{\gamma} < 0$). This is not a bound state; it appears to have been strongly affected by dissipation so that there is perhaps a central soliton in a background of linear dispersion. The numerical inviscid solution (fig. 3.42b) indicates a bound state type character. There is a growing modulation (figs. 3.41b and 3.42b), a slight demodulation at 76.2 m where the phase becomes more uniform, followed by growing modulation. The phase modulation

(fig. 3.42b) contains jumps within the group. The frictional solution (fig. 3.41c), from amplitude modulation, is more strongly damped than the observations. The phase modulation (fig. 3.42c) suggests that it is totally dominated by radiation.

The next example is for a group of 15 waves of steepness $ak = .16$ (Exp 22). Figures 3.43 and 3.44 show the full numerical solutions. Figure 3.45 shows the dimensional initial condition. The evolution was done for $-33.5 < \gamma < 33.5$ and $0 < \bar{t} < 45$.

The amplitude modulations are shown in figs. 3.46 a, b, c. The observations (fig. 3.46a) and the frictional NLS solution (fig. 3.46c) agree fairly well. Dissipation becomes important at 76.2 meters.

The phase modulations are shown in figs. 3.47 a,b,c. As in the previous case for the same group length and slightly smaller steepness, there appears to be more coherence in the observed phase modulation (fig. 3.47a) than linear dispersion would give. The central region of phase is uniform with jumps occurring within the group where local amplitude minima occur (45.7 m, 76.2 m). The bound state type of modulation, with growing and decaying modulation, is observed in the inviscid model solution (fig. 3.47b) but not in the observations. The

Fig. 3.43 Inviscid NLS numerical evolution for a wave group of 15 waves, initial steepness $ak = .16$ (Exp 22). Spatial frame $-33.5 < X < 33.5$ and time interval $0 < T < 45$.

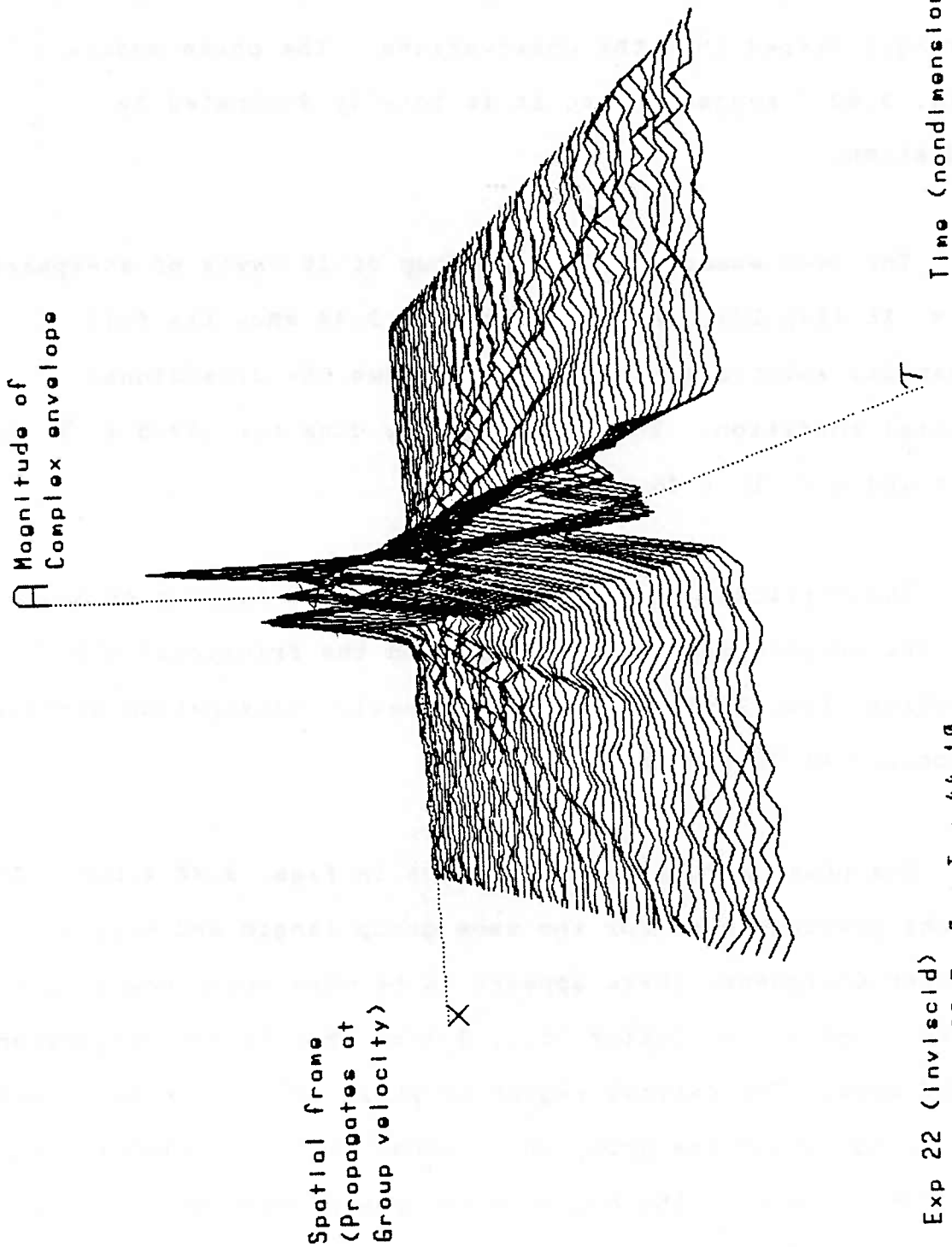
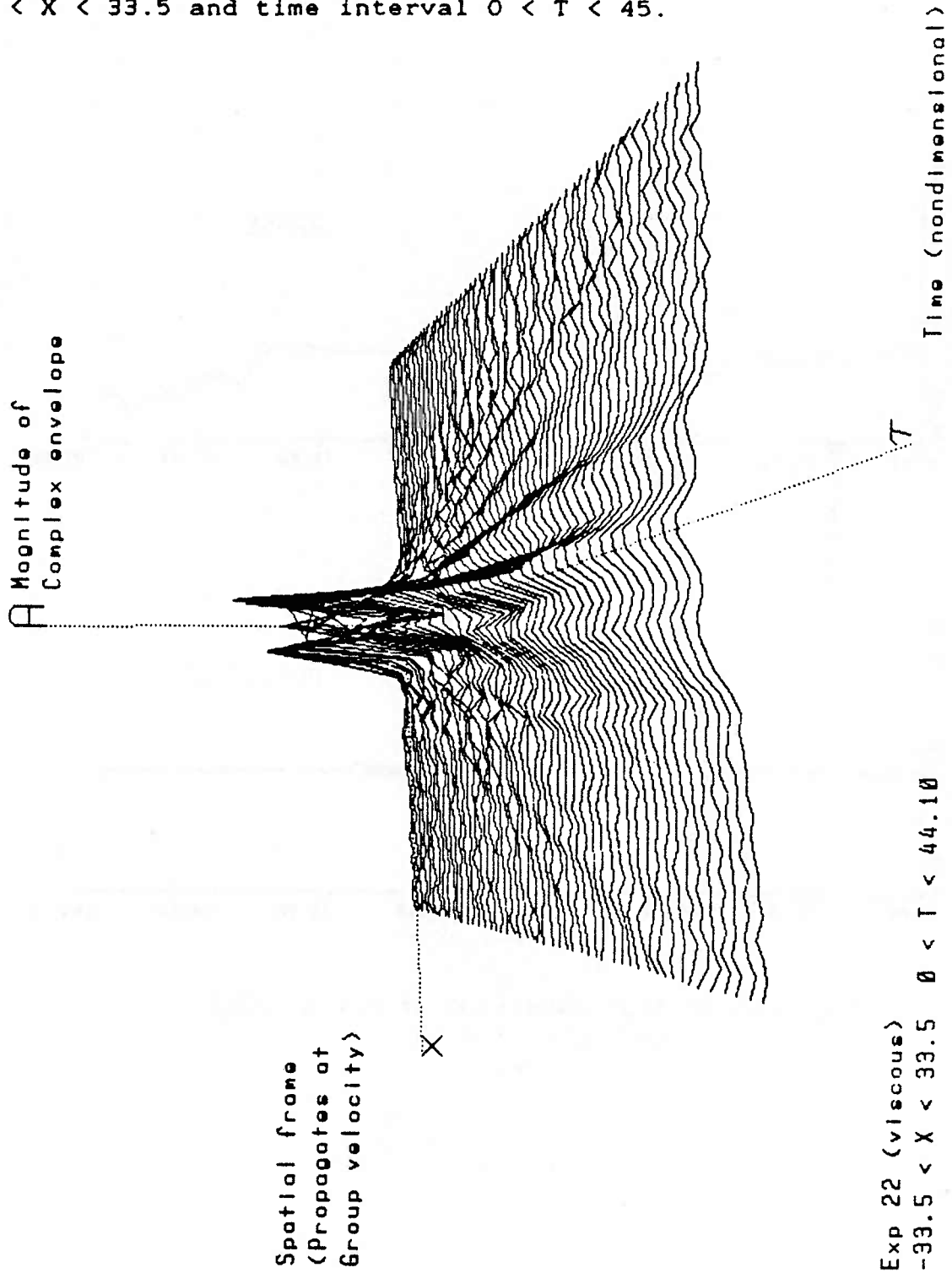


Fig. 3.44 Viscous NLS numerical evolution for a wave group of 15 waves, initial steepness $ak = .16$ (Exp 22). Spatial frame $-33.5 < X < 33.5$ and time interval $0 < T < 45$.



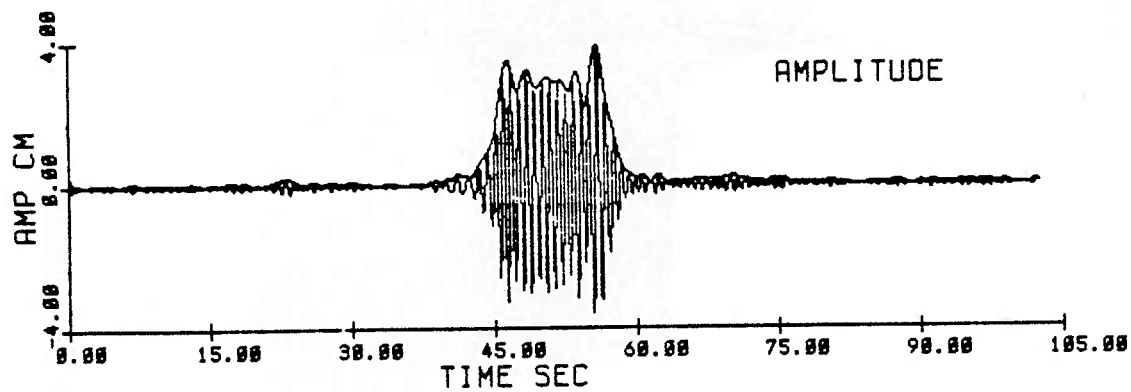
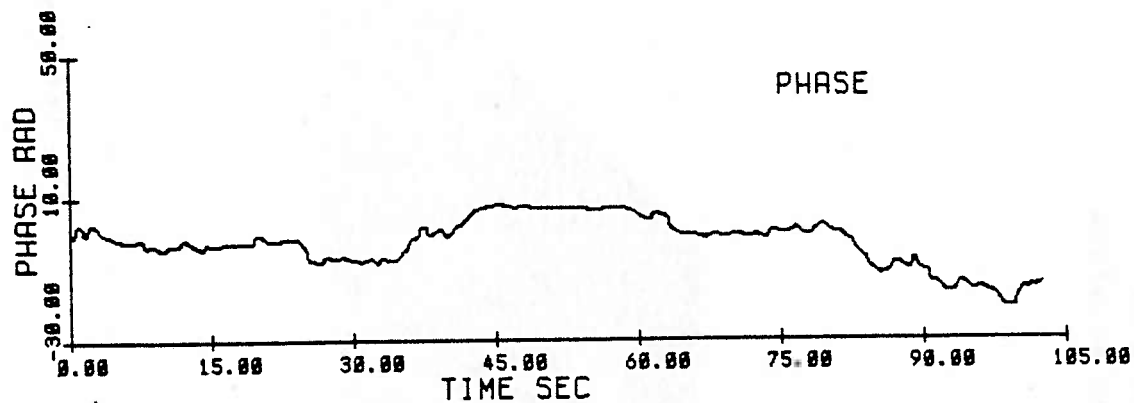


Fig 3.45 Initial condition at 6.1 m (E22)
ak = .16, N = 15

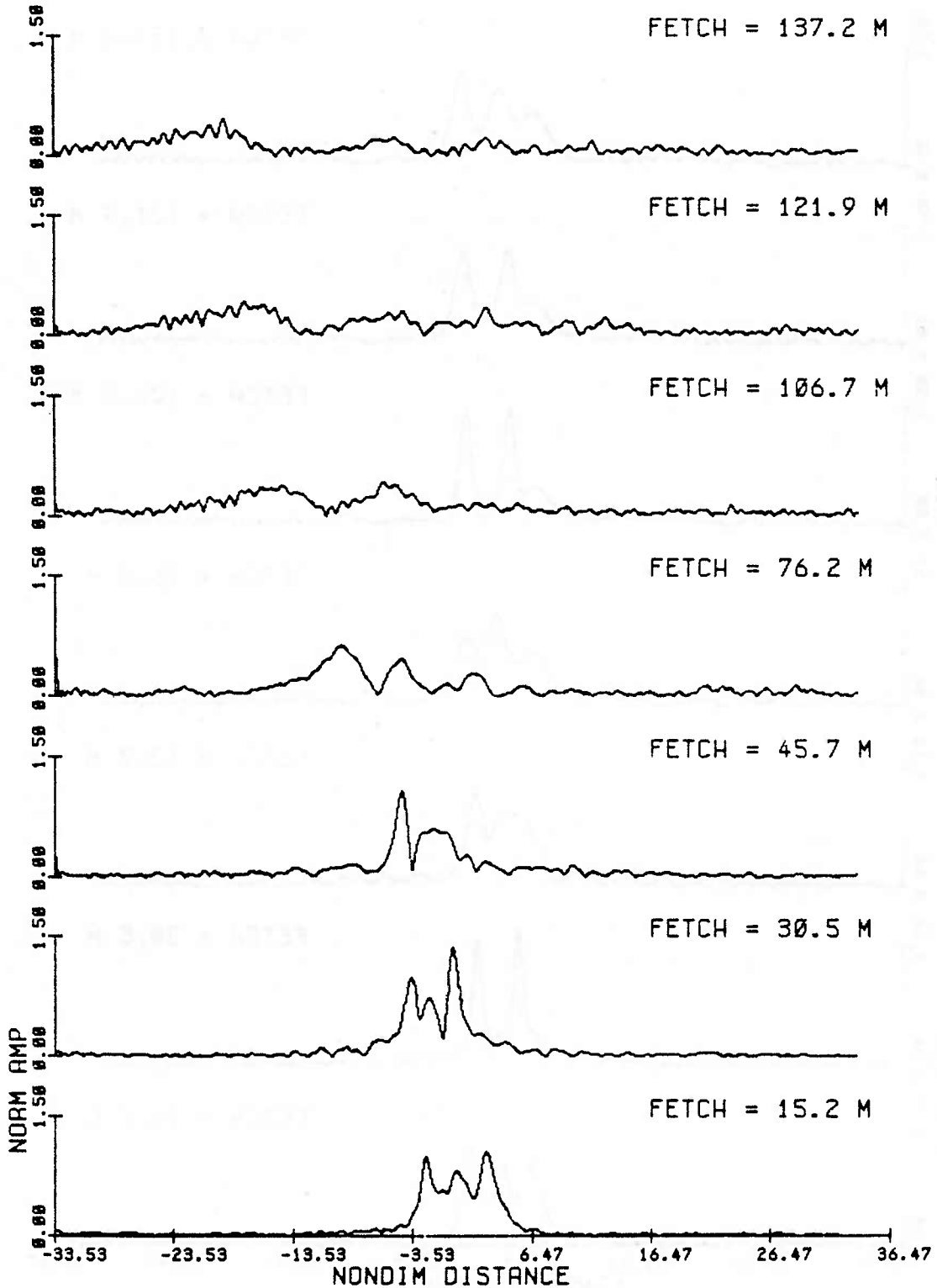


Fig. 3.46a Amplitude modulations from observations, nondimensionalized at each fetch by the initial condition scaling, for the evolution of a group of 15 waves, initial steepness $ak = .16$ (Exp 22).

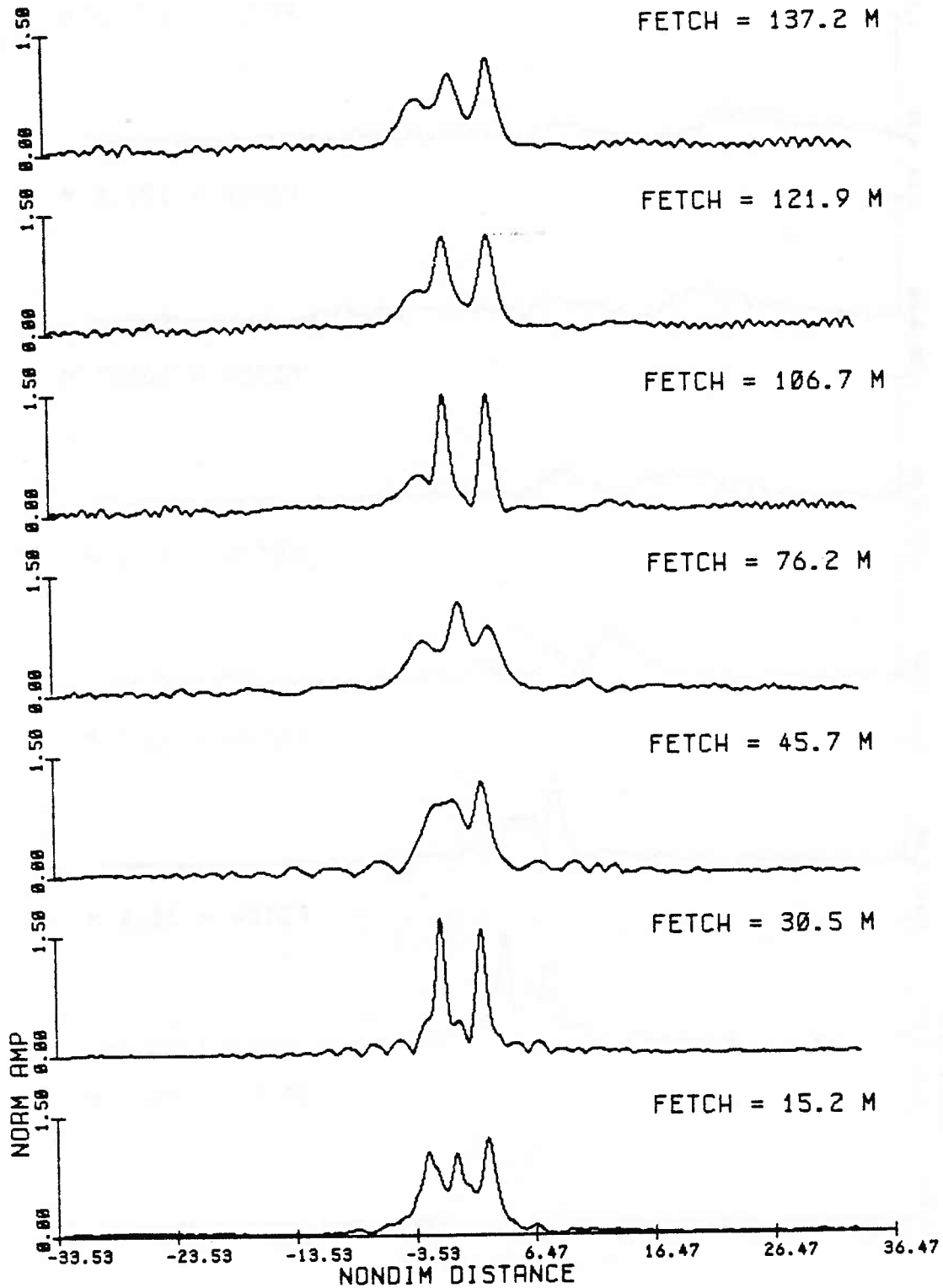


Fig. 3.46b Amplitude modulations from the inviscid NLS solution, at times corresponding to the fetches in (a), for the evolution of a group of 15 waves, initial steepness $ak = .16$ (Exp 22).

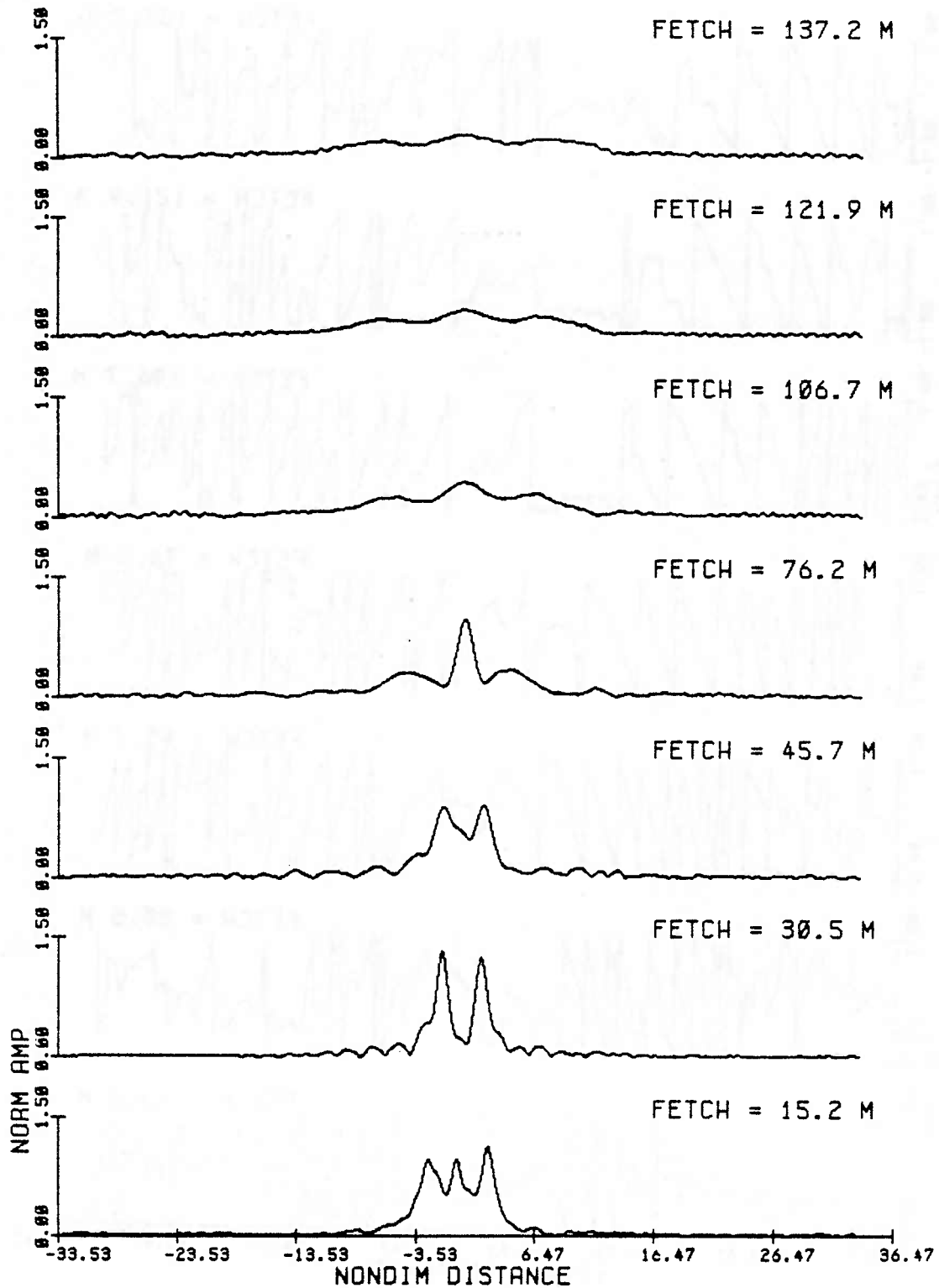


Fig. 3.46c—Amplitude modulations from the viscous NLS solution, at times corresponding to the fetches in (a), for the evolution of a group of 15 waves, initial steepness $ak = .16$ (Exp 22).

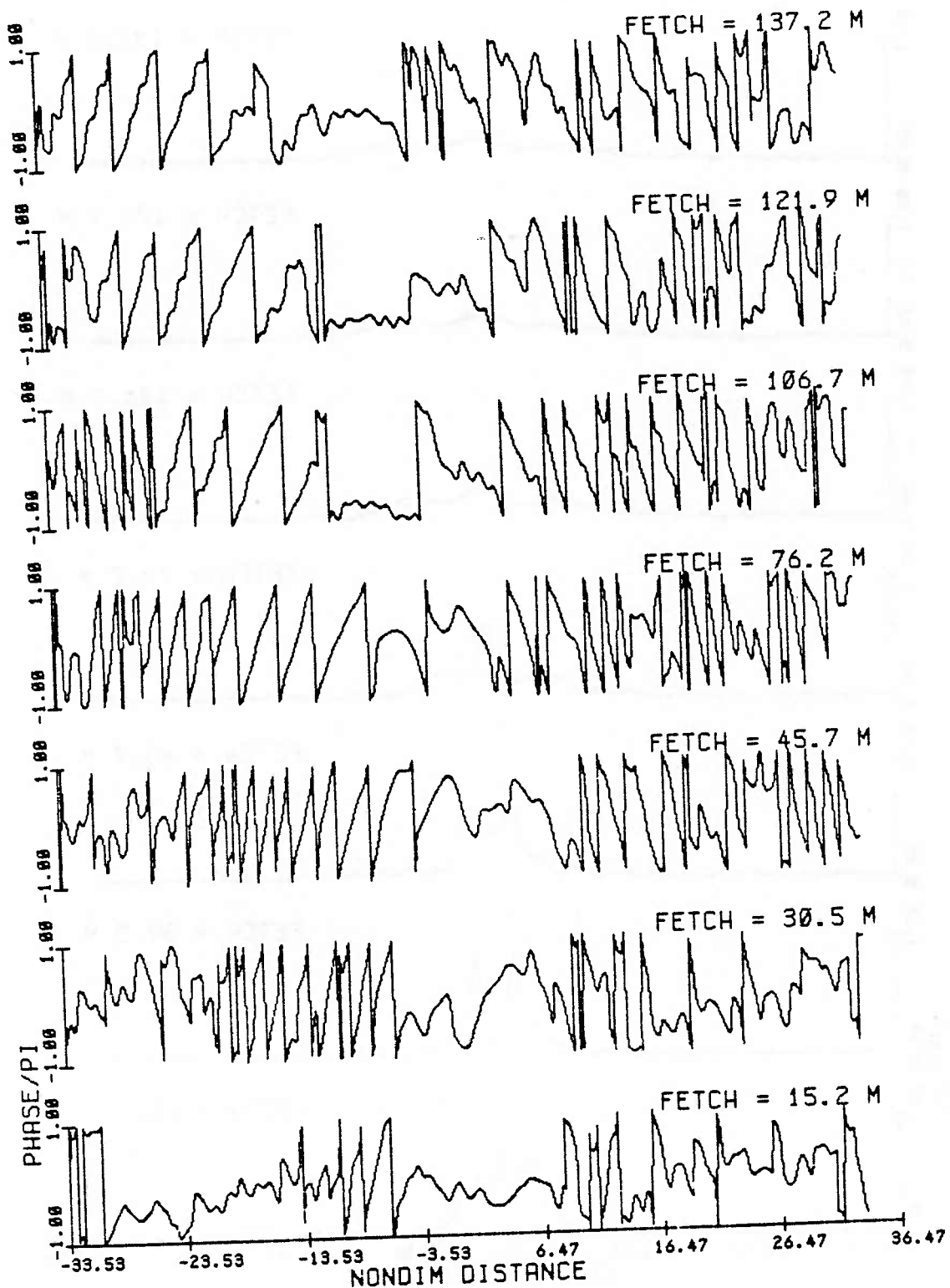


Fig. 3.47a Phase modulations from observations, principal value and normalized by pi, for successive fetches for the evolution of a group of 15 waves, initial steepness $ak = .16$ (Exp 22).

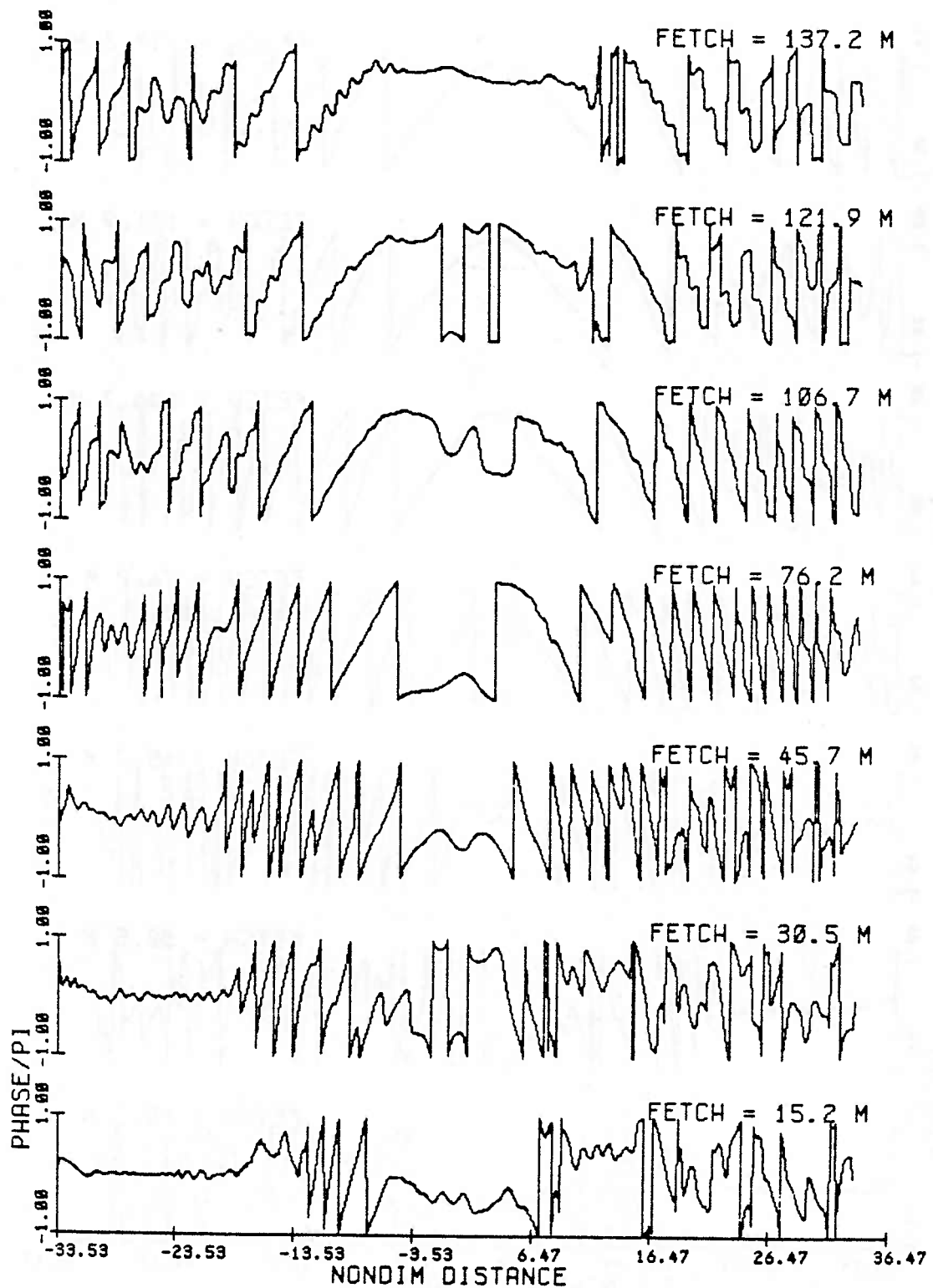


Fig. 3.47b Phase modulations from the inviscid NLS solution, at times corresponding to the fetches in (a), for the evolution of a group of 15 waves, initial steepness $ak = .16$ (Exp 22).

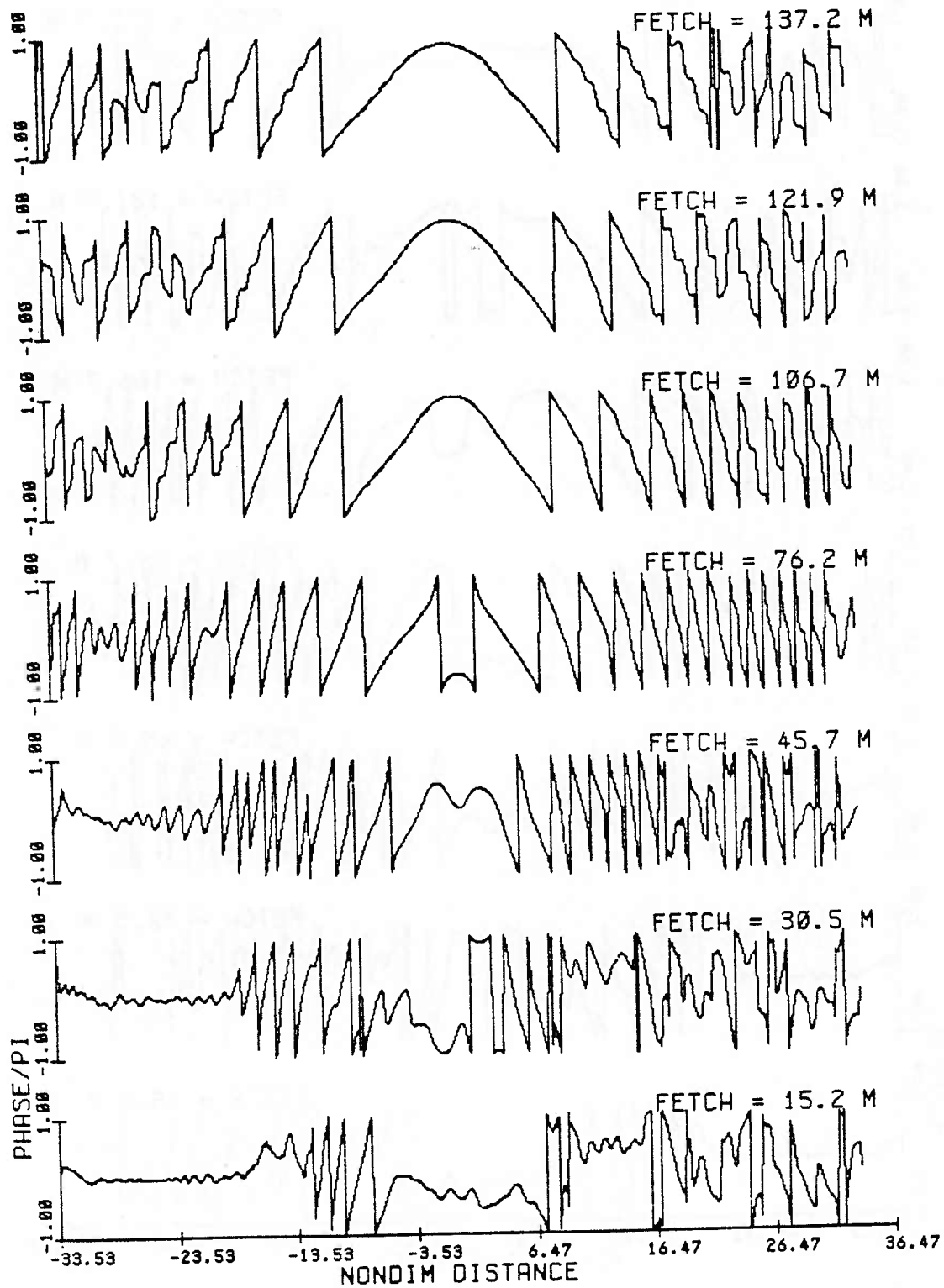


Fig. 3.47c Phase modulations from the viscous NLS solution, at times corresponding to the fetches in (a), for the evolution of a group of 15 waves, initial steepness $ak = .16$ (Exp 22).

frictional NLS solution (fig. 3.47c) is dominated by linear dispersion.

The last example is that of the longest (25 waves) steepest wave group, $ak = .16$ (Exp 23). Figures 3.48 and 3.49 show the full numerical solutions for $-29.1 < \xi < 29.1$ and $0 < \tau < 40$. Figure 3.50 shows the initial condition.

The amplitude modulation can be seen in figs. 3.50 a,b,c. The observations (fig. 3.50a) and the frictional NLS solution (fig. 3.50c) show reasonable agreement.

The phase modulations are shown in figs. 3.52 a,b,c. In all three cases the behavior is characteristic of the bound state. Note in fig. 3.52a the phase jumps occurring near amplitude minima: 30.5 m, 45.7, 121.9. The frictional phase modulation (fig. 3.52c) also suggests bound state type behavior. Although the bound state phase modulation can not really be distinguished here from bound state plus radiation or soliton plus radiation, it is distinct from both pure radiation and simple soliton behavior. What we observe is characteristic of an ongoing interaction of some kind which in amplitude is evidenced by growing and decaying modulation. The phase further supports that it is indeed an interaction and not linear dispersion by its relative flatness ($\partial_{\xi\xi}^2 = 0$) within the group with jumps connecting the regions that occur

Fig. 3.48 Inviscid NLS numerical evolution for a wave group of 25 waves, initial steepness $ak = .16$ (Exp 23). Spatial frame $-29.1 < X < 29.1$ and time interval $0 < T < 40$.

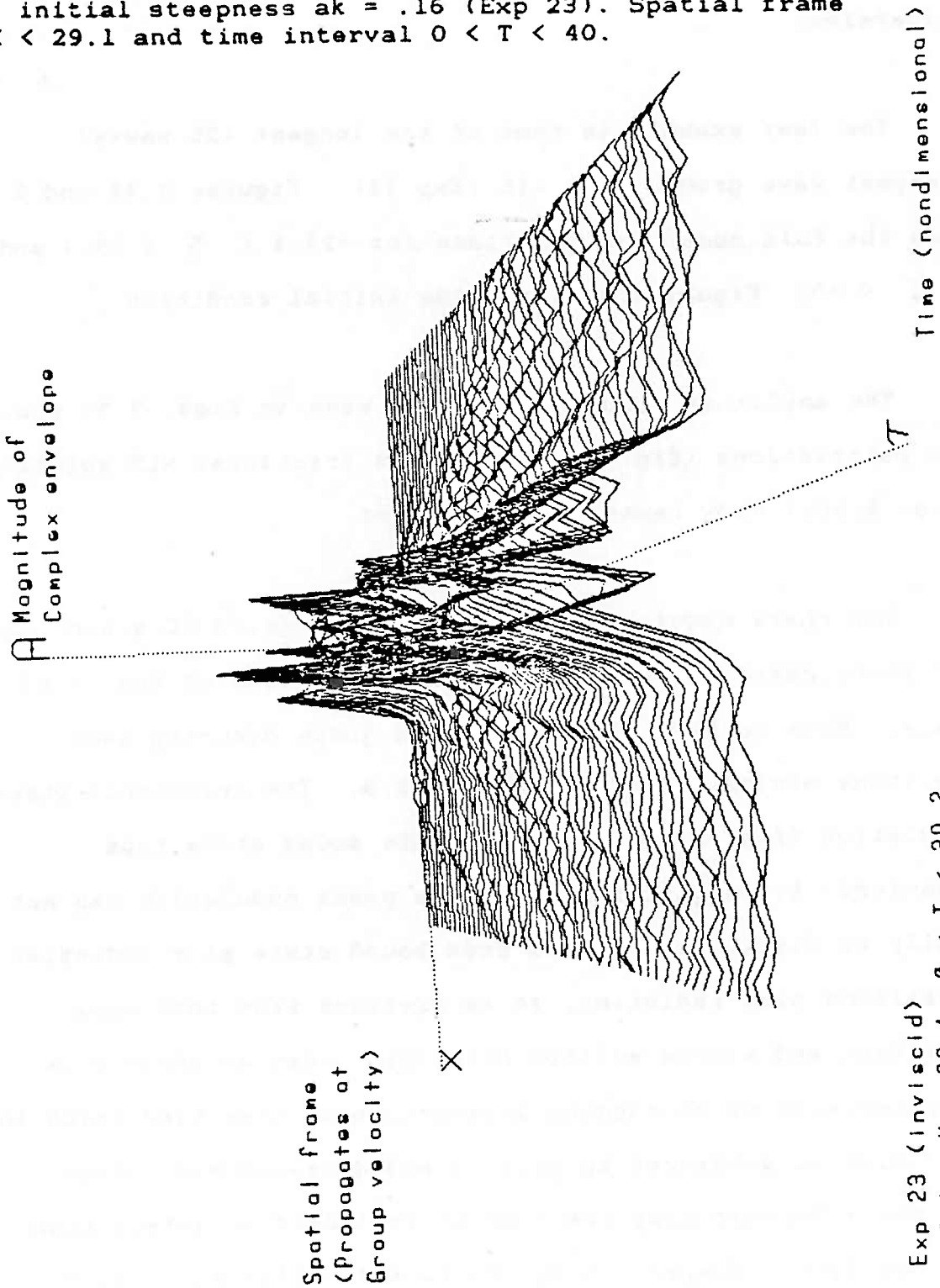
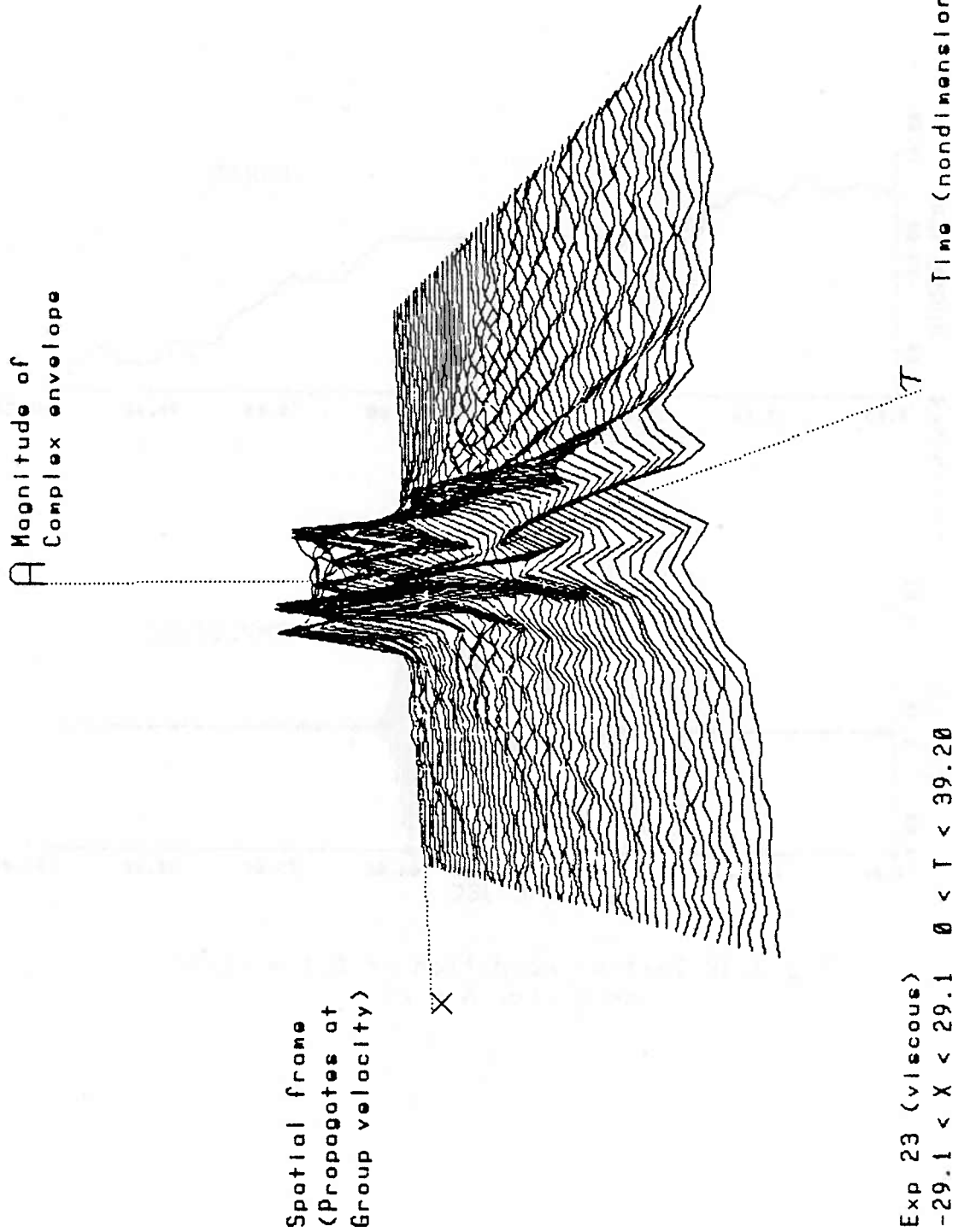


Fig. 3.49 Viscous NLS numerical evolution for a wave group of 25 waves, initial steepness $ak = .16$ (Exp 23). Spatial frame $-29.1 < X < 29.1$ and time interval $0 < T < 40$.



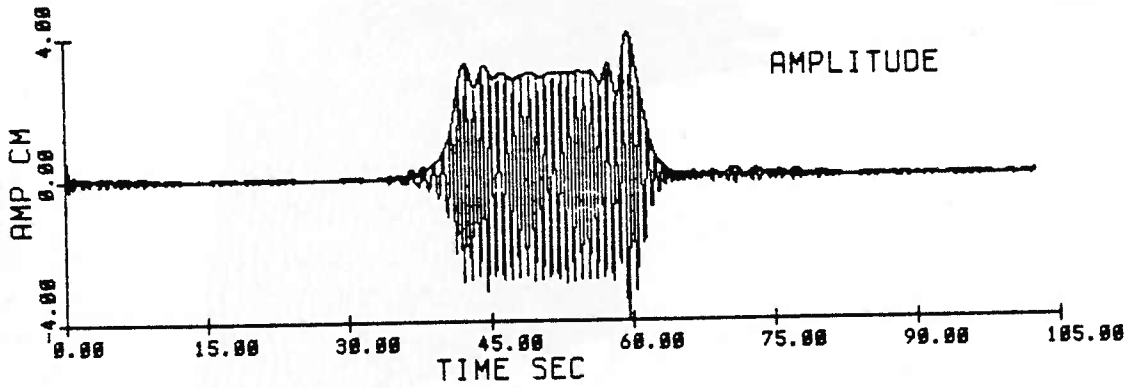
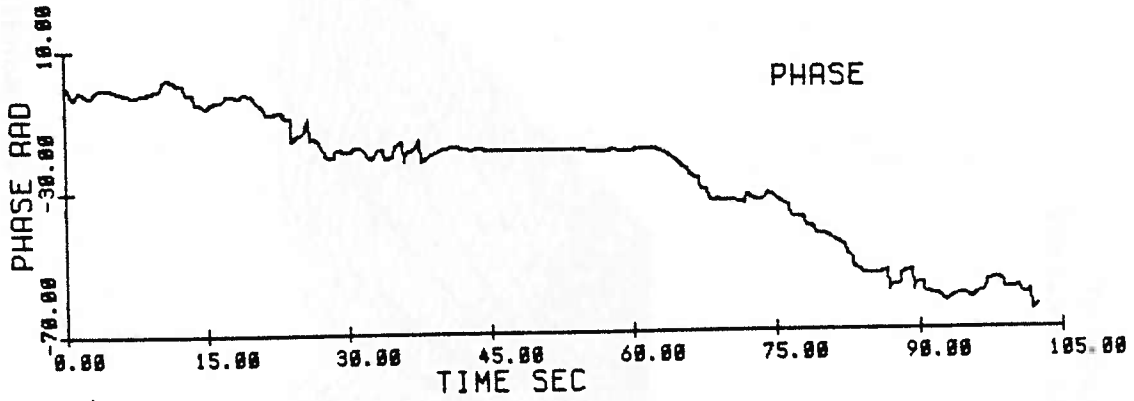


Fig 3.50 Initial condition at 6.1 m (E23)
ak = .16, N = 25

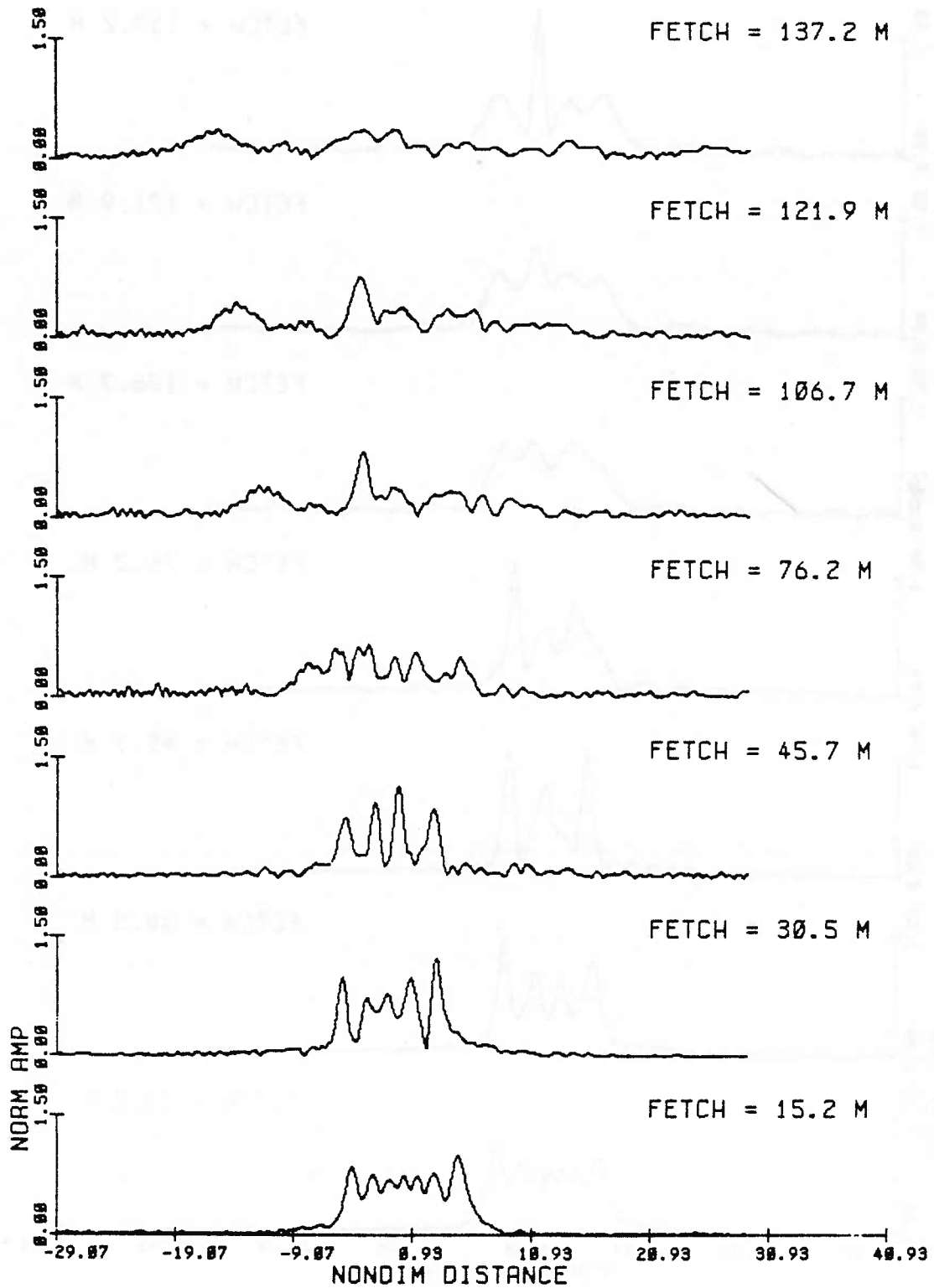


Fig. 3.51a Amplitude modulations from observations, nondimensionalized at each fetch by the initial condition scaling, for the evolution of a group of 25 waves, initial steepness $ak = .16$ (Exp 23).

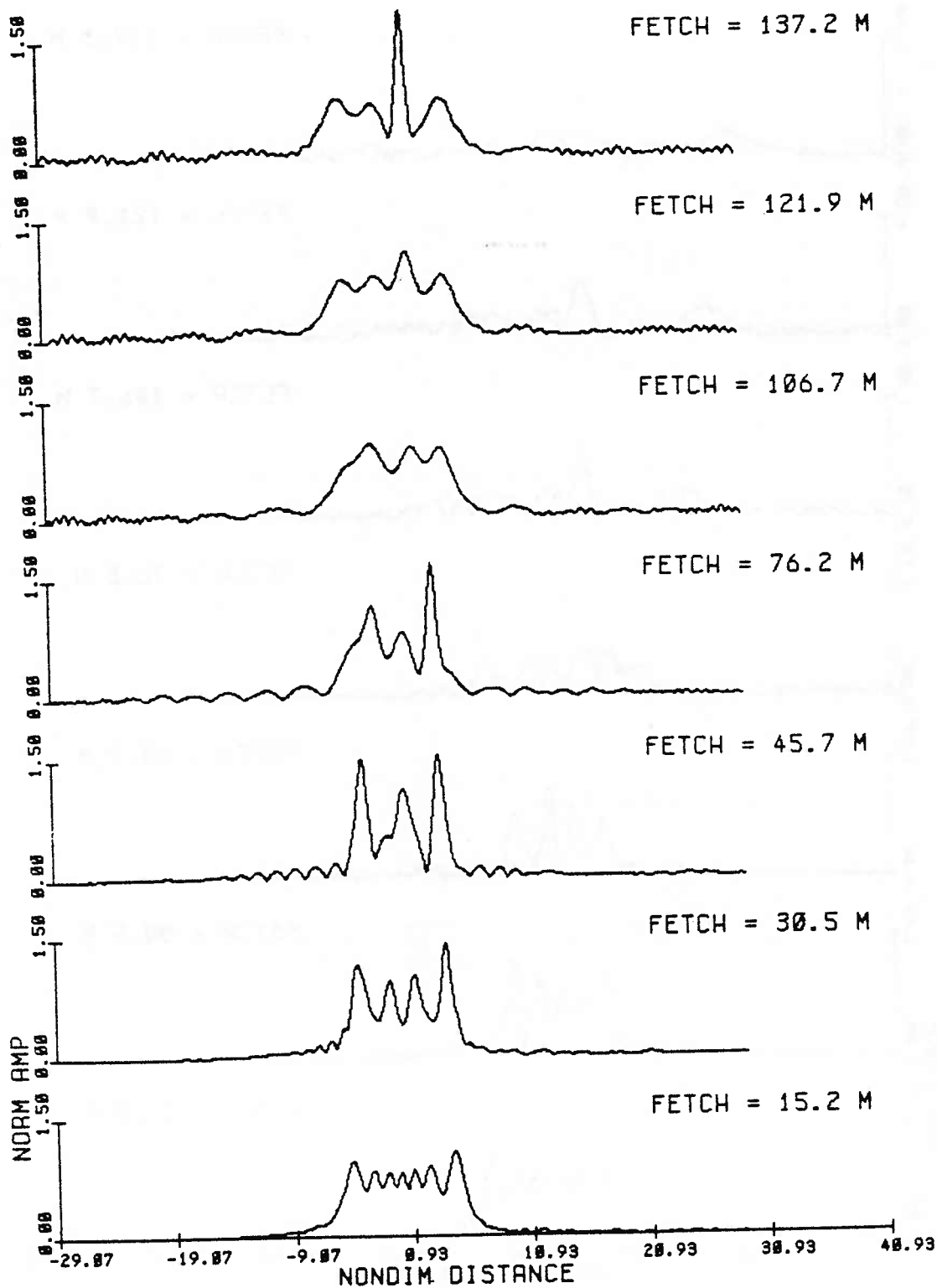


Fig. 3.51b Amplitude modulations from the inviscid NLS solution, at times corresponding to the fetches in (a), for the evolution of a group of 25 waves, initial steepness $ak = .16$ (Exp 23).

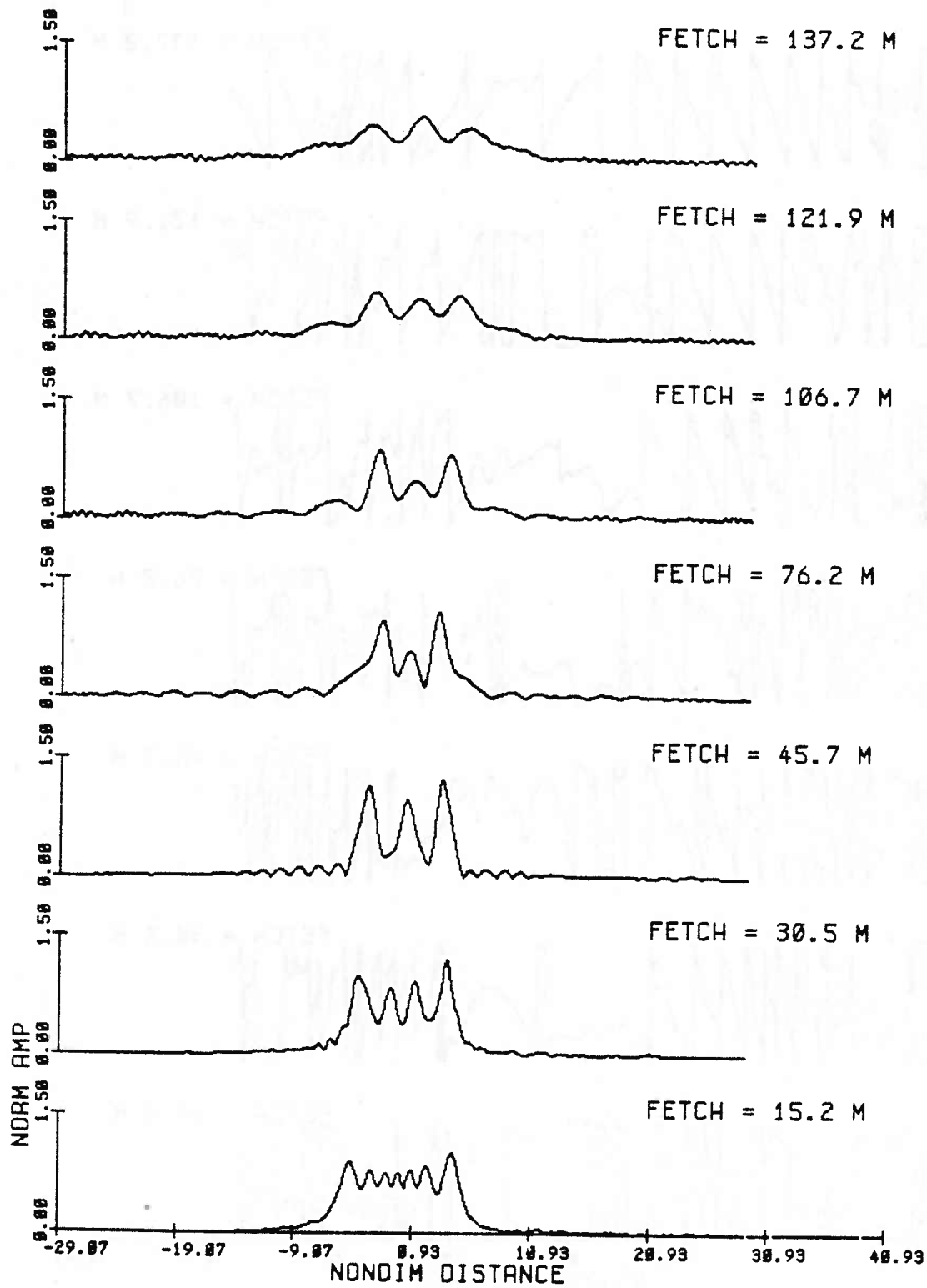


Fig. 3.51c Amplitude modulations from the viscous NLS solution, at times corresponding to the fetches in (a), for the evolution of a group of 25 waves, initial steepness $ak = .16$ (Exp 23).

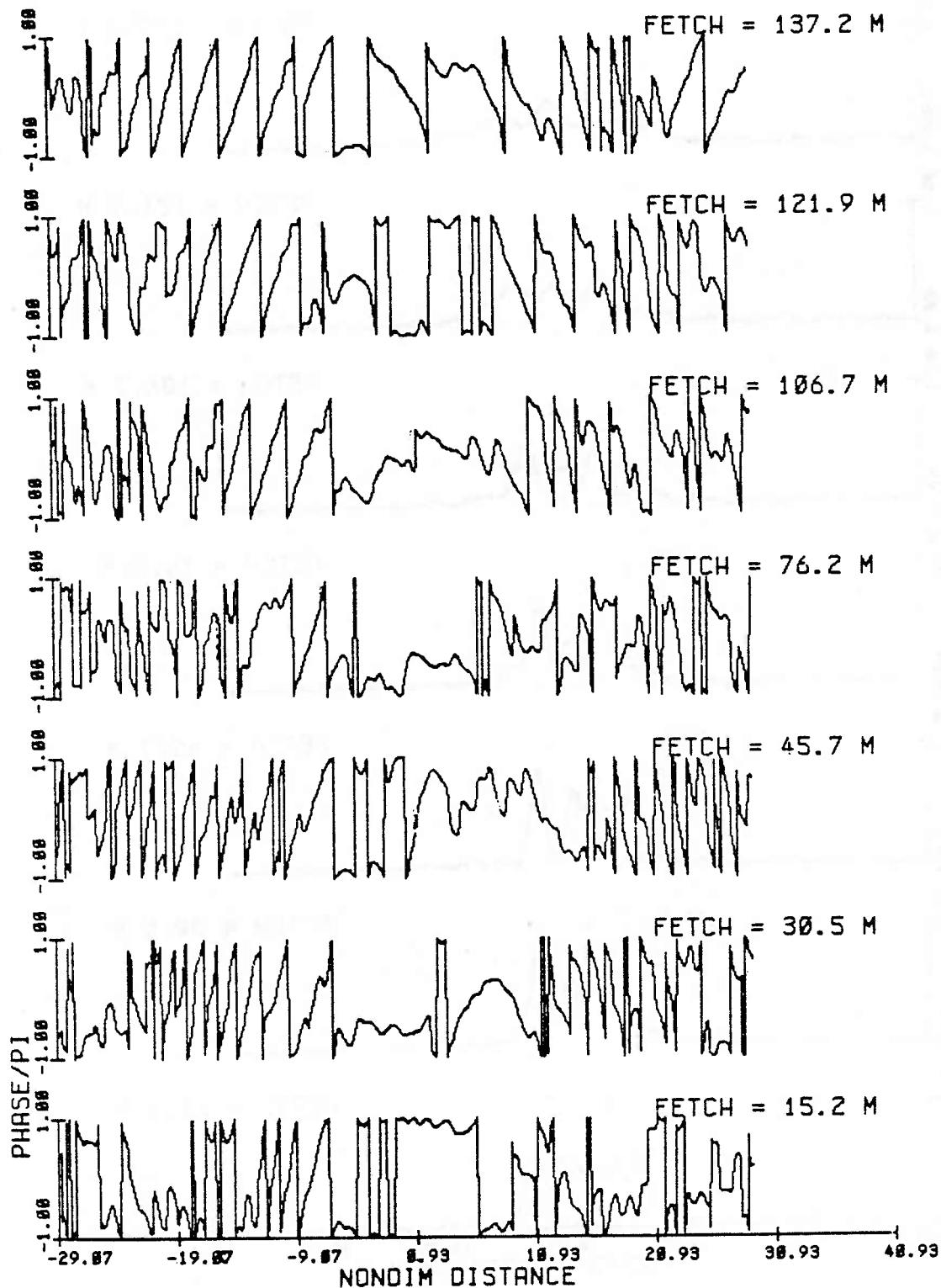


Fig. 3.52a Phase modulations from observations, principal value and normalized by pi, for successive fetches for the evolution of a group of 25 waves, initial steepness $ak = .16$ (Exp 23).

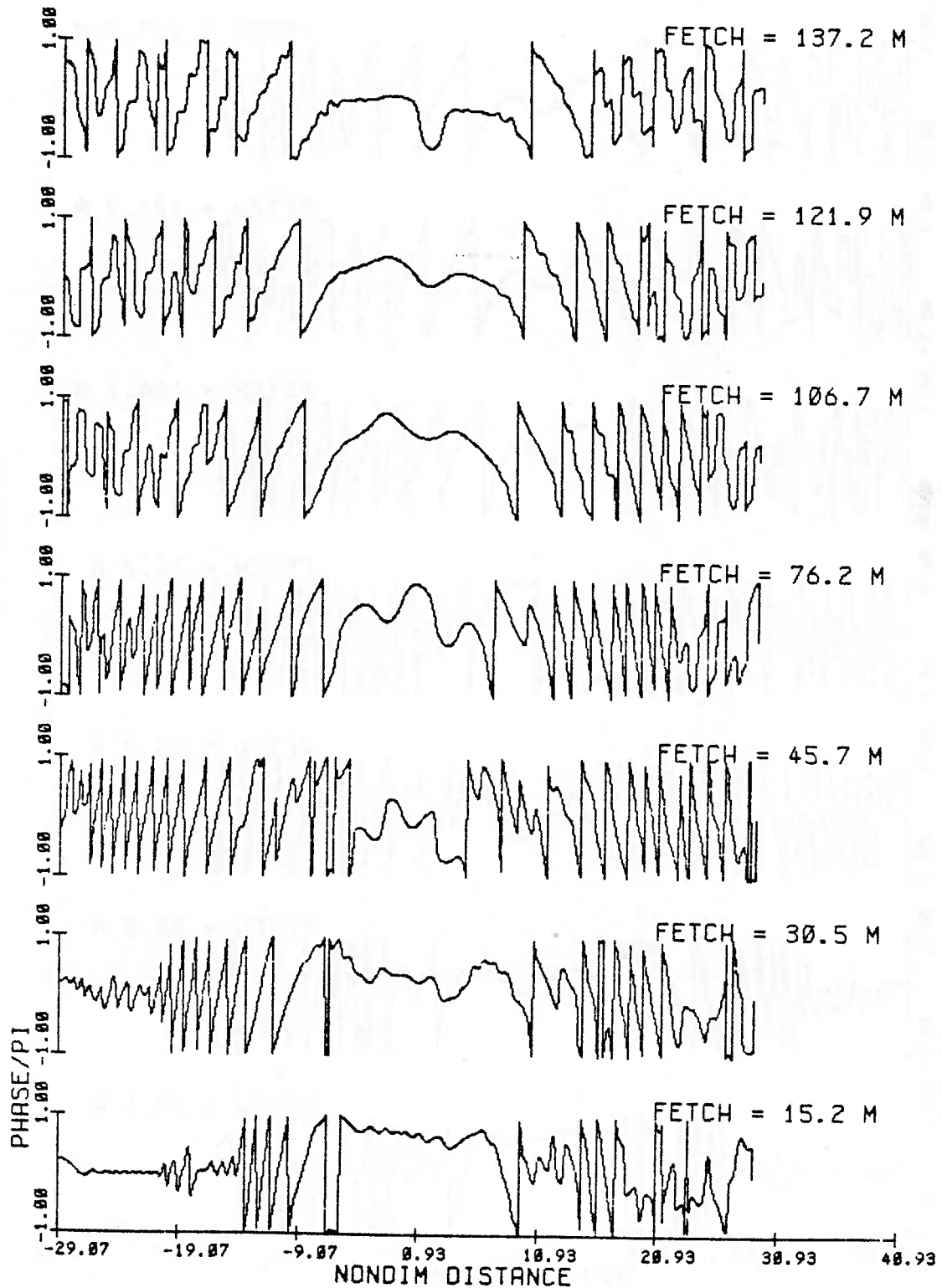


Fig. 3.52b Phase modulations from the inviscid NLS solution, at times corresponding to the fetches in (a), for the evolution of a group of 25 waves, initial steepness $ak = .16$ (Exp 23).

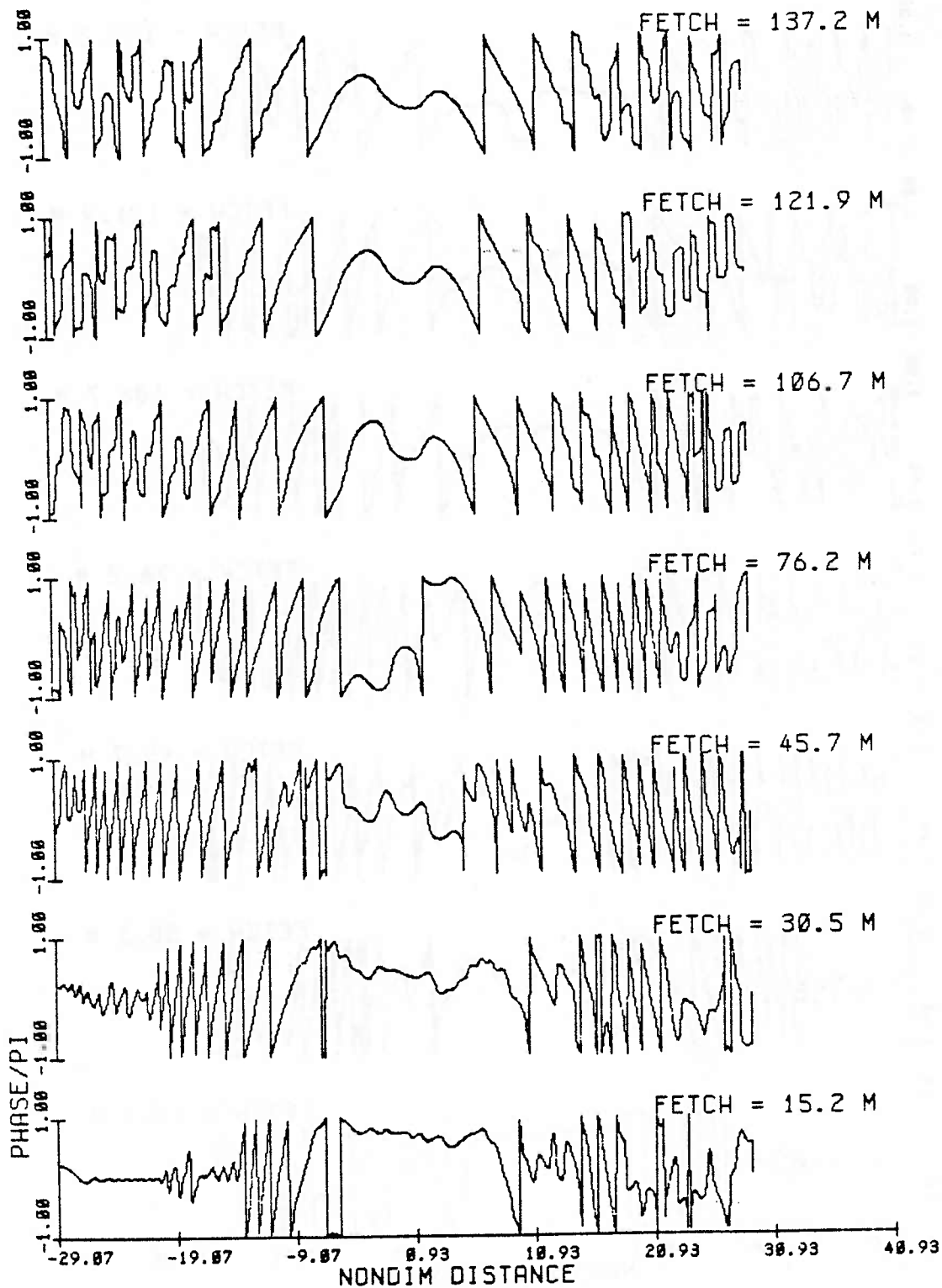


Fig. 3.52c Phase modulations from the viscous NLS solution, at times corresponding to the fetches in (a), for the evolution of a group of 25 waves, initial steepness $ak = .16$ (Exp 23).

between locations of amplitude minima. The phase also seems distinguishable from that of divergent solitons in that the jumps change in time, generally corresponding to locations of nodes, rather than staying fixed in relative position within the group.

3.7 DISCUSSION AND SUMMARY

We have made comparisons between observations and numerical solutions (from real data initial conditions) of narrow-banded wave group evolution. From these comparisons, using the long-time behavior of exact asymptotic model solutions as a guide, we believe that we can distinguish between radiation (linear dispersion) and soliton-like behavior based on characteristics of the phase modulation. This does not appear to have been examined before in observations, primarily due to lack of a method for obtaining a time series of phase modulation from measurements of surface displacement. From amplitude modulation alone, it is difficult to tell whether the wave group development is a forced superposition of linear components which disperse or a truly nonlinear phenomenon. We suggest that, at least for wave groups with a well defined carrier frequency, the phase modulation may give a clearer indication of the type of wave interaction that takes place.

The only published study of the evolution of mechanically generated groups that looks at phase is that of Feir [1967]. We briefly describe his results and compare them to our wave group evolutions. He generated variable amplitude, constant frequency pulses. The amplitude (wavemaker stroke) was varied smoothly from zero to some maximum amplitude back to zero. Wave development was observed at 2 fetches: 4 feet and 28 feet. (Our initial condition is specified from an observation at 20 feet; the final observation is at 450 feet). Frequency was determined from zero crossings in amplitude. This yields frequency averaged over one half wave period.

Qualitatively, our results are consistent with this relatively short term observation. He shows the frequency modulation for 2 wave steepnesses, $ak = .025$ and $ak = .08$. These correspond best to the first two cases discussed in section 3.6 corresponding to radiation and soliton, respectively. However, we really can not determine the long-time behavior from Feir's observations. The initial frequency within the group in all cases (his and ours) is uniform, imposed at the wavemaker. For the smaller steepness, Feir finds that the frequency within the group is still uniform at 28 feet. Linear dispersion is evident at the group edges. Jumps in frequency occur at the edges corresponding to locations of amplitude minima. In the case of the higher steepness, the frequency at 28 feet has what Feir refers to as

a 'kink' or ripple within the group. It is like the undulations we see in cases of overall uniform phase. Again linear dispersion is evident at the edges of the group with jumps in frequency at amplitude nodes. The amplitude modulation also indicates that the group is in an early stage of evolution; the group has spread but is still a coherent pulse with amplitude varying smoothly from zero to a central maximum back to zero.

Feir shows the amplitude modulation of some steeper experiments which are similar to amplitude modulations that we observe (growing modulation of a single envelope to two) but does not show the frequency modulation. He remarks that the frequency modulation varies erratically; we would expect phase jumps within the group to accompany the growing amplitude modulation. He also remarks on a trend for the frequency of leading groups to be lower than that of trailing groups. The results of the frequency downshifting in chapter 2 also indicated that although the peak frequency downshifts with evolution, not all the groups are of lower frequency. Rather, the modulation sorts itself into a succession of groups of increasing frequency.

We cannot resolve very clearly, from the phase modulations of the observations, between a simple soliton state and the bound state (both in a background of radiation).

The type of radiation present in the observations makes the phase much noisier than that which we specified in analytic initial conditions (section 3.4). In one case, that of the steepest and longest initial pulse, the phase was more suggestive of the bound state than that of simple soliton. In all other cases (including some not discussed) where linear dispersion did not dominate the long-time evolution, the phase modulation seemed to indicate soliton plus radiation type behavior. Perhaps due to dissipation one needs longer, steeper initial profiles than predicted by inviscid theory to achieve a bound state. The effect of dissipation is seen to be significant, and in the parameter range investigated acts to lower the 'quantum' or predicted number of solitons that one would estimate from the initial condition.

Due to dissipation, it seems that the bound state or soliton is not manifested by the recurrence or steadiness (in the soliton case) of the initial condition but is manifested by the coherence of the wave group. The phase modulation indicates that the waves remain together and interact in the long-time evolution in contrast to predictions of the linear theory for thermalization of the group. The results of Yuen and Lake (1975) support this interpretation. Although they did not see recurrence of the initial condition, the observed groups did not separate. It would seem that the primary manifestation of the bound state is in this long-time

coherence.

We find that the frictional NLS equation models the long-time evolution extremely well. It is perhaps surprising in view of the the weak nonlinearity of the theory and the crudeness of the dissipation term. Although the form of the dissipation does not directly affect the phase, we find there is an indirect effect on the phase in the long-time evolution by a change of the 'quantum'.

The model cannot predict a frequency downshift such as is observed. Although the downshift is small and only occurs for the steeper wave groups, it is an important, consistent and nonconservative feature of the long-time evolution. It may be due to some higher order effect or more complicated dissipation than was considered.

CHAPTER 4

OCEANIC OBSERVATIONS OF INTERNAL WAVE GROUP DEVELOPMENT

4.1 INTRODUCTION

A field study was undertaken in September 1979 to observe the generation of high frequency internal wave packets in Massachusetts Bay. The propagation of these waves has been previously observed during late summer and early fall when there is a strong seasonal stratification. (The bay is nearly isothermal in winter). They are thought to form from the interaction of the tide with Stellwagen Bank, a local topographic feature (Fig. 4.1). The packet propagation was first looked at by Halpern [1971a] and more recently by Haury, Briscoe and Orr [1979].

There have been relatively few oceanic studies of wave generation from tidal interaction with topography. Some notable exceptions relevant to Massachusetts Bay are the extensive field study by Farmer and Smith [1980a] in Knight

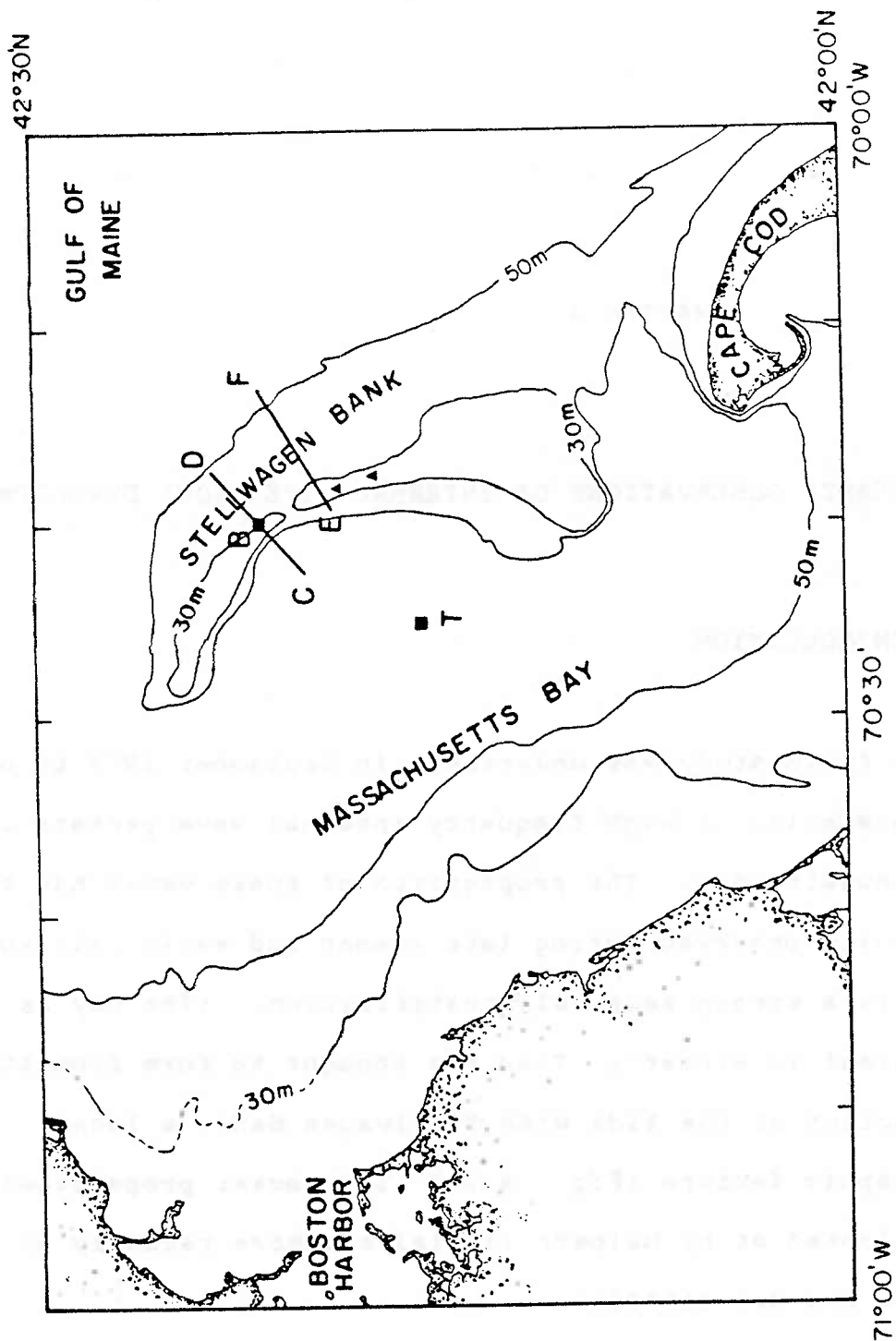


Fig. 4.1 CD shows the steaming track for the acoustic transect, and B is the location of the buoy from the present field experiment. Sites of measurements made in previous studies are also indicated. EF marks an XBT survey by HBO [1979]. T denotes the location of Halpern's [1971a,b] observations. The solid triangles show the position of Orr's acoustic observations of the packet [HBO, 1979]. (Map after HBO, 1979).

Inlet, the observations by Osborne and Burch (1980) in the Andaman Sea and the study done by Gargett (1976) in the Strait of Georgia. These studies show the asymmetry of the topography and the structure of the stratification to be crucial to the types of response that are observed. Although there are numerous theoretical and laboratory studies on this topic, they generally employ a simple stratification and an idealized (smooth and symmetric) topography. Hence the use of these studies to interpret a given oceanic situation is uncertain unless applied in conjunction with actual observations. In particular two theoretical and laboratory studies, the work of Lee and Beardsley (1974) and that of Maxworthy (1979), offered two different generation mechanisms to explain Halpern's wave packet observations. These together with the above field studies were the primary motivation for the present experiment. A brief review of some of the previous work will be included in the discussion.

The goal of the present experiment was to observe the tide-sill interaction over time to determine how the internal waves form. Haury, Briscoe and Orr (hereafter referred to as HBO), from their observations, saw some evidence in support of the lee wave generation mechanism proposed by Farmer and Smith and by Maxworthy for creation of the high frequency packets. Farmer and Smith disagree with Maxworthy on the details of the packet formation. Farmer and Smith see the packet formed as a

nonlinear lee wavetrain (quasi-steady). Maxworthy sees the wavetrain formed from the disintegration of the front of a single depression or massive lee wave (unsteady). HBO did not distinguish between the two explanations (the Farmer and Smith paper was still in preparation at the time). However, HBO's conclusion was of a qualitative nature based on only a few observations of the apparent generation. They did not observe the time development.

In the present study, a ten kilometer track perpendicular to the bank axis and centered over the crest was monitored for one tidal cycle. A commercially available Raytheon fathometer was used as a remote sensor of isopycnal motion. Seven kilometers is both the full obstacle width and the length of the local tidal excursion (Halpern, 1971b). Figure 4.1 shows the location of the steaming track (CD) and the mooring site (B) of the present study as well as the position of an XBT survey by HBO (EF) and the site of Halpern's Station T. To accompany the interpretation of the acoustic record, a time series of Froude numbers was calculated from velocity and CTD measurements made on the crest of the bank.

The most striking aspect of our observations is the asymmetry of the response. It is perhaps not surprising, especially in view of previous studies, since the shape of the bank shows marked asymmetry and represents a large obstacle to

the flow. On ebb tide (flow directed toward the Gulf of Maine), a large isopycnal depression or massive lee wave is formed behind the sill (over the eastern slope). The flow sees a dramatic decrease in depth from 80 meters in the Bay to 30 meters on the crest over a distance of one half to one kilometer. The horizontal scale of the depression is 5 kilometers, the same order as that of the more gently sloping eastern side of the sill. This depression remains stationary as the tide slackens. The observed Froude number (Fr) on the sill crest is almost always supercritical ($Fr > 1$).

Supercritical flow over the crest is also indicated by the lifting of the isotherms over the bank, in analogy with layered hydraulic flows (Fig. 4.2B). The Froude number estimated away from the crest using continuity is always subcritical ($Fr < 1$). There is a short period of subcriticality on the crest when the tide turns. It is during this period of subcriticality that the large depression formed in the lee of the bank is hypothesized to give rise to a train of large amplitude high frequency internal waves. They propagate westward. The speed of these waves is estimated from an internal KdV dispersion relation (Benjamin, 1966). The estimate gives consistent results with an extrapolated packet arrival time at point C (Fig. 4.1). Support for the above interpretation of the flow response on ebb tide comes from acoustic images, Froude numbers, an XBT survey, and an observation of the packet at point C.

The behavior on the flood phase of the tide (flow directed into the Bay) is quite different. The flood tide sets up a much smaller scale lee wave very quickly. Its length is about one kilometer, the same as that of the depth transition on the leeward side of the sill. To the flood tide, the depth transition over the sill should appear much more gradual. As the tide slackens and turns, a train of 4-5 lee waves of the same scale as the first stationary wave appear to form and advance into the decreasing flow. There is less observational support for the interpretation of the flow response on flood tide than there was on ebb. Evidence here comes just from the acoustic images and the Froude numbers. Although it has been conjectured that the packets might not be formed on both phases of the tide due to the asymmetry, no previous attempt has ever succeeded in observing them propagating into the Gulf of Maine, and we did not try to observe them further east in this study. It would seem that waves are generated on flood tide, and that they look quite different from those generated on ebb.

A detailed description of the measurements is given in the next section. This is followed by an analysis of the data and a discussion of the results. Some pertinent previous work is also reviewed in the discussion.

4.2 MEASUREMENTS

The velocity on the crest of the bank was measured using three Endeco Type 105 ducted impellor current meters. These current meters are specifically designed for shallow water applications. They were attached to the mooring cable by a 1.5 meter tether and were thus allowed to orient freely to the flow. They recorded speed and direction at thirty minute intervals for a period of forty six hours throughout the experiment. A slack mooring was used with a 2.5:1 scope. The water depth on the crest was 28 meters, and the current meters were set at depths of 6, 13 and 19.5 meters.

Density was calculated from measurements made on the crest of the bank in the vicinity of the mooring with a Hydrolab hand lowered CTD. Salinity measurements show the Bay is nearly isohaline, and the stratification is primarily due to seasonal heating. Temperature was also measured using XBTs. A dense XBT section was made over the bank as the tide turned from ebb to flood (Fig. 4.2B).

An acoustic time series was made using a 41 kHz wide beam transducer Raytheon fathometer. The acoustic record was made while steaming a 10 kilometer track perpendicular to the bank axis. This track was steamed continuously for a tidal cycle; navigation was by Loran-C. We attempted to duplicate the

track on each successive pass with the largest deviation between the tracks being of order 600 m. The use of a fathometer as a remote sensing tool to observe internal wave motion is not new. Among others it has been used by Farmer and Smith (1980a,b) in Knight Inlet and by HBO (1979) in Massachusetts Bay. The source of acoustic reflection is uncertain, although in our range it is probably from biological scatterers which act as passive tracers of the fluid motion (Orr, 1980). We can show from contouring temperature measurements taken from a densely spaced XBT section on the same scale as the acoustic record that the acoustic scattering layer is coherent with the thermocline (Figs. 4.2A and 4.2B). Although the images produced with the Raytheon are not as clear as those of Farmer and Smith due to a more diffuse scattering layer, they do show the large scale isopycnal motion. In addition, they form a continuous time series that we can use in interpreting our physical measurements. In all of the Raytheon record made while steaming, the chart paper speed limits our horizontal resolution to 200 meters.

In Figure 4.2 the distance scale is not uniform due to slight irregularity in steaming. The contouring was done to correspond exactly to the acoustic record. However the temperature contoured on a uniform distance scale looks basically the same (the irregularity is slight). Figure 4.2

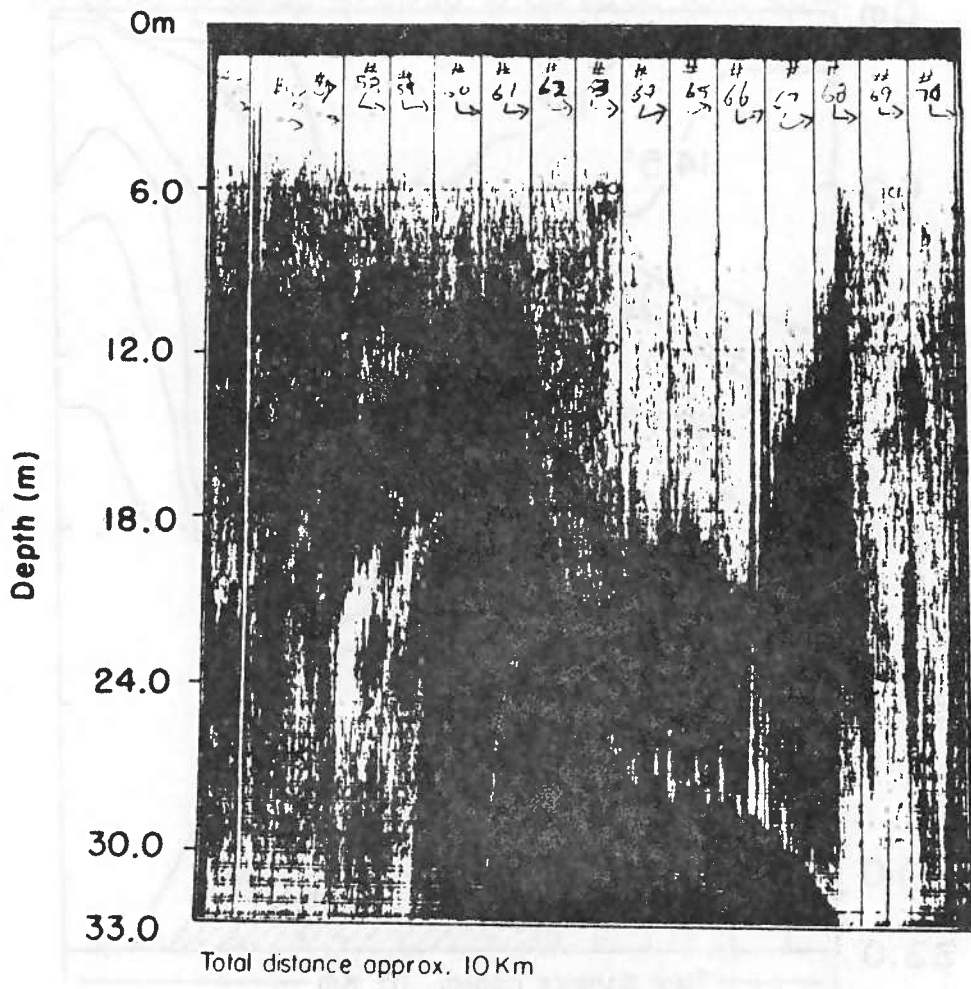


Fig. 4.2A Raytheon acoustic image made while steaming at approximately 9 knots eastward across the bank as the ebb tide slackened. The flow is from left to right and is close to zero. The image shows a large scale near-surface low-scattering region coherent with the depression of the thermocline seen in 2B.

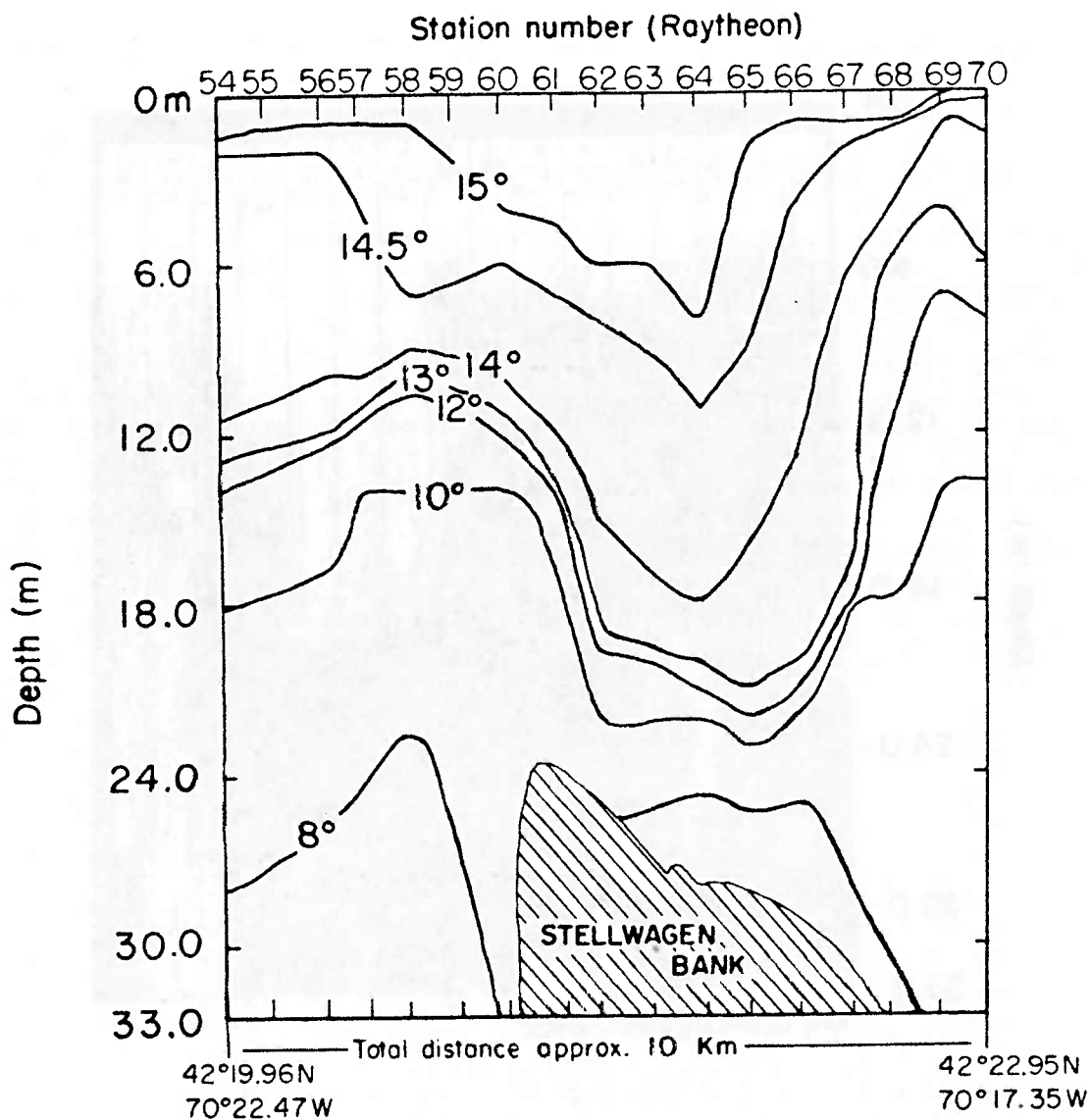


Fig. 4.2B Temperatures from expanded scale XBT traces hand read and contoured on the same scale as the acoustic image of 2A. The numbers at the top of the figures indicate stations where XBT casts were made.

corresponds to the appearance of a large depression or massive lee wave formed on ebb tide over the eastern side of Stellwagen. Its horizontal scale is five kilometers. In the acoustics the isotherm depression appears as a clear low-scattering region, probably from surface mixed-layer water moving down. The time development of the lee wave can be traced in the acoustic record by examining the evolution of this low-scattering region. In this manner, the acoustic record provided us with a continuous real-time picture of the flow.

4.3 ANALYSIS AND RESULTS

An extensive field study of topographic generation of internal waves by a tidal flow has been carried out by Farmer and Smith (1980a,b) in Knight Inlet, British Columbia. The local topography and stratification are considerably different from that of Massachusetts Bay. The topography is also large amplitude, but the mean depth of the water is much greater (500 m in K.I. opposed to 80 m in M.B.) The stratification is more nearly two layer (fjord-type fresh layer over salt). Farmer and Smith classified their flow response based on an internal Froude number which they defined as the ratio of the maximum tidal velocity to modal internal wave phase speeds where the modal speeds were calculated from the observed density profiles. This definition is equivalent to

Maxworthy's except that Maxworthy used directly measured phase speeds instead of calculated modes. Farmer and Smith's Froude number differs from the usual definition (which uses density structure over total depth) in that only density structure to sill depth was used. The reason for their definition was the feeling that the sill was controlling the flow, and hence only stratification down to sill depth would be important in determining the response. Both the field study of Farmer and Smith and the laboratory study of Maxworthy categorized their results based on a Froude number dependence.

In the present study, a time series of Froude numbers was calculated to accompany the acoustic time series. There is an acoustic image on the crest of the bank every half hour as well as a current measurement. The Froude number calculation is the same as that stated above:

$$Fr_i(t) = U(t) / C_i \quad (4.3.1)$$

U is the mean value of the flow component perpendicular to the bank axis averaged over the three depths. The axis of the bank is 38 degrees west of north. The flow was resolved into components along and perpendicular to the bank axis. The observed velocity was fairly depth independent. The phase speeds were computed from CTD observations of density on the sill crest using a fourth order Runge-Kutta shooting method. The phase speeds for the first three modes were found to be 23

cm/sec, 10.4 cm/sec and 7.1 cm/sec, respectively. Figure 4.3 is a plot of the Brunt-Vaisala frequency and the first three vertical eigenmodes.

Table 4.1 lists the calculated Froude numbers. An asterisk is used to denote all values greater than 1 (supercritical). The Froude numbers for the second and third modes were almost always supercritical, while the Froude number for the lowest mode was supercritical at times of maximum ebb tide. Maximum flood tide occurred from 2000 to 2130 hours in Table 4.1 and the first mode Froude numbers were just subcritical.

HBO estimate a Froude number from their measurements and from those of Halpern (1971a) taken at a site 9 km west of the crest (Station T, Fig. 4.1). They find $Fr = \frac{U \bar{\rho}}{NH} = 0.33$. By mass conservation, this is consistent with our measurements on the crest. Again using conservation of mass, we extrapolate to 5 km east of the crest and estimate a value of the Froude number equal to 0.57. These results indicate subcritical flow on either side of the bank.

We now use the time series of Froude numbers to interpret the acoustic images. Any Froude number reference is to the first mode value unless otherwise stated. The evolution was noted by following the development of the near-surface

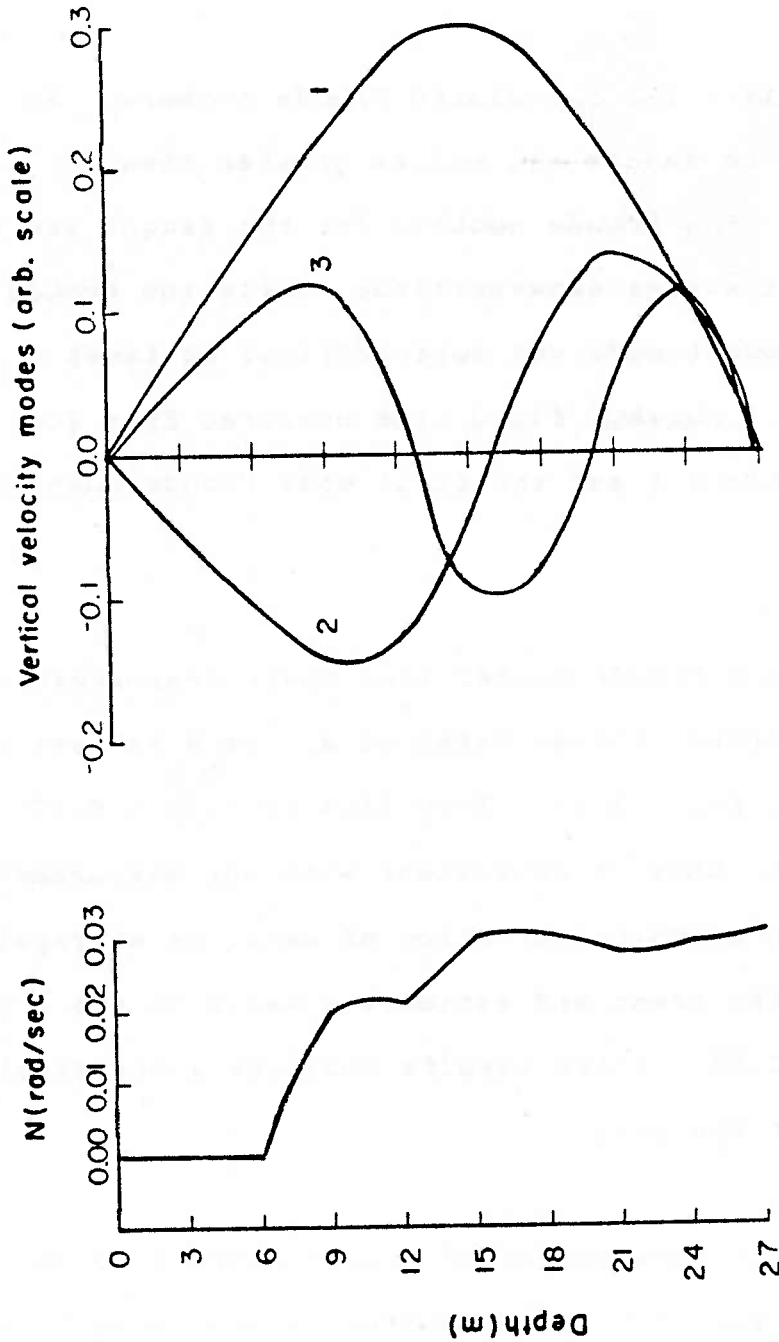


Fig. 4.3 Vertical profile of Brunt-Vaisala frequency and the first three vertical eigenmodes. The Brunt-Vaisala frequency was calculated from density inferred from an average of 6 hand-lowered CTD casts made in the vicinity of the mooring. The surface mixed layer resulted from the passage of a storm. The eigenmodes were also calculated from inferred density using a fourth order Runge-Kutta shooting method. The corresponding first three modal phase speeds were 23 cm/sec, 10.4 cm/sec and 7.1 cm/sec respectively.

Table 4.1 Time series of Froude numbers

	TIME (1/2 HR)	MODE 1 FROUDE NO.	MODE 2 FROUDE NO.	MODE 3 FROUDE NO.	
9/7/79	1300	0.80	1.76 *	2.58 *	
	1330	1.08 *	2.40 *	3.51 *	
	1400	1.33 *	2.94 *	4.31 *	
	1430	1.56 *	3.46 *	5.06 *	
	1500	1.72 *	3.81 *	5.59 *	
	1530	1.86 *	4.12 *	6.04 *	
	1600	1.73 *	3.83 *	5.61 *	
	1630	1.83 *	4.04 *	5.92 *	
	1700	1.62 *	3.58 *	5.24 *	
	1730	1.46 *	3.23 *	4.73 *	
	1800	0.80	1.77 *	2.59 *	
	1830	0.56	1.24 *	1.82 *	
	1900	0.06	0.12	0.18	
	1930	0.60	1.33 *	1.94 *	
	2000	0.99	2.20 *	3.22 *	
	2030	0.97	2.15 *	3.15 *	
	2100	0.88	1.96 *	2.87 *	
	2130	0.87	1.92 *	2.81 *	
	2200	0.56	1.24 *	1.81 *	
	2230	0.40	0.88	1.28 *	
	2300	0.35	0.78	1.14 *	
	2330	0.27	0.60	0.88	
	9/8/79	2000	0.15	0.33	0.48
		0030	0.20	0.45	0.66
0100		0.19	0.43	0.62	
0130		0.50	1.11 *	1.62 *	
0200		0.82	1.81 *	2.64 *	
0230		1.04 *	2.31 *	3.39 *	
0300		1.14 *	2.52 *	3.70 *	
0330		1.35 *	2.99 *	4.38 *	
0400		1.32 *	2.91 *	4.26 *	
0430		1.55 *	3.42 *	5.01 *	
0500		1.42 *	3.14 *	4.60 *	
0530		1.00 *	2.22 *	3.25 *	
0600		1.01 *	2.24 *	3.29 *	
0630		0.99	2.20 *	3.22 *	
0700		0.54	1.18 *	1.73 *	
0730	0.26	0.58	0.85		

low-scattering region in the acoustic record. As stated earlier, Figure 4.2B shows that this feature is associated with a large scale isothermal depression. For purposes of this discussion, we will refer to the depression as a lee wave.

Figure 4.4 is a schematic of the development of two related features in the acoustic record. The first is the clear near-surface feature that we identify with a lee wave. This clear region is outlined from the acoustic record, and its development with time in relation to the sill crest and a second feature is followed. The second feature is also a clear area in the acoustic record which occurs on the bottom. It is conjectured to be well mixed water of a different type than the ambient bottom water and thus has different scattering properties. Its movement seems definitely related to the tidal cycle and lee wave formation. It may indicate a pattern in flow separation similar to that observed in Knight Inlet. In each sequence of the schematic, the bank appears slightly differently because it was drawn to correspond to a particular acoustic image. As mentioned previously, the steaming track and speed of the ship were slightly irregular. The form of presentation was chosen to mirror the information in the actual image.

Figure 4.5 relates the schematic of Figure 4.4 to the

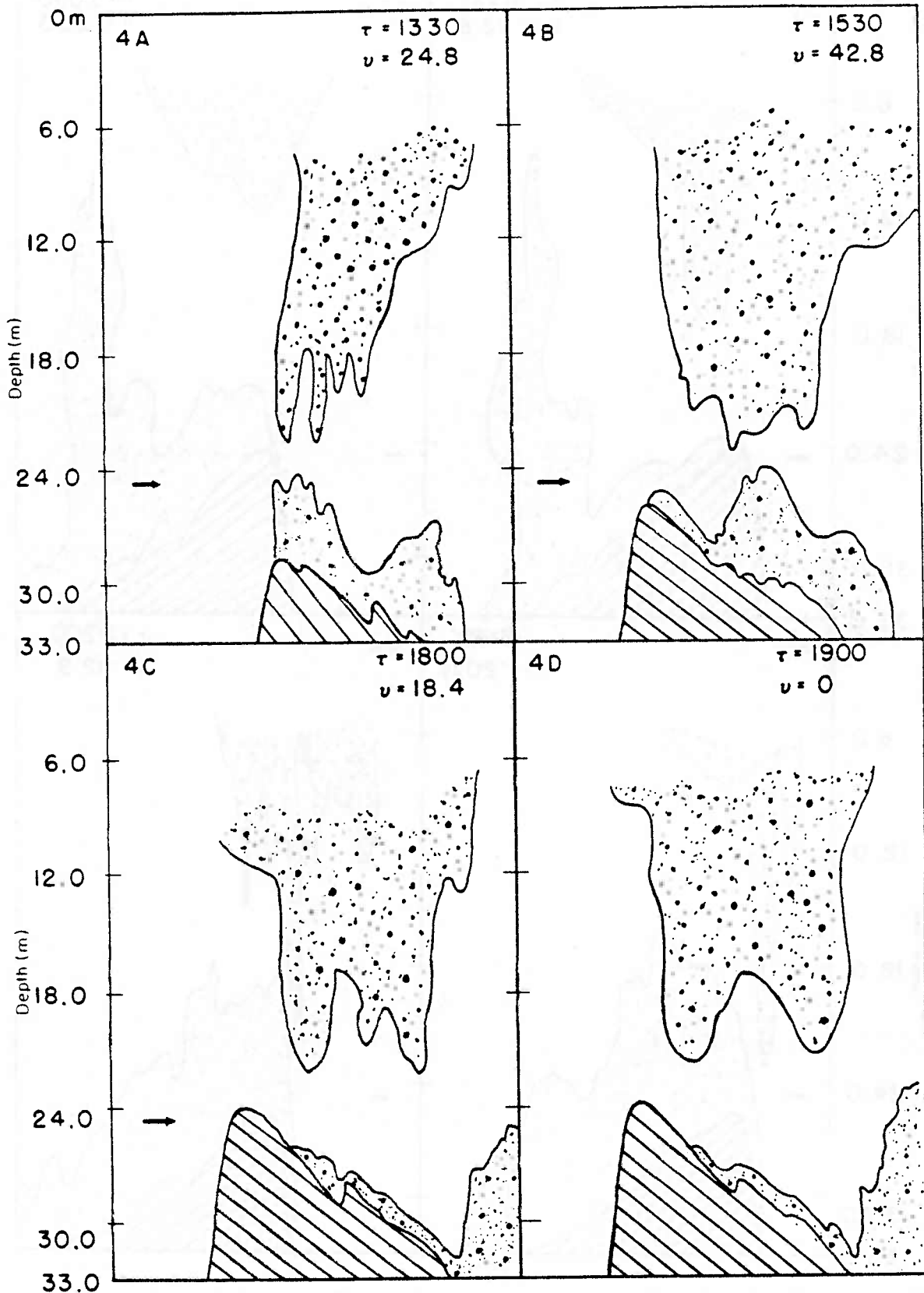


Fig. 4.4A-4D Schematic of the movement of two clear (low-scattering) regions in the acoustic images. The near-surface region is identified in the text as a lee wave. The bottom clear region may be associated with a pattern of flow separation. 4A-4D show the set-up and stationarity of the ebb tide lee wave. The patch of clear bottom water is seen to move from the sill crest to the east of the bank.

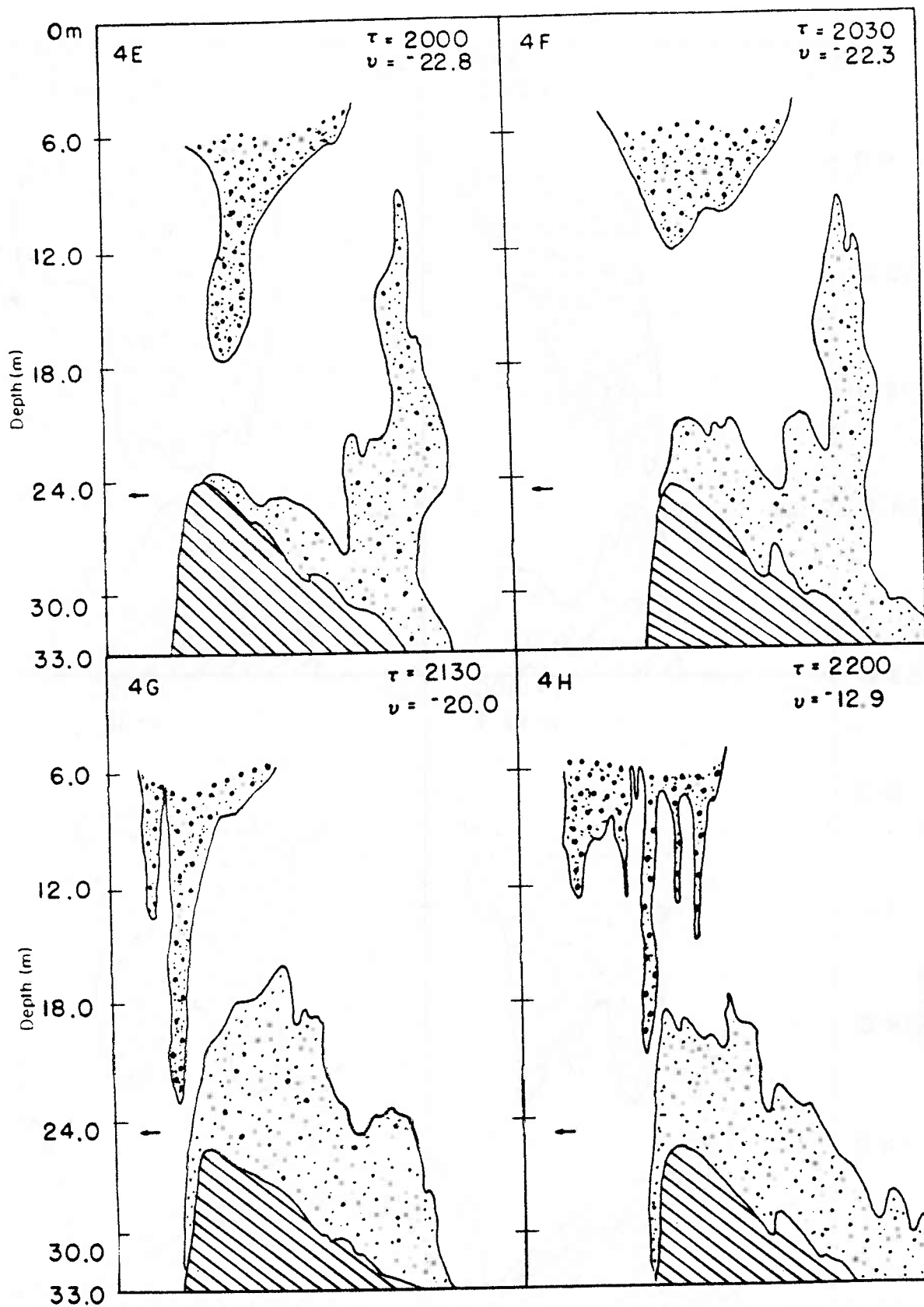


Fig. 4.4E-4H 4E-4F show the lee wave shortening and steepening; the bottom water begins to move back up the bank. 4G-4H show the set-up of 1-2 lee waves by the flood tide and the propagation of 4-5 of these lee waves as the tide turns. The bottom water has moved back up and over the sill crest. The arrows indicate the direction of the flow. The time in hours and the mean flow are marked in each schematic. These values correspond to the Froude number time series listed in Table 1.

Froude number calculations from Table 4.1. It shows the magnitude of the mean velocity component across the bank and the magnitude of the first mode internal wave phase speed. Where the current speed exceeds the phase speed, the Froude number is supercritical. The times corresponding to elements of the schematic of Figure 4.4 have been marked to indicate where each element occurs in the tidal cycle and to indicate the criticality at these times.

We observed that the lee wave on the eastern side of Stellwagen was already present when the acoustic transect began (Figs. 4.4A and 4.6). It seemed to be a single large depression. This is consistent with Maxworthy's large depression and with Farmer and Smith's single massive lee wave or jump. If shorter lee waves were present, they could have been resolved (although not shorter than 200 m) as will be seen on the flood tide response. In the Froude number sequence (Table 4.1, Fig. 4.5) this corresponded to the 6 hour time interval 1300 to 1900 hours when the mode 1 Froude number on the crest of the bank was almost always supercritical (Figs. 4.4A to 4.4D). As the tide slackened, the Froude numbers became subcritical (flow speed less than mode 1 phase speed). The lee wave remained stationary but became shorter and shallower, and finally it was no longer discernable (Figs. 4.4E, 4.4F, 4.7). This occurred rather quickly, from 1900 to 2030 hours. The time period corresponds

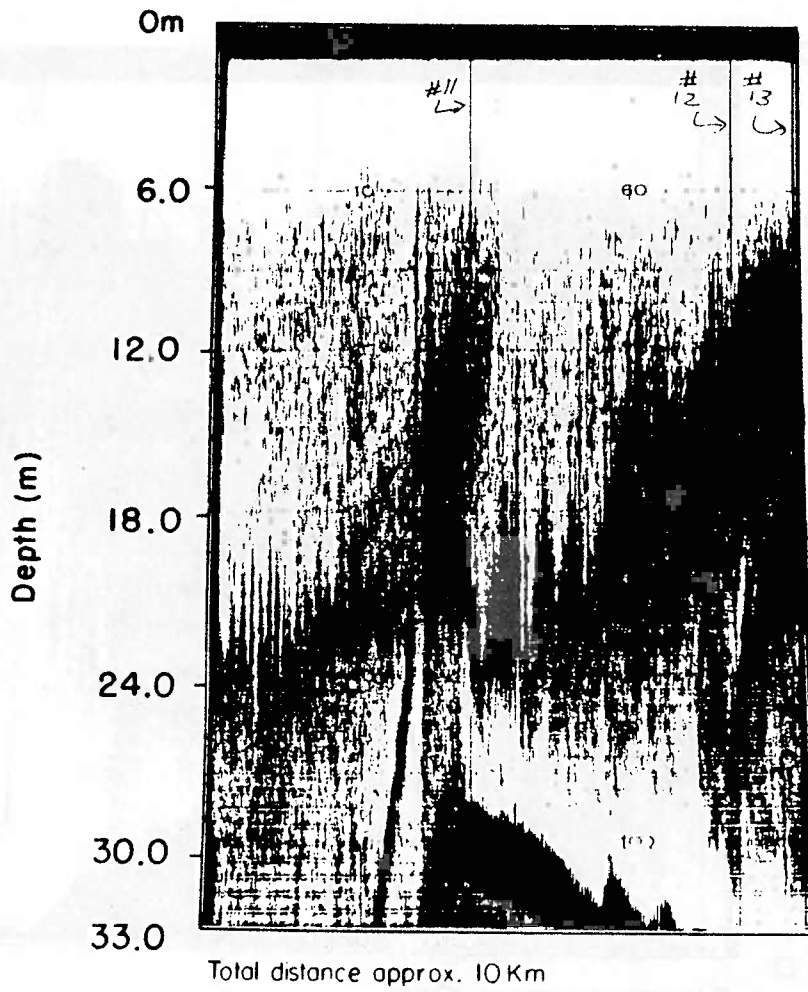


Fig. 4.6 Raytheon acoustic image corresponding to Figure 4.4A.

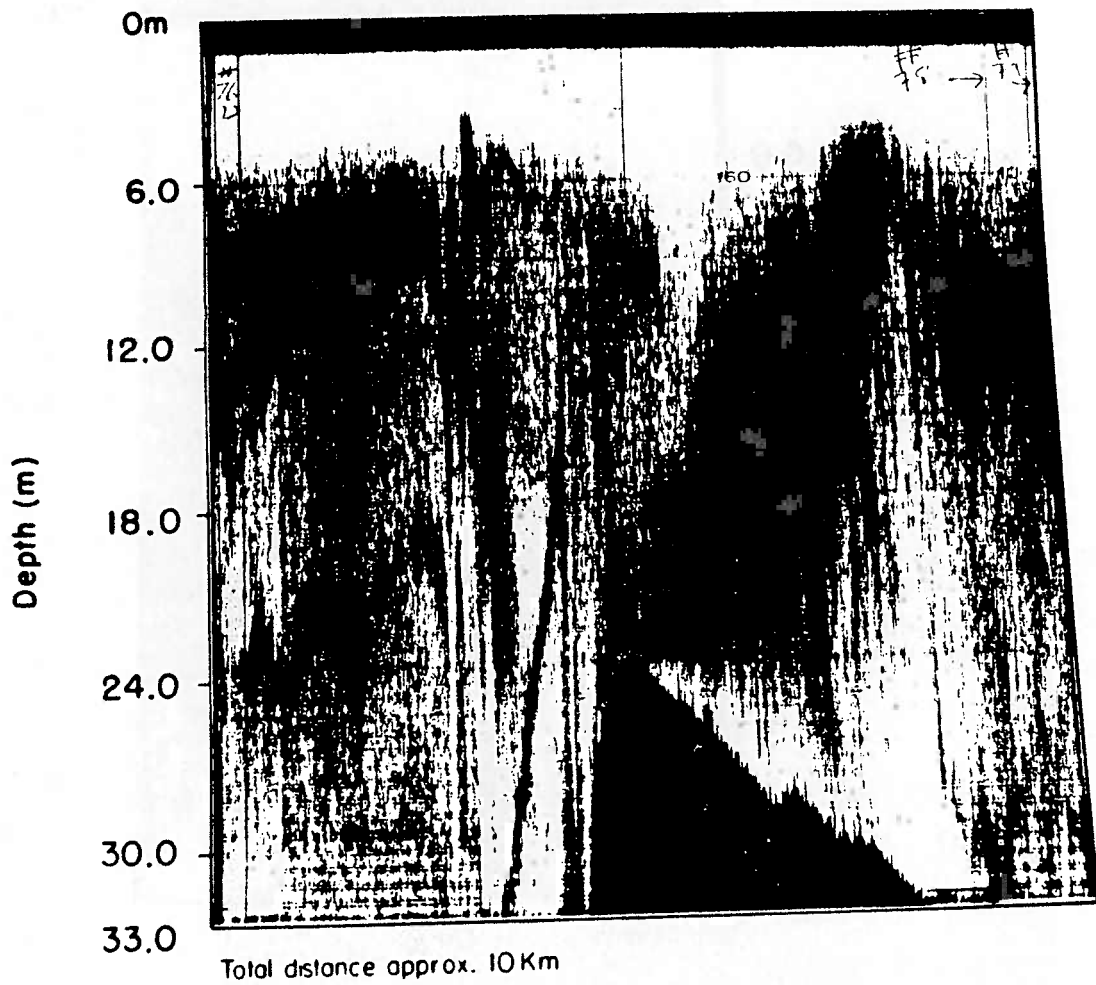


Fig. 4.7 Raytheon acoustic image corresponding to Figure 4.4E.

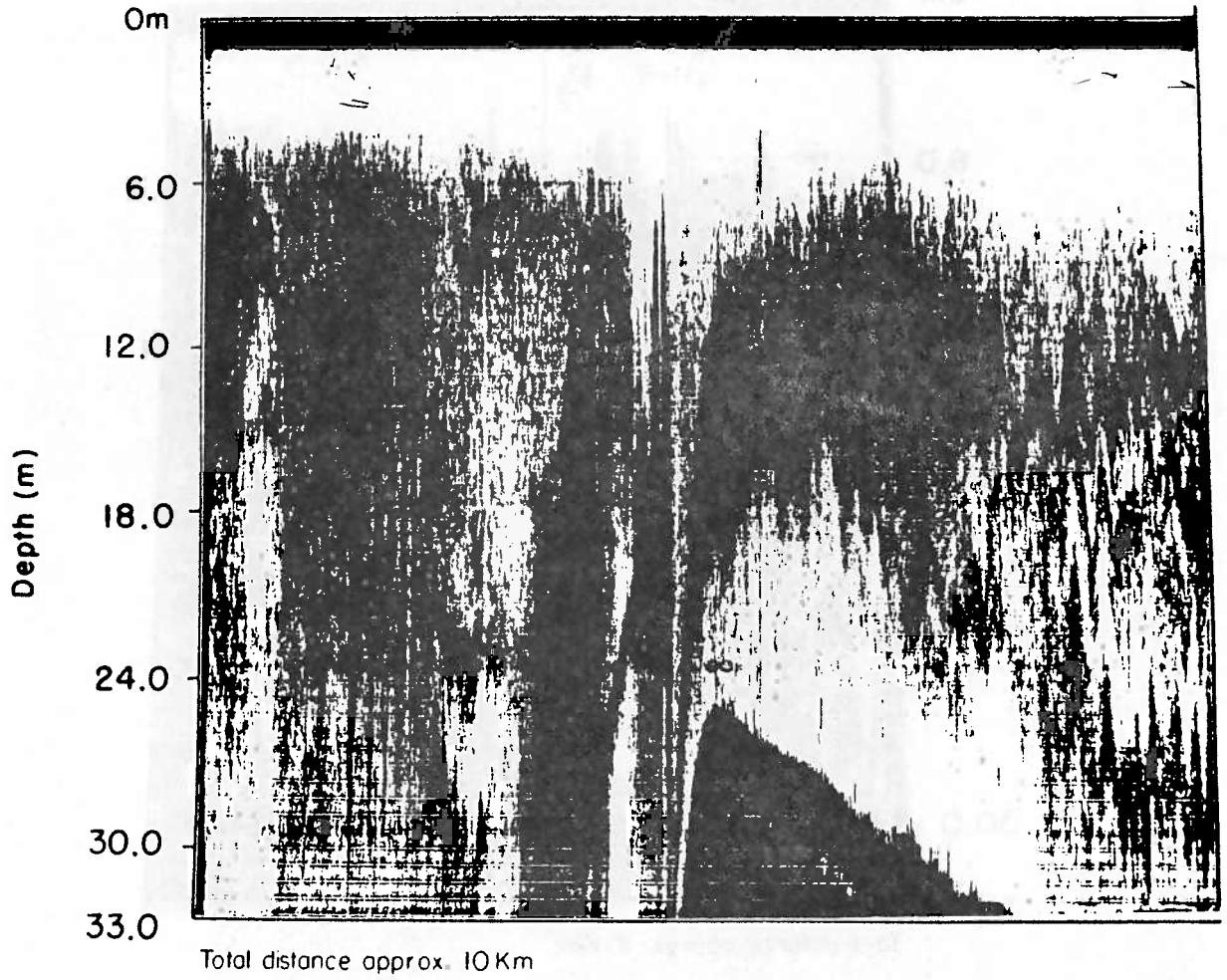


Fig. 4.8 Raytheon acoustic image corresponding to Figure 4.4G.

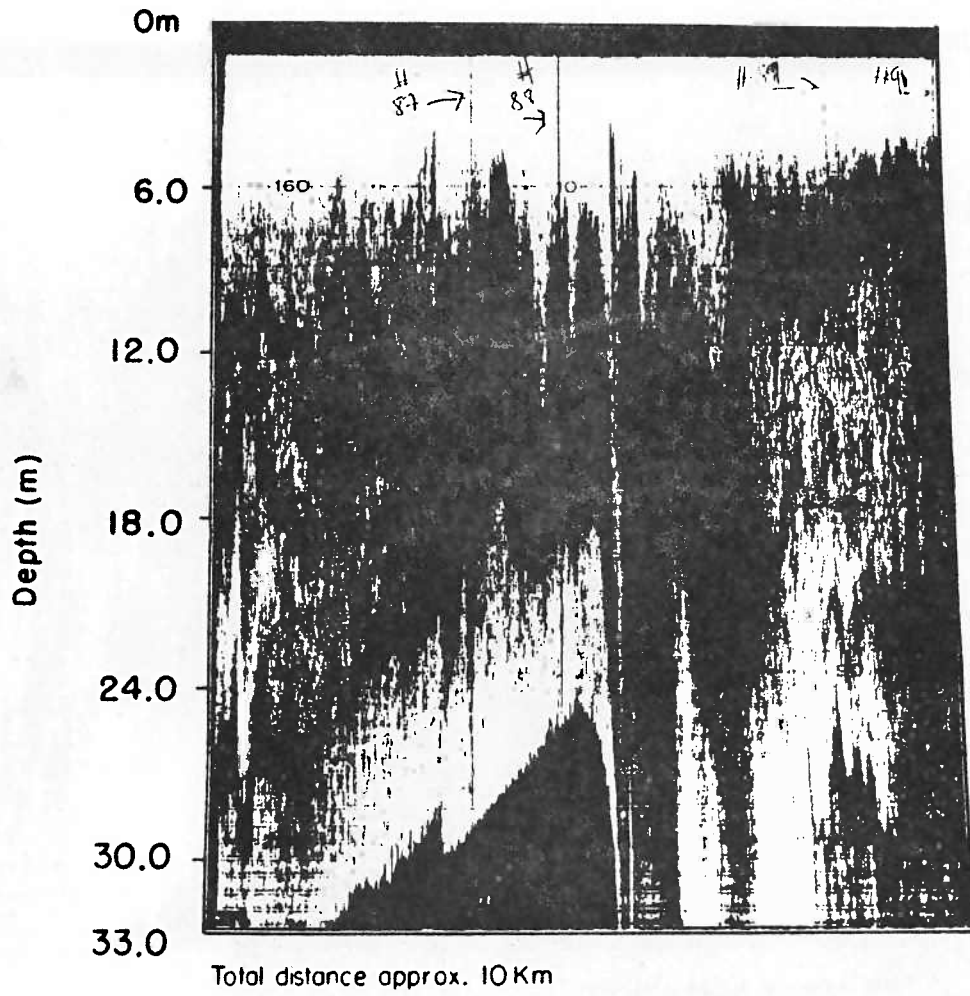


Fig. 4.9 Raytheon acoustic image corresponding to Figure 4.4H.

to subcritical flow over the crest before the tide starts to approach maximum flood.

The lee wave was not seen to propagate upstream (i.e., the low-scattering region was not seen to move upstream over the western side of the bank). We hypothesize that the lee wave disintegrates into a train of solitary waves over the crest of the bank as observed in the laboratory experiments of Maxworthy (1979). This hypothesis is based on the following observations and wave speed calculations.

The first question to answer is whether the depression could propagate quickly enough that it was missed in the acoustic transect. To make a speed estimate, we use the distance the feature must propagate to be beyond the steaming track (from points B to C, Fig. 4.1) and the maximum amount of time that the feature could have to propagate without being observed (assumes the ship is steaming east at the time the depression starts moving westward). We find that to be missed the feature must move westward at a speed of -139 cm/sec. This speed estimate does not take into account the advective speed of the flow which ranged from 0 cm/sec at 1900 hours to -22 cm/sec (westward) at 2030 hours. The advective speed is taken from the mean velocity over the crest and thus represents an upper bound on the flow in the Bay. The time interval 1900-2030 hours is examined since this was when the

feature disappeared over the eastern side of the bank.

We can compare this speed with two estimates of phase speed. The estimates were calculated using the relation given by Benjamin (1966) for finite amplitude internal waves in a 2-layer fluid. The layer depths, wave amplitude and density difference were taken from measurements made in the deeper water of the Bay immediately west of the sill crest. The speed of an infinitesimal long wave, the fastest linear wave, is calculated to be 45 cm/sec. The nonlinear-dispersive (KdV) phase speed is 58 cm/sec. Despite the large possibility for error in the estimates and including the advective speed of the flow, it seems unlikely that the propagation of the massive lee wave would have gone undetected.

We can check the consistency of the KdV speed with another estimate of the packet speed based on an observation of the high frequency wave group at point C (Fig. 4.1). First we briefly describe the observation. The waves were observed at point C using a thermistor suspended from the side of a freely drifting ship. The onset of the wave packet was marked by an abrupt rise in temperature recorded by the thermistor coincident with a downward plunge of the scattering layer in the acoustic record (Fig. 4.10) and the advance of a pattern of surface slicks oriented parallel to the bank axis. The period of the waves was approximately 10 minutes. The

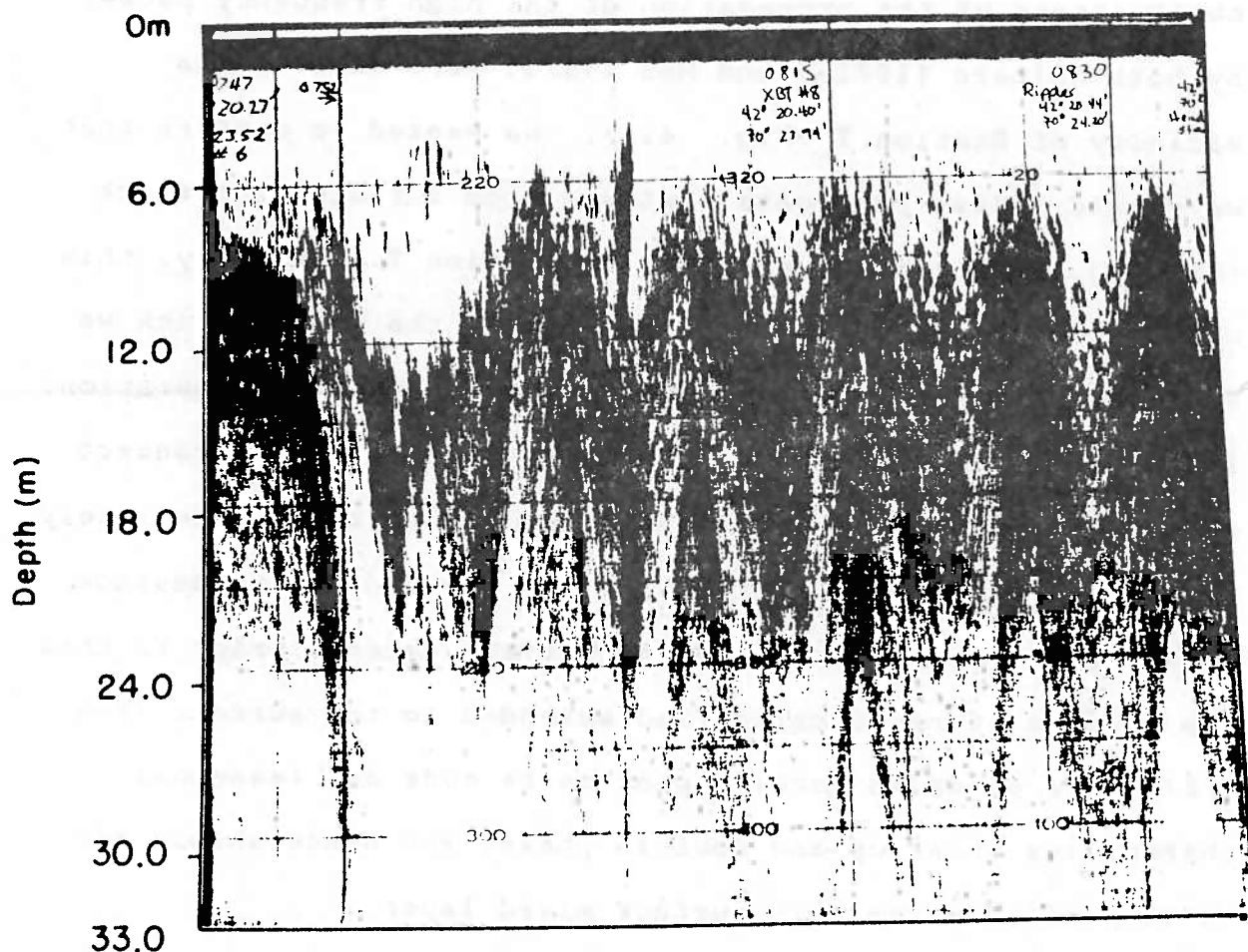


Fig. 4.10 Raytheon acoustic image of high frequency internal wave packet observed while ship was freely drifting 5 km west of Stellwagen at point C.

motivation for this observation was twofold. Prior observations of the propagation of the high frequency packet by both Halpern [1971a] and HBO [1979] were made in the vicinity of Station T (Fig. 4.1). We wanted to confirm that waves did indeed propagate westward from our steaming track (CD, Fig. 4.1) which was north of Station T. Secondly, this observation fixed a time and position of the packet which we will now use in determining the timing of the wave generation. It should be mentioned that the continuous acoustic transect over a complete tidal cycle was scheduled to begin immediately after this packet observation but was delayed due to passage of a storm. The storm mixed the surface layer; prior to this the seasonal stratification had extended to the surface (Fig. 4.3). The observed waves appear to be mode one (seasonal thermocline moves up and down in phase) and hence should not be very affected by this surface mixed layer.

From the observed packet arrival we can project subsequent arrivals since the waves are tidally generated. We estimate a packet speed taken as the ratio of distance to time defined as follows. The distance is from the sill crest to point C. The time interval is from when the Froude number first became subcritical on the crest until the projected packet arrival at C. With error bars of (+/-) a half hour we find lower and upper estimates of the packet speed to be 44 and 62 cm/sec, respectively. This estimate disregards the

mean flow advection. We note that if the packet starts to propagate much earlier than estimated, the mean flow is large and against the waves (mean flow is of order 40 cm/sec east). If the packet starts to propagate later than estimated, the mean flow is directed westward and will advect the packet. Hence, the phase speed probably falls within the calculated bounds. These bounds are consistent with both the linear long wave and KdV phase speed estimates.

From the above observations and estimates, we conclude that the large scale depression did not propagate westward as a massive lee wave. Rather, at the time it disappears from our acoustic record, it disintegrates into a train of large amplitude high frequency internal waves which we can no longer resolve in our record, but whose speed we can estimate from both theory and observations. These estimates show that the observed packet speed is consistent with KdV theory. Some additional support for this immediate breakup of the front of the massive lee wave into large amplitude high frequency waves comes from two acoustic observations taken by Orr (personal communication). The positions of the observations are shown in Figure 4.1 and are located on the crest of the bank. They were made by a 200 kHz acoustic backscatterer with much higher resolution than the Raytheon. Orr observed the packet at these locations which correspond to our proposed site of wave packet generation (on the crest). However, whether the timing

of his observations is consistent with the tide has not been verified.

Finally, we note that it is impossible to identify uniquely the feature that remained stationary behind the sill. Perhaps a succession of lee waves, each with a correspondingly slower velocity, was generated in the lee of the bank as the flow speed decreased. The front of each of these lee waves may have disintegrated into a train of finite amplitude high frequency waves.

Between 2100 and 2130 hours we saw the rapid setup of 1-2 lee waves on the western side of Stellwagen formed by the flood tide (Figs. 4.4G,4.8). They were about one fifth the scale (half to one kilometer) of the ebb tide lee wave. There was no XBT section to compare temperature with this feature. By 2200 hours a train of 4-5 lee waves appeared to be propagating over the crest into the decreasing flow (Figs. 4.4H,4.9). This is consistent with the Froude number series which shows the flow over the crest to be subcritical. It was quite different from the ebb tide lee wave in both scale and duration. The flood tide lee waves appeared over the western side of the bank for less than 2 hours as opposed to 6 hours on ebb.

The second feature that was followed in the acoustics is

the clear region on the bottom. As the tide approached maximum ebb, this feature was seen to move off the crest of the bank to the east (Figs. 4.4A,4.4B). It continued to move eastward even as the tide slackened (Figs. 4.4C,4.4D). As the ebb tide lee wave became shorter and shallower, the fluid moved back over the crest (Figs. 4.4E,4.4F). Eventually, it seemed to cascade over the sill (Figs. 4.4G,4.4H). This may indicate that the flow is not blocked. Additional remarks regarding the relation of this feature to the flow separation observed by Farmer and Smith will be made in the discussion.

4.4 DISCUSSION

Halpern's field observations of the waves which propagate into the Bay motivated two theoretical/experimental studies aimed at describing the generation of these finite amplitude waves from an initial disturbance. The first of these, by Lee and Beardsley (1974), associated the generation with the flood phase of the tide (flow directed from the Gulf of Maine into Massachusetts Bay). The generation is described in three phases. First, it is postulated that a warm front forms from a partial blocking of the incoming stratified flow over the bank. Second, this large amplitude propagating front steepens nonlinearly. Thirdly, the front disintegrates into a train of solitary waves which result from the interplay between the

nonlinearity and the dispersion of the steepening front. Lee and Beardsley modelled the evolution of such a solitary wavetrain from a front-like initial disturbance numerically using an internal Korteweg-deVries equation. The solutions were compared with laboratory experiments for the second and third phase of the proposed generation mechanism. Comparison with Halpern's field data was also done for the end of the third phase. These comparisons seemed to give reasonable agreement with the observations.

Halpern's field observations and the explanation given by Lee and Beardsley motivated a second study by Maxworthy [1979]. Maxworthy proposed that the waves were actually formed from a disturbance created on the ebb phase of the tide (the opposite phase from Lee and Beardsley's explanation). He suggested the following sequence for the generation. The ebb tide produces a supercritical flow over the bank which creates a downstream depression or lee wave behind the submarine sill. As the tidal flow slackens and turns, the depression advances over the crest. The front of the depression disintegrates into a train of solitary waves that propagate upstream into the decreasing flow and evolve according to KdV-type dynamics. This physical situation was simulated in a laboratory model by towing an obstacle through a stratified fluid over one half of a tidal cycle. The period of oscillation was varied. The amplitude of the tidal cycle and the ambient stratification

were kept fixed. The flow was characterized in terms of an internal Froude number; two regimes were found. The first regime is for Froude numbers exceeding F_{rm} (m denotes mixing). For this case the amplitude of the quasi-stationary disturbance in the lee of the obstacle becomes so large that it breaks and mixing occurs. As the tide slackens and turns, waves propagate in both directions. Wave generation is hypothesized from two different mechanisms. Some are generated from the nonlinear evolution of the front. They advance upstream into the decreasing flow and evolve as solitary waves. Others are generated from the collapse of the mixed region. They propagate in both directions and are much weaker. For lower values of the Froude number, no mixing takes place. Only the solitary wavetrain is seen to evolve in the direction of decreasing flow. As the Froude number decreases a critical value, F_{rc} , is reached below which no waves are formed. By fitting observations to a sech^{**2} initial condition, the number of solitary waves are estimated for both the experiments and Halpern's field observations. Reasonable agreement is obtained for the experiments. Although Maxworthy also claims reasonable agreement with the field observations, the number he gives seems at least twice the observed number of waves. He gets 60 as his estimate. Both by counting Halpern's waves and by estimating the number of 6-8 min period oscillations that can occur in the 2.5 hour span over which the waves are seen yields about 30 as an upper

estimate. However, the main area of contention between Maxworthy's explanation and that of Lee and Beardsley lies in the phase of the tide that generates the disturbance. They are in agreement on the evolution of the front into a series of solitary waves according to nonlinear-dispersive theory. Due to the different phase of the tide, the position of generation also differs. Lee and Beardsley's hypothesized evolution occurs inside the Bay west of the bank. Maxworthy's waves are observed in the experiments to form directly over the crest of the obstacle as the front of the disturbance starts to come across.

From our experiment in Massachusetts Bay the waves which propagate into the Bay appear to evolve according to Maxworthy's hypothesis. They seem to be generated by the steepening of the front of a large depression formed on ebb tide. The front appears to disintegrate directly over the crest of the bank. The nonlinearity of the waves and the consistency of the phase speed estimates together with the steepening and shortening of the stationary front point towards an evolution governed by nonlinear-dispersive theory. However, based on Maxworthy, this theory seems to overpredict the number of waves. Also, the waves seem more weakly dispersive than might be expected. This is pointed out by Farmer and Smith for Maxworthy's results: they calculate that the amplitude dispersion of the solitary waves should cause

them to separate more rapidly than is observed. This weak dispersion seems to be present in Massachusetts Bay also. With the possible exception of the leading waves, the wavelength within the group remains fairly uniform. From three different sets of observations, each made in different years and at different locations, we find a wavelength of 200 meters. Halpern observed a wavelength of 200 m at Station T, 9 km west of Stellwagen (Fig. 4.1). In their KdV model, Lee and Beardsley estimated the location of the initial front based on the wavelength and amplitude observed at Station T. They estimated the front location to be 5 km west of Stellwagen, which is the site of our observation of the packet. The wavelength there was already of order 200 meters. Lee and Beardsley made further field measurements and observed the packet at a point 11 km west of the bank and found a wavelength of 200 m. Of course, each of these observations was made in different years.

There are also several similarities between the ebb tide response and the quasi-steady lee wave theory of Farmer and Smith. They see two different types of response to tidal flow over the sill in Knight Inlet. The first type is most like the ebb response in Massachusetts Bay and is characterized by a single large isopycnal depression behind the sill. They use the term hydraulic jump to describe this response; it could also be a large breaking lee wave. It forms when the Froude

number is critical or just supercritical with respect to the lowest mode and supercritical with respect to all higher modes. The length scale of their jump is the same as the length of the sill. We see the same type of length scale and Froude number dependence in Massachusetts Bay. When the tide slackens and turns, they see this jump collapse to form an undular bore which propagates upstream into the decreasing flow. Farmer and Smith disagree with Maxworthy's appeal to nonlinear-dispersive theory to account for the generation of the wavetrain. They see linear lee wave theory as accounting for most of the observed features of both their observations and his experiments. However, our observations seem to support the evolution of a solitary wavetrain from the observed steepening of the apparently stationary front.

The flood tide response in Massachusetts Bay is best described by Farmer and Smith's second type of response. This second type is the formation of a lee wavetrain behind the sill. This response is obtained for Froude numbers subcritical with respect to the lowest mode but supercritical with respect to higher modes. The length scale of the waves is much smaller, on the order of the sloping portion of the topography. We see the same Froude number dependence. Our observed length scale is also smaller due to the bank's asymmetry. Flow separation plays an important role in this second type of response.

In Knight Inlet, the generation of lee waves appears delayed by flow separation on the downstream face of the sill (perhaps by smoothing the obstacle shape as the flow sees it). When the lee wave reaches some critical length, flow separation is suppressed by the modification of the pressure field on the downstream face of the sill by the accelerating flow. Then a train of lee waves is able to form behind the sill, controlling the boundary layer separation as the flow speed drops. In Massachusetts Bay, the behavior of the second clear feature in the acoustic record, the patch of low-scattering bottom water, may indicate a similar pattern. In brief, although our acoustic images are not clear enough to detect the flow separation boundary, the bottom water we observe is probably behind the separation, and its movement indicates a possible flow pattern. If this is indeed the case, then a possible explanation for the low-scattering properties of this patch of bottom water may be from the turbulent mixing that takes place behind the separation point from shear flow instabilities. In Figure 4.4A the patch of water was observed on top of the sill crest, indicating flow separation also occurring close to the crest. The lee wave was already present. It may be the formation of the lee wave and its continued presence that modifies the pressure field and suppresses flow separation. By suppression we mean that flow separation moves downstream of the crest, as shown by the movement of bottom water to the east (Figs. 4.4B-4.4D). As

the flow speed drops and the front shortens and steepens, the bottom water advances up the sill, indicating possibly that flow separation occurs near the crest again (Figs. 4.4E-4.4H).

4.5 SUMMARY

This study in Massachusetts Bay shows the importance of in-situ observations in determining the flow response in a complex physical situation. The large amplitude and asymmetry of the topography are seen to be crucial elements to the behavior that was observed. There are few theoretical or laboratory studies which examine these effects. The response on ebb tide is consistent with the laboratory experiments of Maxworthy (1979) and shows the formation of a single massive depression in the thermocline downstream of the sill. As the tide slackens and turns, the front of this depression disintegrates and gives rise to a train of solitary waves. The formation of a single depression when the Froude number is supercritical with respect to all internal modes agrees with the observations by Farmer and Smith in Knight Inlet (1980a). The evolution of a wavetrain according to nonlinear-dispersive theory disagrees with Farmer and Smith's model for the propagation of a lee wavetrain. However, a lee wavetrain best describes the flood response. On this phase of the tide, a lee wavetrain forms downstream of the sill and propagates

upstream into the decreasing flow when the tide turns. The Froude number during maximum flood is just subcritical with respect to the lowest internal wave mode and supercritical with respect to all higher modes. Besides the difference in Froude numbers, the response length scale and duration also differ markedly between the two phases of the tide due to the asymmetry of the bank. The time and length scales on ebb tide are longer than those on flood; the length scales on the respective phases of the tide are on the order of the topographic slope.

As in previous studies, we have tried to classify the behavior with a Froude number dependence. In a continuously stratified fluid, where a finite amplitude disturbance is generated by flow over a large amplitude obstacle (with the possibility of upstream influence or partial blocking), it is unclear what the appropriate parameter for describing the flow should be. To our knowledge, the study by Farmer and Smith was the first to attempt such a classification of oceanic sill flows. Our Froude number results for the ebb and flood tide fall into the two main types of response categorized by them and seem to give good agreement with their observed behavior, despite the considerable difference in topography and stratification. Additional oceanic observations in differing situations are needed to obtain a more complete classification.

CHAPTER 5

CONCLUSIONS

In this thesis we have applied some of the wealth of existing theory of nonlinear waves to observations of surface and internal wave group development.

5.1 SURFACE WAVES

The surface wave observations show the long-time development of surface gravity wave packets in a laboratory wave channel. The groups examined are constant amplitude, single frequency wave groups for a variety of initial wave steepnesses and group lengths. The evolution of amplitude, phase and frequency modulations with distance is described. The modulations were obtained using the Hilbert transform.

The most important effects that we observed were the cumulative effect of dissipation and, for groups of sufficient steepness, the downshifting of the carrier frequency. At the

final observation, the wave packet's energy was typically 25 per cent of its initial value. Damping coefficients estimated from the observations were in reasonable agreement with theoretical estimates. The downshifting in wave groups is different from that previously observed in continuous wavetrains. Although the peak frequency downshifts, as estimated from maximum entropy spectral estimates, not all the groups have the downshifted frequency. Rather, the modulation sorts into a succession of groups. The leading groups are of larger amplitude and lower frequency than the trailing groups which are of the initial carrier frequency.

There is almost no variation in the initial phase or frequency modulation within the group, as imposed at the wavemaker. Small variations are seen to develop with propagation distance as well as small regions of quite large variation. These regions of large variation correspond to local reversals in phase or jumps located at local amplitude minima. At times of minimum modulation, the phase is fairly uniform. When the modulation is growing or decaying, with amplitude minima or nodes located within the group, we see jumps in phase at node positions. Melville (1981) has suggested these jumps may be the mechanism of crest pairing observed by Ramamonjiarisoa and Mollo-Christensen (1979). Crest pairing may be the visual manifestation of the frequency downshifting.

The amplitude and phase modulations at the most upstream value of fetch were specified as an initial condition to the cubic nonlinear Schrodinger equation, which was then allowed to evolve numerically. A dissipative form of the NLS equation was also solved numerically, with damping coefficients estimated from the observations. By analyzing the evolution of exact asymptotic solutions it was seen that the phase modulations could be used to characterize the type of behavior: linear dispersion, soliton, bound state, etc. We used the exact solutions as a guide in interpreting and comparing the long-time observations with the numerical model evolutions.

It appears that dissipation rules out the possibility of recurrence. The bound state was not observed in the sense of recurrence of the initial condition, but the wave groups did exhibit long-time coherence. This could be best be seen in the phase evolution. Dissipation typically becomes important over half the evolution distance. The frictional NLS equation modelled the long-time evolution extremely well. Although the form of the dissipation term had a direct effect only on the amplitude modulation, there was an indirect effect on the phase.

Some problems for further study are suggested by these results. Careful experiments to examine the dissipation of

surface waves are needed. In particular, an investigation of the effect that a higher order dissipation might have on wave phase, dispersion and frequency downshifting is suggested as a consequence of our results. Another question we pose is that of the mechanism of the frequency downshifting. Finally, an application of nonlinear wave theory, in light of experimental investigations, to ocean waves is needed. Demodulated surface swell (using the Hilbert transform) from the CODE experiment exhibits the characteristics of weakly nonlinear waves (Bill Grant, personal communication). These are the only ocean data that we are aware of to be analyzed in this manner, and the results look quite promising.

5.2 INTERNAL WAVES

The internal wave study looked at the generation of packets of large amplitude internal waves resulting from tidal interaction with a submarine sill. The flow response was classified with a Froude number dependence as in the study by Farmer and Smith (1980a,b). The Froude number results for the ebb and flood tide fall into two different categories. The ebb response shows the formation of a single large depression in the thermocline downstream of the sill. As the tide slackens and turns, the front of this depression disintegrates and gives rise to a train of solitary waves. On the flood tide, a lee wavetrain forms downstream of the sill and

propagates upstream when the tide turns. The response length scale and duration differ markedly between the two phases of the tide, due to asymmetry of the bank. This study focused primarily on the generation. The propagation of the packet formed on ebb tide has been well documented in previous studies (Halpern 1971a,b, Haury, Briscoe and Orr 1979). The wavetrain formed on flood tide should develop differently, and its propagation has not been observed. Observation of these waves is suggested as further work. Also, additional Froude number classifications of oceanic sill flows in different situations are needed to obtain a more complete classification

REFERENCES

- Apel, J. R., H. M. Byrne, J. R. Proni and R. L. Charnell (1975) Observations of oceanic internal and surface waves from the Earth Resources Technology Satellite. *Journal of Geophysical Research*, 80, 865.
- Barnett, T. P. and K. E. Kenyon (1975) Recent advances in the study of wind waves. *Rep. Prog. Phys.*, 38, 667-729.
- Benjamin, T. B. (1966) Internal waves of finite amplitude and permanent form. *Journal of Fluid Mechanics*, 25, 241-270.
- Benjamin, T. B. (1967) Instability of periodic wave trains in nonlinear dispersive systems. *Proc. Roy. Soc. A*299, 59.
- Benjamin, T. B. and J. E. Feir (1967) The disintegration of wave on deep water. *Journal of Fluid Mechanics*, 27, 417.
- Chu, V. H. and C. C. Mei (1970) On slowly-varying stokes waves. *Journal of Fluid Mechanics*, 41, 4, 873-887.
- Chu, V. H. and C. C. Mei (1971) The nonlinear evolution of stokes waves in deep water. *Journal of Fluid Mechanics*, 47, 2, 337-351.
- Davey, A. (1972) The propagation of a weak nonlinear wave. *Journal of Fluid Mechanics*, 53, 4, 769-781.
- Davis, R. E. and A. Acrivos (1967) Solitary internal waves in deep water. *Journal of Fluid Mechanics*, 29, 563-607.
- Farmer, D. M. and J. D. Smith (1980a) Tidal interaction of stratified flow with a sill in Knight Inlet. *Deep Sea Research*, 27A, 239-254.
- Farmer, D. M. and J. D. Smith (1980b) Generation of lee waves over the sill in Knight Inlet. In *Fjord Oceanography*, ed. H. J. Freeland, D. M. Farmer and C. D. Levings. Plenum Publishing Co., N.Y., 259-269.

- Feir, J. E. (1967) Discussion: some results from wave pulse experiments. Proc. Roy. Soc. A299, 54.
- Gardner, C. S., J. M. Green, M. D. Kruskal and R. M. Miura (1967) Method for solving the Korteweg-deVries equation. Phys. Rev. Lett. 19, 19, 1095-1097.
- Gargett, A. E. (1976) Generation of internal waves in the Strait of Georgia, British Columbia. Deep Sea Research, 23, 17-32.
- Halpern, D. (1971a) Observations on short period internal waves in Massachusetts Bay. Journal of Marine Research, 29, 116-132.
- Halpern, D. (1971b) Semidiurnal internal tides in Massachusetts Bay. Journal of Geophysical Research, 76, 6573-6583.
- Haury, L. R., M. G. Briscoe, and M. H. Orr (1979) Tidally generated internal wave packets in Massachusetts Bay. Nature, 278, 312-317.
- Hui, W. H. and J. Hamilton (1979) Exact solutions of a three-dimensional nonlinear Schrodinger equation applied to gravity waves. Journal of Fluid Mechanics, 93, 1, 117-133.
- Hunt, J. N. (1952) Viscous damping of waves over an inclined bed in a channel of finite width. La Houille Blanche, 7, 836.
- Janssen, P. A. E. M. (1981) Modulational instability and the Fermi-Pasta-Ulam recurrence. Physics of Fluids, 24, 1, 23-26.
- Kay, S. M. and S. L. Marple (1981) Spectrum analysis - a modern perspective. Proc. of the IEEE, 69, 11, 1380.
- Kinsman, B. (1965) Wind Waves. Prentice-Hall, Englewood Cliffs.

- Lake, B. M. and H. C. Yuen (1977) A note on some nonlinear water-wave experiments and the comparison of data with theory. *Journal of Fluid Mechanics*, 83, 1, 75-81.
- Lake, B. M., H. C. Yuen, H. Rungaldier and W. E. Ferguson Nonlinear deep-water waves: theory and experiments. Part 2: Evolution of a continuous wave train. *Journal of Fluid Mechanics*, 83, 1, 49-74.
- Lamb, H. (1932) *Hydrodynamics*, 6th ed. Cambridge University Press.
- Lee, C. Y. and R. C. Beardsley (1974) The generation of long nonlinear internal waves in a weakly stratified shear flow. *Journal of Geophysical Research*, 79, 453-462.
- Levi-Civita, T. (1925) Determination rigoureuse des ondes permanentes d'amplitude finie. *Math. Ann.*, 93, 264.
- Lighthill, M. J. (1965) Contributions to the theory of waves in nonlinear dispersive systems. *J. Inst. Math. Appl.*, 1, 269-306.
- Longuet-Higgins, M. S. (1978a) The instabilities of gravity waves of finite amplitude in deep water I. Superharmonics. *Proc. Roy. Soc.*, A360, 471-488.
- Longuet-Higgins, M. S. (1978b) The instabilities of gravity waves of finite amplitude in deep water II. Subharmonics. *Proc. Roy. Soc.*, A360, 489-505.
- Mascarenhas, A. S. (1979) Characteristics of upper heated oceanic layer from satellite observations. M. S. Thesis, Massachusetts Institute of Technology.
- Maxworthy, T. (1979) A note on the internal solitary waves produced by tidal flow over a three dimensional ridge. *Journal of Geophysical Research*, 84, C1, 338-346.

- McClellan, J. H., T. W. Parks and L. R. Rabiner (1973) A computer program for designing optimum FIR linear phase digital filters. IEEE Trans. Audio Electroacoust., AV-21, 506-516.
- Melville, W. K. (1981) Wave modulation and breakdown. submitted to Journal of Fluid Mechanics.
- Miles, J. W. (1967) Surface wave damping in closed basins. Proc. Roy. Soc., A297, 459.
- Mollo-Christensen, E. and A. Ramamonjiarisoa (1978) Modelling the presence of wave groups in a random wave field. Journal of Geophysical Research, 83, 4117-4122.
- Mollo-Christensen, E. and A. Ramamonjiarisoa (1982) Sub-harmonic transitions and group formation in a wind wave field. Journal of Geophysical Research, S7, C8, 5699-5717.
- Oppenheim, A. V. and R. W. Schaffer (1975) Digital signal Processing, Prentice-Hall.
- Orr, M. H. (1980) Remote acoustic sensing of oceanic fluid and biological processing. Woods Hole Oceanographic Institution Technical Report 80-2.
- Osborne, A. R. and T. L. Burch (1980) Internal solitons in the Andaman Sea, Science, 208, 451-460.
- Phillips, O. M. (1977) The dynamics of the upper ocean, 2nd ed. Cambridge University Press.
- Rader, C. M. (1970) An improved algorithm for high speed autocorrelation with application to spectral estimation. IEEE Trans. Audio Electroacoust., AV-18, 439-441.
- Ramamonjiarisoa, A. R. and E. Mollo-Christensen (1979) Modulation characteristics of sea surface waves. Journal of Geophysical Research, 84, 7769-7775.

- Roskes, G. (1976) Comments on "Nonlinear deep water waves: theory and experiment". *Physics of fluids*, 19, 5, 766.
- Sahar, G. (1981) Modulation of Sea Surface Waves: Observations and Processing Methods. M. S. Thesis. Massachusetts Institute of Technology.
- Satsuma, J. and N. Yajima (1974) Initial value problems of one-dimensional self-modulation of nonlinear waves in dispersive media. *Supplement of the Progress of Theoretical Physics*, 55, 284-306.
- Schwartz, M., W. R. Bennett and S. Stein (1966) *Communications systems and techniques*. McGraw Hill.
- Segur, H. (1981) Viscous decay of envelope solitons in water waves. *Physics of Fluids*, 24, 12, 2372-2374.
- Stokes, G. G. (1847) On the theory of oscillatory waves. *Trans. Camb. Phil. Soc.*, 8, 441.
- Su, M. Y. (1980) Experiments on nonlinear instabilities and evolutions of steep gravity wave trains. (unpublished manuscript).
- Turner, J. S. (1973) *Buoyancy effects in fluids*. Cambridge University Press.
- Van Dorn, W. G. (1966) Boundary dissipation of oscillatory waves. *Journal of Fluid Mechanics*, 24, 4, 769-779.
- Whitham, G. B. (1965) Non-linear dispersive waves. *Proc. Roy. Soc.*, A283, 238-261.
- Whitham, G. B. (1974) *Linear and nonlinear waves*. Academic Press.
- Yue, D. K.-P. (1980) Numerical study of Stokes' wave diffraction at grazing incidence. Ph.D. Thesis. Massachusetts Institute of Technology.

- Yuen, H. C. and W. E. Ferguson (1978) Fermi-Pasta-Ulam recurrence in the two-space dimensional Schrodinger equation. *Physics of Fluids*, 18, 8, 956-960.
- Yuen, H. C. and B. M. Lake (1975) Nonlinear deep water waves: theory and experiment. *Phys. Fluids*, 18, 8, 956-960.
- Yuen, H. C. and B. M. Lake (1976) Reply to comments of G. Roskes. *Physics of Fluids*, 19, 5, 767.
- Yuen, H. C. and B. M. Lake (1980) Instabilities of waves on deep water. *Ann. Rev. Fluid Mech.*, 12, 303-334.
- Zakharov, V. E. (1968) Stability of periodic waves of finite amplitude on the surface of a deep fluid. *J. Appl. Mech. Tech. Phys.*, 9, 2, 190-194.
- Zakharov, V. E. and A. B. Shabat (1972) Exact theory of two-dimensional self-focusing and one-dimensional self-modulation of waves in nonlinear media. *Sov. Phys. JETP*, 34, 1, 62-69.

BIOGRAPHICAL STATEMENT

Teresa K. Chereskin was born in 1954 in Berwyn, IL. She attended Augustana College in Rock Island, IL. and the University of Wisconsin-Madison. She received a Bachelor of Science degree in mathematics from the University of Wisconsin in 1976. She worked for the U. S. Forest Service as a research computer programmer at Forest Products Laboratory in Madison for one year. She entered the Massachusetts Institute of Technology/Woods Hole Oceanographic Institution Joint Program in physical oceanography in June 1977.